ESRF HIGHLIGHTS
2009

A light
for science

ESRF

A LIGHT FOR SCIENCE

HIGHLIGHTS
2009

ESRF

European Synchrotron Radiation Facility

Dear Reader,

2009 has been an important and successful year for the ESRF, filled with events confirming its outstanding scientific activities and preparing an even brighter future with the start of the Upgrade Programme. Technically, the ESRF has performed better than ever before, making possible the many scientific achievements of users and staff that are illustrated by the examples and facts and figures within this edition of the Highlights. The Upgrade Programme is reaching full speed and important progress has been made. We are very thankful to the ESRF staff, who rise to the double challenge to deliver excellent user support and frontline science and at the same time build the ESRF of tomorrow.

The number of proposals, experimental sessions, user visits and publications in peer-reviewed journals were once more higher than in any previous year. Details on user operations are outlined in the chapter on *Facts and Figures*. The six beamlines for Macromolecular Crystallography were in the limelight on 7 October 2009 when two long-term users of the ESRF won the Nobel Prize in Chemistry. Ada Yonath of the Weizmann Institute in Israel and Venki Ramakrishnan of the MRC Laboratory of Molecular Biology in Cambridge, two long-term users of the ESRF, received this award together with Thomas Steitz, from Yale University in Connecticut, for their study of the structure and function of the ribosome. Ada and Venki have been regular visitors to the ESRF since the early days and during the last year their teams came once a month on average, bringing around 500 samples each time for analysis. The other scientific areas have been very successful too, both the traditional disciplines such as materials science and soft matter systems, and the new fields of application of synchrotron radiation such as palaeontology and environmental sciences.

The accelerator and X-ray source complex delivered more than 99% of scheduled beam time to users for the first time ever. According to our data, this record figure has never been equalled at any synchrotron radiation facility in the world. 2009 has also been the best year in terms of mean time between failures and average duration of a failure. This achievement is the result of many years of experience in operating and maintaining the accelerator complex, which has been obtained despite many challenges in vacuum and radio frequency (RF) technologies. A new beam position monitoring system has been installed and commissioned. It has a much higher sensitivity and will result in an improved beam stability once the renovation of the orbit correction system has been completed. Similarly, a new electron gun for the LINAC injector has improved the bunch timing purity from the injector. Within the Upgrade Programme, important contracts have been established for the procurement of a new high power RF amplifier system based on solid-state amplifiers, and for three prototypes of a new RF cavity featuring strong high-order-mode damping.

The construction of a new data centre has started in the Central Building. It will enable the ESRF to contend with the increasing computing needs in synchrotron science. With imaging detectors becoming more readily available on all beamlines, and with their spatial and time-frame resolution increasing steadily, real-time data processing and reduction, as well as data storage, require extraordinary resources for computation power and storage memory. The new data centre will become operational in 2011.

The progress of the Upgrade Programme is outlined in a dedicated chapter. A key event in 2009 was the signature of the contract for the Experimental Hall extension, which marked the end of a long and difficult process to identify strict criteria for the floor stability, and the need for new laboratory and office space within the limits dictated by our budgetary means. In parallel, a thorough process for selecting the eight Upgrade Beamlines and the beamlines to be moved and refurbished took place with the help and involvement of the ESRF's Science Advisory Committee (SAC). As a result, our new buildings, to be completed by 2013, can be considered as tailor-made for our 2015 beamline portfolio.

The grant by French national and regional authorities (*Contrat de Projets Etat-Région*) to fund new infrastructures on the joint ILL/ESRF site was increased to 18 million Euros. A tender for three new buildings: site entrance, a restaurant extension and a 4000 m^2 Science Building for partnerships with the ILL and other leading institutes was launched. Completion of these buildings is foreseen in early 2013.

Scientific opportunities at the ESRF are continuing to grow thanks to a new agreement for the operation of BM14, a macromolecular crystallography beamline which will be operated by a consortium of scientists from the EMBL and the Indian National Institute of Immunology (NII). This new project will provide 40% of its time to the ESRF users, starting in 2010. The ESRF Council also agreed to the relocation of the *Institut de Biologie Structurale* to a new building on the joint site. This decision will strengthen even further the very successful structural biology programme presently carried out by the EMBL, ESRF, ILL and the PSB partners.

We would like to thank our Member and Scientific Associate countries, and in particular their delegates to the Council, Administrative and Finance Committee (AFC) and SAC for their continued support and trust, despite the difficult budgetary environment and competition for support between large scale research

infrastructures. A special thanks goes also to the European Commission which, by awarding the ESRFUP grant, has enabled the period 2008-2011 to proceed with crucial steps to prepare the ESRF Upgrade and in particular the positive decision of the ESRF Member Countries. We would also like to extend our special thanks to the French authorities, and in particular, the *Ville de Grenoble*, the Grenoble community – *Alpes – Métropole (METRO)*, the *Conseil Général de l'Isère* and the *Région Rhone-Alpes*, for their CPER contract grant that will greatly enhance the scientific visibility of the ESRF/ILL joint-site. We are also very grateful to the members of the Beamtime Allocation Panels and the Beamline Review Committees for their hard work to ensure the scientific life of the facility. Last but certainly not least, we wish to thank the thousands of users and the ESRF staff for the outstanding science, outlined by a few examples in the pages that follow.

P. Elleaume, R. Dimper, S. Pérez,
H. Reichert, A.E. Röhr, J. Susini, P. Thiry
and F. Sette

Status of the Upgrade Programme

The ten-year Upgrade Programme will preserve the ESRF's lead and competitiveness. It will enable significant progress in the highest priority areas of research such as nanoscience and nanotechnology, environment, energy and transport, climate change mitigation, information technology and materials engineering, biomedical research and human health, as well as fundamental research.

The Upgrade Programme addresses these challenges by developing the necessary key areas of X-ray beam technology with a considerable enhancement to the ESRF beamlines and user support facilities, whilst being complementary to the national light sources. The new beamlines will cater for the research highlight areas of Nanoscience and Nanotechnology, Pump-and-probe Experiments and Time-resolved Science, Science at Extreme Conditions, Structural and Functional Biology and Soft Matter, and X-ray Imaging. In particular, the Upgrade will give a decisive advantage in the routine use of small X-ray beams, less than 100 nm, able to probe a wide range of materials under real conditions and, often, in real time.

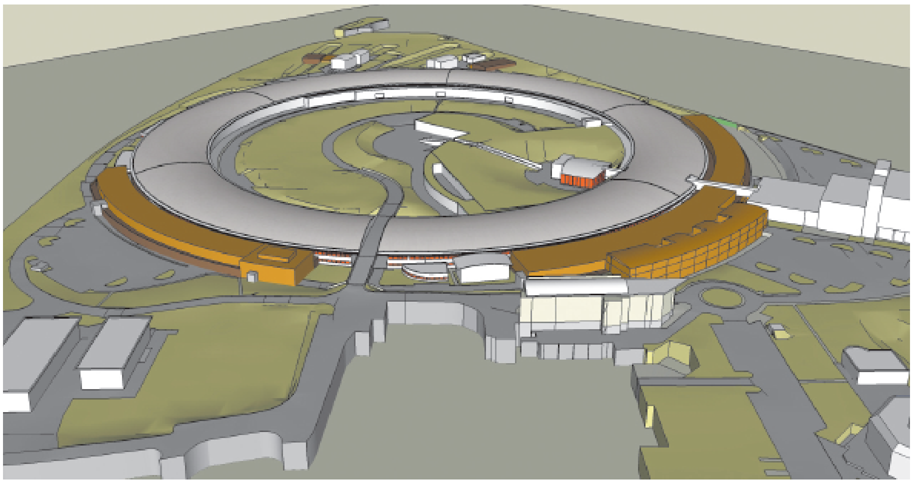

Fig. 1: Artists view of the future experimental hall (*Credit: Sud Architectes*).

Phase 1 deliverables

Phase 1 sets in place the infrastructure of buildings and the first part of the instrumentation developments and accelerator upgrades necessary for the new beamlines, and a first set of eight new beamlines consisting of fourteen end-stations.

The main deliverables are:

- Extension of the Experimental Hall for eventually up to 16 long (mostly nanofocus) beamlines and new space for experiment preparation and collaborations.
- Eight new and innovative beamlines for novel science.
- First set of improvements to the accelerator complex for higher intensity X-ray beams and continued reliability.
- First section of a programme of specialised instrumentation development to underpin the next generation of beamlines, including optics, detectors, and sample environments.
- Science-driven partnerships, embracing both academia and industry.

Progress during 2009

2009 marks the first year of the seven-year period of Phase I of the Upgrade Programme and good progress has been made in all of the five key Upgrade areas. Many important elements of the Upgrade Programme such as the Instrument Services and Development Division and the Project Coordination Service have been set in place and are already fully operational.

New buildings

In June 2009 the ESRF Council approved the award of an industrial architect contract for the extension of the experimental hall to the company Séchaud & Bossuyt. With the signature of the contract between ESRF and Séchaud & Bossuyt, the detailed design on the buildings is now underway (**Figure 1**).

Some of the challenging issues to be addressed include:

- Design of the so-called "golden" slab (~7,500 m^2). An international advisory panel of experienced slab specialists (from ALBA, SOLEIL, DIAMOND, LASER MEGAJOULE and DESY) has been formed and will advise ESRF on technical solutions for a stable concrete slab.
- Scheduling of construction works to minimise interference with user operation and to respect existing operating constraints in the experimental hall in order to limit the impact of works on the operation of the facility.
- Sustainable design approach in the building design and integration into the existing site whilst maintaining comfortable and agreeable working conditions.

Works on a new data centre have already started in the ESRF's Central Building.

Renewal of beamlines

Work on the new beamlines started with the production of Conceptual Design Reports (CDRs) for the entire beamline portfolio of 31 public beamlines. The CDRs were discussed at the SAC meeting of May 2009 and recommendations were received from SAC in July 2009. The science cases of all of the conceptual design reports were published on 5 November on the ESRF web site.

Following the review of eleven candidate Upgrade beamline (UPBL) projects by SAC and the subsequent approval by Council, the ESRF management launched the first batch of four UPBL projects. Technical Design Reports (TDRs) have been initiated for four of the UPBL projects in the following sequence:

- UPBL11: Pushing the limits of energy dispersive X-ray absorption spectroscopy towards the nano in spatial and temporal resolution.
- UPBL10: Large-scale automated screening, selection and data collection for macromolecular crystallography.
- UPBL4: Beamline for imaging, fluorescence and spectroscopy at the nanoscale
- UPBL6: High-energy resolution inelastic scattering in the hard X-ray range with micro- and nano-focus capabilities.

Upgrades to the source

The source upgrades are progressing well for a number of key areas:

- Electron beam position monitoring. The 20 year old electronics system of the 224 storage ring beam position measurement stations was renovated with significant improvements in stability measurements.
- New LINAC pre-injector. A new electron gun and associated transport system was put into full time operation in August 2009.
- Solid state power amplifiers. The order has been launched for the manufacture of a 600 kW solid state RF power amplifier for the booster synchrotron and a 450 kW system for powering three new single cell cavities to be installed on ID23 (replacement of one of the current five cell cavities that will be removed from ID07).
- RF cavity. A single cell HOM damped RF cavity, derived from the European-ALBA type cavity, has been numerically and mechanically designed at the ESRF. Three prototypes have been ordered.
- 6 m straight sections. The ID30 straight section has been lengthened to 6 metres.
- Two 7 m straight sections will be created to open the space for a new beamline on the ID07 straight section. New quadrupoles with higher field gradients have been designed and ordered. The mechanical design of the vacuum chambers is under preparation.
- Canting of insertion devices. The canting angle has been determined for each of the future canted beamlines. Different scenarios for steering have been studied. A prototype steerer has been built and field measured. A call for tender has been launched for the manufacture of modified sextupoles. A tender for permanent magnet steerers is under preparation.

Enabling technologies and instrumentation

The newly created ESRF Instrumentation Services and Development Division is at the heart of the implementation of the ESRF's project management system. The ISDD engineers and scientists have been intimately involved in the Technical Design Reports and initial feasibility studies. With the first beamlines now being approved, the programme of enabling technologies and instrumentation in X-ray optics, detectors, sample handling, and software will start.

Partnerships

During 2009 a number of partnerships and initiatives have been identified: for Soft Condensed Matter, Materials Engineering, Science at Extreme Conditions and Palaeontology. The most advanced of these is the Soft Condensed Matter Partnership with the signature of the Memorandum of Understanding between ESRF and ILL on 27 November 2009. The French authorities have confirmed their participation in the development of the ESRF and ILL site, to the level of 18 million Euros. This will be shared between a new site entrance, canteen, and, most significantly, a science building acting as a home to the Partnerships.

E. Bruas, P. Elleaume, S. Pérez and H. Reichert

Dynamics and extreme conditions

Following the reorganisation of the Experiments Division group structure in April 2009, the two high pressure beamlines ID09A and ID27 as well the Large Volume Press project joined the former High Resolution and Resonance Scattering Group to constitute the Dynamics and Extreme Conditions Group. Without forgetting the other high-pressure programmes, a large portion of high-pressure science is now conducted within our group, thus further strengthening joint efforts, developments and collaborations. Beyond this, research on the beamlines covers all classical domains of natural sciences with a significant impact in condensed matter physics and focus on applied fields such as environmental and planetary science, catalysis, soft matter, material synthesis, and nanoscience.

The highlights selected for this chapter represent only a small sub-set of many exciting results which have been published over the course of 2009. They reflect the broad spectrum of scientific applications, and clearly confirm previously witnessed trends; (i) the combination of synchrotron-based techniques with additional probes such as Raman and infrared spectroscopy, and resistivity measurements, and (ii) the importance of theoretical calculations in support of the experimental results.

The first part of the chapter is dedicated to high pressure structural studies. The first two contributions feature studies on FeSe and $SrFe_2As_2$, combining X-ray diffraction at high pressures and low temperature with resistivity measurements. Here, pressure was used to effectively tune interatomic interactions and study their effect on the magnetic order and atomic structure in this class of novel superconductors. Using the same experimental techniques, the third contribution clarified the role of structural distortions and spin degrees of freedom in the metal-insulator transition in $TbBaCo_2O_{5.5}$. The structure determination of the oxygen η- and ζ-phase underlines the advantages of single crystal work, revealing an amazingly complex arrangement of atoms.

The second part of the chapter focuses on electronic and magnetic structure and dynamics. The first example exploits the isotope selectivity of nuclear resonance scattering to determine the chemical and magnetic state of an iron oxide layer grown *in situ*. The study reveals how the anti-ferromagnetic state of a layer only 2 nm thick can be stabilised by the surrounding ferromagnetic iron. The second contribution presents a combined X-ray absorption near edge structure (XANES) and X-ray emission spectroscopy (XES) study on sulphur-bearing compounds. It is highlighted that XES provides a powerful tool to precisely determine the valence state, and to quantify the amount of sulphur species in heterogeneous systems. The following two articles address fundamental issues. Using resonant inelastic X-ray scattering, the argon 1s3p double photoexcitation spectrum was studied in detail, and resonant contributions could be separated from other multielectron processes, thus providing valuable input for a detailed comparison with model calculations. The study of the dielectric response of potassium valence electrons by inelastic X-ray scattering (IXS) reveals large deviations from a free-electron behaviour which can be attributed to empty electronic bands of d symmetry.

The last part of the chapter is devoted to phonons and collective atom dynamics. The work on the high-frequency dynamics in glasses clearly underlines how important high energy resolution is. This holds true not only for the present example of an IXS study in which a resolution of 1.3 meV could be achieved, but also for nuclear inelastic scattering where already sub-meV resolution is being reached. A concept to push the energy resolution further down to 0.1 meV is discussed in the Enabling Technologies chapter.

The last two contributions are devoted to geophysical applications. The work on Fe_3C concludes a series of experiments to determine the density dependence of the sound velocity in iron and iron-bearing compounds with the aim to predict the amount of light elements present in Earth's inner core. Finally, the IXS study on stishovite exploits a novel methodology to extract the complete lattice dynamics from polycrystalline materials, therefore allowing, for example, the determination of the full elasticity tensor.

Besides on-going research and developments on the beamlines, related activities kept the momentum high. The ID18 and ID22N nuclear resonance stations were reviewed in fall 2009. Furthermore, work on the technical design report for UPBL6 (IXS from electronic excitations) has started. Two meetings were held to discuss a possible partnership for extreme conditions science, which would allow users of the ESRF and ILL to access the best possible instrumentation and environment. The case has been presented to the ESRF Science Advisory committee and was well received. It is hoped that a Memorandum of Understanding will be signed in 2010.

M. Krisch

High-pressure studies

High temperature superconductivity in the high pressure phase of FeSe

Principal publication and authors
G. Garbarino (a), A. Sow (b), P. Lejay (b), A. Sulpice (b), P. Toulemonde (b), M. Mezouar (a) and M. Núñez-Regueiro (b), *European Physics Letters*, **86**, 27001 (2009).
(a) ESRF
(b) Institut NEEL, CNRS & Université Joseph Fourier, Grenoble (France)

In March 2008, the discovery of superconductivity with a critical temperature at 26 K in the fluorine doped layered iron arsenides [1] has encouraged broader exploration of phases with iron in a similar tetrahedron environment in the hope of finding new superconducting compounds that would possess an even higher critical temperature. This discovery had great impact on the condensed matter community, not only due to the presence of iron in these compounds but also because of the enormous amount of compounds that could be synthesised by doping in the many possible atomic locations (see Figure 2a). Consequently, several hundreds of articles have since been published in the most important journals. Over the same period, high pressure structural, magnetic and transport property measurements have seen a very important technical development. X-ray diffraction, ac susceptibility and resistivity studies can be routinely carried out at Mbar conditions (1 Mbar = 100 GPa ≈ 10^6 atm). Furthermore, studying samples using a combination of different techniques allows greater comprehension of the physical properties.

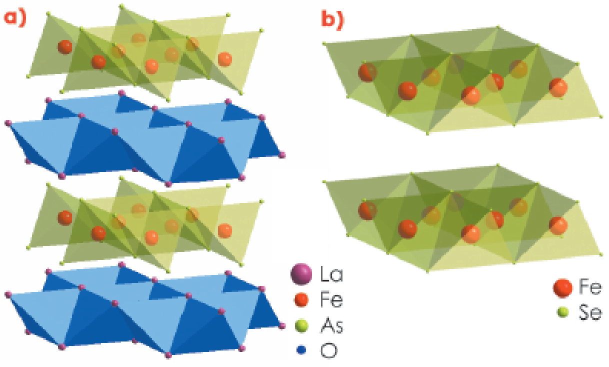

Fig. 2: Crystallographic structures of Fe based compounds at ambient conditions: a) LaFeAsO; b) FeSe.

In earlier studies, we performed the first diffraction experiment at high pressure on $LaFeAsO_{1-x}F_x$ (x~0.1) [2], where we correlated the structure and transport properties under pressure. One of the simplest examples of iron based compounds with tetragonal *PbO* structure is FeSe. In this system, the report of superconductivity in the tetragonal phase [3] (see Figure 2b) is tantalising, as pronounced pressure effects at relatively low pressures seem to strongly increase T_C up to around 25 K for the onset of the transition. Furthermore, partial replacement with tellurium also noticeably increases T_C. However, superconductivity seems to coexist with magnetically-ordered states accompanied by lattice distortions that are much more stable than superconductivity. Here, we report one of the first simultaneous studies of the evolution of both structure and superconductivity under pressure on the compound FeSe. These studies have been developed at beamline ID27 and at the *Matière Condensée et Basses Témperatures* Department of the *Institut Néel*. We find an orthorhombic high pressure phase, which develops above 12 GPa in our samples (see Figure 3b). The high pressure resistivity measurements show that T_C has a linear increase below 12 GPa (in the tetragonal phase) with a kink at higher pressure reaching its maximum of 34 K at 22 GPa (see Figure 3a). Analysis of the pressure evolution of the crystallographic structure shows that the separation between FeSe layers is reduced by 30% at 12 GPa, while the thickness of the FeSe layer remains constant. The anisotropic compression, that is typical of layered compounds, may reach a threshold at this pressure, forcing the phase transformation observed at high pressures. A detailed study as a function of subtle changes in Fe stoichiometry is necessary to understand the differences found in several reports on this material.

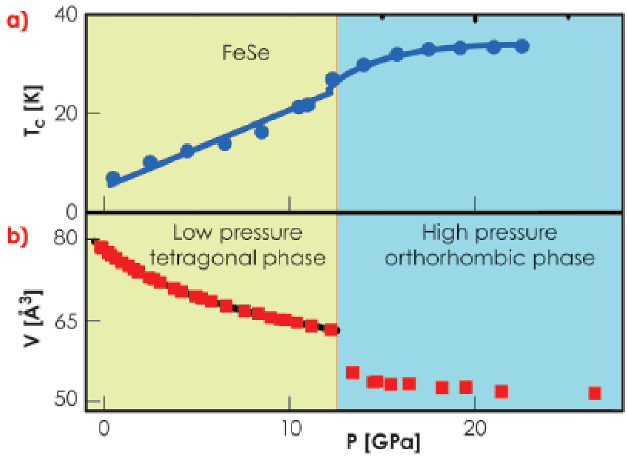

Fig. 3: Pressure evolution of a) the superconducting transition temperature, and b) the unit cell volume. The change of pressure dependence of T_C at the crystallographic phase transition can be seen clearly.

In summary, we have revealed a linear relationship between structural and superconducting properties under pressure for the FeSe system. We obtained one of the highest critical temperatures in this Fe based compounds, which opens the possibility to design new materials with even higher T_C with perspective of greater comprehension of the superconducting state.

References

[1] H. Hosono, *J. Phys. Soc. Jpn.* **77**, *Suppl. C*, 1 - 8 (2008).

[2] G. Garbarino, P. Toulemonde, M. Álvarez-Murga, A. Sow, M. Mezouar and M. Núñez-Regueiro, *Phys. Rev. B (RC)* **78**, 100507 (2009).

[3] F.C. Hsu, J.Y. Luo, K.W. Yeh, T.K. Chen, T.W. Huang, P. M. Wu, Y.C. Lee, Y.L. Huang, Y.Y. Chu, D.C. Yan and M.K. Wu, *PNAS* **105**, 14262 - 14264 (2008).

Symmetry-breaking transition in the new supeconductor $SrFe_2As_2$

The discovery of vanishing electrical resistance in iron arsenides has stimulated a worldwide interest in this class of materials. Since some of the multinary arsenide phases exhibit surprisingly high transition temperatures of up to 55 K, these pnictides clearly belong to the group of high-temperature superconductors. Even more important for applications are the exceptionally high and rather isotropic critical magnetic fields. However, despite extensive investigations of this effect in other materials within the last two decades, the understanding of superconductivity is still incomplete so that the underlying mechanisms are still a topic of basic research.

As a characteristic feature, the crystal structures of these new materials comprise layers that are formed from iron and arsenic atoms. In a subset of these compounds, a symmetry breaking transition is observed at temperatures below typically 200 K. The distortion is associated with a special type of magnetic ordering – the so called columnar ordering – where the iron moments order in an antiparallel fashion along the *a*-axis and in a parallel fashion along the *b*-axis which becomes approximately one percent longer (see Figure 4). The microscopic origin of this special type of magnetic order is a subject of intense ongoing discussions.

Principal publication and authors

M. Kumar (a), M. Nicklas (a), A. Jesche (a), N. Caroca-Canales (a), M. Schmitt (a), M. Hanfland (b), D. Kasinathan (a), U. Schwarz (a), H. Rosner (a), C. Geibel (a), *Physical Review B* **78**, 184516 (2008).

(a) MPI für Chemische Physik fester Stoffe, Dresden (Germany)

(b) ESRF

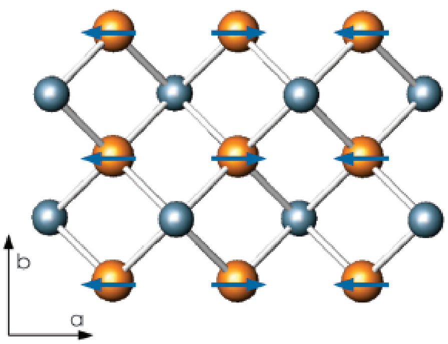

Fig. 4: Projection of the crystal structure of superconducting $SrFe_2As_2$ along the crystallographic *c* axis. Shown is a slightly corrugated layer (decorated 4^4 net) formed by arsenic (blue) and iron atoms (orange). The orientation of the magnetic moments in the ordered phase is indicated schematically by arrows.

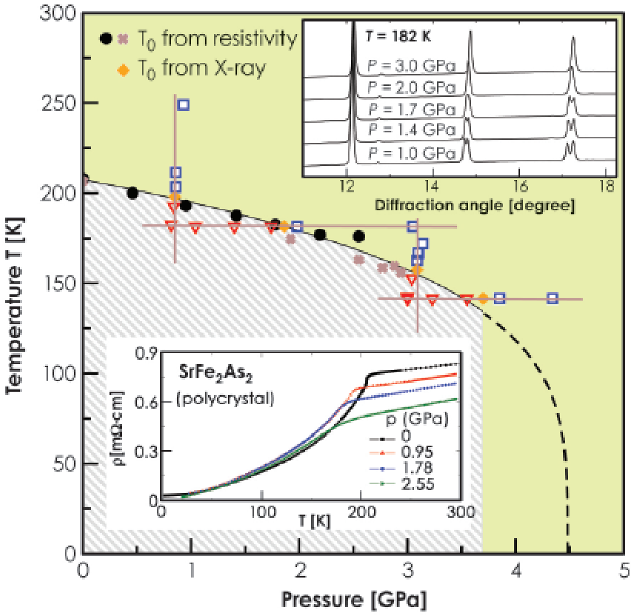

Fig. 5: Stability fields of high (green) and broken symmetry (shaded grey) of superconducting $SrFe_2As_2$. The investigations show perfect agreement between results obtained by electrical resistivity measurements (T_0 extracted from ρ) and the structural distortion (T_0 obtained from X-ray diffraction experiments, XRD). Transition temperatures extracted from ρ are indicated by brown crosses or black dots; open blue squares symbolise diffraction diagrams that are compatible with tetragonal symmetry, open red triangles stand for peak splitting, an indication of orthorhombic symmetry, and filled orange diamonds correspond to interpolated transition temperatures from XRD. Upper inset: Suppression of the lattice distortion as evidenced by the experimental observation of vanishing splitting of X-ray diffraction profiles at elevated pressures. Lower inset: Resistivity as a function of temperature at different pressures. The discontinuous changes indicate that the phase transition is shifted towards lower temperatures at higher pressures.

By changing the chemical composition, the onset of this ordering can be shifted in the direction of lower temperatures and can even be completely suppressed. In parallel to the disappearance of the magnetic order, an onset of superconductivity is observed with transition temperatures T_c up to 38 K. A disadvantage of chemical substitution is that the exchange interaction of the atoms is not only influenced by changing the interatomic distances, but also by differences in the electronic structure of the compounds due to a modified electron count. To study the effect of the atomic spatial separation in pure form, we performed angle-dispersive X-ray diffraction measurement at high pressures and low temperatures at beamline **ID09A**. By combining the results of this structural investigation with laboratory measurements of the electrical resistivity, we could characterise the interrelation between magnetic order and atomic arrangement in a rather extended part of the parameter field (see **Figure 5**).

The onset of the magnetic ordering yields a pronounced change of the temperature dependence of the electrical resistivity. With increasing pressure, the transition shifts in the direction of lower temperatures. The related change of symmetry is directly observed by following the splitting of diffraction lines in the powder diffraction diagrams (see upper inset in **Figure 5**). In full agreement with the results of the resistivity measurements, the structural transition is shifted in the direction of higher pressures at lower temperatures (see lower inset of **Figure 5**). Density functional electronic structure calculations demonstrate that the structural and the magnetic phase transition in this class of materials are intimately linked. With increasing pressure, the interatomic overlap increases, the electronic bands broaden and, in consequence, the density of states at the Fermi level, responsible for the magnetic instability, decreases. Thus, the experimental results are in very good agreement with our theoretical prediction that the transition temperature decreases strongly with pressure.

The results clearly show that the new class of compounds differs fundamentally from the copper- and oxygen-containing high-temperature superconductors which have been studied intensely over the last twenty years. In these materials, the magnetic ordering temperature increases with pressure while the new materials show a decrease and are, thus, similar to classical superconducting intermetallic compounds. Compared to the classic intermetallic superconditors, the significantly higher transition temperatures and the increased stability in high magnetic fields qualify the new materials as very promising candidates for scientific and technical applications.

Pressure-induced insulator-to-metal transition in $TbBaCo_2O_{5.48}$

A key aspect of cobalt oxides that eclipses the conventional charge, spin and orbital degrees of freedom, is the possible variety of spin states of the cobalt ions. For this reason, cobalt layered perovskites represent a unique system that allows the study of the effect of spin-state degrees of freedom on the metal-insulator charge- and spin-ordering transitions.

The complex oxide $TbBaCo_2O_{5.5}$ contains Co^{3+} ions in octahedral or pyramidal coordination of oxygen atoms. Each Co^{3+} ion can be found in a low, intermediate, or high spin state (LS, IS, or HS) having different ionic radii. $TbBaCo_2O_{5.5}$ shows an insulator-to-metal transition on heating, and at the same temperature, T_c~335K, there is a structural change from Pmma ($2a_c \times 2a_c \times 2a_c$) to Pmmm ($a_c \times 2a_c \times 2a_c$). This transition agrees with a partial ordering of cobalt ions in different spin and orbital states. The deactivation of a “spin blockade” mechanism (associated with the LS states) has been suggested for this insulator-to-metal transition, assuming that heating would promote HS states and suppress LS states [1].

There are several reasons to also expect a change in structural and transport properties of insulating oxides of 3d-metals as a function of pressure. Pressure could favour the orbitally-disordered phase thus giving an increase of conductivity. A change of spin-state for cobalt ions from HS or IS to LS is accompanied by a decrease of ionic radius, thus pressure could favour the spin conversion toward LS states. In this case one would not expect an increase of conductivity under pressure since LS states effectively block electron mobility via the “spin blockade” mechanism. One more possible pressure effect may be foreseen from symmetry analysis that links the structure and conductivity via an electron transfer integral through the Co-O-Co path. For this mechanism, one would expect a symmetry change under pressure.

As no change in physical and structural properties has been found so far between ambient pressure and 1.2 GPa [2], the “spin blockade” has been considered the primary mechanism for the temperature induced metal-to-insulator transition in rare earth cobaltites.

By combining diffraction and transport measurements, we have recently shown that there is an insulator-to-metal transition, but at pressures higher than probed before, at ~10 GPa (Figures 6 and 7). In the same pressure range we observe changes in resistivity and in the ratio of the lattice constants of the average orthorhombic Pmmm ($a_c \times 2a_c \times 2a_c$) cell; the same behaviour holds for the spontaneous strains. The change in the ratio of the lattice constants is very similar to that observed as a function of temperature (Figure 7), thus suggesting a common mechanism for the two transitions. We can exclude the spin blockade mechanism as candidate, as it should be suppressed under pressure due to the higher ionic radius of HS ions. Temperature favours disorder

Principal publication and authors

D. Chernyshov (a),
G. Rozenberg (b), E. Greenberg (b),
E. Pomgakushina (c) and
V. Dmitriev (a), *Phys. Rev. Lett.* **103**, 125501 (2009).
(a) Swiss-Norwegian Beam Lines at ESRF, Grenoble (France)
(b) School of Physics & Astronomy, Tel-Aviv University (Israel)
(c) Laboratory for Developments and Methods, PSI Villigen (Switzerland)

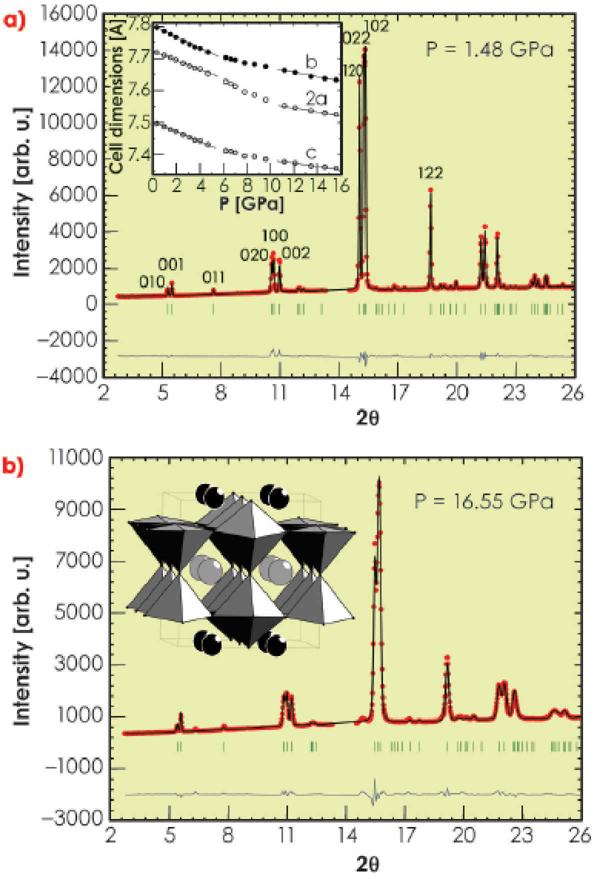

Fig. 6: Diffraction patterns for $TbBaCo_2O_{5.48}$ with experimental points, fitted profile, difference curve (bottom), and positions of Bragg reflections (vertical bars). a) P=1.48 GPa; the inset shows the unit cell dimensions as a function of pressure. b) P=16.55 GPa; the inset shows the high temperature/high pressure orthorhombic Pmmm ($a_c \times 2a_c \times 2a_c$) structure. Colour code: Tb (black), Ba (grey), cobalt ions are coordinated by oxygen forming octahedrons and pyramids.

via the entropy term, but pressure does not; ordering of spin states can therefore be excluded as well as common mechanisms. We propose instead that the change of the Co-O-Co angle affects the electron transfer integral, and consequently the conductivity. This mechanism assumes a strong link between structural deformation and transport properties while the spin-state degree of freedom only plays a secondary role.

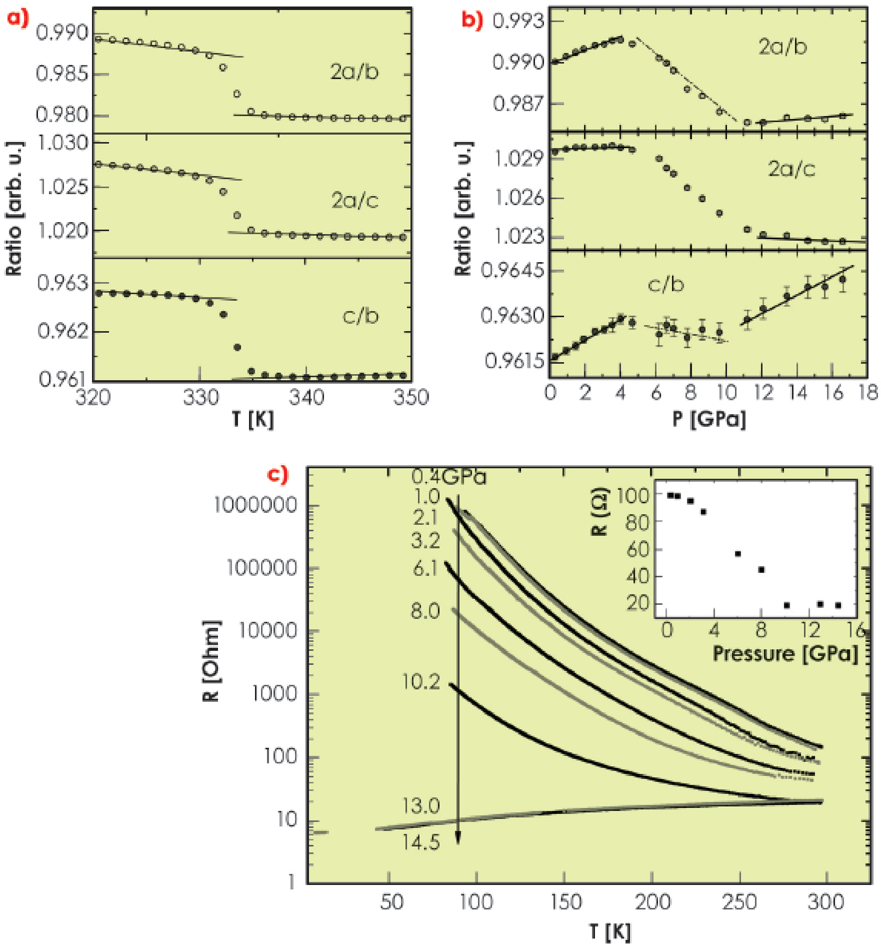

Fig. 7: Ratio of unit cell dimensions as a function of a) temperature, and b) pressure. c) Temperature dependence of the resistivity measured at different pressures. The inset shows the pressure dependence of the resistivity at 298 K.

References

[1] A. Maignan, V. Caignaert, B. Raveau, D. Khomskii and G. Sawatzky, *Phys. Rev. Lett.* **93** 026401 (2004).

[2] A. Podlesnyak, S. Streule, K. Conder, E. Pomjakushina, J. Mesot, A. Mirmelstein, P. Schützendorf, R. Lengsdorf, and M.M. Abd-Elmeguid, *Physica B-Condensed Matter* **378-80**, 537 (2006).

Hot oxygen: the structure of the η-phase

Principal publication and authors

L.F. Lundegaard (a), C. Guillaume (a), M.I. McMahon (a), E. Gregoryanz (a), and M. Merlini (b), *The Journal of Chemical Physics* **130**, 164516 (2009).

(a) The University of Edinburgh (UK)

(b) ESRF

Solid oxygen is unique amongst the elements in being both molecular and magnetic. As a consequence, it has a rich and complex phase diagram (Figure 8) and numerous phases with unusual magnetic, thermal and optical properties [1]. Solid oxygen is the only elementary molecular magnet; it exhibits a number of complex magnetic phases; on compression it changes colour from pale-blue to light orange to dark red; and at pressures above 96 GPa it becomes a superconducting metal. The perceived highly-reactive nature of oxygen under high-temperature conditions, particularly in the liquid state, has limited most static high-pressure studies of oxygen to room or low temperatures. But recent studies of solid oxygen to temperatures as high as 1250 K have suggested the existence of a further new phase of oxygen, η-oxygen, existing just beneath the melting curve [2,3]. We investigated the structure of the η phase by using a diamond anvil pressure cell and high-temperature high-pressure single-crystal diffraction techniques on beamline ID09A.

Figure 9a shows a micro-photograph of a polycrystalline sample of “red” ε-oxygen at 18.1 GPa and 293 K, which, on heating to 675 K at the same pressure, anneals into a number of single crystals, which optical spectroscopy reveals to be a mixture of the ε and η phases (**Figure 9b**). Further annealing at 16.6 GPa and 650 K, results in crystals of only η-oxygen (**Figure 9c**).

A high-quality single crystal of η-oxygen suitable for diffraction experiments was grown *in situ* on beamline **ID09A** at 15.9 GPa and 625 K, just below the melting temperature at this pressure. From the positions of 43 reflections, the structure of η-oxygen was found to be hexagonal with lattice parameters *a* = 2.561(2) Å and *c* = 6.575(6) Å, with two molecules per unit cell. The intensities of a total of 66 individual reflections were measured, and analysis showed them to be consistent with spacegroups $P6_3/mmc$, $P\bar{6}2c$ and $P6_3mc$. Spacegroup $P6_3/mmc$ is the same as that of the hexagonal close-packed (*hcp*) structure found in many elemental metals, while the c/a ratio of η-oxygen is very close to two thirds of that expected for rhombohedral β-oxygen at 15.9 GPa, the structure of which comprises layers of aligned O_2 molecules in a face centred cubic (*fcc*) like stacking sequence. All of this suggested a structural model for η-oxygen in which aligned O_2 molecules are arranged in an *hcp*-like stacking, rather than the *fcc*-like stacking of β-oxygen. Exactly the same structural model for η-oxygen can be constructed in space groups $P\bar{6}2c$ and $P6_3mc$. The fit of the data to this model is excellent.

The structure of η-oxygen is shown in **Figure 10** and is closely related to the known high-pressure α, β, δ, and ε phases, particularly the rhombohedral β phase. All of these high-pressure structures comprise sheets of O_2 molecules in which the molecular axes are aligned parallel to each other. The η structure comprises two such layers of molecules, stacked alternately in an *hcp*-like ABAB arrangement along the *c* axis, while the β structure comprises three such layers in an *fcc*-like ABCABC stacking. However, the packing of the dumbbell-shaped O_2 molecules results in the symmetry of the β phase being trigonal rather than cubic, with the rhombohedral angle being about 45° instead of 60° for the *fcc* structure.

While the study of η-oxygen confirmed its existence and determined its structure, we were unable to map out the stability range of this phase due to the failure of the diamonds in the pressure cell. Subsequent spectroscopic studies are planned. However, the present study illustrates the quality of single-crystal diffraction data that can now be collected at the ESRF from weakly-scattering samples such as oxygen, even at high temperatures and pressures. Such a capability bodes well for even more extreme studies in the future.

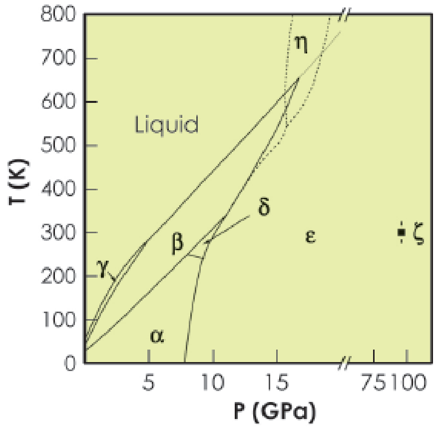

Fig. 8: The reported phase diagram of oxygen to 120 GPa and 800 K [1]. Note the break in the pressure axis at 20 GPa. The dotted extension to the melting line is that reported by Weck *et al.* [3], while the dashed lines show the phase boundaries proposed by Santoro *et al.* [2].

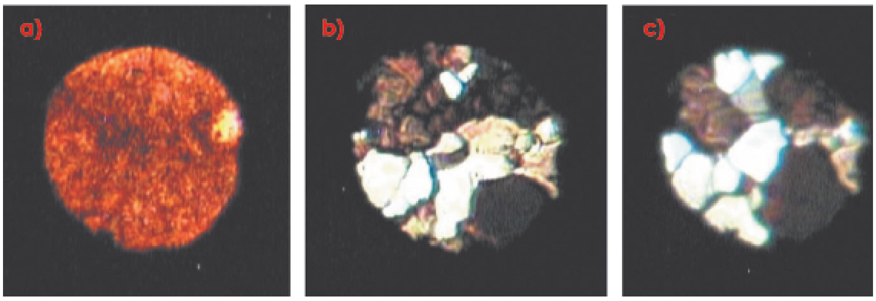

Fig. 9: Microphotographs of a) polycrystalline ε-O_2 at 18.1 GPa and 293 K, b) crystallites of ε-O_2 and η-O_2 at 18.1 GPa and 675 K, and c) crystallites of η-O_2 at 16.6 GPa and 650 K.

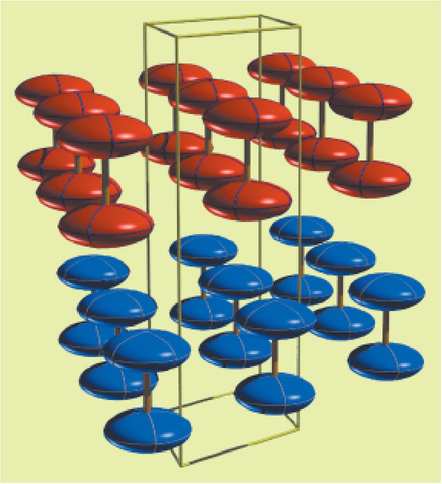

Fig. 10: The structure of η-O_2, showing the molecular layers that make up the structure. The two molecules within each unit cell are shown using different colours. The thermal ellipsoids are shown at the 90% probability level.

References

[1] Y.A. Freiman and H.J. Jodl, *Phys. Reports* **401,** 1 (2004).
[2] M. Santoro, E. Gregoryanz, H.K. Mao and R.J. Hemley, *Phys. Rev. Lett.* **93**, 265701 (2004).
[3] G. Weck, P. Loubeyre, J.H. Eggert, M. Mezouar and M. Hanfland, *Phys. Rev. B* **76**, 054121 (2007).

Structural transition in metallic dense oxygen

Principal publication and authors
G. Weck (a), S. Desgreniers (b), P. Loubeyre (a), and M. Mezouar (c), *Phys. Rev. Lett.* **102**, 255503 (2009).
(a) CEA, Bruyères le Châtel (France)
(b) Laboratoire de physique des solides denses, Université d'Ottawa, Ottawa (Canada)
(c) ESRF

Solid oxygen exhibits both simple molecular and magnetic properties. Below 10 GPa, dense solid oxygen is a spin-controlled crystal and as such exists under four structural arrangements presenting different magnetic ordering. Above 10 GPa, solid oxygen transforms into a dark-red solid known as the ε phase. The exact structure of the ε phase (monoclinic, C2/m) was determined only recently, revealing an intriguing condensed state for which the association of four O_2 molecules into O_8 entities prevail [1,2]. Beyond the stability field of its ε phase, *i.e.*, above 96 GPa, solid oxygen has been shown to present a metallic state corresponding to the molecular ζ phase. The study of the metallic ζ phase has remained an outstanding experimental challenge for years because of the weak scattering power of oxygen in the 100 GPa range. Characterisation of the structural changes at the onset of metallisation is essential to understand the mechanism of the insulator-to-metal transition. Advanced single crystal growth techniques at high pressure and temperature and use of optimised conditions for performing microdiffraction are key to unravelling the elusive nature of metallic oxygen.

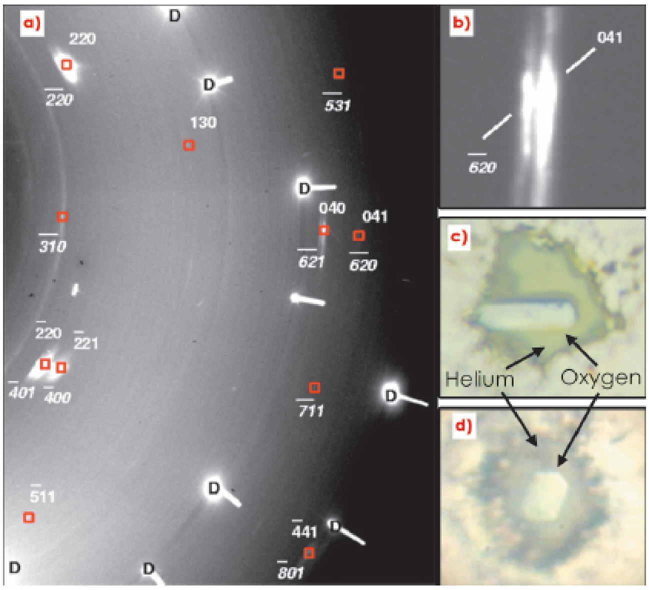

Fig. 11: a) Details of a diffraction image of solid oxygen at 133 GPa, overlaid with the indexing of reflections arising from identified twins, indicated by normal and italic indexing, respectively. b) A magnification of (a), illustrating two different reflections belonging to twin crystals. c) and d) Photomicrographs of two of the oxygen single crystals, oriented differently in surrounding He at 125 GPa in a diamond anvil cell. The field of view is approximately 75 µm.

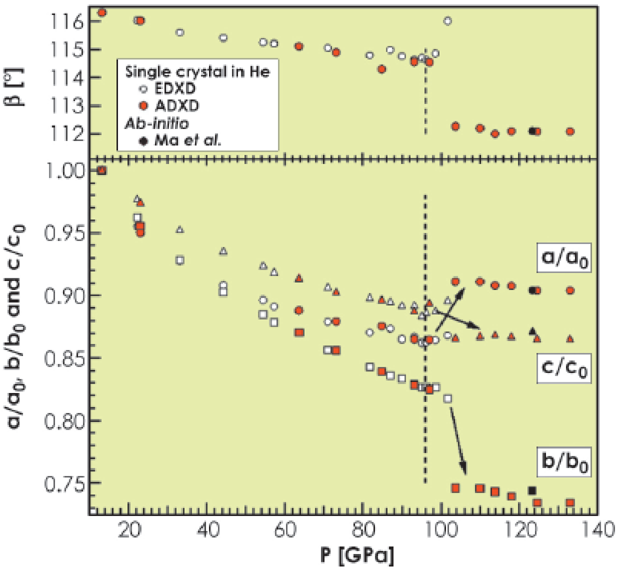

Fig. 12: Pressure dependence of lattice constants a, b, c and angle β of the C2/m monoclinic unit cell compared with values from a previous energy dispersive X-ray diffraction experiment [4] and *ab initio* calculations.

To address this problem, we carried out angle-dispersive X-ray diffraction experiments at beamline ID27 on single crystals of solid oxygen embedded in helium, the best hydrostatic pressure transmitting medium. Crystals were grown with different orientations as assessed by the anisotropic optical properties of the ζ phase (see Figure 11). X-ray diffraction images were collected over the full high pressure cell aperture (2Θ+/-35°). Below 96 GPa, all observed reflections were well indexed to the known monoclinic C2/m unit cell of the ε phase. Upon pressure increase, twinning was reproducibly observed in all crystals. Nevertheless, the crystal mosaicity remained very small up to 96 GPa owing to the good hydrostatic conditions. Upon transition to the metallic ζ phase, diffraction images (Figure 11) showed significant changes characterised by broadening and sliding of the Bragg diffraction spots, the latter being indicative of the displacive nature of the structural transition. The crystalline structure of the metallic ζ phase was shown to present the same symmetry and space group (C2/m) as ε oxygen, in good agreement with *ab initio* calculations [3]. This result was corroborated by Raman spectroscopy carried out on single crystals in the ζ phase. The sharp change measured for the monoclinic lattice parameters above 96 GPa, illustrated in Figure 12, indicated a first-order transition taking place essentially in the *ab* plane. The structural change is characterised by the connection of the O_8 units along the *b*-direction as indicated by the strong contraction of the *b*-axis between 96 and 106 GPa.

In brief, the present X-ray diffraction and spectroscopic results in combination with the *ab initio* calculations indicate that the metallisation of solid oxygen takes place by a band gap closure in the ε phase and is followed by the destabilisation of the molecular lattice towards the denser structure of the ζ phase, in which dissociation of the O_8 units occurs.

References
[1] L.F. Lundegaard *et al.*, *Nature*, **443**, 201 (2006).
[2] H. Fujihisa *et al.*, *Phys. Rev. Lett.*, **97**, 085503 (2006).
[3] Y. Ma, A.R. Oganov and C.W. Glass, *Phys. Rev. B*, **76**, 064101 (2007).
[4] G. Weck *et al.*, *Phys. Rev. Lett.* **88**, 035504 (2002).

Electronic and magnetic structures and dynamics

Stabilisation of magnetism in ultrathin iron oxide layers

Magnetic data storage technology is driven by the quest to decrease the length scale of the magnetic bit cell. Since the typical layer thicknesses involved in devices has decreased to only a few nm, maintaining the stability of the magnetic state over time has become a key issue. Indeed, it is well known that a ferromagnetic layer enters a super paramagnetic state (*i.e.* the magnetic state is continuously changing) once its thickness decreases below a critical value. This poses a limit for the size of the bit cell that can be used in conventional magnetic recording.

Therefore, it is of particular interest to explore any possible mechanism that leads to stabilisation of magnetic order beyond the superparamagnetic limit. Of special interest in this field are oxide antiferromagnets, where long range magnetic correlations are maintained through nearest neighbour interactions that couple to adjacent ferromagnetic layers to form an exchange-bias system.

Following the pioneering work of Beach *et al.* who revealed intriguing magnetic properties of ultrathin native iron oxide layers [1], we studied the chemical and magnetic properties of oxidised iron layers *in situ* using nuclear resonant scattering (NRS) at beamline **ID18**. We used the isotope sensitivity of NRS to isolate the signal originating from the oxide layer. This proved to be of utmost importance to discriminate against the strong magnetic signal of the neighbouring Fe metal, which normally prevents the detection of the oxide's magnetic state using conventional techniques. In an NRS experiment, the time delayed de-excitation of the ^{57}Fe nucleus is recorded after excitation by pulsed synchrotron radiation. The magnetic state of the ^{57}Fe atoms is encoded in the shape of the measured temporal beat patterns. For instance, a non-magnetic material would show only a simple exponential decay of the signal whereas a magnetic one shows a beat

Principal publication and authors
S. Couet (a,b), K. Schlage (a), R. Rüffer (c), S. Stankov (c), Th. Diederich (a), B. Laenens (b) and R. Röhlsberger (a), *Phys. Rev. Lett.* **103**, 097201 (2009)
(a) HASYLAB at DESY, Hamburg (Germany)
(b) Instituut voor Kern- en Stralingsfysica, K.U. Leuven (Belgium)
(c) ESRF

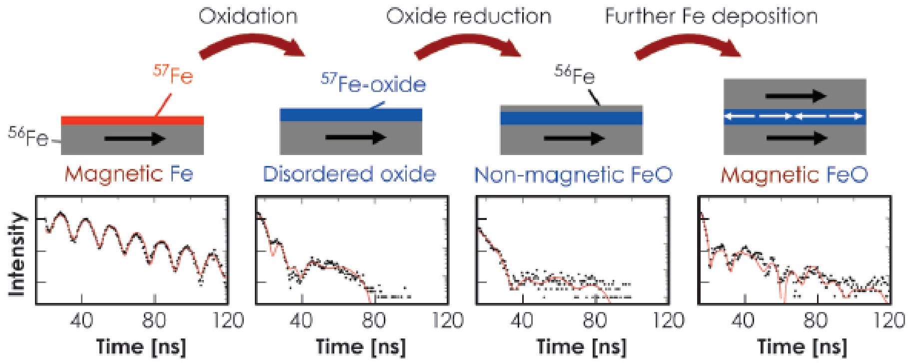

Fig. 13: Evolution of the magnetic state of a thin FeO layer during growth. The layer is being stabilised magnetically by the surrounding ferromagnet. The corresponding NRS spectra and their fits are shown at the bottom.

frequency which is a signature of its particular magnetic configuration.

This property was used to monitor the chemical and magnetic state of the growing oxide layer. The complete process is summarised in Figure 13. We start with a 2 nm ^{56}Fe layer on top of which a 0.6 nm ^{57}Fe layer (the NRS active isotope) is deposited. This layer is subsequently oxidised by controlled admission of oxygen into the vacuum chamber. A sudden change from pure magnetic Fe to a chemically disordered, predominantly non-magnetic oxide is observed. Remarkably, the deposition of one atomic layer of Fe on top leads to the formation of a chemically pure FeO layer [2], which is non-magnetic. This is not surprising as the bulk Néel temperature T_N of FeO is found to be around 200 K. However, with further deposition of Fe, a sharp magnetic transition is observed in the oxide, which means that T_N has effectively risen above room temperature. We expect that this magnetic transition coincides with the appearance of long range ferromagnetism in the top Fe layer, which is only possible once a critical thickness is reached. *Ex situ* temperature dependent measurements allowed the T_N to be estimated as being as high as 800 K, very close to the Curie temperature T_C of the neighbouring Fe layer. This similarity is not a coincidence, as the proximity of very thin ferromagnetic layers can lead to a convergence of T_N towards the T_C of the ferromagnetic material.

This study unravels how the magnetic state of ultrathin antiferromagnetic layers can be stabilised by an adjacent ferromagnet such that its effective Néel temperature can be increased by several hundreds of Kelvin. In the case of FeO, it leads to antiferromagnetic order at room temperature, an effect which proved to be very effective to mediate strong interlayer coupling in Fe/FeO heterostructures.

References
[1] G.S.D. Beach, F.T. Parker, D.J. Smith, P.A. Crozier and A.E. Berkowitz, *Phys. Rev. Lett.* **91**, 267201 (2003).
[2] S. Couet, K. Schlage, K. Saksl and R. Röhlsberger, *Phys. Rev. Lett.* **101**, 056101 (2008).

The electronic structure of sulphur studied by X-ray absorption and emission spectroscopy

Principal publication and authors
R. Alonso Mori (a,b), E. Paris (b), G. Giuli (b), S.G. Eeckhout (a), M. Kavčič (c), M. Žitnik (c), K. Bučar (c), L.G.M. Pettersson (d) and P. Glatzel (a), *Anal. Chem.* **81**, 6516 (2009).
(a) ESRF
(b) Dipartamento di Scienze della Terra, Camerino University (Italy)
(c) J. Stephan Institute (Slovenia)
(d) FYSIKUM, Stockholm University (Sweden)

Sulphur forms chemical bonds with atoms with very different electronegativity values resulting in large variations of its local electronic structure. This polyvalence makes sulphur an abundant element that plays a key role in various fields such as in catalytic and biological processes and in environmental systems. The chemical state of sulphur has therefore been widely studied by means of XANES (X-ray absorption near edge structure) spectroscopy [1]. XANES is a powerful tool to study the density of unoccupied electronic states with element selectivity. However, the strong influence of the number and type of ligands and the local geometry as well as possible experimental artefacts (*e.g.* self-absorption in fluorescence detected XANES) may lead to difficulties in the interpretation of the XANES spectra. The chemical dependence is considerably simpler in Kα X-ray emission spectroscopy (XES) than in XANES [2]. In this work we report a comprehensive experimental and theoretical study of the Kα fluorescence lines in a variety of sulphur compounds with a critical comparison with the corresponding XANES spectra. The measurements were carried out at beamline ID26.

Figure 14a shows the XANES spectra of various sulphur compounds. The profound variations in the spectral shape reflect the strong influence of the local structure and the type of cation on the orbital hybridisation around the sulphur atom. The absorption edge position depends on the oxidation state via charge screening effects and a shift of 12 eV (Figure 15a) is observed between sulphides (S in oxidation state -2) and sulphates (S in oxidation state +6). In sulphides, the sulphur atom is bonded directly to the metal cation and the resulting bonding character of the sulphide has a considerable influence on the position of the S K-edge. The energy position of

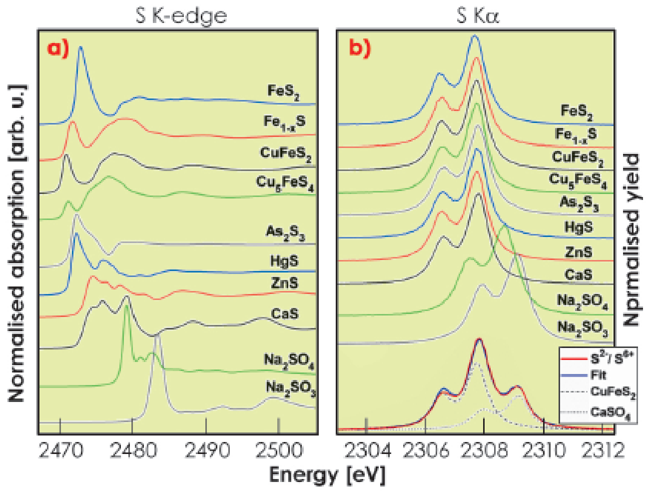

Fig. 14: a) S K-edges and b) S Kα X-ray spectra of some sulphur-bearing compounds and a mixture of sulphate/sulphide together with the fit result using reference systems.

the S Kα XES - arising from 2p to 1s transition - reflects the chemical state by a similar screening effect that changes the core level binding energy but the spectral shape is little sensitive to the chemical environment (**Figure 14b**). The S Kα_1 position shows an energy shift of 1.5 eV with the change in the formal oxidation state (**Figure 15a**). Even though the spectral changes on an absolute scale are an order of magnitude smaller in XES than in XANES, a very detailed analysis of the energy position is possible because the Kα energy can be measured with high accuracy and the relative peak intensity is barely influenced by self-absorption in the sample. The absence of strong interactions between the 2p core hole and the valence electrons in the Kα XES makes the screening effect the dominant source of the chemical sensitivity. The simple chemical sensitivity provides an opportunity for a quantitative analysis in heterogeneous systems. A sulphide/sulphate mixture with 66.7% of sulphur present in the chemical state S^{2-} is shown in **Figure 14b**. Fitting of the experimental data with a weighted sum of representative spectra for S^{2-} and S^{6+} gives a contribution of 66.3% from the S^{2-} spectrum, demonstrating that XES can be used to quantitatively determine the amount of sulphur species in mixed-valence systems.

The energy positions of the sulphides (S^{-2}) are spread over a large range. The ordering within the sulphides is different between XES and XANES. We investigated this discrepancy by comparing the experimental results to the charge density as extracted from quantum chemical calculations. **Figure 15a** shows the energy positions of the Kα_1 emission line and K absorption edge as a function of the calculated number of 3p and 3s electrons. This approach shows a monotonic relation between the Kα_1 line position and the sulphur charge, in particular within the series of sulphides, which is not observed for the XANES edge position.

We find that XES can serve as a probe of the local charge density with considerably higher accuracy than XANES. The more complex XANES spectral shape arises from its sensitivity to a multitude of mechanisms.

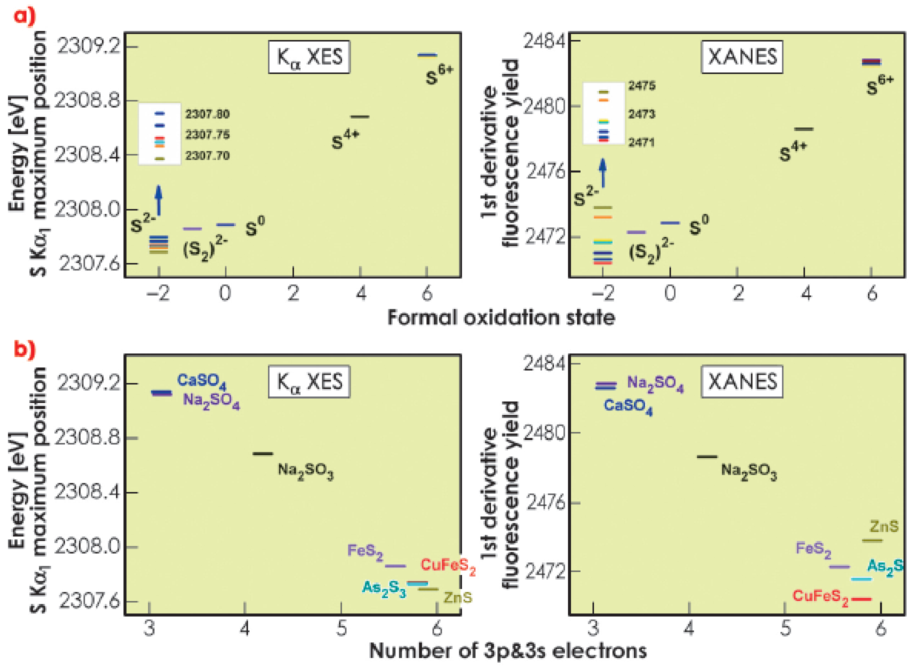

Fig. 15: S Kα_1 and S K-edge energy position versus a) formal oxidation state, and b) charge density (number of 3p and 3s electrons calculated by density functional theory).

The more selective sensitivity of Kα XES greatly facilitates interpretation of experimental results. Comparison with calculations shows that the Kα$_1$ energy can be correlated to high accuracy with the valence-shell electron population and good agreement is achieved for the Kα lines. Furthermore, the selectivity of XES can be used to quantify the amount of sulphur species in heterogeneous systems and its simple spectral shape renders such a quantitative analysis considerably more robust than a similar approach in XANES.

References
[1] E. Solomon *et al.*, *Coord. Chem. Rev.* **249**, 97 (**2005**).
[2] M. Kavčič *et al.*, *Nucl. Instrum. Meth. B* **222**, 601 (**2004**).

Two-electron atomic processes induced with a single photon

Principal publication and authors
M. Kavčič (a), M. Žitnik (a), K. Bučar (a), A. Mihelič (a), M. Štuhec (a), J. Szlachetko (b,c), W. Cao (b), R. Alonso Mori (d) and P. Glatzel (d), *Phys. Rev. Lett.* **102**, 143001 (2009).
(a) J. Stefan Institute, Ljubljana (Slovenia)
(b) Physics Department, University of Fribourg (Switzerland)
(c) Jan Kochanowski University, Institute of Physics, Kielce (Poland)
(d) ESRF

According to the nature of photon-electron interaction, a single photon can interact directly with only one electron in the atom. A double photoexcitation is therefore necessarily mediated by an electron-electron interaction. Near the double ionisation threshold, three different types of transitions can occur:

- shake-off (double ionisation) where both electrons are ejected out of the atom,
- shake-up transition where ejection of one inner shell electron is accompanied by the simultaneous excitation of another electron into an unoccupied bound atomic state,
- resonant double excitations where both electrons are excited to unoccupied bound states of the neutral atom.

X-ray satellite lines are emitted in the radiative decay of these multielectron states. They are shifted in energy with respect to the diagram line arising from single photoionisation but the spectral contributions of different multielectron processes within the satellite line overlap and cannot be resolved. Resonant inelastic X-ray scattering (RIXS) measurements overcome this limitation; a series of RIXS spectra can be used to effectively separate shake-off, shake-up, and resonant contributions through their characteristic near-threshold behaviour. Since structural solid-state effects would obscure resonant spectral features related to multiple atomic excitations such studies need to be performed on gaseous atomic targets.

A series of RIXS spectra was recorded to analyse the [1s3p] photoexcitation in Ar using the high-resolution Johansson type spectrometer of the J. Stefan Institute at beamline **ID26**. **Figure 16** presents two high resolution KM$_{2,3}$ X-ray emission spectra recorded at excitation energies slightly below and above the 1s3p threshold. While the first spectrum exhibits only a strong diagram line corresponding to the 1s-3p transition, an additional satellite line appears in the spectrum taken above the threshold, which is attributed to the 1s3p double vacancy state. The inset of **Figure 16** presents the RIXS spectral plane for the satellite line in the 1s3p near-threshold region. Along the excitation energy axis of the RIXS plane, two resonant contributions are clearly observed exhibiting a linear Raman-Stokes dispersion. They are followed by a sharp edge typical of the shake-up process. In contrast to the two resonant contributions, no strong dependence on excitation energy is observed above the edge, as expected for excitations into continuum states.

Figure 17 shows the Ar [1s3p] photoexcitation spectrum given as the integral yield of the extracted satellite line versus excitation energy. A simple phenomenological model employing a cumulative distribution together with an exponential saturation functional form for the shake-up and shake off contributions, respectively, and an

Fig. 16: High resolution Ar KM$_{2,3}$ X-ray emission spectra recorded below and above the double [1s3p] threshold. The inset shows a 2D RIXS map of the KM-M$_{2,3}$M satellite contribution over the [1s3p] near-threshold region.

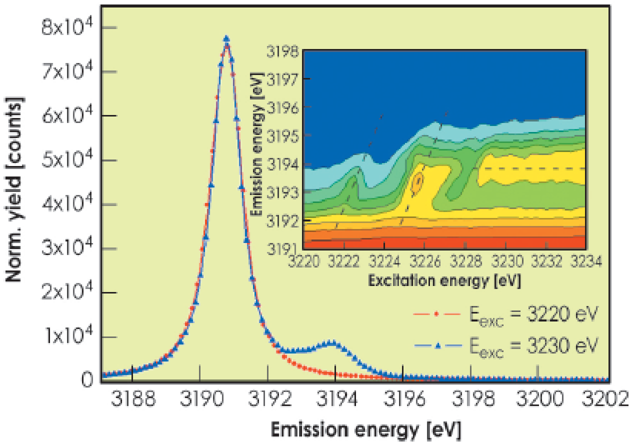

additional peak to account for the [1s3s] resonant excitation at 3238 eV, accurately reproduces the measured spectrum well above the 1s3p threshold. The signal before the first shake-up edge corresponds to the resonant [1s3p]*nln′l′* excitation cross section, and is presented in the inset of Figure 17. The absolute units were obtained by scaling the total measured KM X-ray yield at a given excitation energy with the corresponding absolute photoabsorption cross section of Ar [1]. The experimental spectrum is compared to the model spectrum based on the calculated dipole oscillator strengths of [1s3p]*nln′l′* states, taking full account of atomic relaxation. Apart from obtaining good general agreement with experiment, our calculations also reproduce the peak observed at 3222.3 eV excitation energy confirming that it originates from the conjugate process, where the roles of 1s and 3p electrons in the corresponding dipole-monopole excitation are reversed.

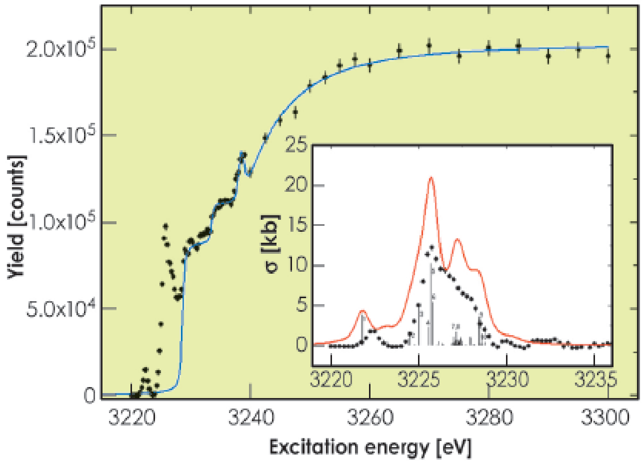

Fig. 17: Intensity evolution of the KM-M$_{2,3}$M satellite line as a function of the excitation energy. The solid line represents the fit of the phenomenological model adopted for the region above the double [1s3p] threshold. The inset shows the resonant part of the measured [1s3p] spectrum compared with our calculated spectrum.

In conclusion, we have measured the Ar resonant 1s3p double photoexcitation spectrum employing high-resolution RIXS spectroscopy on a gas phase target. A detailed comparison with model predictions with respect to energy levels as well as the strength of resonant double excitations was performed. With an effective separation of different two-electron near-threshold contributions, RIXS spectroscopy reaches beyond the standard absorption technique and provides new possibilities to study electron correlation effects in the photoexcitation process.

Reference
[1] M. Deutsch, N. Maskil, and W. Drube, *Phys. Rev. A* **46**, 3963 (1992).

Is potassium indeed a jellium-like metal?

The valence electrons in alkali metals are typically considered as nature's closest realisation of a free-electron gas, the so-called jellium, where the valence electrons move freely on a uniform positively charged background of ions. In jellium-like metals, *e.g.* aluminium and the alkali metals lithium, sodium, and potassium, it is assumed that the valence electrons interact only weakly with the ion cores. When the jellium is exposed to electromagnetic radiation with a sufficiently short wavelength, collective charge-density excitations called *plasmons* may be induced. Typically the required wavelength is shorter than that of visible light. As a consequence, jellium-like metals have a shiny luster because they cannot absorb visible light. When a photon has enough energy to excite a plasmon (*e.g.* 4 eV in potassium), it can be absorbed by the metal. These optical properties are described by the dielectric function $\varepsilon(q,E)$ which depends on the momentum (q) and energy (E) transferred to the electrons. Optical light probes the response at $q = 0$, but studies as a function of both q and E are possible using, for example, inelastic X-ray scattering (IXS) spectroscopy [1].

We investigated the dielectric response of potassium valence electrons at ID16 using inelastic X-ray scattering (IXS). The experiment measures the dynamic structure factor $S(q,E)$ which is related to the dielectric function by being proportional to $\mathrm{Im}(-1/\varepsilon(q,E))$. Figure 18 shows the measured spectra, which near to q=0 are dominated by a sharp peak at 4 eV, *i.e.* the plasmon, as expected for a jellium metal. This peak should broaden when q is increased

Principal publication and authors
S. Huotari (a), C. Sternemann (b), M.C. Troparevsky (c), A.G. Eguiluz (c), M. Volmer (b), H. Sternemann (b), H. Müller (a), G. Monaco (a), and W. Schülke (b), *Phys. Rev. B* **80**, 155107 (2009).
(a) ESRF
(b) Fakultät Physik/DELTA, Technische Universität Dortmund (Germany)
(c) Department of Physics & Astronomy, University of Tennessee; and Materials Science & Technology Division, Oak Ridge National Laboratory, Oak Ridge, Tennessee (USA)

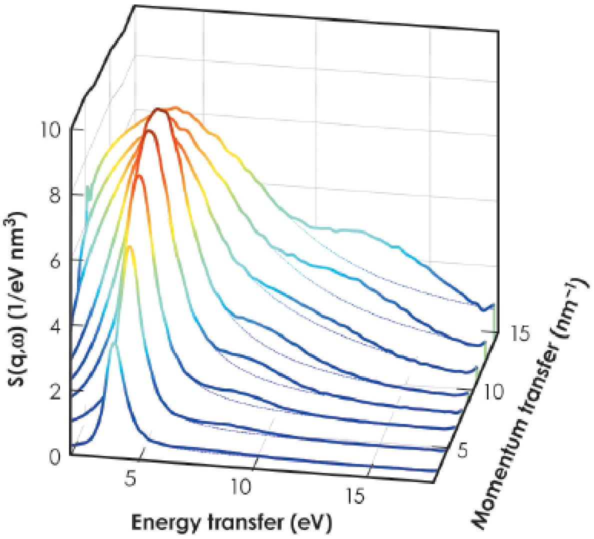

Fig. 18: Experimental dynamical structure factor *S(q,E)* of potassium. With increasing *q*, a strong shoulder develops between 8 and 15 eV. This shoulder-like structure is isolated by subtracting a sloping background function (dashed lines) and shown in **Figure 19a**.

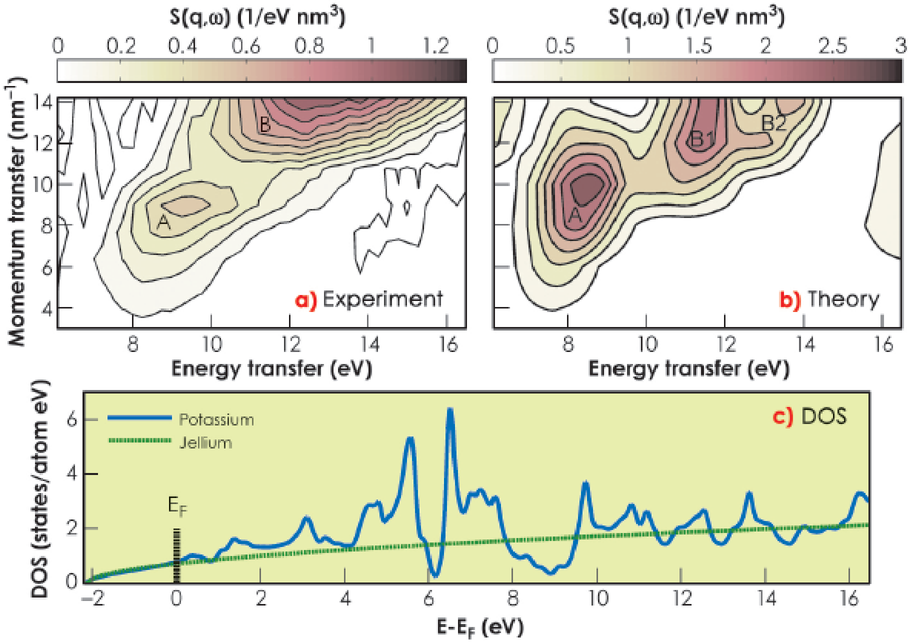

Fig. 19: a) The structure obtained after subtraction of the background shown in **Figure 18**, b) the corresponding theoretical prediction, and c) the density of states of potassium valence electrons.

since then the collective excitation starts decaying rapidly into electron-hole pairs. Indeed, this also happens in potassium, but to our surprise, a significant new structure appears at 8-15 eV energy transfers. This is highly untypical for the dielectric response of a simple metal [2]. To study the origin of this new unexpected excitation structure, a sloping background was subtracted from the spectra. The result is shown in **Figure 19a**. Clearly two separate peaks can be observed, labelled A and B. To understand these spectral features, we performed calculations within the frame of time-dependent density-functional theory, shown in **Figure 19b**. The theory shows a good agreement with experiment (with a small exception that the peak B splits into B1 and B2). The reason for the new structures can be understood in terms of the ground-state electron density of states (DOS), shown in **Figure 19c**. The DOS follows a jellium behaviour until the Fermi energy (E_F), indicating that the ground state of potassium is indeed jellium-like. On the other hand, above E_F deep gaps appear in the DOS at 6 and 9 eV, which we attribute to empty states of *d* symmetry. The comparison of the theoretical spectra and the DOS shows that the dip-and-peak structures of *S(q,E)* are caused by the corresponding structures of the DOS. The striking result of the study is that the dynamic response of potassium is strongly affected by the empty *d* bands and is far from being jellium-like. Why aren't the excitations to the *d* bands visible in optical spectroscopies and only appear at increased *q*? The answer resides in the non-dipole character of the transitions: they reflect a change of electron's state from *s*-type into *d*-type, forbidden by optical selection rules, but allowed in IXS when the measurements probe *ε(q,E)* at nonvanishing values of *q*. The remaining differences between experiment and theory, especially that of the experimentally observed merging of the peaks B1 and B2, may be due to further lifetime broadening or effects of electron-electron interactions.

In conclusion, we have found surprisingly large deviations from a jellium behaviour in the dielectric response of potassium valence electrons when studied by IXS. Further experiments while modifying the band structure *in situ*, *e.g.* by high pressure, may become interesting in illuminating the surprisingly complicated character of this textbook example of a "free-electron" metal.

References

[1] W. Schülke, *Electron dynamics by inelastic X-ray scattering*, Oxford University Press, Oxford (2007).
[2] C. Sternemann, S. Huotari, G. Vankó, M. Volmer, G. Monaco, A. Gusarov, H. Lustfeld, K. Sturm and W. Schülke, *Phys. Rev. Lett.* **95**, 157401 (2005).

Phonons and collective dynamics

Breakdown of the continuum elasticity theory in glasses on the nanometric length-scale

Principal publication and authors

G. Monaco (a) and
V.M. Giordano (a), *Proc. Natl. Acad. Sci. USA* **106**, 3659 (2009).
(a) ESRF

The thermal properties of insulating crystals at low-temperature are governed by low-frequency acoustic excitations. These can be understood using a simple continuum elasticity theory – the Debye model – and are characterised by a linear dispersion relation: their characteristic frequency is proportional to the wavenumber, the proportionality constant being the sound velocity. Compared to crystals, glasses display a set of anomalous universal low-temperature properties [1]. In particular, at a temperature (T) of ~10 K, the thermal conductivity shows a plateau and the specific heat is characterised by an excess over the $\propto T^3$ prediction of the Debye model. This excess is related to the so-called boson peak, an excess in the number of vibrational modes in the THz frequency (ν) range with respect to the $\propto \nu^2$ prediction of the Debye model. The physical origin of these universal properties has been lively discussed in the literature for many decades; however, an accepted solution is still lacking.

One of the main reasons for this longstanding debate lies in the experimental difficulties of studying the acoustic excitations in disordered systems in the THz and sub-THz frequency range. As a consequence, the experimental data available in the literature are scarce and often even conflicting. The recent advent of the inelastic X-ray scattering (IXS) technique has opened access to the wave-number (q) and frequency dependence of the longitudinal acoustic excitations in the THz frequency range [2]. However, the IXS experiments are currently limited to $q \geq 1$ nm^{-1} with an instrumental resolution of ~0.3 THz: the (q, ν) region crucial for studying the boson peak remains then close to the edge of the capabilities of the technique. Early IXS results [2] suggested that the longitudinal acoustic excitations in glasses are unaffected across the frequency range where the boson peak appears. More recent results [3] have clarified that they actually experience a regime of strong scattering below the boson peak frequency position where their lifetime very quickly decreases on increasing frequency. Following the continuous development of the IXS technique, we have collected data of unprecedented quality that shed new light on the high frequency dynamics of glasses.

The IXS experiment was carried out on a sample of glassy glycerol at beamline ID16. IXS spectra, characterised by Brillouin peaks corresponding to a longitudinal acoustic excitation, were collected for different q values. As for simple crystals, the frequency position of the maximum of the Brillouin peak divided by q gives a sound velocity. The point here is that this velocity is characterised, at q-values of a few nm^{-1}, by an unexpected and marked decrease (negative dispersion) with respect to the macroscopic value, see Figure 20a. In the same q range, the acoustic attenuation, *i.e.* the broadening 2Γ of the Brillouin peak, shows a marked increase with a high power of q, and changes slope at a q value, q_c, related to the end of the negative dispersion observed in the sound velocity data. This implies that well-defined sound modes for $q<q_c$ rapidly lose their plane wave character

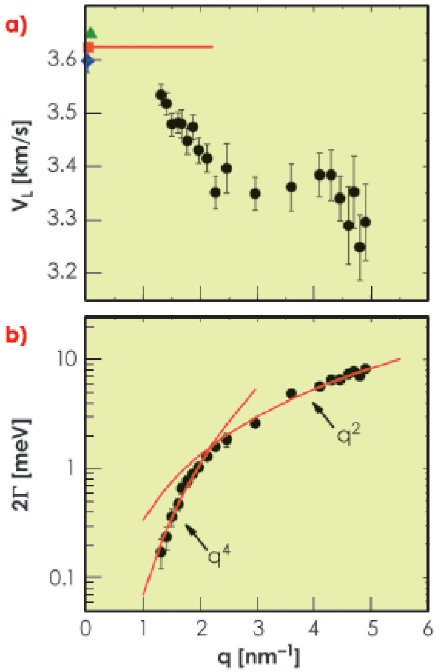

Fig. 20: Wavevector dependence of a) the longitudinal sound velocity and b) the sound attenuation, 2Γ, of a glass of glycerol at 150.1 K obtained using inelastic X-ray scattering (black circles). In a), the data are compared to those from the literature measured with lower frequency techniques: stimulated Brillouin gain spectroscopy (blue diamond), Brillouin light scattering (red square), and inelastic ultraviolet scattering (green triangle) - see principal publication for references to the original papers.

and transform, on increasing q, into a complex superposition of atomic vibrations. Moreover, q_c corresponds to frequencies of ~1 THz, *i.e.* exactly to the frequency range where the boson peak appears in this glass. This connection between boson peak and high-frequency acoustic excitations can in fact be made quantitative, and clarifies that the boson peak and the aforementioned universal excess over the Debye model prediction found in the specific heat of glasses at temperatures of ~10 K originate indeed from the peculiar acoustic properties of glasses observed here.

In other words, in crystals, the continuum elasticity model holds true on a length-scale much larger than the interatomic spacing and gradually breaks down on approaching the microscopic scale. In glasses, the structural disorder undermines the continuum Debye model in a subtle way: the continuum elasticity theory breaks down abruptly on the mesoscopic length-scale of about ten interatomic spacings characteristic of the medium range order, where it would still work well for the corresponding crystalline systems.

References

[1] W.A. Phillips, *Amorphous Solids: Low Temperature Properties* (Springer, Berlin, 1981).
[2] F. Sette, M. Krisch, C. Masciovecchio, G. Ruocco and G. Monaco, *Science* **280**, 1550 (1998).
[3] B. Rufflé, G. Guimbrètiere, E. Courtens, R. Vacher and G. Monaco, *Phys. Rev. Lett.* **96**, 045502 (2006).

Sound velocity in iron carbide (Fe_3C) at high pressure

Principal publication and authors

G. Fiquet (a), J. Badro (a), E. Gregoryanz (b), Y. Fei (c) and F. Occelli (d), *Phys. Earth Planet. Int.* **172**, 125-129 (2009).
(a) Institut de Minéralogie et de Physique des Milieux Condensés (IMPMC), Université Pierre et Marie Curie, CNRS, Université Paris Diderot, Institut de Physique du Globe de Paris (France)
(b) Centre for Science at Extreme Conditions (CSEC), University of Edinburgh (UK)
(c) Geophysical Laboratory, Carnegie Institution of Washington, Washington DC (USA)
(d) Département de Physique Théorique et Appliquée, CEA, Bruyères-le-Châtel (France)

The Earth's core is thought to be made of iron alloyed with light elements [1]. The inclusion of light elements is required to account for the discrepancies in density and sound wave velocity between seismological models and pure Fe or Fe–Ni alloys. Carbon is one of the possible alloying elements; its stability in carbides is greatly enhanced at high pressure. Extrapolation to inner core pressures indicates that iron carbide Fe_3C would crystallise preferentially to the classical high-pressure phase of iron (hcp), which could make Fe_3C a major phase in the Earth's inner core [2].

A linear dependence of longitudinal acoustic (LA) velocity as a function of density holds for many iron alloy compounds. This provides a way to compare sound velocity properties of pure iron or iron alloyed compounds with seismological models for the Earth's core [3]. Our idea was to estimate the relative abundance of Fe_3C in the Earth's core, not only on the basis of density comparison but also by using acoustic sound velocity measurements. Such measurements can be obtained at high pressure using the inelastic X-ray scattering (IXS) technique. We have thus collected IXS spectra to 83 GPa on a synthetic polycrystalline sample of Fe_3C in a diamond-anvil cell. Sound velocities were measured at high pressure by very high resolution IXS at ID28, with an

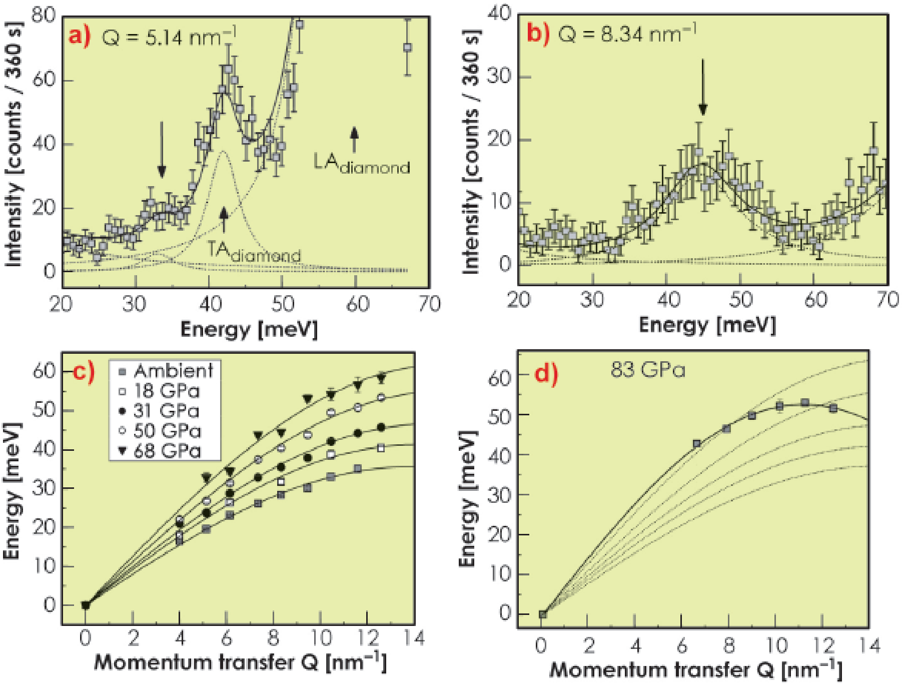

Fig. 21: a) and b) IXS spectra of a polycrystalline Fe_3C sample at 68 GPa for selected momentum transfers *Q*. The experimental data are shown along with the best fit results to the dataset (solid line) and the corresponding individual components (thin dotted line and arrow). c) Dispersion curves for polycrystalline Fe_3C to 68 GPa. d) Experimental points and dispersion curve (solid line) obtained at a pressure of 83 GPa showing a clear softening of the longitudinal acoustic branch at high *Q*.

incident photon energy of 15.817 keV and a total instrumental energy resolution of 5.5 meV full width at half maximum.

IXS patterns (Figures 21a and 21b) are characterised by an elastic contribution, centred at zero energy, and an inelastic contribution from an LA mode from Fe_3C and a transverse acoustic (TA) phonon from diamond visible at low Q values. The dispersion curves presented in Figures 21c and 21d can be well described by a sine function. Such a sine fit made to the experimental dispersion then yields the average LA velocities for the high-pressure aggregate.

At pressures exceeding 70 GPa, we also observed anomalous behaviour in the dispersion curve. The IXS data collected at 83 GPa (Figure 21d, bottom) indeed displays a strong softening of the LA branch, which could correspond to a second-order magnetic transition as proposed from theoretical calculations [4]. At lower pressures, the observed increase of the phonon frequencies corresponds to an increase of the longitudinal wave velocity (V_L) from 6100 to 9375 ms^{-1}. Angle-dispersive X-ray diffraction patterns were also collected in order to obtain the molar volume and hence, the density. Sound velocities and corresponding densities of Fe_3C are reported in Figure 22, along with results obtained for other iron light element alloys [3]. The longitudinal wave velocity of Fe_3C scales linearly with its density. We then used a simple model to describe the average density and the longitudinal velocity V_L of a two-component ideal solid, combined with a known thermal equation of state for pure iron, to estimate the optimal amount of light element Fe_3C in the alloy.

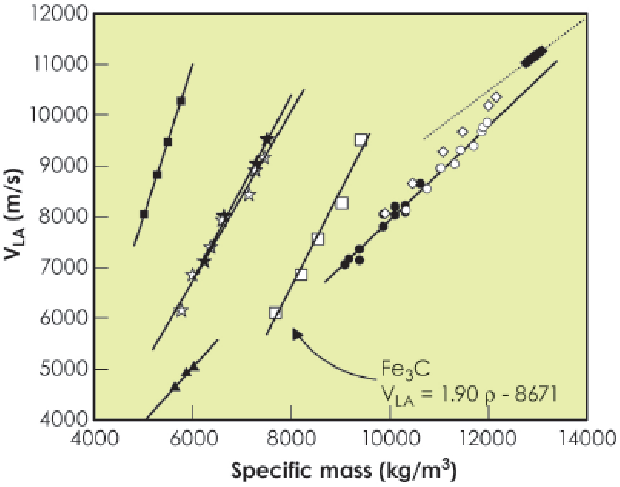

Fig. 22: LA velocities of *Pnma* Fe_3C as a function of density (hollow squares), along with results obtained for other light elements alloyed with pure iron. Solid squares: FeS_2 pyrite; hollow stars: FeSi; solid stars: FeO; solid triangles: phase IV FeS, circles: pure iron. Data are compared with seismic observations for the liquid outer core (hollow diamonds) and solid inner core (solid diamonds). See [3] for further details.

Assuming that our sound velocity model holds for low light element contents, and that the magnetic transition may be shifted to higher pressures for low carbon content, the main result is that about 1 wt% carbon in the solid inner core could account for the difference between the measured longitudinal velocity and density, and the seismological Earth's inner core data. With silicon also shown to be abundant in the solid core [3], we are thus left with silicon and carbon as possible alloyed light elements to be further investigated in the Fe-Si-C ternary system.

References

[1] F. Birch, *J. Geophys. Res.* **57**, 227–286 (1952).
[2] B. Wood, *Earth Planet. Sci. Lett.* **117**, 593–607 (1993).
[3] J. Badro, G. Fiquet, F. Guyot, E. Gregoryanz, F. Occelli, D. Antonangeli and M. d'Astuto, *Earth Planet. Sci. Lett.* **254**, 233–238 (2006).
[4] L. Vočadlo, J. Brodholt, D.P. Dobson, K.S. Knight, W.G. Marshall, G.D. Price and I.G. Wood, *Earth Planet. Sci. Lett.* **203**, 567–575 (2002).

Lattice dynamics of stishovite from powder inelastic X-ray scattering

Principal publication and authors

A. Bosak (a), I. Fischer (a), M. Krisch (a), V. Brazhkin (b), T. Dyuzheva (b), B. Winkler (c), D. Wilson (c), D. Weidner (d), K. Refson (e) and V. Milman (f), *Geophysical Research Letters* **36**, L19309 (2009).
(a) ESRF
(b) Institute for High Pressure Physics RAS, Troitsk Moscow region (Russia)
(c) Geowissenschaften, Goethe-Universität, Frankfurt a.M. (Germany)
(d) Mineral Physics Institute, Stony Brook University, Stony Brook (USA)
(e) Rutherford-Appleton Laboratory, Chilton, Didcot (UK)
(f) Accelrys, Cambridge (UK)

Elastic and thermodynamic properties of minerals play a central role in Earth science, and are required to obtain insight into pressure-temperature stability fields and the validity of geochemical models. Quantities such as specific heat, entropy, free energy, Debye temperature and velocity can in principle be derived from the vibrational density of states (VDOS). The complete momentum resolved lattice dynamics, however, provides much more information, *e.g.* all components of the elastic stiffness tensor. An often encountered major obstacle to overcome in order to obtain the complete set of phonon dispersion curves is that conventional inelastic X-ray (IXS) and neutron scattering (INS) approaches require single crystals. In a previous work we have shown that this limitation can be overcome by recording IXS spectra from polycrystalline materials over a sufficiently large momentum transfer (Q) range, and to interpret them using an adjustable force constant model [1]. Here, we apply this methodology to the case of stishovite, a high pressure SiO_2 polymorph. Stishovite has been chosen as a benchmark case, since (i) its geophysical relevance is currently

Ref.	C_{11}	C_{33}	C_{12}	C_{13}	C_{44}	C_{66}	B	V_D
BLS [3]	455(1)	762(2)	199(2)	192(2)	258(1)	321(1)	310(2)	7.97(2)
from DFT (this work, see text)	441(4)	779(2)	166(3)	195(1)	256(1)	319(1)	300(3)	7.98(4)

Table 1: Comparison of elastic moduli C_{ij} and bulk modulus B (in GPa) and Debye velocity V_D (in km/s) with the most recent data set from Brillouin light scattering (BLS).

discussed in relation to the seismic signature of the X-discontinuity at a depth about 300 km [2], and (ii) there is no complete experimental data set for its lattice dynamics.

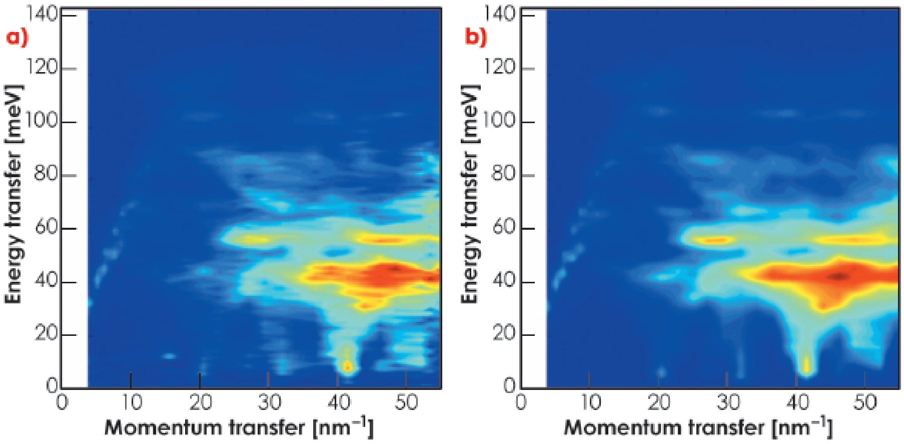

Fig. 23: (*E-Q*) intensity maps for polycrystalline stishovite: a) experiment; b) calculation. Elastic line subtraction and renormalisation are applied to the experimental spectra; the energy axis of the calculated map is scaled by a factor 1.05.

The IXS spectra were recorded at beamline **ID28** between Q = 3.9 nm^{-1} and 54.8 nm^{-1} with an overall energy resolution of 3 meV. As nine IXS spectra at different Q-values are recorded simultaneously, the desired Q-range could be covered with only three spectrometer settings, with a total data acquisition time of two days. Lattice dynamics calculations were performed using CASTEP software employing density functional perturbation theory in its DFT-GGA version.

The excellent agreement between the experimental and theoretical data can be appreciated in **Figure 23**, which displays the energy (E) and momentum transfer (Q) dependence of the inelastically-scattered intensity. We emphasise that a single scaling factor was applied to the theoretical energy scale. Furthermore, the validity of the model is proven for *any* crystallographic direction, as orientation averaging probes the low-symmetry directions as well. Relative intensities of phonons are naturally embedded in the experimental spectra thus providing the instrument to check the consistency of the phonon eigenvectors within the model. The phonon dispersion for high symmetry directions naturally appears as a by-product (see principal publication).

The agreement of elastic moduli derived from the DFT-GGA calculation by the stress-strain method with those determined experimentally from Brillouin light scattering was significantly improved by rescaling the sound velocity, density and cell shape, where scaling factors were derived from comparison of calculations to the experimental polycrystalline data. A significant deviation (~20%) remains for C_{12}, while all other moduli and the integral properties (bulk modulus B and Debye velocity V_D) converge very well (see **Table 1**), thus confirming the predictive power of DFT-GGA stress-strain calculations.

To obtain the elastic anisotropy from polycrystalline data makes the employed approach attractive for Earth science. When the anisotropy of individual phases is known, the macroscopic anisotropy observed in many parts of the Earth can be related to the preferable orientation pattern. While the current study is limited to ambient pressure and temperature, an extension to high pressures is feasible. This would allow the derivation of reliable elastic and thermodynamic data for materials such as polycrystals that cannot be quenched to ambient conditions and can only be synthesised in minute amounts, *e.g.* in a diamond anvil cell.

References
[1] I. Fischer, A. Bosak and M. Krisch, *Phys. Rev. B.* **79**, 134302 (2009).
[2] Q. Williams and J. Revenaugh, *Geology* **33**, 1-4 (2005).
[3] F. Jiang, G.D. Gwanmesia, T.I. Dyuzheva and T.S. Duffy, *Physics of the Earth and Planetary Interiors* **172**, 235-240 (2009).

Structure of materials

The reorganisation of the Experiments Division during 2009 saw the creation of the new Structure of Materials group, combining the beamlines dedicated to surface and interfacial science – ID01, ID03 and ID32 – with those for structural studies of bulk materials and buried interfaces using predominantly hard-energy photons to penetrate through dense absorbing samples and sample environments, ID11, ID15 and ID31. Understanding bulk, surface and interfacial characteristics is of crucial importance in designing and optimising the performance of modern materials and systems composed from them. Furthermore, this provides a rich domain for the investigation of fundamental physical and chemical properties of natural and synthetic substances. Many user groups and beamlines at ESRF carry out research important to the broader materials area, especially our colleagues in the CRG beamlines. Hence this chapter has evolved into a substantial compilation, with nineteen highlight articles -the tip of the iceberg- drawn from some fifteen beamlines. They cover a variety of themes.

One theme is the phenomenon of self organisation or self assembly: the way in which surfaces or molecules adsorbed on surfaces organise themselves spontaneously to optimise their mutual interactions. Surface roughness, molecular coverage and aggregation can hold profound influence over the optical, magnetic and electronic properties, and can affect resistance to corrosion, etc. Very small objects such as quantum dots and nano-islands grown on substrates have modified properties because of the confinement of the electrons within these structures, further modified by the effects of strain or chemical composition gradients, allowing, potentially, the possibility to tune such properties for specific applications.

In situ studies, in which a system is monitored while undergoing chemical or physical evolution, require rapid data acquisition with a time resolution appropriate for the process under investigation. Detailed information about the underlying mechanisms can be extracted, from which more effective and efficient processes can be envisaged. Two of the examples presented here are of relevance to a cleaner environment and energy research, with investigation of the oxidation of carbon monoxide over a precious metal catalyst, used to reduce the toxicity of the exhaust gas from a car, and the investigation of the distribution of the crucial water component in the proton exchange membrane in a working hydrogen fuel cell.

Finally, there is atomic structural characterisation of a range of bulk materials, such as metallic glasses, or investigation of the evolution of structure at low temperatures or when applying pressure. These systems often have electronic, magnetic, or superconducting properties and the behaviour under changing conditions can reveal subtle details of the underlying electron, spin and orbital-ordering interactions.

These studies exploit the properties of ESRF's synchrotron X-rays, *i.e.* great intensity, stringent collimation and an ability to focus the beam to sub-micrometre dimensions, wavelength tunability (with access to very hard photon energies), coherence, and the time structure of the source. With the upgrade underway, plans for future developments to the group's capabilities include the two beamline projects UPBL01 and UPBL02, evolutions of ID01 and ID15, respectively. Instrumental progress during the last year includes the installation of an in-vacuum, white-beam, refractive-lens transfocator on ID11, allowing great flexibility for focussing or condensing the beam with impressive increases in photon density at the sample. Such is the success of this

device that ID15 will also be installing one in early 2010. ID32 has commissioned a new setup for hard X-ray photoelectron spectroscopy (HAXPES) and X-ray standing wave measurements. The new spectrometer allows up to 15 keV electron kinetic energies and 50 meV resolution and is also equipped with a UHV preparation chamber, cryostat (30 K) and a load lock. The old XSW chamber and analyser have been removed from the experiments hutch. Finally, Till Metzger has left ID01 after nearly ten years as scientist in charge of the beamline where (among many other achievements) he built up the current programme on coherent diffraction imaging. We send him our very best wishes for his sabbatical leave and future retirement.

A. Fitch

Transition from smoothening to roughening of ion-eroded GaSb surfaces

Principal publication and authors
A. Keller (a), A. Biermanns (b), G. Carbone (c), J. Grenzer (a), S. Facsko (a), O. Plantevin (d), R. Gago (e), and T.H. Metzger (c), *Applied physics letters* **94**, 193103 (2009).
(a) Institute of Ion Beam Physics and Materials Research, Forschungszentrum Dresden-Rossendorf, Dresden (Germany)
(b) Festkörperphysik, Universität Siegen (Germany)
(c) ESRF
(d) Centre de Spectrométrie Nucléaire et de Spectrométrie de Masse, Univ. Paris-Sud, Orsay (France)
(e) Instituto de Ciencia de Materiales de Madrid (Spain)

Bombarding a surface with energetic ions leads to the removal of surface material. This process of ion beam sputtering (IBS) is a common tool for surface modification. It is well known that optical, magnetic, tribological and other properties of thin films are strongly influenced by the roughness of surfaces and interfaces. Therefore, controlling the roughness is a main issue in a broad variety of technological applications. With IBS the roughness of solid surfaces can be modified on lateral scales of a few nanometres to micrometres or even further. Depending on the conditions, IBS can lead to surface smoothening or roughening, leading eventually to periodic patterns, *i.e.* ripple and hexagonal dot patterns. In 1988, over 20 years after the first observation of ripple-like patterns in 1962 by Navez *et al.*, Bradley and Harper proposed a mechanism based on Sigmund's sputtering theory to explain the experimentally observed features. In the current understanding, the interplay of roughening and smoothening processes leads to the formation of these self-organised patterns [1].

Here we report on *in situ* measurements of the surface roughness during IBS of GaSb surfaces under normal incidence of the ion beam. In particular we address the early time regime, which gives insight into the detailed mechanisms governing the dynamics at the beginning of pattern formation. In contrast to earlier investigations that were only able to probe a few intermediate steps by alternate manipulations between IBS and an analytical method *e.g.* AFM, we exploited an *in situ* setup taking advantage of contactless and non-destructive X-ray scattering techniques. During IBS, we used X-ray reflectivity to probe the surface roughness as well as the thickness of the sputtered layer, and grazing-incidence small-angle X-ray scattering (GISAXS) to investigate the lateral structure. For the first time we have observed a transition in the surface morphology: first, the GaSb surface was smoothened, followed by roughening and the formation of a dot pattern proving that the initial smoothening has the same physical origin as the relaxation mechanism for the formation of periodic structures.

Sputtering was carried out with Ar$^+$ ions at an energy of 450 eV and an ion flux of $1x10^{15}$ cm^{-2}s^{-1} in a compact high vacuum chamber equipped with a

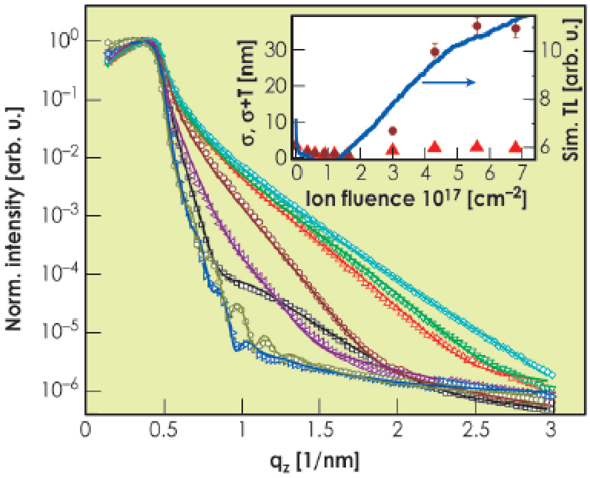

Fig. 24: XRR at different fluences (thin lines are the simulation); inset: Evolution of the roughness σ (triangles) and of the transition layer (TL) thickness (experimental: dots; simulation: thick line).

Kaufman type ion source mounted on the goniometer at beamline ID01. Reflectivity and GISAXS spectra were measured at an energy of 8 keV after sequential steps of sputtering, stopping the sputtering during the X-ray measurements.

Figure 24 shows reflectivity measurements of the surface in initial, untreated, and after sputtering states. Prior to IBS, the reflectivity reveals a rather rough surface with a thin surface layer that is probably due to the native oxide on top of the GaSb. After the first sputtering cycles up to a total fluence of 1.6x10^{17} cm^{-2} Ar^{+} ions, the reflectivity increases significantly, indicating a smoothening of the surface. Thereafter, the trend is reversed and the reflectivity decays again. The appearance of thickness fringes indicates the onset of pattern formation. The reflectivity data were analysed assuming a transition layer on top of a GaSb substrate that is characterised by a constant lower electron density, by its thickness T, and by introducing a surface roughness σ (inset). The GISAXS patterns in Figure 25 are in good agreement with the reflectivity: at the beginning the strong diffuse scattering is reduced, having its minimum at almost the same fluence resulting in an rms roughness of below 1 nm. At a fluence of 3x10^{17} cm^{-2}, satellite peaks appear, demonstrating the existence of a periodic surface pattern. The position of these peaks is related to the mean interdot distance λ, whereas the number and width of the satellite peaks are related to the correlation length ξ. While λ is almost constant and about 31 nm, ξ increases by a factor of 2.

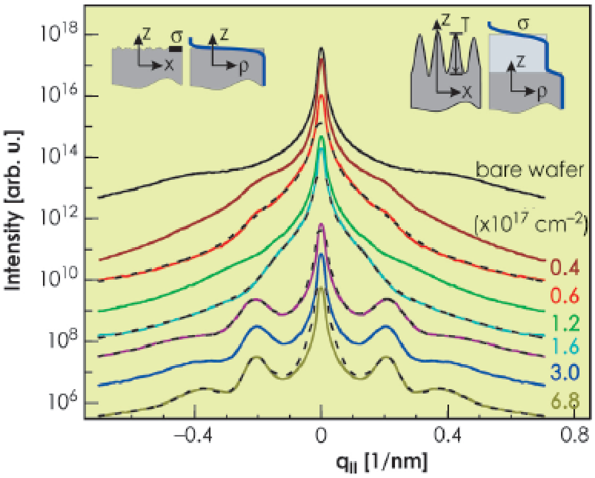

Fig. 25: GISAXS spectra (dashed lines are the simulation); inset: model used for simulation; curves are shifted for clarity.

The experimental results have been compared with numerical calculations of the surface dynamics by a continuum Kuramoto-Sivashinsky equation that is based on the Bradley and Harper theory extended by non-linear terms (thick line in the inset of Figure 24).

In summary, we present *in situ* measurements of nanodot formation on an Ar-eroded GaSb surface using X-ray reflectivity and GISAXS. We show that the sputtering process leads to an initial smoothening of the surface, followed by a roughening process associated with the formation of a nanodot pattern. Both processes are the result of the same diffusion mechanism.

References

[1] W.L. Chan and E. Chason, *J. Appl. Phys.* **101**, 121301 (2007).

New insights into the interface structure of alkanethiol self-assembled monolayers

Principal publication and authors
A. Chaudhuri (a), M. Odelius (b), R.G. Jones (c), T.-L. Lee (d), B. Detlefs (e) and D.P. Woodruff (a), *J. Chem. Phys.* **130,** 124708 (2009).
(a) University of Warwick, Coventry (UK)
(b) Stockholm University, Stockholm (Sweden)
(c) University of Nottingham, Nottingham (UK)
(d) Diamond Light Source Ltd, Didcot (UK)
(e) ESRF

Alkanethiols, $CH_3(CH_2)_{n-1}SH$, on the (111) face of gold (typically in the form of an evaporated film) are the archetypal self-assembled monolayer system, and underpin a wide range of applications including sensors, molecular electronics and corrosion protection through functionalisation of the molecular end-group. In all cases the thiol hydrogen is lost by interaction with the surface to produce a thiolate, and the molecule is attached through the S head-group atom. However, even for the simplest system, that of methylthiolate, CH_3S^-, the structure of the Au/thiol interface remains in doubt [1]. For many years it was assumed that the S atoms occupied the highest (three-fold) coordination 'hollow' sites on the hexagonal close-packed outermost surface layer of Au atoms, and subsequent theoretical total energy calculations appeared to support this view, or favoured occupation of two-fold coordinated 'bridging' sites. However, two more recent independent experimental studies concluded that the S head-group atom actually bonds atop a single Au surface atom. It is now believed that this apparent inconsistency of theoretical and experimental studies is due to an incorrect underlying assumption of all of the earlier theoretical studies – namely that the Au(111) surface is structurally unchanged by the adsorption. New experiments indicate that the thiolate species are actually bonded to Au adatoms, and that the 'self-assembly' in these systems is of Au-thiolate moieties, rather than the thiolate molecules alone. There are, however, two distinctly different adatom models that have been proposed on the basis of previous experiments, namely an Au-adatom-monothiolate, in which the S sits atop a single Au adatom in a hollow site of the underlying surface, and an Au-adatom-dithiolate, in which the Au adatom occupies a bridging site, and the two attached thiolate species occupy adjacent atop sites on opposite sides of the Au adatom (**Figure 26**).

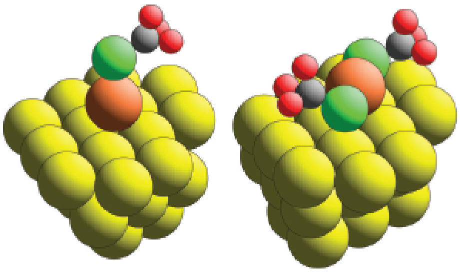

Fig. 26: The two alternative Au-adatom-thiolate models for methylthiolate on Au(111).

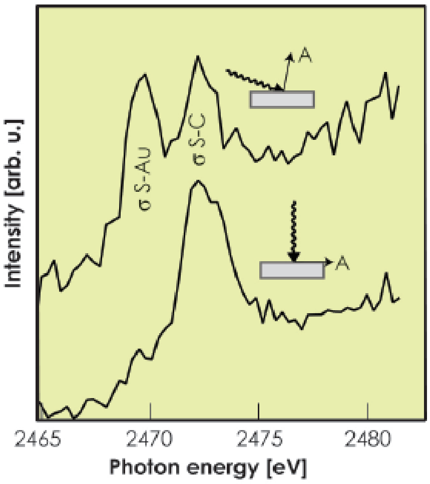

Fig. 27: Sulphur K-edge NEXAFS recorded at grazing (10°) and normal incidence from an Au(111)/methylthiolate surface.

In an attempt to resolve this question of which adatom model is correct, we have used sulphur K-edge near-edge X-ray absorption spectroscopy (NEXAFS) at beamline **ID32**. Conventionally, the main peaks seen in NEXAFS from molecular adsorbates are assigned to intramolecular scattering resonances. However, aided by theoretical simulations of the spectra, we have shown that, for this adsorption system, one of the two dominant NEXAFS peaks is due to excitation to a σ-symmetry S-C intramolecular resonance, but the other involves excitation to a σ-symmetry S-Au resonance (**Figure 27**). The dependence of the amplitude of this latter feature on the direction of the polarisation vector of the incident X-radiation therefore provides a direct indication of the direction of the associated S-Au bond. The data show this bond to be perpendicular to the surface, consistent with atop site adsorption. While both Au adatom structural models have the S head-group atom atop a surface Au atom, in the Au-adatom-dithiolate model the S atom also has an Au atom (the adatom) to one side, creating an additional S-Au bond essentially parallel to the surface. The fact that the NEXAFS resonance assigned to S-Au scattering is only seen under conditions consistent with the S-Au bond being perpendicular to the surface would therefore seem to exclude this model. Further theoretical modelling, however, shows that this is not the case. Specifically, the fact that the Au adatom in this model is bonded to two S atoms causes an energy shift in the NEXAFS peak associated with the parallel S-Au bond such that it overlaps the intramolecular σ S-C peak. As such, although the NEXAFS data provide further support for the local atop site of the S head-group atom, they fail to distinguish clearly the two alternative Au-adatom-thiolate reconstruction models.

Additional information in the S and C atoms sites was also obtained from normal-incidence X-ray standing wave (NIXSW) measurements, providing further confirmation of the atop location of the S atom, but also indicating that the C atoms lie above hollow sites. The S-C bond orientation on the surface implied by this information does appear to favour the monothiolate adatom model.

Reference

[1] D.P. Woodruff, *Phys. Chem. Chem. Phys.* **10**, 7211-7221 (2008).

3D Ordered gold strings by coating nanoparticles with mesogens

Principal publication and authors
X. Zeng (a), F. Liu (a),
A.G. Fowler (a), G. Ungar (a),
L. Cseh (b,d), G.H. Mehl (b) and
J.E. Macdonald (c), *Advanced Materials* **21**, 1746-1750 (2009).
(a) Department of Engineering Materials, University of Sheffield (UK)
(b) Department of Chemistry, University of Hull (UK)
(c) School of Physics and Astronomy, Cardiff University (UK)
(d) Present address: Romanian Academy, Institute for Chemistry, Timisoara (Romania)

Gold nanoparticles associate into highly-ordered structures when coated with ligands formed from mesogens, the rigid parts of a liquid-crystal molecule. The nanoparticles no longer follow the usual packing of spheres and form columnar structures, strings, with interparticle spacing that can be controlled by the choice of co-ligand.

Metallic nanoparticles have attracted great interest for their potential electronic [1], optical [2], photonic [3] and medical [4] applications. These applications normally require the fabrication of bulk 3-D arrays of metal nanoparticles, or "meta-atoms", with prescribed geometrical layouts. So far most of these arrays could only be produced with exceptionally uniform nanoparticles, and the range of array types was limited by the particle shape; *e.g.* cubic arrays from spherical particles. Recently Mehl and Cseh managed to graft liquid crystal molecules side-on to the nanoparticles [5]. Following on from this work, we have created self-assembled 3-D and 2-D arrays of these liquid-crystal-coated gold nanoparticles.

Two different mesogen-covered gold nanoparticle systems were studied, as shown in **Figure 28**. Small nanoparticles (ca. 2 nm in diameter) were used. Such materials preserve the ability of the mesogens to form a liquid crystalline phase. The alignment of the mesogens breaks the cubic symmetry that the nanoparticles would normally adopt, and introduces anisotropy to the periodic lattices that form.

Grazing incidence small-angle X-ray scattering (GISAXS) experiments, carried out at beamline **BM28** (XMaS),

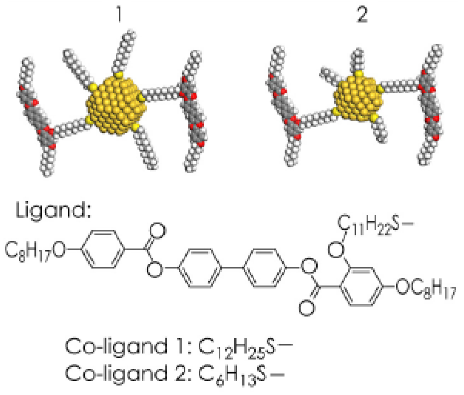

Fig. 28: Schematic structure of the gold nanoparticles coated with mesogens and alkylthiols.

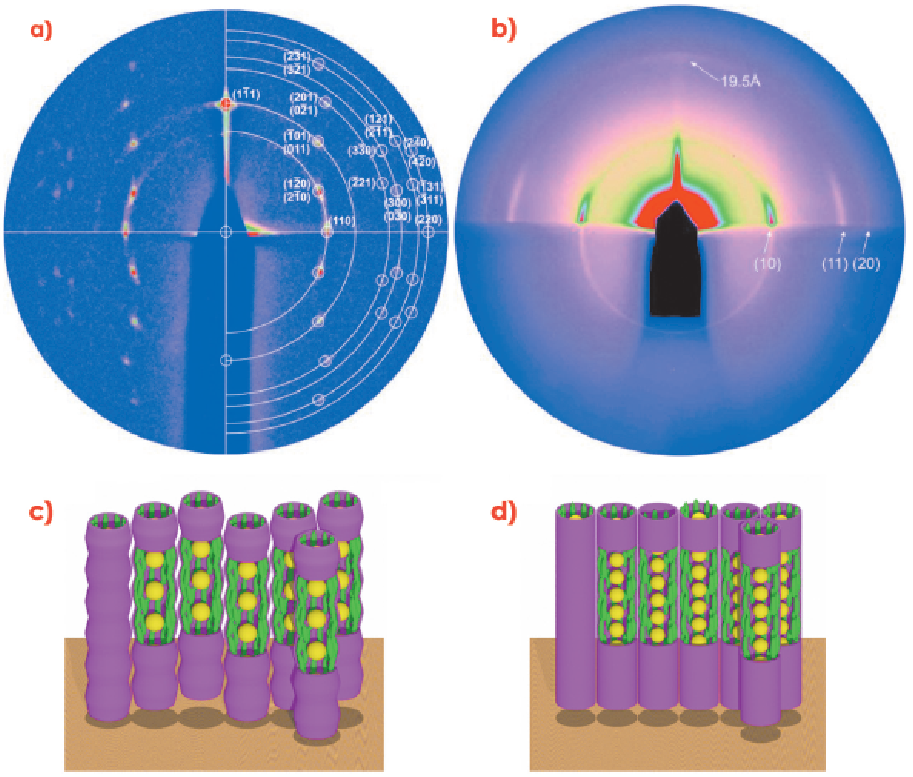

Fig. 29: GISAXS diffraction patterns of a) system **1** and b) system **2**, and corresponding schematic models of c) the rhombohedral phase in system **1**; d) the hexagonal columnar phase in system **2**; yellow: gold nanoparticles, green: mesogens.

were extremely useful in determining the structures of these anisotropic arrays. GISAXS patterns from well-oriented films of systems **1** and **2**, prepared on silicon substrate, are shown in **Figures 29a** and **29b**. On the basis of these patterns, **1** was found to form a 3D rhombohedral lattice with space group $R\bar{3}m$, while **2** was shown to organise into a 2D hexagonal columnar lattice. The schematic models of the two phases are shown in **Figures 29c** and **29d**.

GISAXS experiments on oriented films of **2** provided additional information about the columnar phases. **Figure 29b** shows that the nanoparticle columns stand perpendicular to the substrate surface. A weak diffuse meridional scattering peak indicates that the average distance between neighbouring gold nanoparticles within a column is just 2.0 nm.

The mesophase structure of both **1** and **2** can be described as consisting of strings of nanoparticles surrounded by a sheath of axially aligned mesogens. A significant feature illustrated by the present results is the remarkable scope for varying the interparticle distance in the column direction simply by varying the length of the co-ligand thioalkyl chains. Thus, while in **1** the interparticle gap is 1.7 nm, in **2** the gap virtually disappears and the nanoparticles touch in the direction of the string.

This work demonstrates that highly-ordered superlattices of metal nanoparticles other than those expected from mere packing of spheres can be created by coating the particles with liquid crystals. The results establish the first rules on which to base future designs of more complex lattices with a view to building self-assembled metamaterials.

References
[1] S.W. Boettcher, N.C. Strandwitz, M. Schierhorn, N. Lock, M.C. Lonergan and G.D. Stucky, *Nat. Mater.* **6**, 592-596 (2007).
[2] S. Eustis, M.A. El-Sayed, *Chem. Soc. Rev.* **35**, 209-217 (2006).
[3] P.N. Prasad, *Nanophotonics*, John Wiley & Sons, Inc. Hoboken, New Jersey (2004).
[4] J. Kim, Y. Piao, T. Hyeon, *Chem. Soc. Rev.* **38**, 372-390 (2009).
[5] L. Cseh, G.H. Mehl, *J. Mater. Chem.* **17**, 311-315(2007).

Looking underneath fullerenes on Au(110): formation of dimples in the substrate

Principal publication and authors
M. Hinterstein (a,b), X. Torrelles (a), R. Felici (c), J. Rius (a), M. Huang (d), S. Fabris (d), H. Fuess (b) and M. Pedio (e), *Phys. Rev. B* **77**, 153412 (2008).
(a) Institut de Ciència de Materials de Barcelona, ICMAB-CSIC (Spain)
(b) Technische Universität Darmstadt (Germany)
(c) ESRF
(d) CNR-INFM DEMOCRITOS National Simulation Center, Grignano, Trieste (Italy)
(e) TASC National Laboratory, INFM-CNR, Trieste (Italy)

Adsorption of organic molecules on metal surfaces can lead to complex nanostructuration of the supporting substrate [1]. The precise atomic and electronic structures of the C_{60}/Au(110) interface have been unveiled by combining synchrotron-based diffraction and spectroscopic techniques with density functional theory (DFT) calculations. Using the experimentally determined structure, DFT shows that the formation of strong directional C-Au bonds arising from the hybridisation between the molecular π orbitals and the surface *s* metal states. This is the driving force of a massive interface reorganisation that leads to the Au(110)-*p*(6x5) substrate reconstruction [2] and to the formation of surface nanodimples. The fullerenes are located above these nanodimples, which are one and two layers deep and allow a large increase in the metal/molecule contact area. This new configuration alters the electronic properties of the molecule and substrate system as detected by photoemission (UPS) and inverse photoemission (IPE).

The detailed structure of the C_{60}-substrate interface has been determined by using surface X-ray diffraction (SXRD) at beamline **ID03**. The structural SXRD analysis was performed on the basis of an extensive data set containing 1096 reflections, specific to the p(6x5) structure. These are reduced to 834 after averaging between the equivalent reflections with symmetry *p2mg* that form part of 48 fractional-order rods and 8 crystal truncation rods. The resulting surface substrate structure contains two symmetry-independent nanopits, one or two layers deep, where the fullerenes are hosted. **Figure 30** shows top and lateral views of the C_{60}/Au(110)-p(6x5) interface structure.

The calculated bonding charge, the density of electronic states (DOS), and the partial DOS (C p-DOS, resulting from projecting the wave functions on the atomic C-2p states) by DFT provide evidence of strong directional C-Au bonding (**Figure 31**). The bonding charge density is mostly localised between the lateral C atoms in contact with the nanopit edges, while the interstitial region directly underneath the C_{60} is not primarily involved in bond formation. The degree of directional electronic contribution to the bonding is shown in **Figure 31a** by charge accumulation (red pockets) localised along the shortest C-Au bond lengths (marked by dashed lines and ranging between 3.1-3.3 Å). Moreover, molecular adsorption induces the polarisation of the C_{60} molecule, involving mostly the C atoms on the lower half of the molecule.

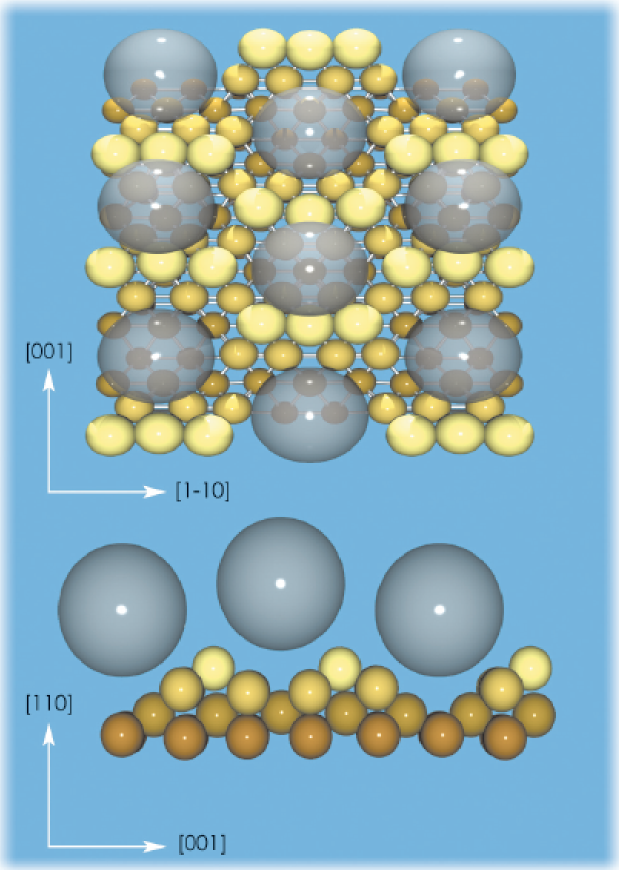

Fig. 30: Top and lateral views of the C_{60}/Au/110-*p*(6x5) interface structure. The transparent spheres simulate the C_{60} molecules and indicate the absence of preferential orientation.

The photoemission spectrum and the calculated DOS (**Figure 31b**) do not show any feature between the Fermi level and the C_{60} HOMO susceptible to be assigned to an ionic contribution to bonding between C and Au atoms. The same conclusion can be drawn from the analysis of the unoccupied states (conduction band inverse photoemission data [3] IPE, and DOS in **Figures 31b and 31c**). With respect to an isolated C_{60} molecule (**Figure 31c**), the LUMO and LUMO+1 states (labelled b) are shifted to lower energies upon adsorption (**Figure 31b**) but no sizeable fraction of the C_{60} LUMO is transferred below the Fermi level. The broad feature above the Fermi level in the IPE spectrum (a and a` in **Figure 31d**) results from two different origins: a flat contribution from the Au *s* states (a) and the molecular LUMO (a'). At higher energies, the spectrum is dominated by the three distinct molecular peaks (b, c, and d in **Figure 31d**). The additional charge available after C_{60} adsorption is redistributed in the contact interfacial region and substrate mass transport takes place in order to form and maximise the number of directional bonds.

These results have general implications on the adsorption of large organic molecules on metal surfaces and could lead to the revision of their interaction mechanisms as inferred by STM analysis.

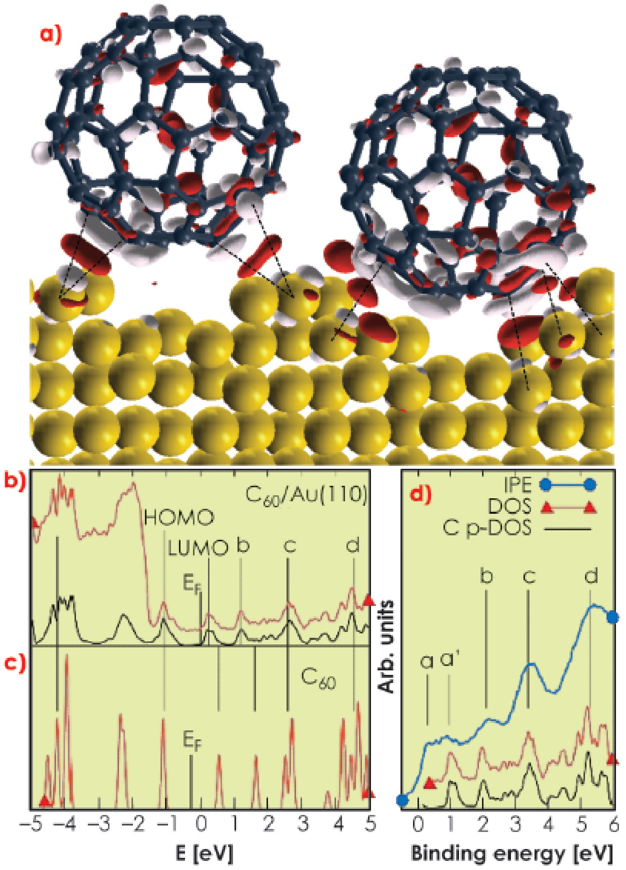

Fig. 31: a) Bonding charge density obtained from DFT calculation of the structure model of **Figure 30**, showing positive (red) and negative (light grey) electron density isosurfaces (|0.005| e/Å^{-3}). b) Experimental PE spectrum (red), calculated DOS (black) for C_{60}/Au(110), and c) C p-DOS for an isolated C_{60} molecule. d) Conduction band IPE data (blue) and C p-DOS (black) for C_{60}/Au(110).

References

[1] R. Felici, M. Pedio, F. Borgatti, S. Iannotta, M. Capozi, G. Ciullo and A. Stierle, *Nat. Mater.* **4**, 688 (2005).
[2] M. Pedio, R. Felici, X. Torrelles, P. Rudolf, M. Capozi, J. Rius, and S. Ferrer, *Phys. Rev. Lett.* **85**, 1040 (2000).
[3] M. Pedio, M.L. Grilli, C. Ottaviani, M. Capozi, C. Quaresima, P. Perfetti, P.A. Thiry, R. Caudano, and P. Rudolf, *J. Electron Spectrosc. Relat. Phenom.* **76**, 405 (1995).

Wurtzite-type CoO-nanocrystals in ultrathin ZnCoO films

Principal publication and authors
H.L. Meyerheim (a), C. Tusche (a), A. Ernst (a), S. Ostanin (a), I.V. Maznichenko (b), K. Mohseni (a), N. Jedrecy (c), J. Zegenhagen (d), J. Roy (d), I. Mertig (b), and J. Kirschner (a), *Phys. Rev. Lett.* **102**, 156102 (2009).
(a) Max-Planck-Institut f. Mikrostrukturphysik, Halle (Germany)
(b) Inst. f. Physik, Martin-Luther-Universität Halle-Wittenberg, Halle (Germany)
(c) Inst. des Nano Sciences de Paris, Univ. P. et M. Curie-Paris 6, Paris (France)
(d) ESRF

Diluted magnetic semiconductors have become a central theme in solid state research over the last decade. They offer unique possibilities to combine new spintronic applications into existing semiconductor device architectures. In spintronic systems, information storage is based on the direction of the magnetisation (up or down) of a magnetic material. Zinc oxide (ZnO) doped with 5-20 at.% Co represents a prototype example for the class of spintronic materials, in which the Co atoms substitute Zn atoms within the wurtzite structure. In the wurtzite structure each metal atom is tetrahedrally coordinated by four oxygen atoms. Several theoretical models have been proposed to explain ferromagnetism in Zn(Co)O alloys. Most recently, Dietl *et al.* [1] have suggested the presence of uncompensated spins at the surface of antiferromagnetic wurtzite-type CoO nanocrystals within the ZnO host lattice, however direct experimental evidence for this model is so far lacking. This can be attributed to the similarity of the atomic species obscuring any clear cut discrimination using scattering and microscopy techniques.

At beamline ID32 we have carried out a surface X-ray diffraction study on cobalt doped (20%) ZnO films deposited on Ag(111) using pulsed laser deposition in the thickness range of about 1 nm. A previous study [2] has shown that in the first layer adjacent to the Ag(111) surface wurtzite-type ZnO adopts the hexagonal-boron-nitride (h-BN) structure, in which the metal atom is surrounded by oxygen atoms in a threefold planar coordination.

Fig. 32: Structural model for Zn(Co)O at the interface between ZnO (left) and CoO (right). Oxygen atoms are shown as large spheres. Layers are numbered from 1 to 6. Interatomic distances given in angstroms. The lower left side (a) shows the PDF of the first layer metal site on an enlarged scale. Note the presence of two distinct metal positions indicative of static disorder.

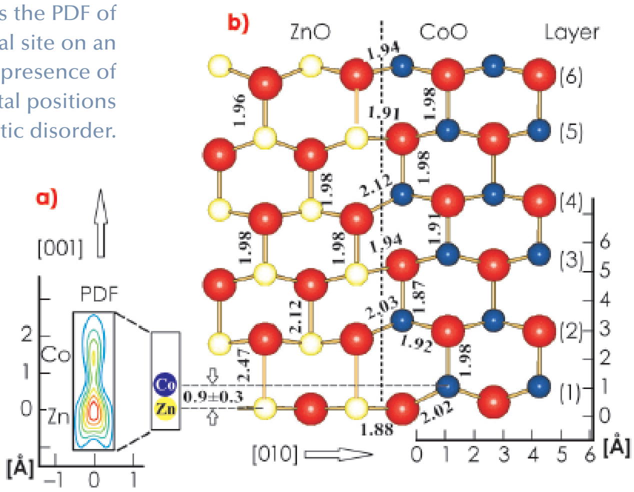

The most important result of the analysis of the X-ray data is the pronounced vertical disorder observed for the first layer metal atomic site, which diminishes in the subsequent layers. Figure 32a shows in detail the probability density function (PDF) for the first layer metal site, representing the distribution of the atomic positions. Two well defined maxima are identified separated by 0.9±0.3 Å indicating the presence of two different atomic sites. According to their relative magnitudes (3:1), the lower and upper PDF maxima can be attributed to Zn and Co, respectively. When developing a structural model, the large vertical disorder requires the separation of the ZnO and CoO phase, ruling out random alloying, since the latter would involve many metal-oxygen distances below 1.5 Å, which is incompatible with the sizes of the atoms. While ZnO adopts the planar h-BN structure, CoO crystallises in the wurtzite-phase, in which the Co atom is located several tenths of an angstrom above the plane of oxygen atoms making the two metal (oxide) species distinguishable.

This different behaviour of ZnO and CoO is supported by first principles calculations. The wurtzite to h-BN transition follows a transformation path characterised by a decreasing c/a lattice parameter ratio. The a lattice parameter is kept constant at the experimental value $a = 3.27$ Å and the height of the metal atom above the plane of oxygen atoms (labelled as uc in Figure 33) is relaxed from the value of $uc = 0.63$ Å corresponding to the WZ-phase to $uc = 0.0$ Å characterising the h-BN structure. Whereas, for ZnO we find that the transition takes place from $c = 5.22$ Å ($c/a = 1.61$, $uc = 0.63$ Å) to $c = 4.21$ Å ($c/a = 1.3$, $uc = 0.0$ Å) as shown by the solid (black) line in Figure 33. Although CoO exists in the wurtzite phase with almost the same c

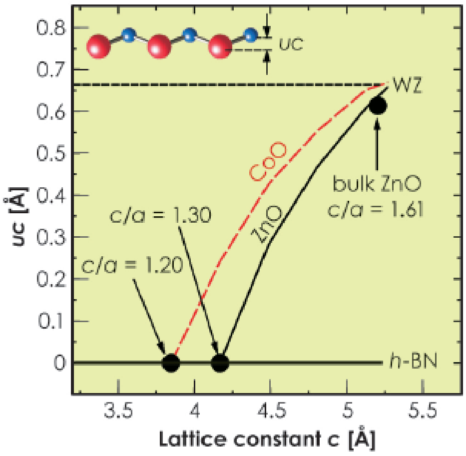

Fig. 33: Calculated *uc* vs. *c* for bulk ZnO and CoO (solid and dashed line). Parameters *uc* and *c* for wurtzite, bulk ZnO and h-BN are indicated for comparison.

lattice parameter as ZnO, the transition to the h-BN-phase requires a larger compression ($c = 3.88$ Å ($c/a = 1.2$)) directly reflecting the tendency of CoO to avoid the h-BN structure (red line in **Figure 33**).

In summary, our study has given evidence for the presence of CoO-nanocrystals in ZnO supporting the phase decomposition model [1].

References
[1] T. Dietl, T. Andrearczyk, A. Lipińska, M. Kiecana, M. Tay, and Y. Wu, *Phys. Rev. B* **76**, 155312 (2007).
[2] C. Tusche, H.L. Meyerheim, and J. Kirschner, *Phys. Rev. Lett.* **99**, 026102 (2007).

Squeezing single nanostructures

The spatial confinement of low-dimensional materials can influence their physical properties. The plastic regime has been investigated by nanoindentation, compression and tensile tests, whereas the *elastic* properties of individual nanoscale objects such as single nanowires were studied and contradictory results reported on the size dependence of Young's modulus. In order to study the elastic properties of individual nanostructures we combined micro X-ray diffraction (μXRD) and an *in situ* atomic force microscope (AFM, Small Infinity) which allows both topographical imaging of the sample surface and selection of a specific nanoobject. The electrochemically blunted AFM tungsten tip can be used to deform an object by applying a well-defined force. The experimental setup is presented in **Figure 34a**. During the application of pressure, μXRD images are simultaneously recorded giving direct access to the lattice deformation in the object. For alignment of the sample, the AFM tip, and the microfocussed X-ray beam, we employ scanning X-ray diffraction mapping (SXDM) and photocurrent imaging (PI). The focussed X-ray beam is scanned across the sample and the X-ray signal of the nanoobjects is recorded resulting in a positional 2D map of the structures. When the X-ray beam hits the AFM tip, photoelectrons are emitted inducing a photocurrent which is simultaneously recorded with the SXDM, facilitating the alignment.

In the present study, we investigated the elastic properties of individual SiGe islands, at beamline **ID01**. **Figures 34b and 34c** present an AFM image of a SiGe island and a superposition of a scanning X-ray diffraction map and a PI image, respectively. **Figure 34c** demonstrates the excellent alignment employing these two imaging techniques simultaneously.

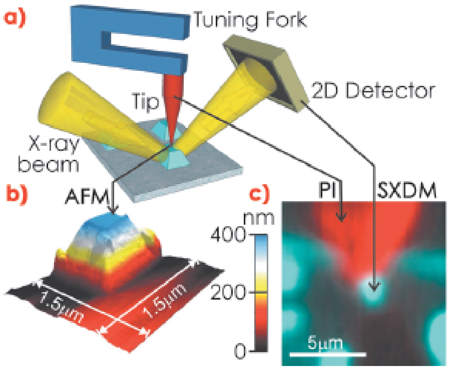

Fig. 34: a) Schematic of the experimental setup. b) Atomic force micrograph of a SiGe island. c) Superposition of simultaneous SXDM (blue) and PI (red) images.

Figure 35a shows the calculated three-dimensional reciprocal space map (3D-RSM) of a SiGe island grown on a Si(001) substrate. In the experiment, a two-dimensional detector is used, cutting through reciprocal space and thus recording only a 2D-RSM. The corresponding detector plane is represented by the semitransparent plane in **Figure 35a**. The related XRD pattern is displayed in **Figure 35b**

Principal publication and authors
T. Scheler (a), M. Rodrigues (a), T.W. Cornelius (a), C. Mocuta (a), A. Malachias (a), R. Magalhães-Paniago (a), F. Comin (a), J. Chevrier (a,b) and T.H. Metzger (a), *Appl. Phys. Lett.* **94**, 023109 (2009);
M.S. Rodrigues (a), T.W. Cornelius (a), T. Scheler (a), C. Mocuta (a), A. Malachias (a), R. Magalhães-Paniago (a), F. Comin (a), T.H. Metzger (a) and J. Chevrier (a,b), *J. Appl. Phys.* **106**, 103525 (2009).
(a) ESRF
(b) Institut Néel, CNRS-UJF, Grenoble (France)

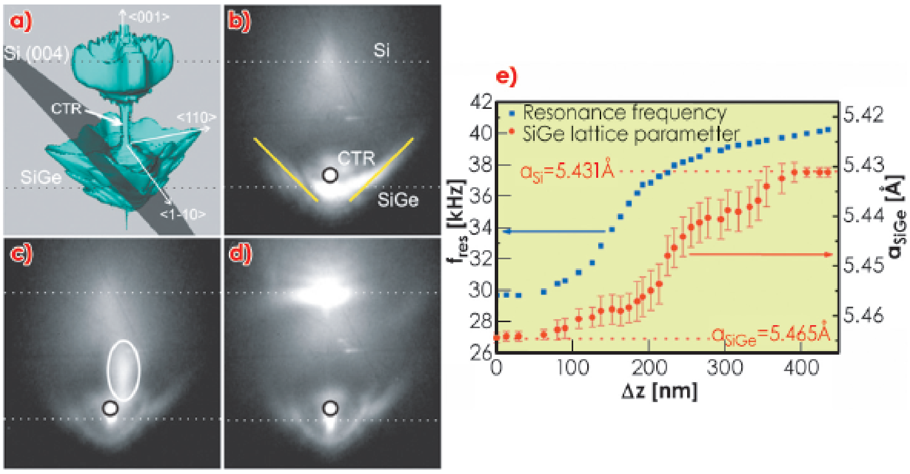

Fig. 35: a) Calculated 3D-RSM of an SiGe island in the vicinity of the Si(004) Bragg peak. The semitransparent plane depicts the interception of the reciprocal space by the detector plane for the images (b-d). b) 2D µXRD pattern of a non-compressed island. The flares (yellow lines) originate from the truncation rods of the island's {111} side facets. c) and d) the same X-ray maps for different pressures. e) Variation of both the SiGe island lattice parameter and the tuning fork resonance frequency as a function of the piezo travel Δz.

showing the substrate Bragg peak (Si(004)), the crystal truncation rod of the substrate, and the signal of the SiGe island including the truncation rods originating from the island's {111} side facets. **Figures 35c** and **35d** display the XRD patterns for the SiGe island under different pressures. For the highest pressure, the SiGe island intensity maximum is superimposed onto the Si substrate peak. Thus, the change in lattice parameter of the island can be followed *in situ* as a function of the applied pressure.

To quantify these results, the lattice parameter *a* of the SiGe island under investigation as a function of the piezo travel is presented in **Figure 35e**. In addition, the resonance frequency *f* (which is related to the applied force) of the AFM force sensor – a quartz tuning fork – is displayed shifting to larger values with increasing force applied. The two parameters, *a* and *f*, follow each other revealing a direct correlation between them. The shift of the resonance frequency originates from the stiffness of the contact area between the AFM tip and the island. This contact stiffness *S* can be derived by employing the Hertzian contact model. The effective Young's modulus of the system consisting of the SiGe island and the tungsten tip, was determined from the data *S* and *a* as 108 GPa. This is in excellent agreement with the bulk value of 105 GPa. Moreover, the pressure needed to compress the island lattice to the value of pure Si is in very good accordance with finite-element method calculations using bulk properties. Thus, no size effects of the elastic properties were found as expected for islands of this size (1 µm base length). The excellent agreement of experiment and theory demonstrates the very good performance of the *in situ* combination of AFM and µXRD and opens the door to *in situ* elasticity studies of nanostructures.

The *in situ* AFM tuning fork allows the determination of frequency shifts ranging from 0.1 to 10^4 Hz and hence cover five orders of magnitude. Owing to the direct correlation between elastic modulus and frequency shift, a broad class of materials can be investigated ranging from soft to hard matter.

Combining spectroscopy and simulations to probe the structural properties of Ge/Si(001) nano-islands

Both long- and short- range scales are of interest when studying structural properties of matter such as hetero nanostructures. This is particularly true for the study of a materials growth mechanism as well as for its electronic and optical properties, strain, chemical composition, interface quality, and atomic ordering [1]. To address such a general issue, we have combined

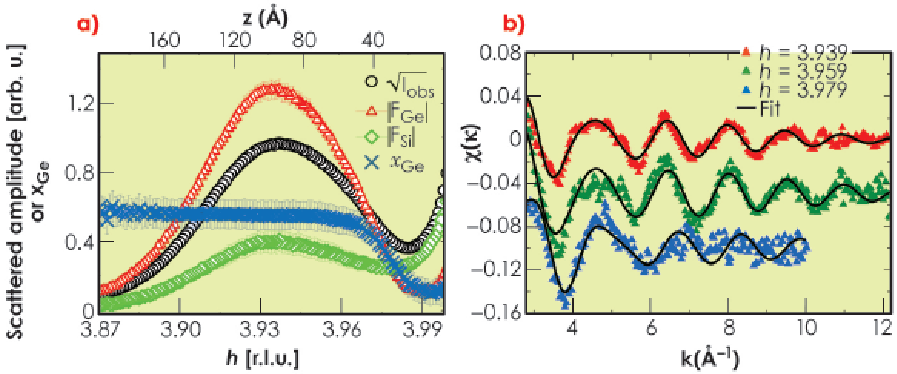

Fig. 36: a) MAD results. Square root of the diffracted intensity measured at 11.053 keV (50 eV below Ge K edge) and at an incidence angle α_i = 0.1°, $|F_{Ge}|$, $|F_{Si}|$ and the Ge composition x_{Ge}. They are plotted as a function of reciprocal index *h,* close to the in-plane Si 400 reflection and as a function of height *z* in the island. b) From top to bottom: raw EDAFS spectra (triangles) and best-fit curves (solid lines) recorded at three different *h* values, 3.939, 3.959 and 3.979, corresponding to heights of *z* = 3 nm, 6 nm and 9 nm, respectively. Curves are shifted for clarity.

grazing-incidence multiwavelength anomalous diffraction spectroscopy (MAD) and grazing-incidence diffraction anomalous fine structure (DAFS) spectroscopy at beamline **BM02**. This unique combination, together with recent atomistic simulations based on molecular dynamics (MD), is a powerful approach to disentangle strain and composition and to detect atomic ordering inside SiGe nano-islands.

We present here some recent results on dome-shaped Ge nano-islands grown on nominally flat Si(001) at 650°C by molecular beam epitaxy (MBE). Their average size and height were about 80 nm and 19 nm, respectively. MAD was performed at the Ge K-edge (11103 eV), close to the in-plane Si 400 Bragg reflection at an incident angle $\alpha_i = 0.1°$ (the Si critical angle $\alpha_c = 0.163°$ at 11 keV). **Figure 36a** shows the square root of the scattered intensity at 11053 eV (I_{obs}), the modulus of the Ge and Si structure factors, as well as the Ge content (x_{Ge}), as a function of the reciprocal lattice index *h* and height (z) above the Si surface (*h* can be associated with different heights *z* in the nano-islands, according to the iso-strain method). MAD results clearly show a strong Si/Ge intermixing, the Ge content is about 0.6, together with a slight linear increase of x_{Ge} starting above *z* = 4 nm. **Figure 36b** shows background-subtracted extended DAFS spectra together with the best-fit curves. The three experimental EDAFS spectra were recorded in grazing-incidence geometry, close to the in-plane Si 440 Bragg reflection, at *h* = 3.939, 3.959, and 3.979, corresponding to *z* = 3 nm, 6 nm and 9 nm, respectively. The fits show that the Ge content increases slightly from the base to top of the dome (x_{Ge} = 0.54 and 0.6 at *h* = 3.959 and 3.939, respectively). The EDAFS results are in very good agreement with MAD results, except near the Si Bragg peak corresponding to the substrate-island interface region (*h* = 3.979). Interestingly, in this region, the Ge content obtained from MAD (x_{Ge} ~ 0.2)

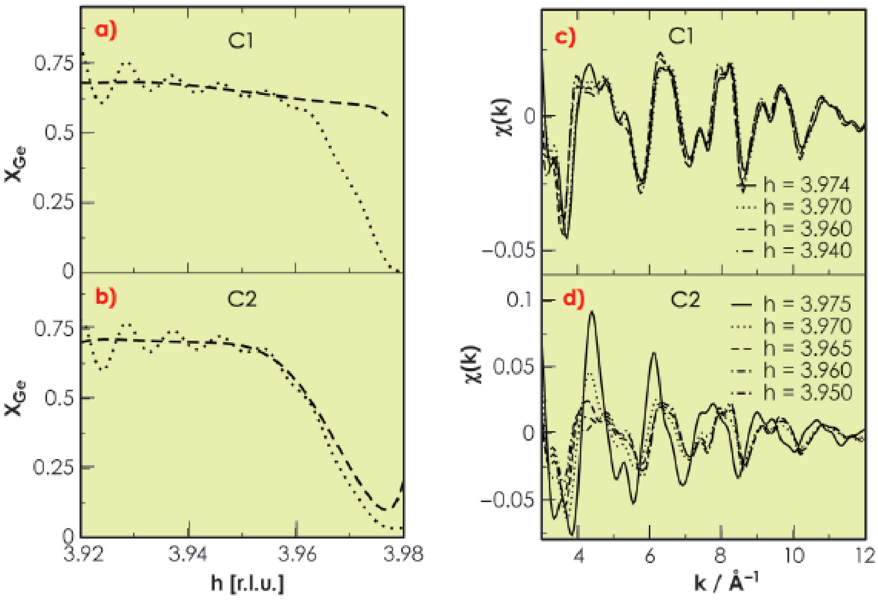

Fig. 37: Molecular dynamics simulations. MAD and extended DAFS of SiGe/Si(100) islands (aspect ratio equal to 0.16, about 20x10^6 atoms). Ge concentration (---) corresponding to a sharp (a, model C_1) and smooth (b, model C_2) composition gradient and Ge concentration (···) extracted back from the simulated MAD. An artificial composition gradient is found in the case of model C_1 (c)-(d) Extended DAFS χ(k) for models C_1 and C_2. The EDAFS oscillations are barely sensitive to the interface in the case of model C_1.

Principal publication and authors

N.A. Katcho (a),
M.-I. Richard (b,c), O. Landré (b),
G. Tourbot (b), M.G. Proietti (d),
H. Renevier (e),
V. Favre-Nicolin (b),
B. Daudin (b), G. Chen (f),
J.J. Zhang (f), and G. Bauer (f),
Journal of Physics: Conference Series, (2009);
M.-I. Richard (b,c),
N.A. Katcho (a), M.G. Proietti (d),
H. Renevier (e),
V. Favre-Nicolin (b), Z. Zhong (f),
G. Chen (f), M. Stoffel (g,h),
O. Schmidt (g,h), G. Renaud (b),
T.U. Schülli (b), and G. Bauer (f),
Eur. Phys. J. Special Topics **167**, 3 (2009).

(a) Univ. Complutense Madrid (Spain)
(b) CEA Grenoble, INAC (France)
(c) Univ. Paul Cézanne, IM2NP, Marseille (France)
(d) Univ. Zaragoza, ICMA (Spain)
(e) Grenoble INP Minatec, LMGP (France)
(f) Johannes Kepler Univ. Linz (Austria)
(g) IFW Dresden (Germany)
(h) MPI Stuttgart (Germany)

is lower than that obtained from EDAFS ($x_{Ge} = 0.55$). MD simulations clearly show (**Figure 37**) that in the case of an island-substrate interface with a sharp change in GeSi composition, information is lost, and an artificially smooth gradient is found by MAD owing to the scattering contribution of the strained Si substrate region beneath the islands (**Figure 37a**). In contrast EDAFS oscillations are much less sensitive to the presence of the interface (**Figure 37c**), since EDAFS spectroscopy probes only the Ge local environment. Therefore, there was no evidence for the presence of a Si-rich core below 4-5 nm in the nano-islands that we have studied, as suggested by others.

In summary, this study demonstrates the great power of combining MAD and EDAFS and shows that atomistic simulations at a realistic scale (20x10^6 atoms in the present case) are of fundamental importance for providing a deeper and more reliable data interpretation.

Reference

[1] J. Stangl, V. Holý and G. Bauer, *Rev. Mod. Phys.* **76**, 725 (2004).

Structure and reactivity of Rh oxides

Principal publications and authors
J. Gustafson (a,b), R. Westerström (a), A. Resta (a,c), A. Mikkelsen (a), J.N. Andersen (a), O. Balmes (c), X. Torrelles (d), M. Schmid (e), P. Varga (e), B. Hammer (f), G. Kresse (g), C.J. Baddeley (b) and E. Lundgren (a), *Cat. Today* **145**, 227-235 (2009);
J. Gustafson (a,b), R. Westerström (a), A. Mikkelsen (a), X. Torrelles (d), O. Balmes (c), N. Bovet (h), J.N. Andersen (a), C.J. Baddeley (b), and E. Lundgren (a), *Phys. Rev. B* **78**, 045423 (2008).
(a) Department of Synchrotron Radiation Research, Lund University (Sweden)
(b) EaStCHEM School of Chemistry, University of St. Andrews (UK)
(c) ESRF
(d) Instituto de Ciencia de Materiales de Barcelona (Spain)
(e) Institut für Algemeine Physik, Technische Universität Wien (Austria)
(f) Interdisiplinary Nanoscience Center (iNANO) and Department of Physics and Astronomy, University of Aarhus (Denmark)
(g) Institut für Materialphysik, Universität Wien (Austria)
(h) MAX-lab, Lund University (Sweden)

More than 80% of all chemical products are produced using catalysts, which facilitate a specific reaction without being consumed. In most cases the catalyst is in a different phase to the reactants, *e.g.* a solid catalyst and gaseous reactants, a situation referred to as heterogeneous catalysis. Industrial catalysts are complicated materials systems consisting of oxide supports with dispersed metal nanoparticles of the active catalyst as well as a wide range of additives to promote or poison specific reactions. Owing to their complexity, information on the functioning of the catalyst at the atomic scale is at best limited, and consequently most catalyst development is done via an empirical approach.

Much effort has recently been directed towards replicating the conditions under which most industrial catalysts work. In such *in situ* studies, the structure is analysed during the reaction under realistic pressures. We have used the batch reactor surface X-ray diffraction (SXRD) setup at beamline **ID03** to follow the oxidation of Rh – one of the active elements in a car's exhaust-gas catalytic converter – and investigated how the catalytic activity varies with the oxidation state. Prior to the formation of a thick bulk oxide, an ultrathin surface oxide is formed, exhibiting a trilayer structure with two hexagonal oxygen layers separated by a single Rh layer. This surface oxide does not grow under UHV compatible conditions, but is found on all surface orientations at intermediate oxygen pressures.

Figure 38 shows the results from the oxidation of CO over Rh(111). At t = –1000 s, 300 mbar of O_2 and close to no CO and CO_2 are present in the batch reactor. At this time, SXRD shows

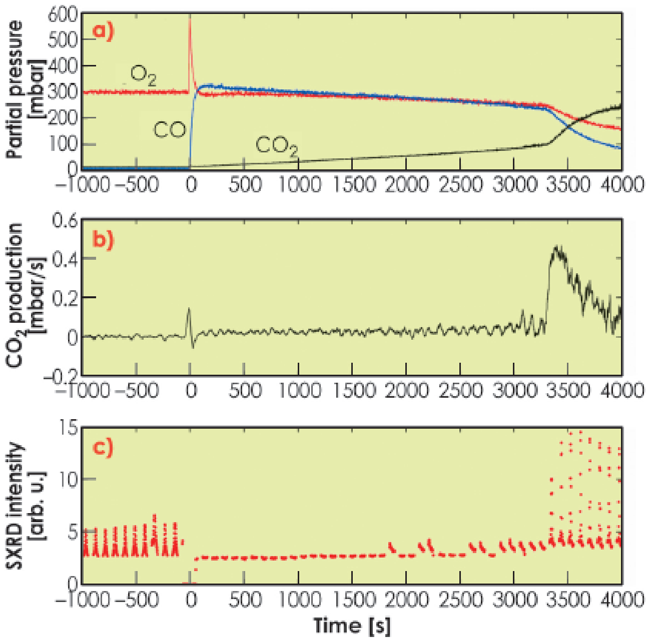

Fig. 38: Activity and surface structure of Rh(111) during CO oxidation. a) the partial pressure of O_2, CO and CO_2, b) the differentiated CO_2 signal, *i.e.* the CO_2 production rate, c) consecutive SXRD scans revealing the presence (or absence) of the surface oxide.

the presence of the surface oxide. At time t = 0, 330 mbar CO is added, and the CO_2 production starts. Here, no surface oxide can be detected. As one O_2 molecule can oxidise two CO molecules, the O_2/CO partial pressure ratio increases as the reaction proceeds, creating a more oxidising environment. At t ≈ 3300 s, we notice a significant increase in the reaction rate, which coincides with the return of the surface oxide. We have found very similar results, where the Rh surface oxide shows a very high CO oxidation reactivity, for Rh(100) as well as $Pt_{25}Rh_{75}(100)$ samples. The bulk oxide, however, is found to be inactive.

The difference in reactivity between the oxidised and metallic surfaces is striking, and indicates that the surface oxide plays a crucial role in the high activity of Rh-based CO oxidation catalysts. Under UHV conditions, however, CO has a very low adsorption energy on the surface oxide, which would imply that the surface oxide rather poisons the catalyst. In order to find an explanation for the behaviour at elevated pressures, Figure 39 shows a number of different phases, in which the catalyst surface can be found. In Figure 39a the surface is in a metallic phase covered by adsorbed CO molecules. Since the O_2 adsorption is dissociative it needs a larger free surface area than can be found between the CO molecules, which makes this phase inactive. Similarly, the oxide surfaces shown in Figure 39b are fully covered by O atoms, which does not allow for CO adsorption, this also resulting in inactive surfaces. To make the surface oxide active, either defects or co-existing metallic areas, where the CO can adsorb, are needed (Figure 39c). Alternatively a surface with adsorbed O atoms, as shown in Figure 39d, will still allow CO adsorption (which is not dissociative) and be active. According to density functional theory calculations, however, the reaction barriers involved in forming CO_2 using chemisorbed O is significantly higher than those for using O from the edge of the surface oxide [1]. Hence the reactivity is expected to be lower in case (d) when compared to (c).

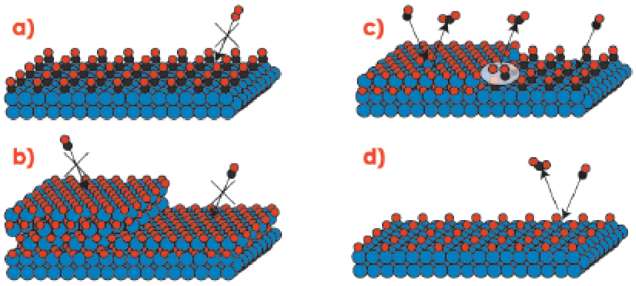

Fig. 39: Different phases in which the Rh catalyst can be found in an atmosphere of O_2 and CO.

In summary, our study indicates that structures that only form under realistic operating conditions may be of major importance for a fundamental understanding of catalysis.

Reference

[1] R. Westerström, J.G. Wang, M.D. Ackermann, J. Gustafson, A. Resta, A. Mikkelsen, J.N. Andersen, E. Lundgren, O. Balmes, X. Torrelles, J.W.M. Frenken and B. Hammer, *J. Phys. Condens. Matter* **20**, 184018 (2008).

Revealing the hydrate formation process at the water-CO_2 interface

Principal publication and authors

F. Lehmkühler (a), M. Paulus (a), C. Sternemann (a), D. Lietz (a), F. Venturini (b), C. Gutt (c) and M. Tolan (a), *J. Am. Chem. Soc.* **131**, 585–589 (2009).

(a) Fakultät Physik/DELTA, Technische Universität Dortmund (Germany)
(b) ESRF
(c) HAYSLAB at DESY, Hamburg (Germany)

Water can form solid clathrate phases in the presence of small molecules. These so colled hydrates are crystalline inclusion compounds where guest molecules, mainly gases, are trapped in an ice-like network of nanometre-sized cages. Methane hydrate is of special importance as it occurs in huge amounts in the sediments of deep sea regions. In recent years hydrates have attracted general interest because of a rising number of possible applications, *e.g.* mining of methane from the ocean floor or the storage of CO_2 or H_2. Thus, for such applications, knowledge of the fundamental processes involved is essential in order to control -inhibit or initiate- hydrate formation. In general, two kinds of model exist describing the formation of hydrates at the molecular level. While cluster models such as the cluster nucleation theory [1] predict hydrate precursors forming around dissolved guest molecules, in stochastic models, like the local structuring hypothesis [2], the hydrate formation happens without such precursors. The difference between the two models is illustrated schematically in Figure 40.

Initial hydrate formation occurs mainly at the water surface owing to the large

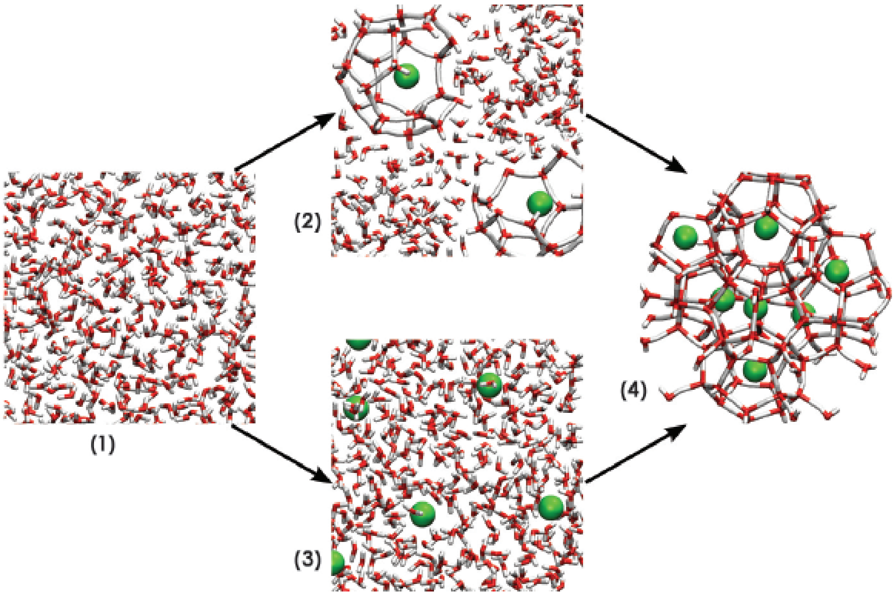

Fig. 40: Hydrate formation models. (1) Water without dissolved guest molecules. (2) Upon dissolution water clusters form around guest molecules. These clusters may agglomerate to larger units. (3) Stochastic arrangement of water and guests. (4) Hydrate growth. The path (1-2-4) demonstrates formation with hydrate precursors; the path (1-3-4) is a stochastic model without precursors.

number of gas molecules present. Therefore, we studied the liquid-gas water-CO_2 interface by means of X-ray reflectivity measurements. This method is highly sensitive to the structural properties of the sample's surface. In particular, its surface roughness and the formation of layers can be analysed with sub-angstrom resolution. Most importantly, the formation of hydrate precursors or a thin hydrate layer would result in changes to the surface roughness or the formation of a surface layer. As CO_2 hydrate is stable at pressures above 12.5 bar at 0.1°C, a special stainless steel pressure cell with aluminium windows was used for this experiment making the use of high energy X-rays essential. X-ray reflectivity measurements of the water-CO_2 interface were performed using the setup for scattering from liquid surfaces at beamline **ID15A** at T = 0.1°C and pressures between 1 bar and close to the condensation pressure of CO_2 at 35 bar.

In **Figure 41a** selected reflectivity curves at various CO_2 pressures normalised to the Fresnel reflectivity of a bare water surface are shown. The Kiessig fringes at higher pressures indicate the formation of a layer on the water surface whose thickness increases with increasing gas pressure. For all pressures, the water's roughness remained constant at the expected value for capillary-wave roughness of 3.2 ± 0.1 Å. From the reflectivity data, electron density profiles were obtained, as shown in **Figure 41b**. The layer's electron density also remains constant at the value of liquid CO_2. In contrast, CO_2 hydrate would have an electron density which is approximately 30% above the measured value. Hence, owing to the constant water roughness and the agreement of the layer's electron density with liquid CO_2, the adsorption of CO_2 on the water surface without formation of hydrate or hydrate

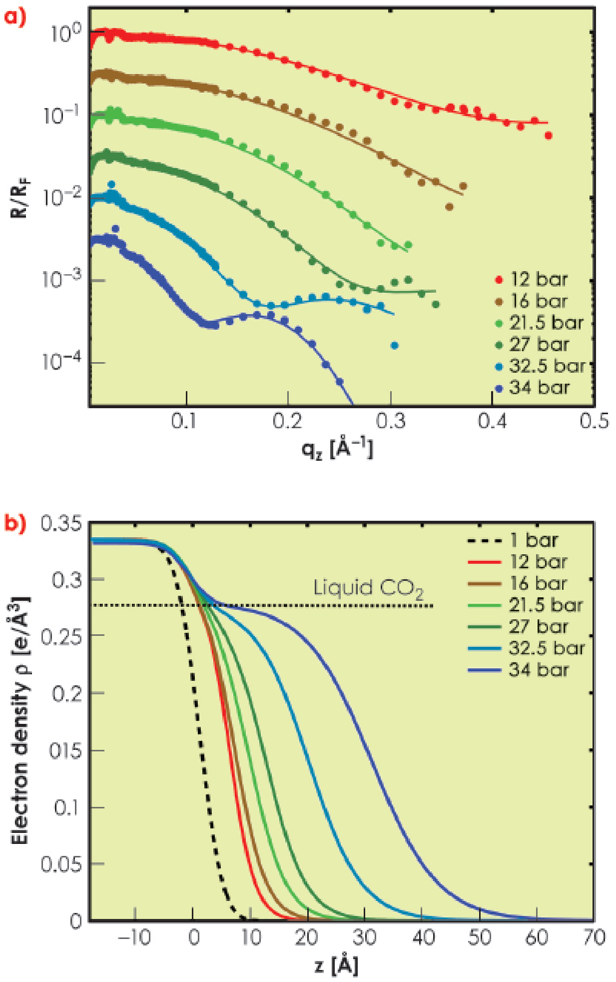

Fig. 41: a) X-ray reflectivity curves normalised to Fresnel reflectivity for different gas pressures. The solid lines are fits to the data, curves are shifted for clarity. b) Electron density profiles of the water-CO_2 interface at different pressures. The density of liquid CO_2 is marked by the dashed line.

precursors was observed. This is supported by a further analysis of the layer's structural properties which agree well with adsorption and capillary wave theory for thin liquid films [3].

In contrast to the liquid-gas interface, X-ray diffraction measurements at the liquid-liquid interface between bulk water and bulk CO_2 performed at beamline ID15A exhibit the formation of small hydrate crystallites [4]. Bragg reflections originating from these crystallites appear and disappear continuously suggesting a fully stochastic formation of mobile hydrate crystallites. Thus, the two interfaces show very different behaviour with respect to gas hydrate formation. The adsorption of CO_2 on the water surface leads to an abundant supply of guest molecules, but does not trigger the hydrate formation process. This happens only in the presence of a macroscopic liquid layer. These findings, *i.e.* the stochastic nature of crystallite formation and the absence of surface covering hydrate precursors, imply that a stochastic hydrate formation model such as the local structuring hypothesis is favoured by our study.

References
[1] E.D. Sloan and C.A. Koh, *Clathrate Hydrates of Natural Gases*, CRC Press Inc. (2007).
[2] R. Radhakrishnan and B.L. Trout, *J. Chem. Phys.* **117**, 1786 (2002).
[3] M. Paulus, C. Gutt, and M. Tolan, *Phys. Rev. E* **72**, 061601 (2005).
[4] Additional data taken at DELTA in Dortmund.

Hydration of a Nafion membrane in a working fuel cell

Principal publication and authors

V. Rossi Albertini (a), B. Paci (a), F. Nobili (b), R. Marassi (b) and M. Di Michiel (c), *Advanced Materials* **21**, 578 (2009).
(a) Istituto di Struttura della Materia, C.N.R, Roma (Italy)
(b) Dipartimento di Scienze Chimiche, Università di Camerino, Camerino (MC) (Italy)
(c) ESRF

Proton exchange membrane fuel cells convert chemical into electrical energy. They are promising candidates for the development of an environmentally-friendly hydrogen-based technology. The fuel cell's performance strongly depends on the degree of hydration of the proton exchange membrane, since proton transfer in such polymeric materials is known to be assisted by water.

Here, a time-resolved vertical stratigraphy of the proton exchange membrane (PEM) was performed, slicing the membrane into a stack of virtual layers from one electrode to the other. The time dependence of the hydration degree in each layer was determined with the highest accuracy ever achieved for the characterisation of such a fuel cell under typical working conditions (polarisation curve) [1]. The same technique could easily be applied to cells operating under different conditions, thus providing a powerful tool to investigate the fundamental relationships between hydration degree and electrochemical performance.

The penetrating power of the high energy radiation at beamline ID15 allowed *in situ* XRD measurements on a test fuel cell with a design equivalent to that of a standard cell, avoiding artefacts due to the modifications usually required to measure working devices.

A membrane electrode assembly with Pt nanoparticles (20% Pt/Vulcan XC-72 powder from E-TEK, Pt loading about $1\ mg/cm^2$) as anode and cathode catalysts, and Nafion® as proton conducting membrane, was used as the active element.

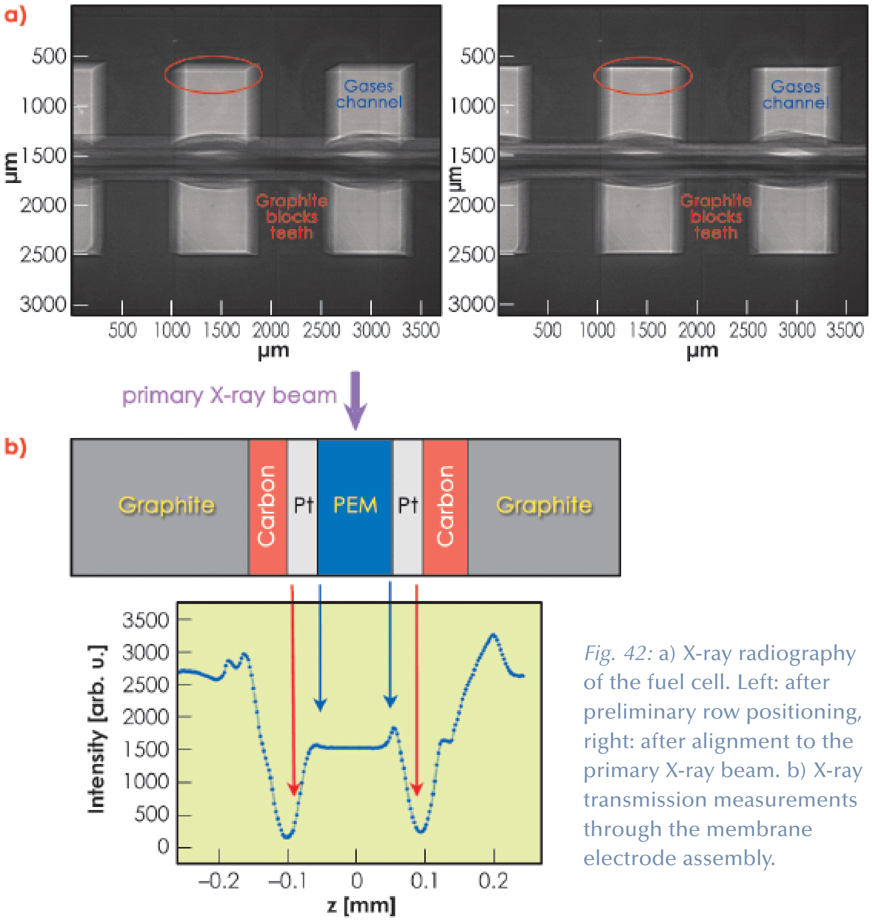

Fig. 42: a) X-ray radiography of the fuel cell. Left: after preliminary row positioning, right: after alignment to the primary X-ray beam. b) X-ray transmission measurements through the membrane electrode assembly.

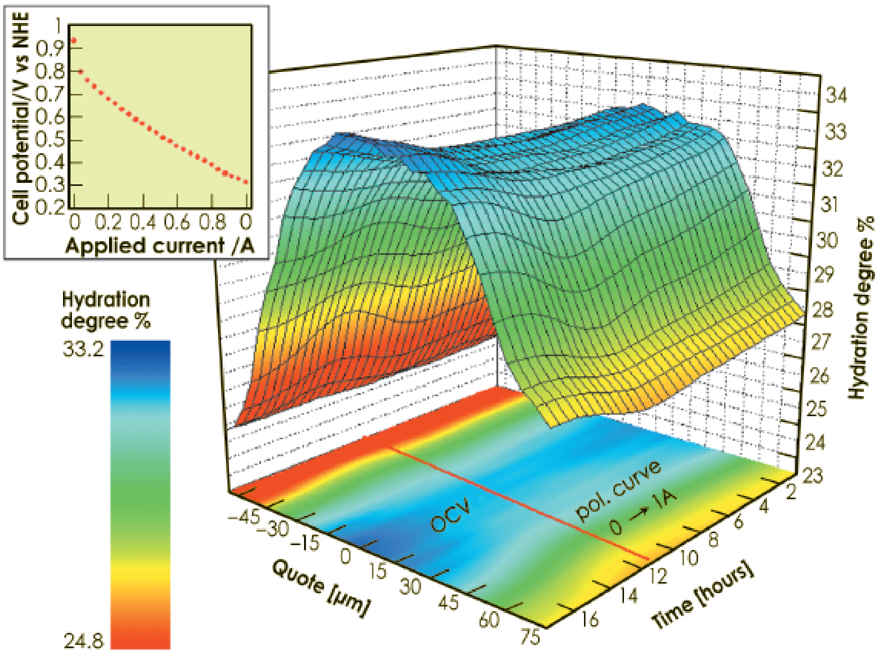

Fig. 43: Space/time-resolved study of the water distribution in the proton exchange membrane. 3D plot of the time-dependent water content in each "slice" of the membrane, carried out under real working conditions (polarisation curve in the inset, followed by an open circuit period). The iso-level projection of the surface on the basal plane is also reported.

A fuel cell is far from an ideal system on which to perform diffraction measurements since both the membrane's amorphous polymers and the water contained within it provide rather weak scattering signals. However, the use of high energy radiation coupled with the adoption of an image plate detector resulted in a fine time sampling of the water dynamics in each layer of the PEM.

Positioning and alignment of the cell was done by taking a sequence of radiographs during a rocking-angle scan (Figure 42a). This also permitted identification of the cell components. Once the cell had been aligned, a subsequent transmission measurement with a narrow X-ray beam through the proton exchange membrane and its adjacent cell components allowed details of the membrane electrode assembly to be finely resolved. (Figure 42b).

Time/space-resolved sequences of diffraction patterns were collected during a polarisation curve (40 mA, steps of 30 minutes duration) from 0 to 1 A (insert of Figure 43). The primary X-ray beam cross section was 100 x 5 μm^2 (horizontal x vertical), the latter corresponding to the spatial resolution which allowed the hydration degree of 31 slices of the membrane to be investigated independently. The information on the quantity of water contained in a portion of membrane was obtained by applying the spectral decomposition method [2]. Several scans were also executed under open circuit conditions after the end of the polarisation, to follow the hydration behaviour during cell relaxation. The rate of change of the cell current was slow enough to consider the membrane to be in quasi-equilibrium conditions during the whole experiment (quasi static process). The result of the time/space-resolved investigation is reported in the 3D plot in Figure 43, which represent a compact summary of the entire information obtainable on the hydration dynamics in the PEM.

The present study paves the way to systematic observations of the water management in any kind of polymeric material (both pure and nanoparticle filled), used as a solid electrolyte in proton exchange membrane fuel cells. The method used has both sufficient spatial and temporal resolution to follow the water distribution within a working fuel cell membrane.

Acknowledgements
This research was partially supported by the NUME project (Italian Ministry of University and Research, FISR 2003).

References
[1] J. St-Pierre, *J. Electrochem. Soc* **157**, 7 B724 (2007).
[2] V. Rossi Albertini, B. Paci, A. Generosi, S. Panero, M. A. Navarra and M. Di Michiel, *Electrochem. Solid-State Lett* **7**, A519J (2004).

Direct synthesis of cubic $ZrMo_2O_8$ followed by ultrafast *in situ* powder diffraction

Principal publication and authors
J.E. Readman (a), S.E. Lister (a), L. Peters (b), J. Wright (c) and J.S.O. Evans (a), *J. Am. Chem. Soc.* **131**, 17560 (2009).
(a) University of Durham (UK)
(b) Christian-Albrechts-Universität zu Kiel (Germany)
(c) ESRF

The cubic AM_2O_8 family of materials (A = Zr, Hf; M = W, Mo) has attracted considerable interest due to the negative thermal expansion properties of its members. Cubic ZrW_2O_8 is the most famous of these materials and contracts isotropically when heated with a thermal expansion coefficient of -9×10^{-6} K^{-1} between 2 and 300 K. It has two potential drawbacks for any practical applications: a discontinuity in cell parameters around 177°C associated with an order-disorder transition, and a transition to a denser structure at pressures above ~0.2 GPa. In contrast, cubic $ZrMo_2O_8$ shows no such discontinuities in cell parameter and pressure-induced transitions are reversible at room temperature. The major issue is the difficulty of its synthesis. Cubic $ZrMo_2O_8$ was thought to be metastable at all temperatures (less interesting monoclinic and trigonal forms are thermodynamically stable) and has only been prepared by complicated low temperature routes via controlled decomposition of precursors. Recently we obtained tantalising evidence in the laboratory that it might be possible to prepare this metastable phase at high temperatures (~1177°C) in a restricted temperature-time window.

We therefore turned to rapid *in situ* experiments at **ID11** to unravel the solid-state chemistry involved in this synthesis. In a typical experiment we pre-mixed metal oxide reactants in a thin-walled Pt capillary then transferred them into a pre-heated mirror furnace (**Figure 44**) and collected a series of powder diffraction patterns. Using a wavelength of 0.2 Å, we could penetrate the Pt capillary and record data of sufficient quality for Rietveld refinement with a time resolution of 0.1 s. This setup allowed synchronous monitoring of the metal oxides as they reacted at high temperatures.

Figure 45 shows data from one of our first experiments on the ZrO_2 + $2MoO_3$ reaction, which gave huge insight into the possible direct synthesis of cubic $ZrMo_2O_8$. Here the sample was introduced into the furnace preheated to 1250°C and the reagents reacted extremely rapidly. **Figure 45a** shows a two dimensional representation of the diffraction data and **Figure 45b** shows results from quantitative refinements with data plotted as "ZMV", a measure of the relative amount of the phases present in the mixture. At low temperatures, the diffraction peaks correspond to ZrO_2, MoO_3 and the Pt

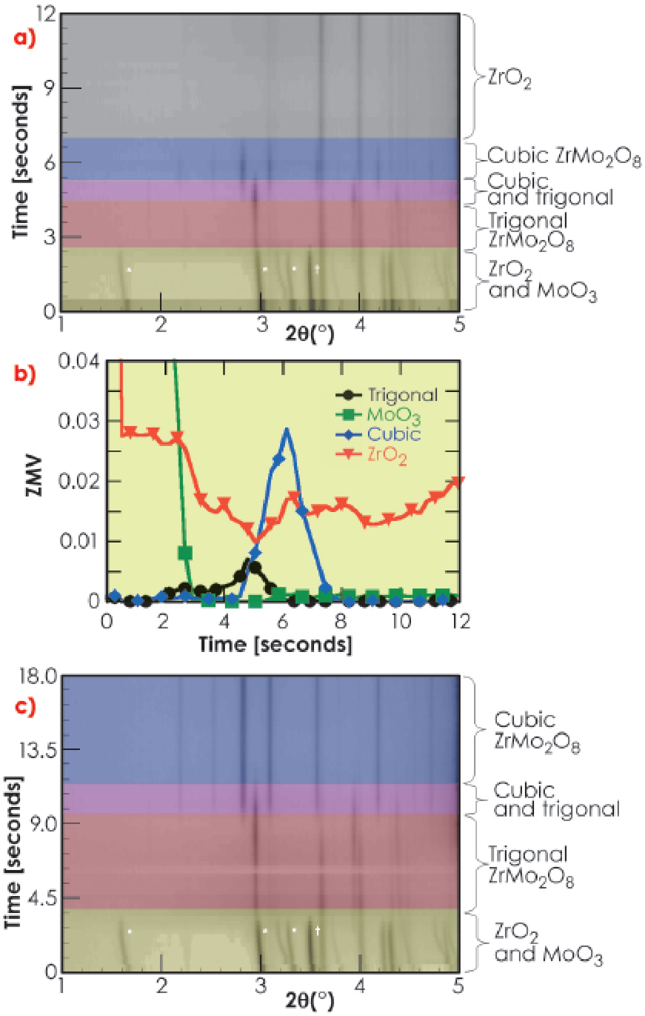

Fig. 45: Data obtained for two reactions: a) (ZrO_2):$2(MoO_3)$ at 1247°C and b) resulting phase fractions; c) (ZrO_2):$3(MoO_3)$ at 1127°C. ZrO_2 and MoO_3 peaks are indicated by † and * respectively.

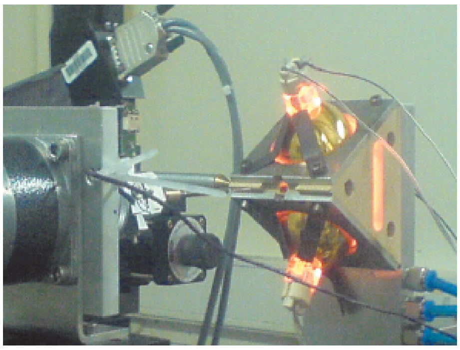

Fig. 44: Mirror furnace.

of capillary walls as expected. Initially all peaks shift to lower 2θ indicating positive thermal expansion on heating. Between approximately 1.6 and 2.5 s (*T* ~757°C and 987°C) peaks due to MoO_3 disappear and those of trigonal α-$ZrMo_2O_8$ are observed for the first time. A drop in the overall diffracted intensity occurs at this point, which is consistent with the melting of MoO_3 (T_{melt} = 795°C). Between 2.5 and 5 s (*T* ~1161°C) the amount of trigonal α-$ZrMo_2O_8$ increases before gradually disappearing. New peaks corresponding to cubic γ-$ZrMo_2O_8$ appear from 4.5 s (*T* ~1127°C). These peaks disappear after a total elapsed time of 8 s (*T* ~1252°C) and ZrO_2 is the only crystalline material remaining. On quenching after 120 s (*T* falls from ~1247°C to ~427°C within 8 seconds), significant quantities of cubic $ZrMo_2O_8$ were again observed in the diffraction data, suggesting a molten phase at the highest temperatures.

This experiment gave us many of the clues needed to synthesise the cubic phase. By lowering the temperature to ~1197°C we were able to stabilise cubic $ZrMo_2O_8$ over a period of 60 s, though with ZrO_2 present as a second phase. By using a small excess of MoO_3 we were able to prepare the cubic phase as the only crystalline product (**Figure 45c**) in a period of just 9 s.

In summary, the high flux, high energy beam available at **ID11** coupled with the fast data acquisition achievable with the FReLoN camera have given unique insight into the synthesis of cubic $ZrMo_2O_8$. We have shown that an apparently metastable material can be prepared directly from its component oxides and in a matter of seconds at high temperature. The extremely fast reaction rate seems to be due to the formation of molten MoO_3 a couple of seconds into the experiment which acts as a reactive flux. Online (and almost real time!) data analysis was essential to allow us to optimise the reaction conditions during the experiment and enabled us to produce the pure target material. These methods could be readily applied to a host of other fascinating systems.

Principal publication and authors

K. Georgarakis (a,b),
A.R. Yavari (b,a,c),
D.V. Louzguine-Luzgin (a),
J. Antonowicz (d), M. Stoica (e),
Y. Li (b), M. Satta (b),
A. LeMoulec (b), G. Vaughan (c)
and A. Inoue (a), *Applied Physics Letters* **94**, 191912 (2009).
(a) WPI-AIMR, Tohoku University, Sendai (Japan)
(b) Euronano-SIMaP-CNRS, INP Grenoble, St-Martin-d'Hères (France)
(c) ESRF
(d) Faculty of Physics, Warsaw University of Technology (Poland)
(e) IFW Dresden, Institute for Complex Materials (Germany)

Detection of deviation from ideal solution behaviour in Zr-Cu metallic glasses with addition of Al

Metallic glasses are metastable materials with unusual structures and remarkable properties. They are made by carefully cooling liquid alloys so that they solidify without crystallising. Thanks to an irregular, tightly packed internal arrangement of atoms, metallic glasses are mouldable like plastic when heated to the glass transition temperature, yet stronger than typical crystalline alloys at room temperature [1].

The use of synchrotron X-rays can be highly advantageous for analysing the structure of metallic glasses. Conventional X-ray beams are completely absorbed near the surface, whereas high energy, high flux radiation penetrates even thick samples, providing a deeper understanding of the unique internal structure of metallic glasses.

Using real space pair distribution functions (PDFs) derived from high precision X-ray diffraction data collected at beamline **ID11**, we attempt to probe the internal structure of metallic glasses based on Zr and Cu and investigate the effect of a third element (Al) on their atomic structure. The results provide a guide for producing thicker alloy glasses with enhanced properties.

The PDFs of the Zr-Cu binary metallic glasses (**Figure 46a**) reveal how the atomic structure changes with the Zr/Cu atomic ratio. Increasing Cu content generates significant differences in the PDFs, suggesting modifications in the short (SRO) and medium range order (MRO) up to 1.5 nm. As expected, the structural changes in the nearest neighbour (nn) shell (inset **Figure 46a**), indicate an

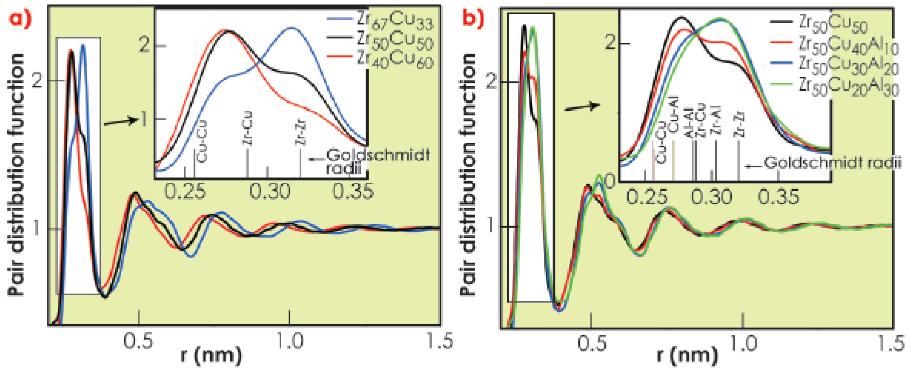

Fig. 46: Pair distribution functions for metallic glasses: a) Zr-Cu binary and b) Zr-Cu-Al ternary. Insets: close-up of the first PDF peak.

increased number of Zr-Zr atomic bonds for the Zr-rich compositions, and an increased number of Cu-Zr and Cu-Cu atomic bonds for the Cu-rich site.

Addition of Al to the Zr-Cu metallic glasses leads to significant modifications of SRO and MRO, Figure 46b. The nn shell (inset Figure 46b) indicates the formation of a significant number of Zr-Al atomic bonds. This behaviour can be attributed to strongly attractive Zr-Al atomic interactions consistent with the highly negative heat of mixing ΔH_{mix} of –44 kJ mol^{-1} which is twice that of Zr-Cu (–23 kJ mol^{-1}), whereas ΔH_{mix} for Cu-Al is negligible (–1 kJ mol^{-1}). Al has an intermediate atomic size between those of Zr and Cu atoms. Because of the strongly negative heat of mixing between Zr and Al atoms, addition of Al promotes chemical short range ordering in the liquid, improves the local packing efficiency and slows down long range atomic diffusion required for crystallisation, leading to increased glass forming ability.

For an ideal solution, the total PDF for Zr-Cu binary alloys would be correlated with the partial PDF of Zr-Zr, Zr-Cu, and Cu-Cu atomic pairs according to the following relation:

$$G(r)=W_{ZrZr}G_{ZrZr}+W_{CuCu}G_{CuCu}+2W_{ZrCu}G_{ZrCu} \quad \textbf{(1)}$$

Approaching the ternary ZrCuAl alloys as ideal solutions, the correlation between total and partial PDFs would be given as:

$$G(r)=W_{ZrZr}G_{ZrZr}+W_{CuCu}G_{CuCu}+W_{AlAl}G_{AlAl}+2W_{ZrCu}G_{ZrCu}+2W_{ZrAl}G_{ZrAl}+2W_{CuAl}G_{CuAl} \quad \textbf{(2)}$$

where $W_{ij}= C_iC_jF_iF_j/(\Sigma\, C_iF_i)^2$, W_{ij} are the ideal solution weight factors, C_i are the atomic concentrations and F_i are the atomic form factors.

The PDFs derived from experimental XRD results for Zr-Cu binary metallic glasses were found to be in good agreement with those expected from the weight factors of **eq. 1** (Figure 47a), indicating that the Zr-Cu metallic glass can be satisfactorily approximated as an ideal solid solution. Because of the weak interactions between Zr-Cu atoms in the binary alloy, only very thin glasses can be cast from Zr-Cu liquid alloys. However, adding a third strongly interacting component, Al, to the liquid alloy leads to a stronger glass that can be cast at thicknesses of up to several millimetres.

We have therefore determined that in contrast to the binary Zr-Cu, ternary Zr-Cu-Al metallic glasses deviate markedly from ideal solution behaviour (Figure 47b). Zr-Cu-Al glasses are

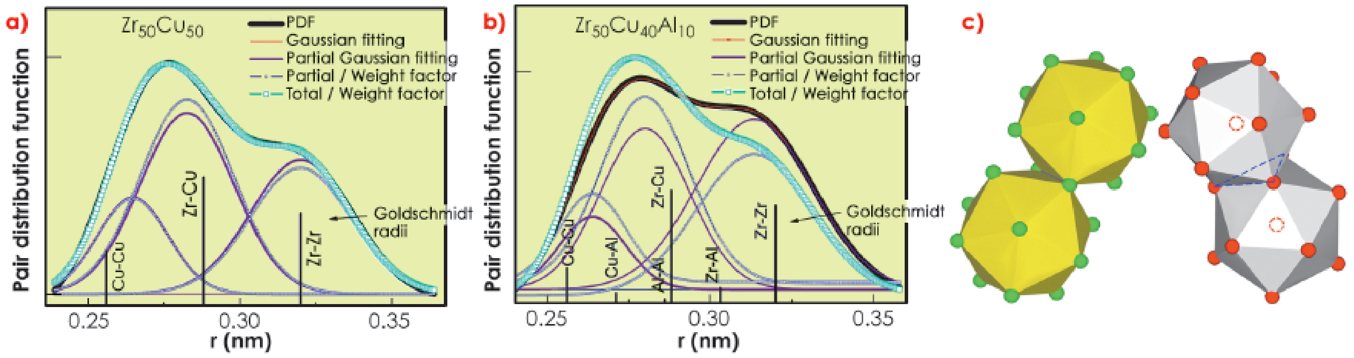

Fig. 47: Gaussian fitting of the first PDF peak for a) $Zr_{50}Cu_{50}$ and b) $Zr_{50}Cu_{40}Al_{10}$ metallic glasses. Experimental PDF (thick black curves); calculated partial PDFs derived from the experimental PDF (thin red curves); Gaussian partial PDFs scaled to the weight factors of an ideal solution (thin blue discontinuous curves); expected total PDFs based on the weight factors (thick discontinuous light blue curves). c) Schematic diagram showing how the atoms in Zr-Cu based metallic glasses form icosahedral clusters that pack tightly together by sharing edges (left) or faces (right) [2].

comprised of finite regions of atomic order, providing the extra support needed to form thicker glasses. This phenomenon is believed to be due to attractive interactions between the *sp* electrons of Al and the *d*-electron shell of the larger Zr atoms. The atoms arrange in clusters resembling icosahedra, which pack together tightly in the glass (**Figure 47c**), as observed in a previous study [2].

References
[1] A.R. Yavari, *Nature* **439**, 405 (2006).
[2] Ch.E. Lekka, A. Ibenskas, A.R. Yavari and G.A. Evangelakis, *Appl. Phys. Lett.* **91**, 214103 (2007).

Following atomic diffusion by coherent X-rays

Principal publication and authors
M. Leitner (a), B. Sepiol (a), L.-M. Stadler (b), B. Pfau (c) and G. Vogl (a), *Nature Mat.* **8**, 717-720 (2009).
(a) Fakultät für Physik, Universität Wien (Austria)
(b) HASYLAB at DESY, Hamburg (Germany)
(c) Helmholtz-Zentrum Berlin für Materialien und Energie GmbH, Berlin (Germany)

The movement of single atoms is at the core of each process in materials science. The diffusion of atoms underlies everything from the synthesis of materials to their deterioration. Knowledge about and understanding of atomic diffusion is therefore of vital importance. Here we show the first successful application of X-ray photon correlation spectroscopy (XPCS) to this problem.

Diffusion in solids has traditionally been studied by the radiotracer technique. This is a macroscopic technique, *i.e.* it is sensitive only to atomic displacements composed of many atomic jumps, and therefore only the diffusion constant can be measured. Microscopic techniques, however, aim at understanding atomic dynamics by measuring the frequency, length and direction of the elementary atomic jump. Existing microscopic techniques such as quasi-elastic neutron scattering (QENS) or Mößbauer spectroscopy can only measure very fast diffusion with jump frequencies in the MHz-range and they work only with special elements or isotopes. XPCS consists in scattering coherent X-rays at the sample and recording the temporal variations of the scattered intensity – the so-called speckle pattern – as a function of the wave vector transfer q. As this is a non-resonant method it is not bound to selected systems, and it can measure jump frequencies as low as one jump per hour.

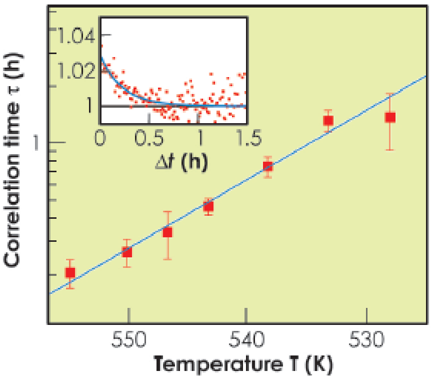

Fig. 48: Arrhenius plot of the correlation time as a function of temperature for fixed q with fit. Inset: Auto-correlation function of the measurement at 543 K.

In this study we investigated the atomic dynamics in $Cu_{90}Au_{10}$. In the temperature region around 540 K, this system forms a solid solution, but the proximity of the long-range ordered Cu_3Au phase leads to certain atomic arrangements being energetically favoured compared to others. It was the goal of the experiment to investigate the influence of this effect on the dynamics.

The experiment was performed with partially coherent radiation at **ID10A** in transmission geometry. The sample was a thin single crystal. Time series of the scattered intensity $I(q,t)$ at a given q and time t were taken with a CCD detector and evaluated via the standard intensity-intensity auto-correlation function:

$$g^{(2)}(q,\Delta t) = \langle I(q,t) I(q,t+\Delta t)\rangle / \langle I(q,t)\rangle^2,$$

where the average is taken over absolute time t and the pixels of the detector. The decay of the auto-correlation function was fitted as an exponential offset by 1 with a q-dependent correlation time τ (q) (see inset of **Figure 48**).

Figure 48 shows that the effect of temperature on the dynamics can satisfactorily be described by an Arrhenius relation, with a fitted activation enthalpy of 2.09 ± 0.15 eV.

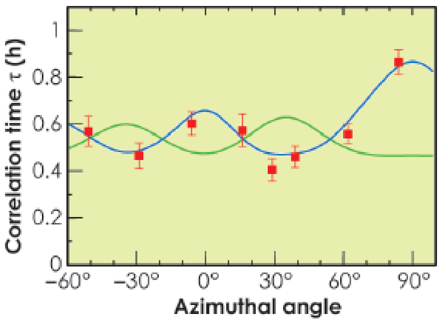

Fig. 49: Variations of the measured correlation time as a function of the crystal orientation at 543 K (red squares) together with the predictions of a model neglecting (green line) and including (blue line) short-range order.

As the sample was a single crystal, rotating the detector around the direction of the incident beam for a fixed scattering angle (corresponding to same length, but different orientation of q) leads to variations of the fitted correlation time due to the discrete and directed nature of the atom jumps. This is shown in **Figure 49** for a number of measurements, all with |q|=1.75 Å^{-1} but with varying azimuthal angle. A theory taking into account only the jump geometry of nearest-neighbour jumps (green line) cannot explain the data, however. This discrepancy is due to short-range order: following ref. [1], the correlation times due to the jump geometry have to be multiplied by the value of the static short-range order intensity. This gives the blue line in **Figure 49**, which fits the data satisfactorily. The only fitted parameter is the residence time, *i.e.* the average time between jumps for a given atom, with a value of 2200 s at 543 K. This is the first observation of the so-called de Gennes narrowing in crystalline media by XPCS, a phenomenon that is well known from measurements in liquids [2], and that is due to the longer life-time of energetically favoured configurations on the atomic scale compared to unfavoured configurations.

In conclusion, our results show that XPCS is a viable method for measuring atomic diffusion, providing new insights into atomic dynamics. Thus XPCS is established as a complementary method to existing techniques such as QENS, which are restricted to jump frequencies in the MHz range.

References
[1] S.K. Sinha, D.K. Ross, *Physica B* **149**, 51 (1988).
[2] C. Caronna, Y. Chushkin, A. Madsen and A. Cupane, *Phys. Rev. Lett.* **100**, 055702 (2008).

Picosecond X-ray diffraction tracking of light-induced spin-crossover switching in a molecular material

Principal publication and authors
M. Lorenc (a), J. Hébert (a), N. Moisan (a), E. Trzop (a), M. Servol (a), M. Buron-Le Cointe (a), H. Cailleau (a), M.L. Boillot (b), E. Pontecorvo (c), M. Wulff (c), S. Koshihara (d) and E. Collet (a), *Phys. Rev. Lett.* **103**, 028301 (2009).
(a) Institut de Physique de Rennes, Université de Rennes1-CNRS, Rennes (France)
(b) Institut de Chimie Moléculaire et des Matériaux d'Orsay, CNRS, Orsay (France)
(c) ESRF
(d) Tokyo Institute of Technology, Tokyo (Japan)

Light can control macroscopic properties of materials such as magnetism, conductivity, ferroelectricity. How fast is such light-induced switching? Does this transformation simply result from laser heating? Which mechanisms stabilise the electronic excited state? These are the most intriguing questions concerning light-induced phenomena in materials and particularly so in the emerging field of photoinduced transformations [1].

Spin-crossover crystals are prototypes of molecular bistability in the solid state. They may be switched from low-spin (LS) to high-spin (HS) states under various external perturbations, including temperature or light irradiation. Such a transformation is manifested by changes of magnetic, optical as well as structural properties such as intra-molecular swelling with a resulting volume expansion [2]. The average <Fe-N> bond length elongation in particular is a well proven fingerprint of increased spin multiplicity. For the [TPA]Fe^{III}[TCC]PF$_6$ crystal, studied here, it varies between 1.965 Å (LS) and 2.125 Å (HS) (**Figure 50**).

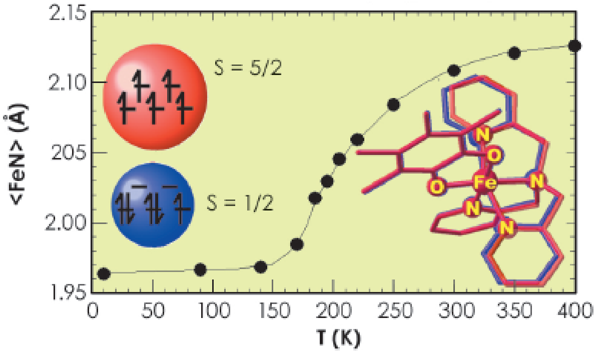

Fig. 50: Thermal spin-crossover associated with the change of molecular structure between HS (red) and LS (blue) states.

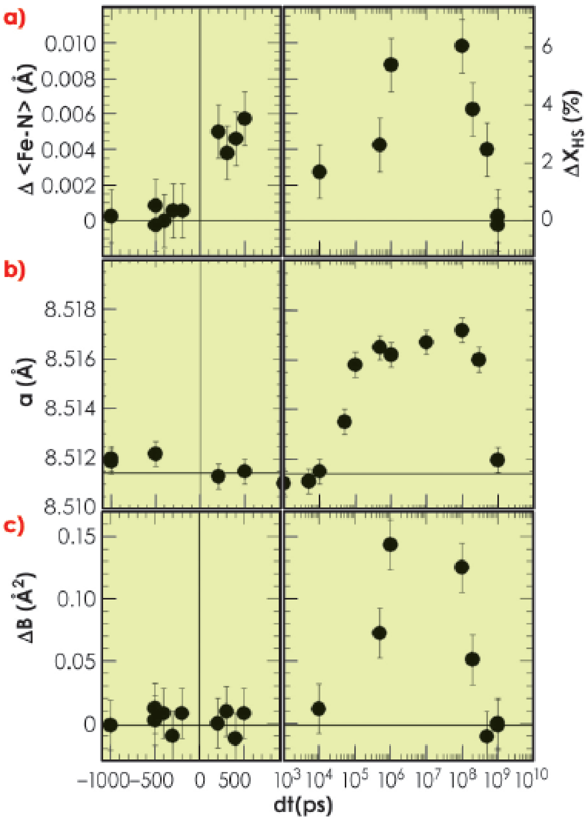

Fig. 51: Structural signatures associated with the different steps of the switching process: a) intramolecular deformation (Fe-N bond), b) unit cell parameter *a*, c) isotropic temperature factor.

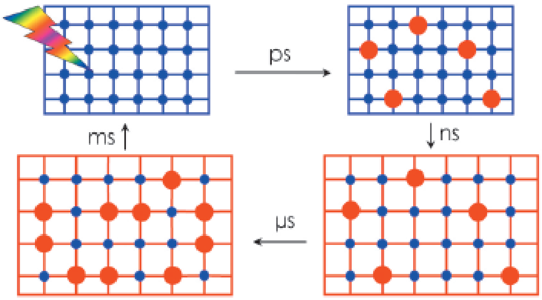

Fig. 52: Schematic drawing of the out-of-equilibrium dynamics: HS molecules (red circles) generated within 1 ps by a laser pulse in the cold (blue) lattice with mainly LS molecules (blue circles), warm lattice (red) expansion on 10s ns, thermal stabilisation of HS population within μs.

While photoswitching of spin-crossover crystals driven by nanosecond laser pulses was observed in different compounds, the duration of the underlying processes remained unknown. By combining femtosecond (fs) optical spectroscopy and picosecond (ps) X-ray diffraction, it was possible to deduce a multi-step process initiated by a fs laser pulse: from sub-ps photoswitching up to the microsecond thermoswitching. Structural analysis sheds new light on the mechanisms that could explain the time domain data.

Optical spectroscopy demonstrated that molecules switch from LS to HS states within 1 ps and that every photon switches a single molecule. Subsequently the HS molecular fraction remains unchanged for another 100 ps. The corresponding variation of the HS molecular fraction (ΔX_{HS}) modifies the molecular structure in the transient state, mainly affecting the Fe-N bonds. This feature was caught by a time-resolved crystallography study performed with 100 ps resolution at beamline **ID09B** (**Figure 51a**). While such elongation of Fe-N bonds of spin-crossover molecules was also observed in solution by ps X-ray spectroscopy, only X-ray diffraction from crystals made it possible to obtain a detailed 3D structural reorganisation. Our study clearly shows that this first step occurs at constant volume. The swelling of photo-transformed molecules, as well as the local heating caused by non-radiative energy dissipation of relaxing LMCT states, will both increase local pressure and consequently drive the propagation of volume expansion. It is demonstrated here that this second step associated with volume expansion occurs on a tens of ns timescale, in agreement with the sound velocity and sample size (10-100 μm) (**Figure 51b**). The third step results from the significant variation of the isotropic temperature factor (ΔB) observed in **Figure 51c**, which is a consequence of the temperature homogenisation process driven by heat diffusion: an additional transformation towards the HS state is observed on the μs timescale. This is the expected timescale for thermal activation across the energy barrier. It is therefore clear that this last step is associated with thermal switching effects due in particular to the increase of the average temperature. Both steps leave their imprints on the time course of the molecular fraction of HS molecules (**Figure 51a**).

The present results reveal the out-of-equilibrium dynamics (**Figure 52**) and underpin the complex switching pathway from the molecular to material length and time scales. Such detailed X-ray diffraction analysis of ultra-fast dynamical processes driven by a fs laser flash has set the stage for the new age of ultrafast crystallography.

References

[1] M. Buron & E. Collet. Editors *Second International conference on Photoinduced Phase Transitions, J. Phys: Conf. Series.* **21** (2005).

[2] E. Collet, M.L. Boillot, J. Hebert, N. Moisan, M. Servol, M. Lorenc, L. Toupet, M. Buron-Le Cointe, A. Tissot and J. Sainton, *Acta Cryst.* B**65**, 474-480 (2009).

Symmetry-raising orbital order in $PbRuO_3$

Principal publication and authors

S.A.J. Kimber (a,b), J.A. Rodgers (b), H. Wu (c), C.A. Murray (b), D.N. Argyriou (a), A.N. Fitch (b), D.I. Khomskii (c,e) and J.P. Attfield (b), *Phys. Rev. Lett.* **102**, 046409 (2009).

(a) Helmholtz-Zentrum Berlin für Materialien und Energie (Germany)
(b) Centre for Science at Extreme Conditions and School of Chemistry, University of Edinburgh (UK)
(c) II. Physikalisches Institut, Universität zu Köln (Germany)
(d) ESRF
(e) Department of Physics, Loughborough University (UK)

Transition metal oxides display a remarkable range of electronic and magnetic phenomena such as high temperature superconductivity in cuprates and colossal magnetoresistances in manganese oxides. Ruthenates based on Ru^{4+} are notable for being metallic conductors without chemical doping and show a variety of phenomena at low temperatures. The perovskite $SrRuO_3$ becomes ferromagnetic on cooling below 160 K and is used in many thin film electronics applications. This material can be prepared at ambient pressure, whereas lead ruthenate, $PbRuO_3$, requires high synthesis pressures and so its properties had not been investigated since it was originally reported, in 1970 [1]. Our investigation has revealed a very different low temperature state to that of $SrRuO_3$, in which ordering of Ru *4d* orbitals results in an anomalous structural change to higher symmetry at low temperatures.

Polycrystalline samples of $PbRuO_3$ were synthesised by heating a pyrochlore-type precursor $Pb_2Ru_2O_{6.5}$ at 11 GPa and 1100°C in a multi-anvil press. Magnetisation and conductivity measurements revealed a transition at 90 K but without magnetic order below this temperature. To determine any structural changes occurring at the transition, high resolution powder X-ray diffraction patterns between 10 and 300 K were collected at beamline **ID31**. The ambient temperature structure of $PbRuO_3$ was found to be very similar to that of $SrRuO_3$. Tilting of the RuO_6 octahedra leads to a primitive orthorhombic superstructure of the perovskite structural arrangement that is described by the space group *Pnma*.

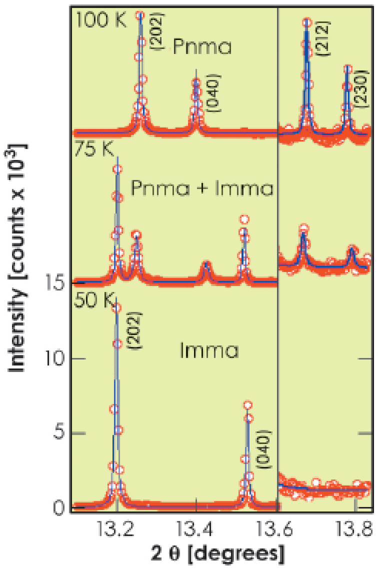

Fig. 53: Part of the powder X-ray diffraction profiles of $PbRuO_3$ at 50, 75 and 100 K (λ = 0.45621 Å) showing the change between high temperature *Pnma* and low temperature *Imma* superstructures, with coexistence of the two at 75 K. The vertically expanded right hand portion demonstrates that the superstructure peaks with odd ($h + k + l$) values disappear on cooling through the transition.

On cooling through the transition, a new set of diffraction peaks belonging to a different superstructure appear and coexist with the *Pnma* phase, showing that the transition is discontinuous (**Figures 53 and 54**). Surprisingly, the *Pnma* superstructure reflections with odd ($h + k + l$) values disappear, which indicates that the low temperature phase has a higher (body-centred) symmetry than the room temperature structure. The low temperature phase has a different tilted arrangement of octahedra with space group *Imma*.

The Ru-O bond distances derived from the refined crystal structure (**Figure 54**) reveal that orbital ordering occurs at the 90 K transition in $PbRuO_3$. The RuO_6

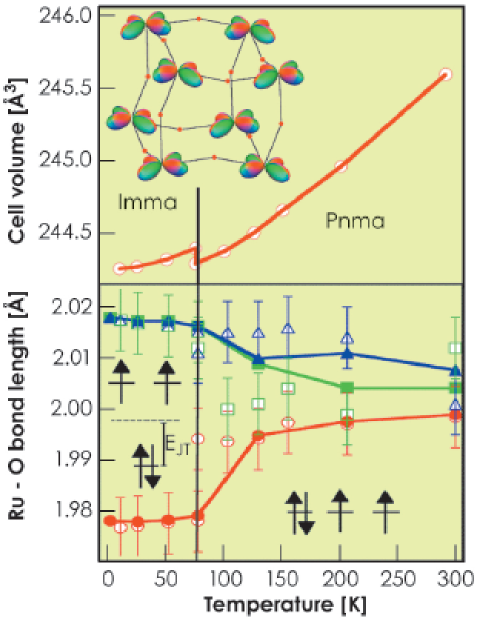

Fig. 54: Temperature variations of the unit cell volume (top) and Ru-O bond distances (bottom, open symbols from **ID31** X-ray structure refinements, filled symbols from complementary GEM@ISIS neutron structure refinements) for $PbRuO_3$. The orbital ordering transition is marked by a volume discontinuity and by changes in the Ru-O distances. The RuO_6 octahedra are almost regular in the high temperature *Pnma* structure, but in the *Imma* phase they are distorted with two short axial bonds (red points) and four long equatorial bonds (blue and green points). This signifies a Jahn-Teller distortion that lifts the degeneracy of the Ru^{4+} t_{2g}-type *d*-orbitals as shown. The long range order of the doubly-occupied d_{xy} orbitals is shown on the upper panel.

octahedra are almost regular in the *Pnma* phase, but below the transition, a Jahn-Teller distortion is apparent in the *Imma* structure, with two short and four long Ru-O bonds. This corresponds to a $d_{xy}^2 d_{xz}^1 d_{yz}^1$ orbital ordering of the Ru^{4+} t_{2g}^4 configuration in the *Imma* phase, creating planes of doubly-occupied d_{xy} orbitals as shown in **Figure 54**. The Ru orbital order is coupled to an unusual distortion of the Pb^{2+} coordination which has a near-regular square pyramid with five short (2.50 Å) Pb-O bonds, while other Pb-O distances are greater than 2.82 Å, although no 'lone pair' distortion is evident.

The (high temperature) *Pnma* to (low temperature) *Imma* transition in $PbRuO_3$ is remarkable as *Pnma* is a subgroup of *Imma* so a continuous transition from (high temperature) *Imma* to (low temperature) *Pnma* would normally be expected. Indeed, it has been observed in many simple perovskites such as $SrSnO_3$ [2]. The symmetry-raising *Pnma-Imma* transition in $PbRuO_3$ would have a negative structural contribution to the transition entropy, but this is evidently outweighed by the large positive electronic contribution from the loss of orbital order at the transition.

In conclusion, a new, orbitally-ordered, low temperature electronic state for ruthenates has been discovered. The orbital distortion appears to be stabilised by coupling to electronic instabilities of the Pb^{2+} cations. The combined order of Pb *s* and *p* hybridised orbitals, Ru *d*-orbitals and O-centred octahedral tilting instabilities results in an anomalously high symmetry ground state structure that inverts the usual group-subgroup symmetry lowering.

References
[1] J.A. Kafalas and J.M. Longo, *Mat. Res. Bull.* **5**, 193 (1970).
[2] E.H. Mountstevens, S.A.T. Redfern and J.P. Attfield, *Phys. Rev. B* **71**, 220102(R) (2005).

Structure, superconductivity and pressure response of LiFeAs

Principal publications and authors
M.J. Pitcher (a), D.R. Parker (a), P. Adamson (a), S.J.C. Herkelrath (a), A.T. Boothroyd (b), R.M. Ibberson (c), M. Brunelli (d) and S.J. Clarke (a), *Chem. Comm.*, 5918-5920 (2008);
M. Mito (b,e), M.J. Pitcher (a), W. Crichton (d), G. Garbarino (d), P.J. Baker (b,c), S.J. Blundell (b), P. Adamson (a), D.R. Parker (a) and S.J. Clarke (a), *JACS* **131**, 2986-2992 (2009).
(a) Department of Chemistry, University of Oxford (UK)
(b) Department of Physics, University of Oxford (UK)
(c) ISIS Facility, STFC-Rutherford Appleton Laboratory (UK)
(d) ESRF
(e) Faculty of Engineering, Kyushu Institute of Technology (Japan)

High temperature superconductivity has recently been reported in several compounds containing FeAs anti-PbO-type (*i.e.* antifluorite-type) layers. LaOFeAs was found to superconduct below 26 K when doped with electrons through the substitution of about 10-20% of the oxide ions by fluoride [1]. This critical temperature, T_c, is only exceeded by layered cuprates, some fullerides and MgB_2. Subsequently several superconducting compounds containing iron arsenide or phosphide antifluorite-type layers separated by electropositive metal cations, or by metal oxide slabs of varying thickness, have been discovered. The high T_cs (up to 50 K) and critical fields exhibited by these materials suggest that they are unconventional superconductors whose properties cannot be described by existing models of superconductivity such as the BCS theory. The superconducting compositions generally lie close in composition to semimetallic antiferromagnetically ordered phases and it is conjectured that the magnetic properties and the superconducting properties are intimately linked.

Over 40 years ago Juza and Langer [2] reported the existence of a range of phases close to the composition LiFeAs with antifluorite-type FeAs layers, but the electronic properties were not measured. We synthesised stoichiometric LiFeAs samples by the reaction of elemental or binary precursors at 700-800°C and discovered that the samples exhibited bulk superconductivity with T_c as high as 17 K. This discovery of superconductivity in stoichiometric LiFeAs (made in parallel elsewhere [3]) suggested that superconductivity may be ubiquitous in compounds containing FeAs antifluorite layers.

The detailed crystal structure of LiFeAs was probed using a combination of powder neutron diffraction measurements on HRPD and POLARIS at the ISIS facility and powder X-ray diffraction measurements using **ID31**. The response of the structure to an applied hydrostatic pressure was probed on **ID27**.

The complementary use of neutrons and X-rays is valuable in this case.

There is the possibility of disorder between Fe and Li, and, because of the opposite signs of the neutron scattering lengths of Fe and Li, disorder could mimic the presence of vacancies. Our complementary refinements from HRPD and ID31 (Figure 55) suggested that the superconducting phase is stoichiometric LiFeAs and there is no measurable Li/Fe site disorder. The compound adopts the anti-PbFCl structure type and is composed of an approximately cubic close packed array of As with Fe in half the tetrahedral interstices and Li displaced from the centres of all the octahedral interstices so as to obtain square pyramidal coordination by As (Figure 55). Our combined neutron and X-ray refinement showed that the second Li site postulated by Juza and Langer [2] is unpopulated. These results are consistent with a single crystal diffraction study by Tapp *et. al.* [3].

LiFeAs has the shortest Fe–Fe distance of any of the iron arsenide superconductors and an FeAs$_4$ tetrahedron that is highly compressed in the basal direction. It also exhibits bulk superconductivity when stoichiometric with Fe formally in the +2 oxidation state, in contrast to the other systems which require doping away from this formal oxidation state in order to realise superconductivity [1]. The relationships between electron count, structural parameters and superconductivity still need to be established. LiFeAs may be an important compound in establishing these relationships because of the differences between it and the other related materials.

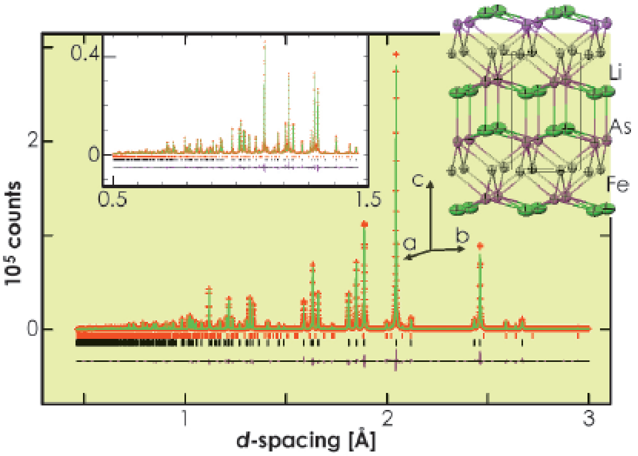

Fig. 55: The structure of LiFeAs and the refinement against **ID31** data.

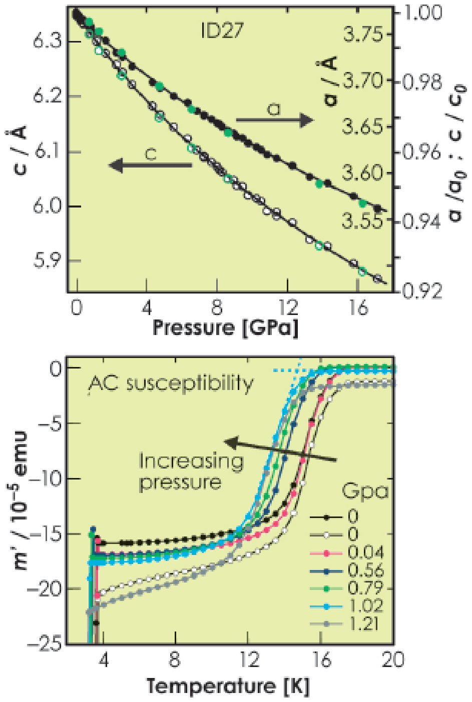

Fig. 56: The pressure response of the lattice parameters refined from **ID27** data (upper) and the AC susceptibility (lower).

Magnetic susceptibility measurements carried out under applied hydrostatic pressure (Figure 56) showed that the superconductivity in LiFeAs is suppressed by the application of pressure. The analysis of powder X-ray diffraction data collected on ID27 from the same sample as the one measured on ID31 shows that LiFeAs is highly compressible with a bulk modulus of 57.3(6) GPa (Figure 56). Refinement of the structural parameters shows that the most compressible part of the structure is the lithium arsenide layer which becomes highly compressed along the stacking direction of the layers. This is presumably because the 5-coordinate site occupied by Li is quite large. In contrast, the FeAs layers become even more compressed in the basal plane and the FeAs$_4$ tetrahedra become even more distorted than at ambient pressure. It has been observed that a high T_c seems to be favoured in systems with very regular FeAs$_4$ tetrahedra, providing the electron count is optimised. The decrease in T_c with increasing distortion of the FeAs$_4$ tetrahedron on LiFeAs is consistent with this observation.

References

[1] Y. Kamihara, T. Watanabe, M. Hirano and H. Hosono, *J. Am. Chem. Soc.* **130**, 3296 (2008).
[2] R. Juza and K. Langer, *Z. Anorg. Allg. Chem.* **361**, 58 (1968).
[3] J.H. Tapp, Z. Tang, B. Lv, K. Sasmal, B. Lorenz, P.C.W. Chu and A.M. Guloy, *Phys. Rev. B* **78**, 060505 (2008).

Non-BCS high-T_c superconductivity in the ordered cubic superconductor Cs_3C_{60}

Principal publication and authors
Y. Takabayashi (a), A.Y. Ganin (b), P. Jeglič (c), D. Arčon (c), T. Takano (d), Y. Iwasa (d), Y. Ohishi (e), M. Takata (e), N. Takeshita (f), K. Prassides (a) and M.J. Rosseinsky (b), *Science* **323**, 1585-1590 (2009).
(a) Department of Chemistry, Durham University (UK)
(b) Department of Chemistry, University of Liverpool (UK)
(c) Institute Jožef Stefan, Ljubljana (Slovenia)
(d) Institute for Materials Research, Tohoku University, Sendai (Japan)
(e) Japan Synchrotron Radiation Research Institute, SPring-8, Hyogo (Japan)
(f) National Institute of Advanced Industrial Science and Technology, Tsukuba (Japan)

C_{60}-based solids have long been recognised as archetypal examples of molecular superconductors with T_c as high as 33 K. The superconducting T_c of face-centred cubic (fcc) A_3C_{60} (A = alkali metal) increases monotonically with the inter-C_{60} separation, which is in turn controlled by the intercalant's A^+ size. However, following such discoveries many years ago, established fulleride chemistry has failed to deliver new materials.

Recent work in our laboratories based on new synthetic ideas coupled with structural and electronic property measurements has made it possible to advance in this area. Firstly, we developed synthetic protocols employing new solvents to access hyper-expanded alkali fullerides near the metal-insulator boundary and at previously inaccessible intermolecular separations [1]. Then we used the accumulated synthetic expertise aided by *in situ* structural characterisation on beamline **ID31** specifically to target high-symmetry (retaining t_{1u} orbital degeneracy in the solid) fullerides with varying C_{60} orientation and packing. This approach culminated in the discovery of bulk superconductivity under pressure at 38 K in bcc-structured A15 Cs_3C_{60} (**Figure 57**), the highest T_c known for any molecular material [2]. This is the first example of a superconducting C_{60}^{3-} fulleride with non-fcc sphere packing. This single non-fcc material has a higher T_c than all the fcc A_3C_{60} fullerides studied previously. Higher T_cs are therefore possible once the constraint of working in fcc systems is broken. Moreover, the electronic ground state in competition with superconductivity not only contains magnetic moments localised on the C_{60}^{3-} anions but is antiferromagnetically ordered with T_N = 46 K. The antiferromagnetic insulator-superconductor transition maintains the threefold degeneracy of the active orbitals in both competing electronic states, and is thus a purely electronic transition to a superconducting state with a T_c dependence on pressure-induced changes of anion packing density that is not explicable by BCS theory (**Figure 58**).

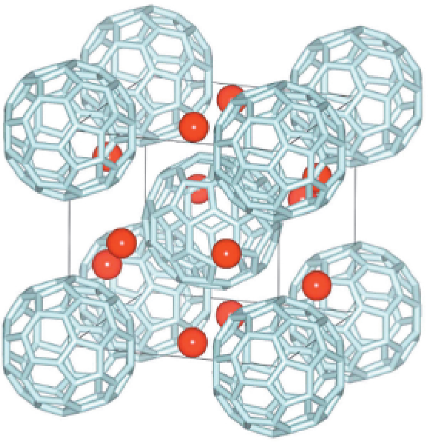

Fig. 57: Crystal structure of A15 Cs_3C_{60} (space group Pm-3n) based on bcc anion packing with orientationally ordered C_{60}^{3-} anions. The lower bcc packing density offers more spacious sites (with four fulleride neighbours) for the large Cs^+ (red) when compared to fcc A_3C_{60}.

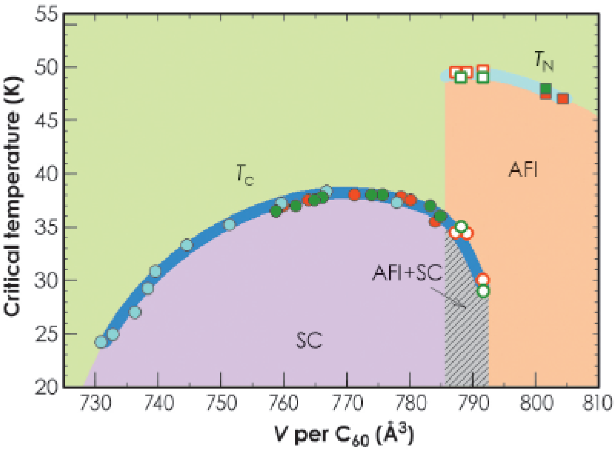

Fig. 58: Electronic phase diagram of A15 Cs_3C_{60} showing the evolution of T_N (squares) and T_c (circles) and thus the isosymmetric transition from the ambient pressure AFI state to the high-pressure SC state as a function of volume occupied per fulleride anion, V, at 14.6 K. Open symbols represent data in the AFI-SC coexistence regime.

The high symmetry of the C_{60} building block imposes a robust cubic three-dimensional structure on A15 Cs_3C_{60}, free of positional, chemical, or orientational disorder, with a fixed charge state in which magnetism is transformed into superconductivity solely by changing an electronic parameter, the extent of overlap between the outer wavefunctions of the anions. The pressure-induced transition from a localised electron AFI to a superconductor with two distinct dependences of T_c on packing density is purely electronic in nature, driven by increased overlap between the C_{60}^{3-} anions and the associated enhanced tendency to delocalise the t_{1u} electrons. The unconventional nature of the superconducting state that emerges from the AFI can be associated with its proximity to the metal-insulator transition. In this case, the conventional Fermi liquid theories are not valid, and quasi-localised effects produced by electronic correlation, which enhances the role of intramolecular Jahn-Teller (electron-phonon) and Hund's rule (electron-electron) coupling, are directly controlled by the persistent orbital degeneracy in both the insulating and superconducting states. The observed maximum in $T_c(P)$ is consistent with theoretical treatments [3] that explicitly take account of the orbital degeneracy and the repulsion between the electrons as well as the classical electron-phonon coupling. These effects are not seen in conventional fcc A_3C_{60} systems, which are too far from the metal-insulator transition for differences from the BCS predictions of the dependence of T_c on $N(E_f)$ to become apparent. Therefore, A15 Cs_3C_{60} emerges as an ideal material for understanding the interactions producing superconductivity in structurally and chemically complex correlated electron systems such as the cuprates and oxypnictides, as it allows the isolation of the influence of only electronic factors without any other complications.

References

[1] A.Y. Ganin, Y. Takabayashi, C.A. Bridges, Y.Z. Khimyak, S. Margadonna, K. Prassides and M.J. Rosseinsky, *J. Am. Chem. Soc.* **128**, 14784 (2006).
[2] A.Y. Ganin, Y. Takabayashi, Y.Z. Khimyak, S. Margadonna, A. Tamai, M.J. Rosseinsky and K. Prassides, *Nature Mater.* **7**, 367 (2008).
[3] M. Capone, M. Fabrizio, C. Castellani and E. Tosatti, *Rev. Mod. Phys.* **81**, 943 (2009).

Structure and properties of single crystals of high-pressure boron

Boron is an unusual element. Its three valence electrons are too localised to make it metallic but insufficient in number to form a simple covalent structure. As a compromise, boron atoms form quasimolecular B_{12} icosahedra that become building blocks of boron and boron-rich crystalline phases. Only α-rhombohedral and β-rhombohedral boron, obtained at ambient pressure, are established as pure boron crystalline forms. The high-pressure behaviour of boron is of considerable interest in physics and materials science. Our investigations of superconducting polycrystalline boron-doped diamonds [1] revealed boron segregation in an intergranular space that may influence the mechanism of superconductivity.

Many of the fundamental questions regarding the solid-state chemistry of boron are still unanswered. Synthesis of single-phase products in macroscopic quantities and in the form of single crystals remains one of the great challenges of boron chemistry [2]. Using a large volume press, at 20 GPa and 1700 K, we have grown single crystals of a high-pressure high-temperature orthorhombic B_{28} boron phase for the first time. The crystals appeared to have a dark-red colour and an elongated prismatic shape (Figure 59). We confirmed the purity of the crystals by chemical analysis, collected single-crystal X-ray diffraction data (BM01), then solved and refined the crystal structure. There is remarkable

Principal publication and authors

E.Yu. Zarechnaya (a), L. Dubrovinsky (a), N. Dubrovinskaia (b,c), Y. Filinchuk (d), D. Chernyshov (d), V. Dmitriev (d), N. Miyajima (a), A. El Goresy (a), H.F. Braun (e), S. Van Smaalen (c), I. Kantor (f), A. Kantor (f), V. Prakapenka (f), M. Hanfland (d), A.S. Mikhaylushkin (g), I.A. Abrikosov (g) and S.I. Simak (g), *Phys. Rev. Lett.* **102**, 185501 (2009).
(a) Bayerisches Geoinstitut, University of Bayreuth (Germany)
(b) Institut für Geowissenschaften, University of Heidelberg (Germany)
(c) Lehrstuhl für Kristallographie, Physikalisches Institut, University of Bayreuth (Germany)
(d) ESRF
(e) Experimentalphysik V, Physikalisches Institut, University of Bayreuth (Germany)
(f) GeoSoilEnviroCARS, University of Chicago (USA)
(g) Department of Physics, Chemistry and Biology, Linköping University (Sweden)

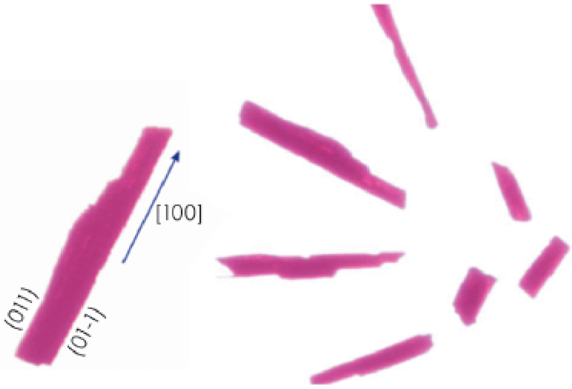

Fig. 59: Single crystals of the orthorhombic high-pressure boron phase.

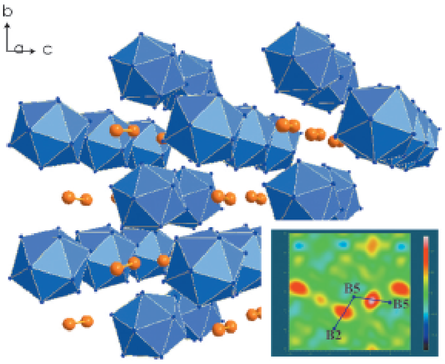

Fig. 60: The structure of the HPHT boron phase shown in the *bc* projection. The insert shows difference electron density plots around the atoms B5 (dumbbell, upper right) and B2 and B5 (dumbbell-icosahedron contact) extracted from single-crystal X-ray diffraction data. The maximum electron density is centred on the middle of the bond, suggesting covalent bonding between the B_2 dumbbell and the B_{12} icosahedron.

agreement between structural parameters obtained from single crystal and powder X-ray diffraction data [3] and those from our *ab initio* calculations. The *bc* projection (**Figure 60**) shows that the structure is built of B_{12} icosahedra and B_2 dumbbells linked together, thus forming a three-dimensional network. The distances B-B within a B_{12} icosahedron (1.766(3)-1.880(3) Å) are slightly longer than those within a dumbbell (1.721(4) Å). Chemical bonds within B_2 dumbbells and B_{12} icosahedra, as well as between icosahedra and dumbbells, are strongly covalent, as evident from the presence of residual electron density in the difference Fourier maps.

The high density and strong covalent bonding in this B_{28} phase suggest that it could be less compressible than the other known boron phases. This was confirmed in the compression experiment (**ID09**) up to ~30 GPa in a diamond anvil cell with Ne as a pressure transmitting medium and a powder of B_{28} that gave values for the bulk modulus of K_{300} = 227(2) GPa and its pressure derivative K´ = 2.2(2). Pure orthorhombic B_{28} is a poor electrical conductor with a resistivity of the order of 10^6 Ω cm at ambient conditions. With increasing temperature, the resistivity decreases indicating semiconducting behaviour. The activation energy (1.9(2) eV) is in reasonable agreement with the value of the band-gap energy (2.1 eV) determined from optical spectroscopy measurements.

Boron is known as a hard material (with the Vickers hardness reported as high as 25-30 GPa for β-boron). We found that samples of B_{28} with submicrometre grain sizes have a hardness of 58(5) GPa. This value is in the range of polycrystalline cBN which makes B_{28} the second (after diamond) elemental superhard material.

In summary, our study demonstrates that the orthorhombic high-pressure high-temperature boron phase, synthesised above 9 GPa, has a structure consisting of covalently bonded B_{12} icosahedra and B_2 dumbbells, and combines unusual properties – it is a wide band gap semiconductor that is superhard, optically transparent, and thermally stable (above 1000 K in air). We have demonstrated the possibility to grow single crystals of this phase, which opens prospects for applications of this material in areas of electronics and optics.

References

[1] N. Dubrovinskaia, R. Wirth, J. Wosnitza, T. Papageorgiou, H.F. Braun, N. Miyajima and L. Dubrovinsky, *Proc. Natl. Acad. Sci. USA* **105**, 11619 (2008).
[2] B. Albert and H. Hillebrecht, *Angew. Chem. Int. Ed.* **48**, 2 (2009).
[3] E. Yu. Zarechnaya, L. Dubrovinsky, N. Dubrovinskaia, N. Miyajima, Y. Filinchuk, D. Chernyshov and V. Dmitriev, *Sci. Tech. Adv. Mater.* **9**, 044209 (2008).

A miniaturised linear pH sensor based on a highly photoluminescent self-assembled europium(III) metal-organic framework

Principal publication and authors

B.V. Harbuzaru (a), A. Corma (a), F. Rey (a), J.L. Jordá (a), D. Ananias (b), L.D. Carlos (b) and J. Rocha (b), *Angewandte Chemie International Edition* **48**, 6476-6479 (2009).
(a) Instituto de Tecnología Química, (UPV-CSIC), Valencia (Spain)
(b) Departments of Chemistry and Physics, CICECO, University of Aveiro (Portugal)

Research in the field of lanthanide-based metal-organic frameworks (Ln-MOFs) is growing rapidly because of the discovery of new structures with potential applications in catalysis, sensors, contrast agents, non-linear optics, display and electroluminescent devices. In particular, photoluminescence applications need high quantum efficiency to minimise energy losses and to allow miniaturisation.

We focused our attention on 1,10-phenanthroline-2,9-dicarboxylic acid (H2PhenDCA) as a suitable organic ligand, since it is well known as a sensitising agent for Eu^{3+} and is able to coordinate Eu centres through the oxygen atoms of the carboxylate groups and the nitrogen of the phenanthroline. $PhenDCA^{2-}$ tends to form zero-dimensional (molecular) water soluble compounds, but we were hoping to obtain a 2D or 3D insoluble equivalent in order to transfer these properties to a solid, which could have practical applications. This was accomplished through a hydrothermal synthetic route, a powerful technique for the preparation of metastable compounds, via which it was possible to obtain a new material, named ITQMOF-3. Its crystal structure was solved using single crystal X-ray diffraction data collected at beamline **BM16** (**Figure 61**).

ITQMOF-3 can be described as a layered compound with two distinct and very different sheets, A and B. Each sheet contains one type of Eu^{3+} ion (Eu1 or Eu2) in a different chemical environment. Sheet A, containing Eu1, has ML_2 stoichiometry and is negatively charged. Each Eu^{3+} ion is octacoordinated by two tetradentate ligands to form isolated $Eu(PhenDCA)_2$ species. The $Eu(PhenDCA)_2$ groups interact with the neighbouring groups in the sheet through multiple π-π interactions of the aromatic rings, producing a two-dimensional self-assembled layer. Sheet B contains Eu2 with stoichiometry $[Eu_2(PhenDCA)_2(OH)^-(OH_2)_4]$, and is thus positively charged. In this case, the sheet is formed by isolated planar chains along the *c* axis, with the OH^- and half of the PhenDCA molecules acting as bridges between neighbouring Eu^{3+} ions. Consequently, Eu2 is also octacoordinated, though in a very different environment from that of Eu1, and is situated close to the neighbouring Eu^{3+} ions. The linkage between adjacent A and B sheets take place mainly through electrostatic interactions because of their respective negative and positive charges.

ITQMOF-3 is insoluble in water, and possesses an excellent thermal stability in air to around 300°C. Moreover, it is stable in aqueous solution in a pH range between around 4 and 8. The photoluminescence of ITQMOF-3 displays a very high absolute emission quantum yield, with the 5D0→7F0 transition in the emission spectra presenting two separated peaks, corresponding to the Eu^{3+} ions in the Eu2 and Eu1 sites. In the case of Eu2, the position and intensity of this transition is dependent on variations of the coordination environment, which suggested its potential use as a sensor (**Figure 62**).

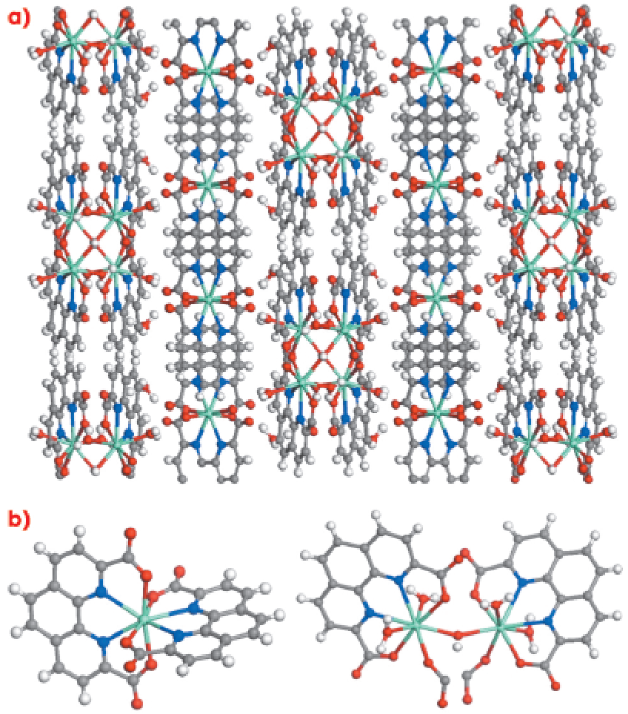

Fig. 61: a) Crystal structure of ITQMOF-3 showing the lamellar packing;
b) Coordination environments of Eu1 (left) and Eu2 (right);
C grey, N blue:
H white, O red,
Eu orange.

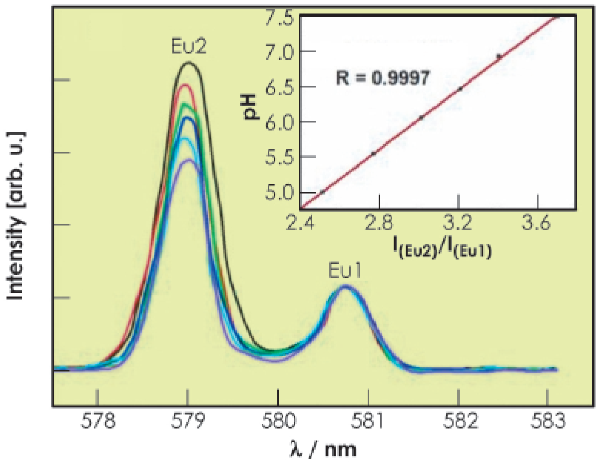

Fig. 62: Intensity variation of the Eu2 5D0→7F0 transition from low (pH 5) to high (pH 7.5) pH values; the inset shows the linear relation between IR and the pH.

Our preliminary results for the use of ITQMOF-3 as a pH sensor have been very encouraging. The intensity of the 5D0→7F0 transition for Eu2 varies linearly and fully reversibly within the pH range in which the material is stable. Interestingly, this pH range corresponds to that required for working with biological fluids, such as blood and cell-culture media. The most outstanding property of this new material for pH sensing is that it requires no calibration because the intensity corresponding to Eu1 is not affected by pH, and can be used as an internal standard. In fact, the pH of a solution can be determined with high accuracy from the linear relationship between the relative Eu2/Eu1 emission intensities (Ir). Thus, by taking advantage of the main properties of ITQMOF-3-Eu (high emission quantum efficiency, insolubility in aqueous media, stability in a relatively wide range of pH, and pH-sensing capability) it has been possible to design a new miniaturised pH sensor prototype by combining the material with a commercial optical fibre. By using this device, we were able to measure continuously the pH in solution in the range 5-7.5 with good accuracy and a rapid response.

Soft condensed matter

With the birth of the Partnership for Soft Condensed Matter (PSCM), the past year marked an important milestone in the Soft Matter activities on site. The PSCM is expected to foster a much broader collaboration among the User communities of both ESRF and ILL and beamlines/instruments involved in Soft Matter Research. The official memorandum of understanding between ESRF and ILL was signed on the 27th of November followed by a workshop on "Scattering and Complementary Techniques" that was primarily oriented to attract Collaborative Partners and set the scientific agenda.

The PSCM will be established in a step-by-step process, initially as a support facility for the better exploitation of synchrotron and neutron scattering instruments in Soft Matter Research. The support infrastructure will be housed in the upcoming Science Building funded by the *Contrat de Projets Etats-Région*. The PSCM, in the medium term, will provide a platform for promoting the complementary aspects of neutron and synchrotron techniques, and aims to collectively enhance the visibility of the Partners in the Soft Matter field. The long-term mission of the PSCM is to streamline neutron and synchrotron based Soft Matter Research to address 21st century challenges in nanomaterials, biotechnology, environmental and energy sciences.

The past year has also been a year of changes with respect to the organisation of beamlines and personnel. The former Soft Condensed Matter group has been reformed with a new name "Structure of Soft Matter" with the addition of the Time-Resolved Pump-Probe beamline ID09B. This change has added a new dimension to the group, especially as pump-probe methods could make much deeper inroads into the activities of the group. Secondly, the upgrade proposals from the group was generally well received, with the SAC endorsing the UPBL 9 (a) and (b) projects which are the evolution of beamline ID02 for time-resolved ultra small-angle scattering and beamline ID09B for time-resolved pump-probe methods, respectively. Refurbishment of the ID10A and B beamlines is also in the pipeline while the ID13 nano-endstation is nearing completion.

As in the previous years, this section provides a selection of highlights which represents only a sub-set of many interesting scientific results and technical developments published over the year. Once again the overlap with other disciplines such as the hard condensed matter and biological sciences is clearly evident. Self-assembly is at the origin of many fascinating features of soft matter. The first article by Lund *et al.* reveals the pathway of a prototypical self-assembly process of block copolymer micelles and models it in terms of a nucleation and growth mechanism. The second article by Shukla *et al.* demonstrates how the improvement of SAXS detection capabilities could be exploited to address longstanding issues such as the nanostructure of highly complex and polydisperse casein micelles, and shed light on the location of calcium phosphate within the complex. The third article by Andersson *et al.* illustrates the ability of the time-resolved pump probe scattering technique to elucidate the structural dynamics in light-driven protein proton pumps such as bacteriorhodopsin and reveal their shared dynamical features.

The next two articles present the most recent advances in coherent imaging and scattering. Lima *et al.* demonstrate the possibility for biological imaging with about 30-50 nm spatial resolution in a hydrated frozen bacterial cell without introducing structural artefacts. Wochner *et al.* depict the power of cross-correlation analysis of two-dimensional

speckle patterns to reveal hidden local symmetries in an otherwise disordered colloidal glassy state. This example also shows the overlap with the hard condensed matter field which is further reiterated in the next two articles dealing with surface and interface studies. In the first article by Vorobiev *et al.*, the enigma of ferrofluid surface layering at the air-water interface is addressed. The second article by de Oteyza *et al.* illustrates the increasing interest in the investigation of buried interfaces, which in this case led to a better understanding of how to tune the morphology of organic *p-n* heterostructures. Finally, Popov *et al.* demonstrate the advances in microbeam diffraction by a single microcrystal diffraction study of a biopolymer, A-amylose, that revealed the location of water molecules and the distortion of intertwined parallel double helices.

T. Narayanan

Pathways of micellar self-assembly probed by time-resolved SAXS

Principal publication and authors
R. Lund (a), L. Willner (b), M. Monkenbusch (b), P. Panine (c), T. Narayanan (c), J. Colmenero (a) and D. Richter (b), *Phys. Rev Lett.* **102**, 188301 (2009).
(a) Donostia International Physics Center/University of the Basque Country, San Seabastian (Spain)
(b) Institute of Solid State Research (IFF), Forschungszentrum Jülich (Germany)
(c) ESRF

In material science and physical chemistry, self-assembly is an important route for manipulation and control for a rational design of nanostructures. Synthetic amphiphilic block copolymers belong to the family of self-assembling systems which, apart from the spontaneous self-assembly property, exhibits tuneability via control over block composition, molecular weight and cosolvents [1]. To fully understand and exploit the properties of self-assembled structures, the pathways of their formation need to be understood [2]. So far, such a study has been exceedingly difficult if not impossible because of the lack of experimental techniques that are able to capture and resolve the early stage of this rapid process.

Here we have taken advantage of advances in modern synchrotron radiation instrumentation and have for the first time been able to capture and describe how self-assembly of amphiphilic block copolymers takes place in real time using beamline ID02. An important prerequisite has been to use a well-defined model system consisting of poly(ethylene-*alt*-propylene)-poly(ethylene oxide) (PEP-PEO) block copolymers in a selective solvent mixture of dimethylformamide and water, both being poor solvents for the PEP block. Block copolymers with large asymmetry in composition (PEP/PEO, 1/20) are molecularly dissolved in pure DMF and micellisation can be induced by simply adding water. This

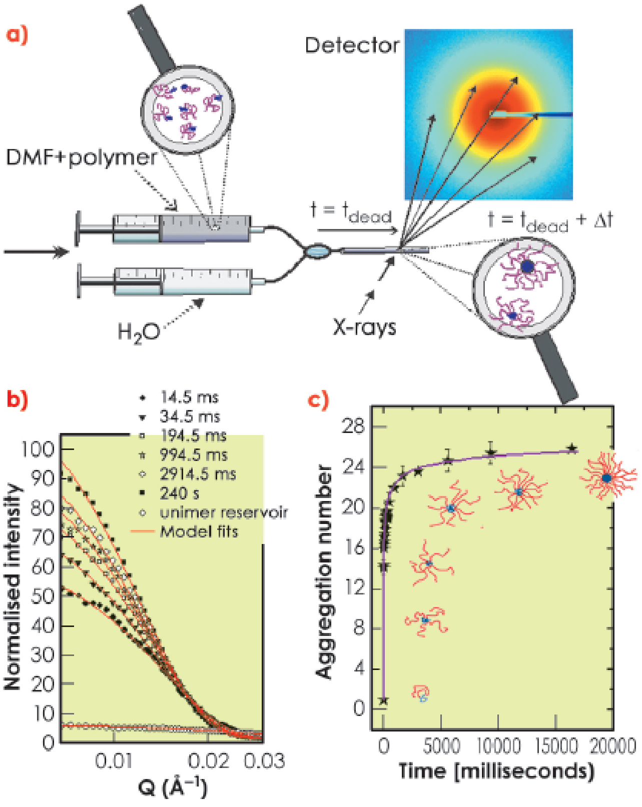

Fig. 63: Illustration of the experimental setup and the real-time scattering data for the self-assembly process of block copolymers. a) The stopped flow setup consists of two motorised syringes containing the reservoirs with polymer solution (PEP-PEO/DMF) and the solvent (water) respectively. Equal amounts of the solution are mixed and then transferred to the observation capillary within a few milliseconds. b) Normalised absolute scattering data from different times during the kinetic process. c) Extracted aggregation numbers as a function of time.

process has been observed experimentally by the setup illustrated in Figure 63, where a stopped flow apparatus [3] is used to realise rapid mixing of the two components (water and polymer in pure DMF solution, respectively) on the millisecond time scale. The reaction itself is monitored directly using fast X-ray shots with some millisecond time resolution that allowed the observation of the birth and growth of the micellar aggregates in time. The evolution of the small-angle scattering for representative times is illustrated in Figure 63b. These curves contain relevant structural characteristics of the micelles, such as sizes, volumes and density profiles. These parameters were extracted by applying detailed core-shell model fits (solid lines). The derived aggregation numbers (number of chains per micelle) are shown in Figure 63c.

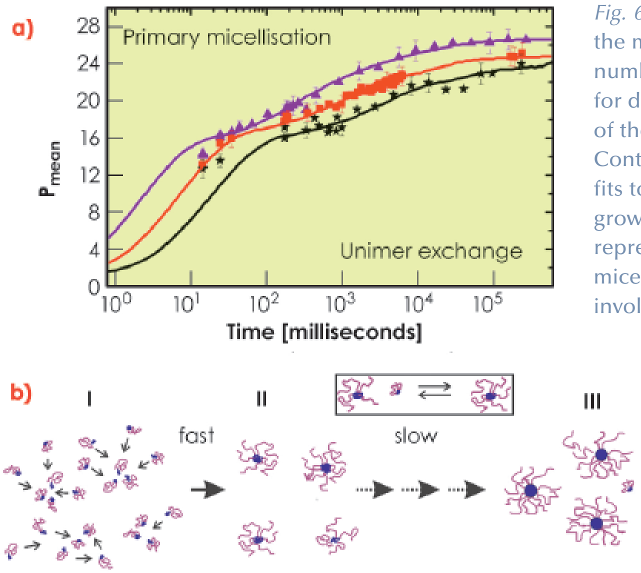

Fig. 64: a) Time evolution of the mean aggregation number of micelles (P_{mean}) for different concentrations of the block copolymer. Continuous lines represent fits to the nucleation and growth model. b) Schematic representation of the micellisation process involving fast nucleation in which the unimer concentration is depleted followed by slow growth to micelle/unimer equilibrium.

The observed behaviour can be quantitatively reproduced using a kinetic model involving insertion and expulsion of single block polymer chains (unimers) by combining classical nucleation and growth theory [4] with the thermodynamic expression expected for block copolymers. It was assumed that only single molecules (*unimers*) can be taken up for each cluster at a time. As seen in the simultaneous fits in Figure 64a, the model agrees very well with the experimental data. In the beginning, a very fast initial nucleation, or primary micellisation, that consumes all the unimers can be observed. This leads temporarily almost to a halt of further growth, which is reflected by the plateau like feature visible at intermediate times in Figure 64a. The final stage of the micellisation is governed by unimer exchange following a type of ripening mechanism where small micelles slowly dissolve to provide further unimers while the larger ones continue to grow. This goes on until the micelles approach the shallow minimum of the equilibrium size and the distribution narrows to reflect the thermodynamic equilibrium. This scenario is summarised schematically in Figure 64b.

The excellent agreement between experimental data and this model strongly suggests that the most effective way for micelle formation is simple addition of unimers from a homogeneous solution. This insight gives novel and valuable information of not only the formation and kinetic pathways of these structures but also the stability and lifetime of metastable nano-particles. This knowledge may be utilised for facile predictive design and manipulation of nano-structures, for example in medicine or material science.

References
[1] R. Lund, L. Willner, J. Stellbrink, P. Lindner, and D. Richter, *Phys. Rev. Lett.* **96**, 068302 (2006).
[2] I.A. Nyrkova and A.N. Semenov, *Macromol. Theory and Sim.* **14**, 569 (2005).
[3] P. Panine, S. Finet, T. Weiss, and T. Narayanan, *Adv. Colloid Interf. Sci.* **127**, 9 (2006).
[4] J.C. Neu, J.A. Cañizo and L.L. Bonilla, *Phys. Rev. E* **66**, 061406 (2002).

Structure of casein micelles and their complexation with tannins

Principal publication and authors
A. Shukla (a), T. Narayanan (a) and D. Zanchi (b), *Soft Matter* **5**, 2884 (2009).
(a) ESRF
(b) LPTHE, Paris (France)

Micellar complexes of natively unfolded casein molecules constitute the major protein component of bovine milk. Casein micelles fluidise different casein molecules and solubilise calcium phosphate well above its solubility limit. The structure of the casein micelles has been the subject of extensive studies over the past decades but the details on the molecular level remain elusive [1]. While the internal structure of the casein micelles is a subject of debate, it has been widely accepted that the stability of the micelles is provided by an outer hairy layer of κ-caseins and the calcium

Fig. 65: a) Typical SAXS intensities of a casein micelle suspension of volume fraction ≈ 0.01. Continuous line represents global fit corresponding to a globular core–shell morphology and an internal structure consisting of colloidal calcium phosphate (CCP) particles reticulated in a protein matrix. The dotted lines indicate the individual globular and internal structural levels. The inset shows the size distribution of the globular micelles. b) Best fit electron density profile of core-shell structure. c) Schematic representation of a casein micelle with core-shell morphology and internal structure with decorated CCP.

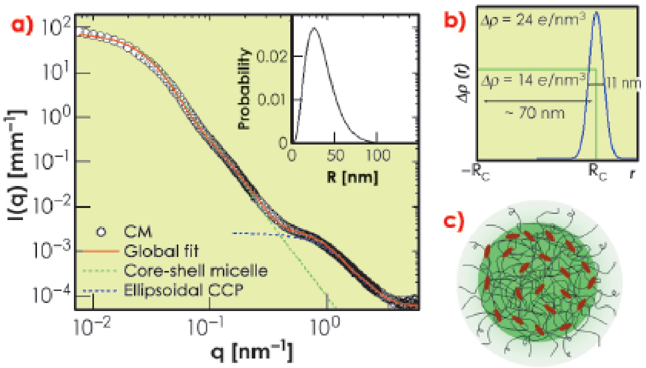

phosphate is contained in the form of colloidal nanoparticles in the core of micelles [1].

In this work, we have exploited the recent improvements in detection capability of SAXS [2] to elucidate the weak structural features of casein micelles otherwise submerged beneath the buffer scattering. Data collected over a wide scattering vector (q) range allowed us to reveal multiple structural levels. **Figure 65a** shows typical SAXS intensities from a casein micelle suspension after buffer subtraction. The data spanning three orders of magnitude in q can be modelled in terms of a polydisperse core-shell morphology with an internal structure consisting of ellipsoidal nanoparticles. The best fit electron density profile of the core-shell structure is shown in **Figure 65b** with a mean core radius (R_C) of about 35 nm, polydispersity of 0.49, and shell thickness of 11 nm. The average size of micelles varies depending on their origin but the overall scattering features remain similar. The outer diffuse shell is primarily attributed to the κ-casein layer stabilising the large micelles.

Fig. 66: Modification of the globular and internal structures of casein micelles (2.5 g/L) with the uptake of tannins (EGCG, 2.5 g/L). The lower inset shows the increase of molecular weight of micelles without a significant change in their average size. The upper inset depicts the rapid modification of the internal structure of the micellar core corresponding to the disintegration of the CCP and the development of a random-coil polymer-like organisation.

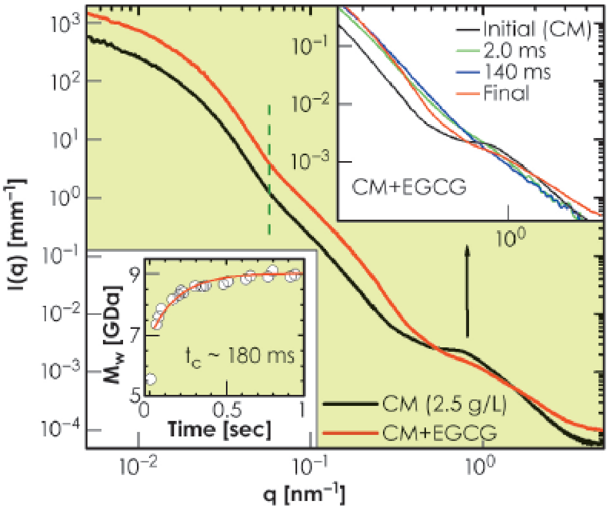

The excess electron density at the outer region of the protein core may be arising from the colloidal calcium phosphate (CCP). The best fit model for CCP corresponds to an ellipsoid scattering function with minor and major radii 2.5 nm and 0.71 nm, respectively. The resulting structure is schematically depicted in **Figure 65c**.

To validate this picture, we used small tannins (EGCG) which are polyphenols with a strong affinity towards proline residues on the caseins [3]. **Figure 66** presents the effect of EGCG on the structure of casein micelles. With the uptake of tannins, the micelles became denser with nearly the same average size as indicated by the vertical dashed line. However, the internal structure was completely modified to a random coil polymer-like feature. To gain further insight, we followed the uptake process in a time-resolved manner by rapid mixing of casein micelles and EGCG using a stopped-flow device. The lower inset in **Figure 66** shows the evolution of the molecular weight of the globular micelles with a time constant of about 0.18 seconds as EGCG molecules are incorporated. The upper inset of **Figure 66** shows the instantaneous modification of the internal structure within the mixing time of about 2 ms. The observed feature corresponds to rapid disintegration of CCP. This suggests that the CCP nanoparticles are localised near the outer region of the micellar core as indicated by the electron density profile in **Figure 65b**. The full uptake, which corresponds to about a million EGCG molecules per micelle, is reached when EGCG fills the core of the micelles, which then rearranges to the random coil polymer-like structure in a slower process of about 10 seconds.

In summary, the structure of casein micelles can be modelled using a polydisperse globular core-diffuse shell morphology and an internal structure consisting of a random protein matrix with decorated ellipsoidal calcium phosphate nanoparticles. The diffuse interface of the shell primarily due to κ-casein is described by a Gaussian electron density profile. The calcium phosphate nanoparticles are preferentially located in the outer region of the core, this could have made their scattering feature more pronounced despite their low mass content. Our results illustrate that small tannins could be used as a probe to elucidate the internal structure of casein micelles and other natively unfolded proteins. Furthermore, by probing the kinetics by SAXS one may infer nanoscale structural features which are otherwise elusive.

References

[1] D.S. Horne, *Curr. Opin. Colloid Interface Sci.* **11**, 148 (2006).

[2] T. Narayanan, *Curr. Opin. Colloid Interface Sci.* **14**, 409 (2009).

[3] D. Zanchi, T. Narayanan, D. Hagenmuller, A. Baron, S. Guyot, B. Cabane and S. Bouhallab, *Europhys. Lett.*, **82**, 58001 (2008).

Tracking global conformational changes in a membrane protein by time-resolved wide-angle X-ray scattering

Principal publication and authors

M. Andersson (a), E. Malmerberg (b), S. Westenhoff (b), G. Katona (b), M. Cammarata (c), A. B. Wöhri (a), L. C. Johansson (b), F. Ewald (c), M. Eklund (d), M. Wulff (c), J. Davidsson (d) and R. Neutze (b), *Structure* **17**, 1265-1275 (2009).

(a) Department of Chemical and Biological Engineering, Chalmers University of Technology, Göteborg (Sweden)

(b) Department of Chemistry, Biochemistry and Biophysics, University of Gothenburg, Göteborg (Sweden)

(c) ESRF

(d) Department of Photochemistry and Molecular Science, Uppsala University (Sweden)

Bacteriorhodopsin and proteorhodopsin are the simplest known light-driven proton pumps. Following the absorption of a photon by a buried retinal molecule bound *via* a protonated Schiff base to a conserved lysine residue of helix G, a sequence of conformational changes occur within these integral membrane proteins that drive proton pumping. Bacteriorhodopsin has been intensely studied for almost four decades using numerous biophysical techniques. On the other hand, proteorhodopsin, a homologue found in ocean bacteria, was discovered only a decade ago, but it is now recognised that this bacteriorhodopsin homologue provides a major primary energy input into the ocean's biosphere.

Several X-ray diffraction studies of the resting state and trapped intermediate states of bacteriorhodopsin have been reported [1]. Although many details concerning the movements of amino acid residues and water molecules were revealed in these earlier intermediate trapping studies performed at low-temperature, these results were somewhat controversial since the nature and magnitude of the observed α-helix movements did not always agree. Time-resolved wide-angle X-ray scattering (WAXS) is a method that has potential to resolve the nature and amplitudes of large-scale structural rearrangements occurring in proteins at room temperature, and to characterise the timescales over which these movements occur. Although the method was originally developed at beamline ID09 for time-resolved studies of structural changes occurring in small-molecules in solution [2], this approach was recently extended to study protein conformational dynamics using hemoglobin in complex with carbon-monoxide as a proof-of-principle [3].

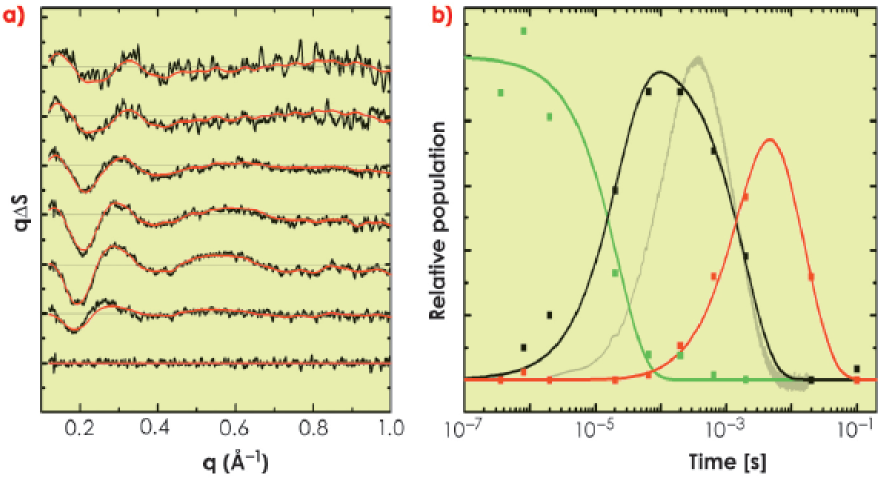

Fig. 67: a) Time-resolved WAXS difference data recorded from bacteriorhodopsin following photo-activation, and b) its decomposition into three components (early, green; intermediate, black; late, red). Solid red lines in the left panel show how this spectral decomposition accurately represents the experimental data (black lines). The transition from the early (green) to the intermediate (black) conformational state precedes the primary proton transfer in the bacteriorhodopsin photocycle (grey line, right panel).

Fig. 68: Large-scale α-helical movements occurring during the photo-cycle of bacteriorhodopsin as observed by time-resolved WAXS. The resting conformation (green), an intermediate conformational state (black) and a late conformational state (red) are represented. Significant outwards movement of the cytoplasmic portions of helices E and F, and an inwards movement of helix C towards the Schiff base, occur already within 22 µs of photo-activation and increase in amplitude later in the photocycle.

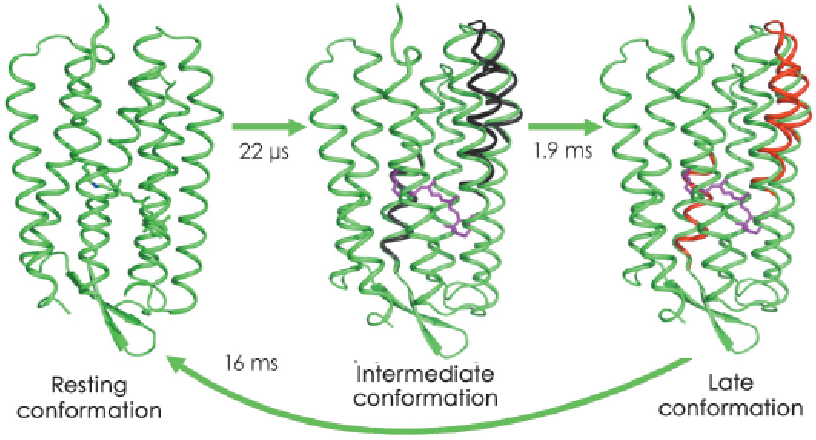

References
[1] R. Neutze, E. Pebay-Peyroula, K. Edman, A. Royant, J.Navarro and E.M. Landau, *Biochim. Biophys. Acta* **1565**, 144-167 (2002).
[2] R. Neutze, R. Wouts, S. Techert, J. Davidsson, M. Kocsis, A. Kirrander, F. Schotte and M. Wulff, *Phys. Rev. Lett.* **87**, 195508 (2001).
[3] M. Cammarata, M. Levantino, F. Schotte, P. A. Anfinrud, F. Ewald, J. Choi, A. Cupane, M. Wulff and H. Ihee, *Nature Methods* **5**, 881-886 (2008).

In a collaborative study involving groups in Gothenburg, Uppsala and the ESRF, we applied time-resolved WAXS to probe the structural dynamics of the light-driven proton pumps of bacteriorhodopsin and proteorhodopsin. As shown in **Figure 67**, difference WAXS data recorded from bacteriorhodopsin could be decomposed into three components, and permits elucidation of the timescales upon which these components rise and fall. Moreover, structural refinement against the difference WAXS data revealed that significant movements of the cytoplasmic halves of α-helices E and F, and of the extracellular half of helix C, occur prior to the primary proton transfer event from the retinal Schiff base to Asp85. The amplitudes of these movements were observed to increase a further 50% during the latter half of the photocycle after the Schiff base was deprotonated (**Figure 68**). This overall picture provides a significantly simpler description of the structural changes that occur during proton pumping by bacteriorhodopsin than emerged from intermediate trapping studies. Moreover, very similar structural conclusions were drawn from time-resolved WAXS data recorded from proteorhodopsin, revealing shared dynamical principles for proton pumping. Finally, by successfully resolving the nature and time-scales of α-helical movements that occur in a well characterised membrane protein like bacteriorhodopsin, this work opens the door to future studies of the structural dynamics of more complex integral membrane proteins.

Principal publication and authors
E. Lima (a, b), L. Wiegart (a, b), P. Pernot (a), M. Howells (a, c), J. Timmins (a), F. Zontone (a), and A. Madsen (a), *Phys. Rev. Lett.* **103**, 198102 (2009).
(a) ESRF
(b) NSLS-II, Brookhaven National Laboratory (USA)
(c) LBNL, Berkeley (USA)

Biological imaging by coherent hard X-ray diffraction microscopy

Imaging of biological material in three dimensions, such as an entire cell, deepens our insight into cellular biology. The highest possible resolution of the images is required as well as an experimental environment preserving the samples in their natural (hydrated) state without introducing structural artefacts, such as staining or sectioning, and radiation damage. Meeting these requirements is obviously a formidable task.

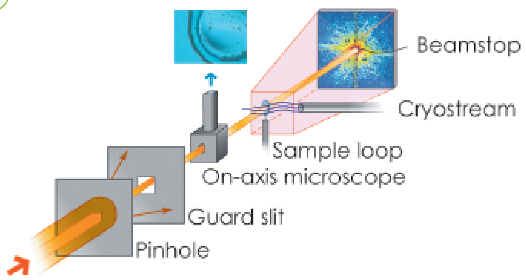

Fig. 69: Sketch of the experimental setup for bio-XDM at **ID10C**.

X-ray diffraction microscopy (XDM also known as CXDI, coherent X-ray diffraction imaging) is an image reconstruction method where the coherent X-ray diffraction pattern of a sample is inverted to yield the real space structure [1]. This technique has potential to reach the goal of 3D biological imaging. **Figure 69** shows the

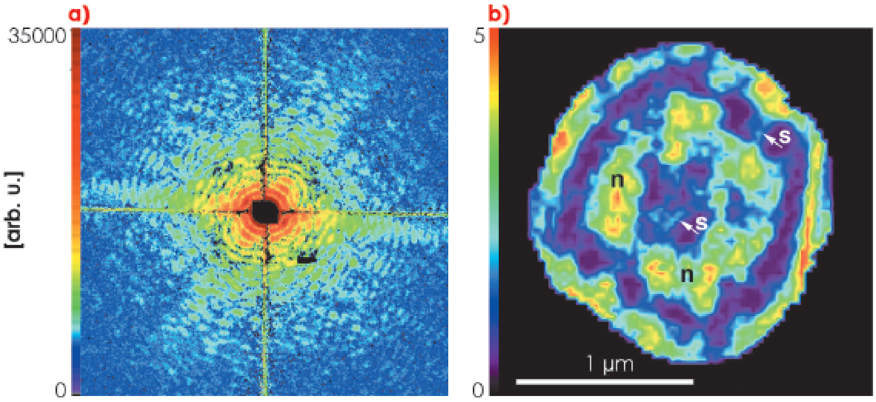

Fig. 70: a) Coherent diffraction pattern (speckle) of a hydrated *D. radiodurans* bacterial cell. b) The reconstructed image where sub-cellular nucleoid structures are clearly visible.

basic XDM experimental setup we employed in this study. The image reconstruction, ρ(**r**), is performed by recovering the phase of the diffracted intensity pattern, I(**Q**), through a phase retrieval algorithm [2]. Thanks to the high penetration power of X-rays, a cell can be imaged as a whole, without sectioning. Unlike most other imaging techniques the ultimate resolution is not determined by a lens (therefore XDM is often denoted as lensless imaging), but rather by the largest momentum transfer Q to which I(**Q**) can be precisely measured. For biological samples, radiation damage thresholds set the resolution limits. Nevertheless, soft X-ray experiments on dry unstained yeast cells have proven the feasibility of the method [3]. Hard X-rays are preferred in XDM since the convergence of the phasing algorithm, especially for three-dimensional reconstructions, is improved within the Born-approximation. However, it was unknown until recently whether the signal-to-noise ratio of scattered hard X-rays from unstained biological material in a hydrated state was sufficient for XDM.

Figure 70 shows the far-field diffraction patterns of unstained frozen-hydrated *Deinococcus radiodurans* bacteria measured at beamline **ID10C** (Troika) using 8 keV X-rays. Samples were rapidly plunge-frozen in the hydrated state to avoid structural artefacts from dehydration and to prevent radiation damage. Mounted on the diffractometer, ice contamination was avoided or reduced to a minimum by keeping the samples in a cold nitrogen gas environment provided by a cryogenic gas stream. Neither staining, nor sectioning was applied to the few-micrometre-thick bacterial cells. Thus the contrast of the diffraction pattern arises only from the cellular material. The spatial frequencies at the edge of the diffraction pattern correspond to a half-period of 25 nm resolution in real space. By filtering and phasing the diffraction pattern, it could be inverted as shown in **Figure 70**. Since this image is just one 2d projection of the three-dimensional cell structure, its interpretation may be difficult. Hence, an extension to 3d cryogenic bio-XDM is desirable, and this is now in progress.

References
[1] J. Miao, P. Charalambous, J. Kirz and D. Sayre, *Nature* **400**, 342 (1999).
[2] J.R. Fienup, *Appl. Opt.* **21**, 2758 (1982).
[3] D. Shapiro *et al.*, *PNAS* **102**, 15343 (2005).

Finding order in disorder by X-ray speckle cross-correlation

Disordered matter, such as glasses and liquids, does not exhibit translational symmetry. A particular system is able to accommodate sequentially different local symmetries, among them the icosahedral local order, which belongs to the forbidden motifs in periodic structures. This mysterious and so far experimentally inaccessible localised order within disorder has been fascinating scientists for many decades [1,2], as it is held responsible for the undercooling of liquids and the existence of the glass state. Yet it has been frustratingly difficult to characterise localised order quantitatively, since the commonly used tools such as X-ray and neutron scattering, which are capable of probing structure at atomic dimensions

Principal publication and authors

P. Wochner (a), C. Gutt (b), T. Autenrieth (b), T. Demmer (a), V.N. Bugaev (a), A. Díaz Ortiz (a), A. Duri (b), F. Zontone (c), G. Grübel (b) and H. Dosch (a,b), *Proc. Natl. Acad. Sci.* **106**, 11511-11514 (2009).
(a) Max-Planck-Institut für Metallforschung, Stuttgart (Germany)
(b) DESY, Hamburg (Germany)
(c) ESRF

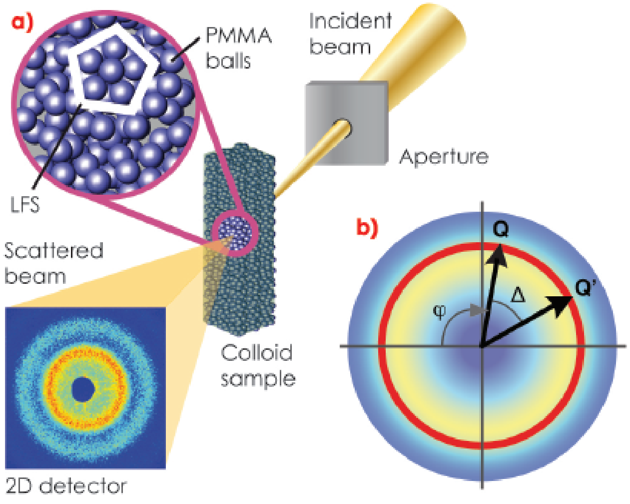

Fig. 71: Sketch of the experimental setup where a speckle diffraction pattern is generated in the far field when coherent X-rays illuminate a disordered sample. a) illustrates the local isosahedral symmetry and b) outlines the XCCA analysis method.

in bulk materials, yield only orientationally-averaged information embodied in the so-called "radial pair distribution function", which simply tells you the average number of particles at a certain distance from a given particle. Without a periodic crystal lattice, the elegant methods of conventional crystallography cannot be applied. This limitation can be overcome if coherent light is scattered, like in a snapshot, from the instantaneous positions of all the atoms in the disordered sample. In this case, a speckle pattern is generated in the far field due to the interference of radiation coming from the entire scattering volume and the (not completely) random phase shifts by the particles. A speckle pattern represents a unique fingerprint via Fourier transform of the individual sample, rather than the usual ensemble average provided by scattering with partially coherent radiation. An example of such a speckle pattern is shown in **Figure 71** together with a sketch of the experiment. In this study, highly concentrated glassy suspensions of sterically stabilised PMMA particles were investigated by coherent X-ray scattering at beamline **ID10A**. The envelope of the fluctuating speckle intensities is in fact the ensemble-averaged S(Q) scattering function that is normally measured from a glass or liquid as shown in **Figure 72a**. S(Q) depends only on pair-correlations and for amorphous samples does not depend on bond angles. To extract information on the local ordering hidden in the speckle pattern, the instantaneous scattered intensity was analysed for angular correlations by calculating a newly developed 4-point correlation function

$$\mathbf{C}_Q(\Delta) = (\langle I(Q,\varphi)\ I(Q,\varphi+\Delta)\rangle_\varphi - \langle I(Q,\varphi)\rangle^2{}_\varphi) \ / \ \langle I(Q,\varphi)\rangle^2{}_\varphi$$

where Δ is the azimuthal angle difference between two points in the speckle pattern (see **Figure 71b**). The averaging indicated by the brackets is taken over the entire ring $\varphi \in [0;2\pi]$ with $|\mathbf{Q}|=Q$. Most fascinating is that $C_Q(\Delta)$ in **Figure 72b** clearly reveals a very pronounced anisotropy with 5-fold symmetry specifically for the intensity ring associated with $Q = 0.04\ \mathrm{nm}^{-1}$, which points to a so far hidden local symmetry in the colloidal system. The different Q-dependent symmetries are a signature of the specific local order. The colloidal glasses investigated here are slowly evolving; hence the analysis could be performed over time intervals much shorter than the typical speckle decay time (~200 s) to yield the temporal evolution of the local ordering. It is found that the bond-orientational order symmetries slowly relax as a function of time and switch *e.g.* from 5-fold to 6-fold at a given Q value. The emerging picture is that clusters of icosahedral order reorganise themselves and are formed either in

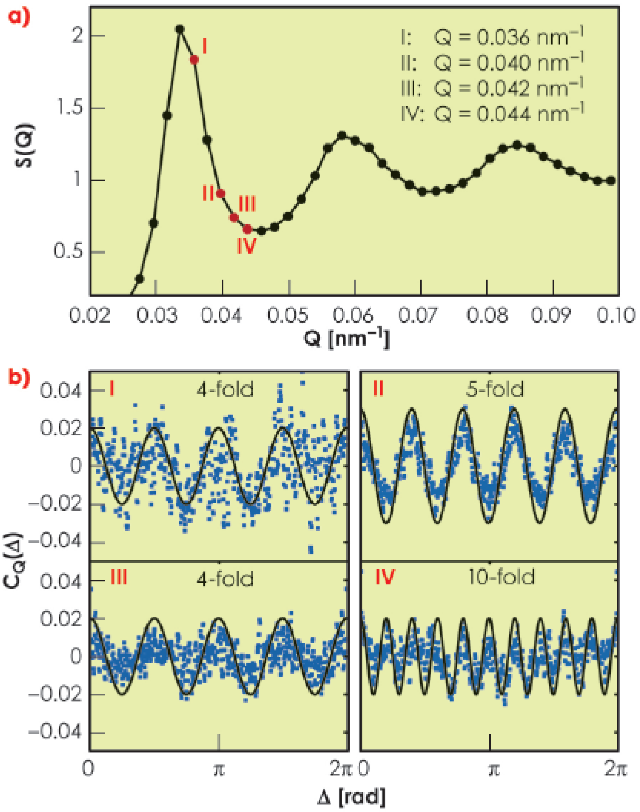

Fig. 72: a) Angular-averaged structure factor, which is the standard radial intensity distribution. b) Experimental result after applying the cross-correlator $C_Q(\Delta)$ to the data at different Q values indicated in (a). Solid lines are a guide to the eye.

nano-crystalline environments or out of complete disorder, all of which involves the breaking and formation of bonds. This bears similarities to the behaviour observed in simulations of supercooled molecular liquid glass-formers and underlines the importance of local rearrangements in the understanding of the dynamical properties of this important class of non-periodic materials. Clearly, there is a wealth of new information about the kinetics and the origin of the glass transition to be mined from such experiments, by *e.g.* applying correlators testing for medium range order. The availability of short-pulse XFEL radiation in the 0.1-nm regime and with sub 100-fs pulse length will open up the fascinating option to analyse the local structure of liquids (in particular water) by applying the new concept of X-ray cross correlation analysis (XCCA) to single laser shot speckle diffraction patterns.

In summary, we have demonstrated that local symmetries in disordered materials can be unravelled by the application of a novel angular cross-correlation technique to coherent X-ray scattering intensities. We uncovered the hidden local symmetries within the glassy disorder of suspensions of sterically stabilised PMMA particles. Four, 6, 10 and most prevalently 5-fold symmetries were observed pointing towards locally favoured structures (LFS) of icosahedral symmetry.

References

[1] F.C. Frank, *Proc. Roy. Soc. Lond. A* **215**, 43-46 (1952).
[2] P.J. Steinhardt, D.R. Nelson and M. Ronchetti, *Phys. Rev. B* **28**, 784-805 (1983).

Surface structure of sterically-stabilised ferrofluids

Principal publication and authors

A. Vorobiev (a), G. Gordeev (b), O. Konovalov (a), and D. Orlova (b), *Phys. Rev. E* **79**, 031403 (2009).
(a) ESRF
(b) Petersburg Nuclear Physics Institute (Russia)

In ferrofluids [1] magnetic nanoparticles are conventionally stabilised by a single or double layer of surface-active molecules (surfactants) [2]. Steric repulsion between surfactant shells assisted by Brownian motion prevents particle coagulation due to attractive dipole-dipole interaction. If no external magnetic field is applied, the particles are randomly distributed and the ferrofluid behaves like a superparamagnetic gas. But even relatively small fields break the force balance, which leads to pronounced spatial correlations between the particles observed in the bulk ferrofluid in the form of ordered chains, columns, and pseudocrystalline structures. These findings give ferrofluids a bright perspective for applications in nanotechnology.

Field-induced ferrofluid ordering at the interface with another material looks particularly interesting because it can be applied to the production of nano-structured magnetic surfaces or multilayers. Employing a ferrofluid-solid interface is one of the most straightforward ways to realise this idea, however, in this case the ordered part of ferrofluids adjacent to the interface [3] is hidden behind a substrate and its practical exploitation requires some non-trivial technological tricks.

The present study focuses on an easily accessible interface of ferrofluids with gas, *i.e.* a "free" ferrofluid surface. Besides its promising practical applications, it has a general scientific interest. In particular, studying field-induced particle ordering in this system brings us new information about famous Rosensweig instability (RI) observed as a system of standing waves appearing on the ferrofluids surface as soon as a critical value of magnetic field H_c is surpassed [1].

Magnetite nano-particles were fabricated by chemical deposition and dispersed either in water or in oil (tetradecane). Mean size of the particles was about 100 Å with 30% dispersion. A double layer of sodium oleate and a single layer of oleic acid were used to stabilise the particles in water-based and oil-based samples respectively. X-ray reflectivity (XR) and grazing incidence diffraction (GID) measurements were performed at beamline **ID10B**, which is especially designed for the scattering on liquid surfaces.

Simultaneous treatment of the XR and GID experimental data allows a

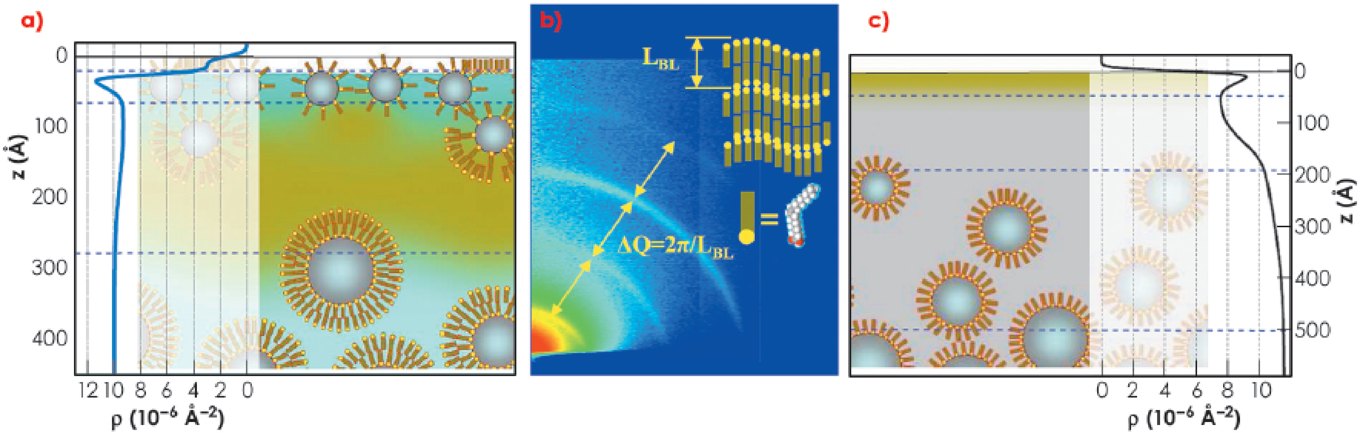

Fig. 73: Ferrofluid surface structure. a) Water ferrofluid, dark clouds schematically show agglomeration of sodium oleate molecules. Horizontal lines separate main structural sub-layers. Experimentally determined scattering length density (SLD) in-depth distribution is superimposed on the left side of the sketch and scaled appropriately. b) Small-angle GID pattern from the water ferrofluid revealing surface organisation of the oleic acid in to multilamellar structures. c) Sketch of the oil ferrofluid with corresponding SLD profile.

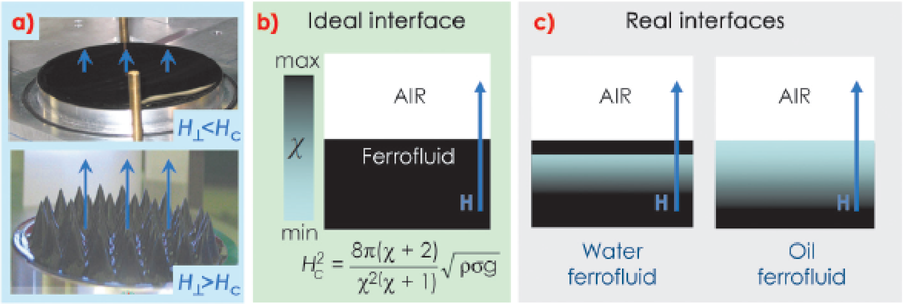

Fig. 74: a) Photos of free ferrofluid surface in sub-critical (top) and super-critical (bottom) magnetic field. b) Colour-coded distribution of magnetic susceptibility χ across the air-ferrofluid interface in the ideal case and corresponding conventional expression for the critical field value, where ρ is ferrofluid mass density, σ is ferrofluid surface tension and g, the gravity constant.
(c) Real χ-distributions corresponding to **Figure 73**.

considerably detailed reconstruction of the gas-ferrofluid interfaces. The interfacial structure differs drastically from the homogeneous state and depends on the liquid carrier and type of surfactant. Schematic arrangement of the ferrofluid surface layer for water and oil samples are shown in **Figure 73**. The surface layer of water-based ferrofluid has complicated structures (**Figure 73a**) provided by the excess of free surfactant. It is partially organised into multilamellar sheets, which can be deduced from the characteristic diffraction patterns (**Figure 73b**). This seems to be unavoidable in the case of polydisperse nano-particles stabilised with a double layer of amphiphilic molecules. In oil-based ferrofluid (**Figure 73c**), the main feature is the gradient of the particles concentration C ranging from $C = 0$ at depth $z = 50\text{-}100$ Å (pure oil) to the nominal $C = 13\%$ at $z = 500$ Å. The topmost layer is the Gibbs layer of oleic acid on tetradecane. These structures self-replicate several times after their gentle removal from the sample surface and qualitatively do not depend on the particle concentration. For this reason, such a top "coating" can appear as an intrinsic feature of sterically-stabilised ferrofluids. It must govern to a greater extent the value of the surface tension and local magnetic susceptibility and, therefore, determine such RI parameters as the critical field H_c and the period of the standing wave (**Figure 74**). The extent of the particle depletion in the ferrofluids surface layer should also define the rate of the RI undulation growth with increasing field. Indeed, we have observed microscopic evolution of the surface topology already at $H = 0.5\ H_c$, *i.e.* in fields much smaller than predicted by the RI theory for an ideal sharp interface.

References
[1] R.E. Rosensweig, *Ferrohydrodynamics*, Cambridge (1985).
[2] L. Shen *et al.*, *Langmuir* **15**, 447-453 (1999).
[3] A. Vorobiev *et al.*, *Phys. Rev. Lett.* **93**, 267203 (2004).

Organic heterostructure growth and the role of the buried interface

The last decade has witnessed an increased emphasis on the development of devices based on organic semiconducting materials, whose attractiveness stems from their potential low production cost and the wide range of novel physical and chemical properties they offer. A key aspect for the device performance is the optimisation of the structure and morphology of the active layers, in particular in proximity to the various interfaces which play pivotal roles for the device functionality. Focusing on organic-organic heterostructures and interfaces, we report how the morphology of diindenoperylene (DIP, p-type semiconductor) films deposited on top of fluorinated cobalt-phthalocyanines ($F_{16}CoPc$, n-type semiconductor) can easily be controlled by the growth temperature, ranging from smooth, layered heterostructures, to the formation of highly crystalline DIP islands.

In a first step, the $F_{16}CoPc$ films on SiO_2 were characterised by X-ray reflectivity (XRR) and grazing incidence X-ray diffraction (GIXD). Subsequently, the heterostructure growth was performed by stepwise deposition of DIP onto previously grown $F_{16}CoPc$ films and characterised *in situ* after each growth step. **Figure 75** shows the XRR and GIXD data associated with a heterostructure grown at 120°C. By fitting the XRR data we access the electron density profiles of the sample, revealing, among other things, the evolution of the topmost film surface and of the organic-organic interface morphologies during heterostructure growth. The heterostructure follows a Stranski-Krastanov type of growth (*i.e.* wetting layer followed by island growth). Most interestingly, this growth behaviour is concomitant with a reconstruction of the two to three $F_{16}CoPc$ buried layers closest to the interface, as observed from the GIXD data in **Figure 75b**. The coincidence between the amount of reconstructed $F_{16}CoPc$ and the percentage of surface area covered by DIP gives insight into the reconstruction process itself, which takes place in those areas covered by the DIP wetting layer (**Figure 75c**). The final heterostructure

Principal publication and authors

D.G. de Oteyza (a),
E. Barrena (b,c), Y. Zhang (b),
T.N. Krauss (b), A. Turak (b),
A. Vorobiev (d) and
H. Dosch (b,c), *J. Phys. Chem. C* **113**, 4234-4239 (2009).
(a) Donostia International Physics Center, San Sebastián (Spain)
(b) Max-Planck-Institut für Metallforschung, Stuttgart (Germany)
(c) ITAP, Universität Stuttgart (Germany)
(d) ESRF

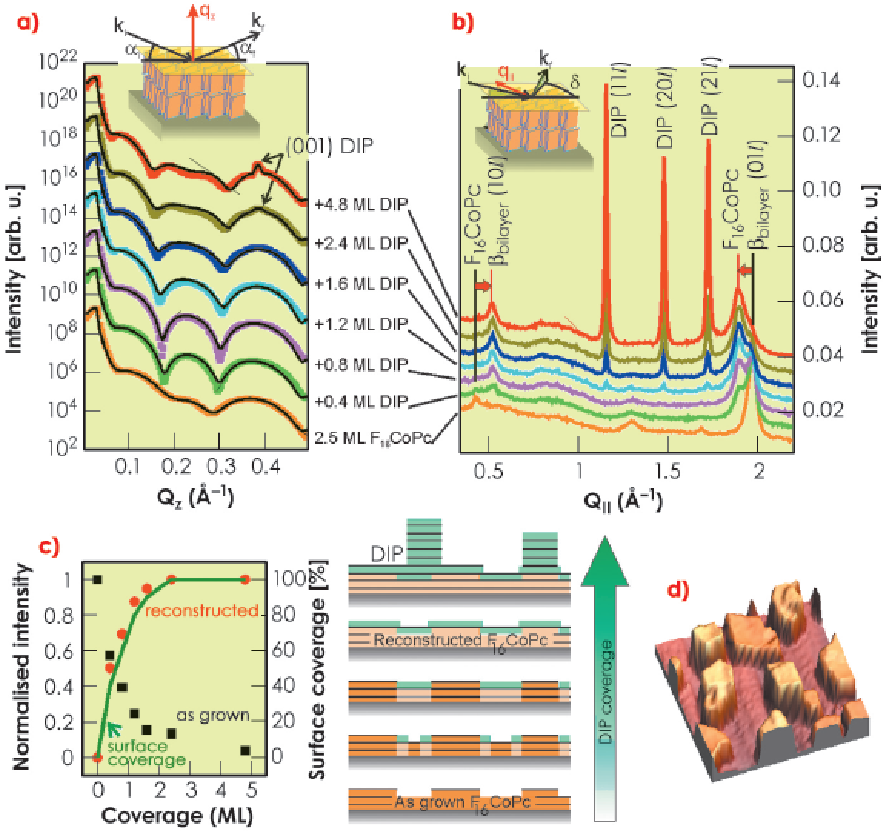

Fig. 75: a) XRR data (symbols) and fits (solid lines) measured *in situ* at different steps of the heterostructure growth at 120°C.
b) Corresponding GIXD data, highlighting the shift of the $F_{16}CoPc$ reflections. The insets in (a) and (b) represent the diffraction geometries. c) Normalised intensity vs. DIP coverage of the "as grown" (black squares) and reconstructed (red circles) $F_{16}CoPc$ (01) $\beta_{bilayer}$ Bragg peak. The green line represents the evolution of the percentage of surface covered by DIP as obtained from the electronic density profiles fitted to the reflectivity data in (a). The schemes at the right depict the suggested growth scenario. d) AFM topography image (2x2 μm^2) of a 6 ML DIP / 3 ML $F_{16}CoPc$ heterostructure grown at 120°C.

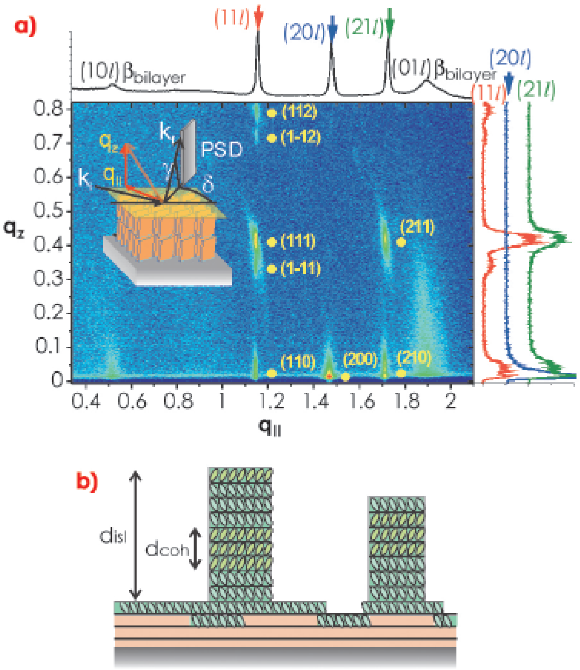

Fig. 76: a) Two-dimensional GIXD data corresponding to 4.8 ML DIP on 2.5 ML F_{16}CoPc grown at 120°C. The upper spectrum corresponds to the integrated intensity along q_z, while the right hand side profiles correspond to the intensity along the DIP rods. The positions for the observed DIP Bragg reflections as calculated from the optimised unit cell parameters are overlaid on the graph (shifted by 0.7 Å^{-1}). The measurement geometry is schematically depicted in the inset. b) Schematic representation of the heterostructure, evidencing the presence of multiple coherently ordered crystalline domains within each of the islands.

features a reconstructed underlayer in proximity to the interface, a DIP wetting layer and highly crystalline DIP islands whose size and density can be tuned by coverage and growth temperature (**Figure 75d**). However, this is a thermally activated process, and for growth temperatures below 70°C, smooth heterostructures form and no F_{16}CoPc reconstruction takes place at the organic-organic interface. The similarities observed with the growth of DIP on F_{16}CuPc highlight the generality of this novel growth scenario to different fluorinated phthalocyanines **[1,2]**.

The use of a position sensitive detector (PSD) provided access to a larger portion of the reciprocal space, thereby allowing us to determine for the first time, not only the thin film structure of F_{16}CoPc, but also the three-dimensional crystallographic structure of the DIP films/islands and their polycrystalline nature (**Figure 76**).

In summary, we have shown a controllable route to finely tune the morphology of organic p-n heterostructures, and have given evidence for its intimate relationship with the structure at the organic-organic interface. This study provides new insight into the mechanisms of organic heterojunction formation and their kinetics, thereby increasing the current understanding on the growth of organic materials for optoelectronic applications.

References
[1] E. Barrena, D.G. de Oteyza, S. Sellner, H. Dosch, J.O. Osso and B. Struth, *Phys. Rev. Lett.* **97**, 076102-1-4 (2006).
[2] D.G. de Oteyza, T.N. Krauss, E. Barrena, S. Sellner, H. Dosch and J.O. Osso, *Appl. Phys. Lett.* **90**, 243104-1-3 (2007).

Crystal structure of A-amylose by synchrotron microdiffraction

Principal publication and authors
D. Popov (a), A. Buléon (b), M. Burghammer (a), H. Chanzy (c), N. Montesanti (c), J-L. Putaux (c), G. Potocki-Véronèse (d) and C. Riekel (a), *Macromolecules* **42**, 1167-1174 (2009).
(a) ESRF
(b) INRA, Nantes (France)
(c) Centre de Recherches sur les Macromolécules Végétales (CERMAV-CNRS), Grenoble (France)
(d) Laboratoire d'Ingénierie des Systèmes Biologiques et des Procédés (LISBP), INSACNRS, Toulouse (France)

The molecular and crystal structure determination of low molecular weight compounds is carried out with great precision on a routine basis. However, for polymer crystals, resolution of the structure is still a major challenge since it requires a number of intuitive guesses together with trial-and-error methods **[1]**. Indeed, many small molecules are susceptible to crystallisation as millimetre or sub-millimetre-sized crystals, yielding extensive diffraction data sets, with frequently more than 10 to 20 observed reflections per independent atom, the minimum ratio that is required for a proper structure refinement. This is not the case for most polymers for which only crystals with dimensions ranging from sub-micrometre to the micrometre range can be obtained. These crystals are far too small to yield substantial X-ray datasets when conventional X-ray diffractometers are used. In most cases, one relies on the study of crystalline fibres by X-ray diffraction and single-crystals by electron diffraction techniques. Both of the methods have severe challenges when compared with single-crystal

X-ray diffraction: unambiguous deconvolution of fibre diffraction diagrams into three dimensional data; and the difficult exploitation of the electron diffraction intensities for crystal structure determination since one needs to subtract dynamic contributions from electron diffraction intensities before any further analysis.

The recent development of microfocus beamlines at third generation synchrotron radiation sources, such as the ESRF [2], has greatly improved the situation as novel X-ray optical systems allow the production of focal spots with diameters in the micrometre and sub-micrometre sizes. In addition, goniometers for keeping a single crystal in the centre of micrometre-sized beams have also been developed. Thus, when applied to very small crystalline objects such as a polymer single crystal, one can envisage recording X-ray datasets that are more complete than those recorded in electron diffraction experiments, and therefore susceptible to yield improved structural models. Here we show how a full three-dimensional dataset was collected on microcrystals of A-amylose (Figure 77) and used to refine the structure of this amylose allomorph. To our knowledge, this is the first polymer structure determined using this technique on such small polymer single crystals. Getting an accurate atomic description of the A-amylose crystal is important since these crystals constitute part of the cereal starches, a food product of capital importance.

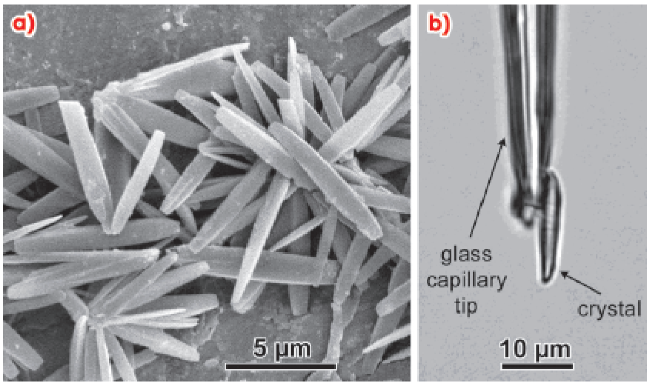

Fig. 77: a) SEM image of A-amylose crystals; b) One of the crystals used for data collection.

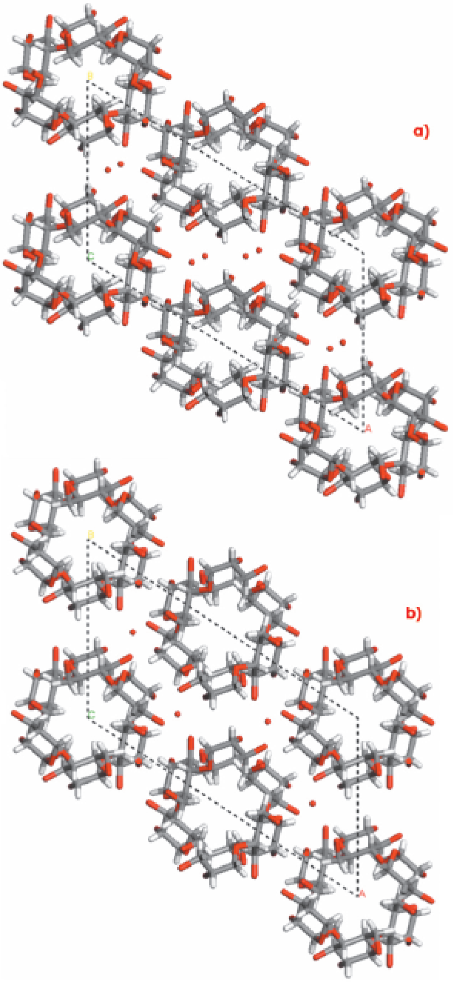

Fig. 78: Structures of A-amylose: a) present and b) past.

Experiments were performed at beamline ID13. The crystal structure was solved using a molecule replacement technique. The final refinement, which was done in the isotropic approach of thermal parameters, gave R1 and $R1_{free}$ values of 0.17 and 0.22 respectively.

In agreement with the earlier structure based on X-ray fibre powder and electron diffraction data, our A-amylose structure also consists of intertwined 6-fold left-handed parallel double helices, packed in a parallel fashion and tightly nested into one another. Furthermore, the existence of two water molecules per maltotriosyl unit was revealed without ambiguity in the crystal structure of A-amylose, whereas, from density consideration, only one was proposed in the earlier structure. This new feature brings substantial difference, not only for the system of hydrogen bonds, which has to account for new possibilities, but also for a distortion of the helices and of their internal cavity. This feature is well illustrated in Figure 78.

References
[1] T. Tadokoro, in *Structure of Crystalline Polymers*; John Wiley and Sons: New-York, p 6 (1979).
[2] C. Riekel, *J. Rep. Prog. Phys.* **63**, 233-262 (2000).

Electronic structure and magnetism

In the past few years there has been a large increase in interest in materials exhibiting more than one type of ferroic order *e.g.* ferromagnetism, ferroelectricity, etc. [1]. The field of multiferroics has become important for both a basic understanding of the interaction between, for example, magnetic and electric coupling and the potential use of such materials in devices. Indeed, one could imagine the switching of magnetic states using an electric field or vice versa. These applications give us magnetoelectronic devices [2].

Although there are many magnetic and ferroelectric materials, there are relatively few multiferroic materials, since the conditions for co-existence of several types of order are stringent (see Figure 79) [3]. Typical materials showing such properties are perovskite transition metal compounds including for example $TbMnO_3$, $HoMn_2O_5$, $LuFe_2O_4$, bismuth compounds like $BiFeO_3$, etc. [4,5]. There are two types of multiferroics; proper (or type I) where the electric and magnetic properties occur for different reasons, but are coupled together *e.g.* $BiFeO_3$; and improper (or type II) multiferroics where both orders are deeply coupled *e.g.* $TbMnO_3$. The latter are of fundamental interest but not of practical use today due to their low critical parameters and the former represent the main area for future applications. There is active research to understand both classes of multiferroics [6]. Consequently, it is not surprising that many of the Highlight articles this year represent investigations in the area of multiferroics and probe many different aspects of the problem.

In common with the studies of multiferroics there are also many other research efforts today to tailor the properties of materials. This is both to increase our understanding of matter and to open up new possibilities for engineering materials with new properties. Whether this be in the control of magnetic anisotropy in molecular magnets [see P. Gambardella *et al.*, p. 67], generating a metallic behaviour at the interface between two insulators [see M. Salluzzo *et al.*, p. 71] or in the magnetic properties of nanoparticles made of non-magnetic atoms [see article J. Bartolomé *et al.*, p. 68], the common theme is exploring and understanding new phenomena.

N.B. Brookes

References
[1] N.A. Spaldin and M. Fiebig "The Renaissance of Magnetoelectric Multiferroics", *Science* **309**, 391 (2005).
[2] M. Bibes and A. Barthélémy, *Nature Materials* **7**, 425 (2008).
[3] For example: D. Khomskii "Classifying multiferroics: Mechanisms and effects", *Physics* **2**, 20 (2009).
[4] T. Kimura *et al.*, "Magnetic control ferroelectric polarization", *Nature* **426**, 55 (2003).
[5] J. Wang *et al.*, "Epitaxial $BiFeO_3$ Multiferroic Thin Film Heterostructures", *Science* **299**, 1719 (2003).
[6] For example: special issue, *J. Phys. Condens. Matter* **20**, 434201-434220 (2008).

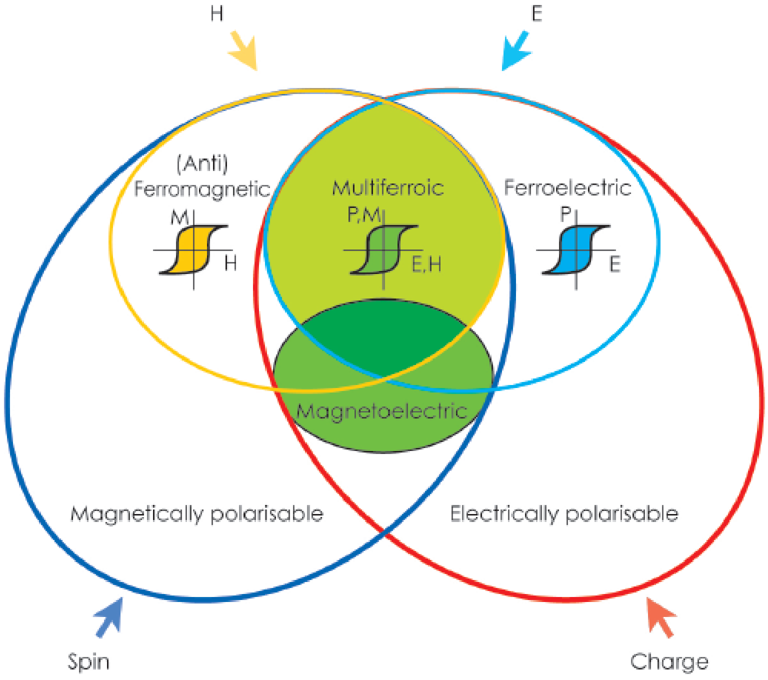

Fig. 79: Multiferroic materials combine magnetic and ferroelectrical properties.

Supramolecular control of the magnetic anisotropy in two-dimensional high-spin Fe arrays at a metal interface

The control of magnetic anisotropy is important for the development of metal-organic materials for magnetic applications, both at the single molecule and extended film level [1]. In so-called single molecule magnets, this is achieved by chemical modification of the environment and variations in the number of metal ions that carry the magnetic moment. For metal-organic layers in contact with a metal substrate or electrode, however, it was unclear whether such a strategy would be effective and whether these layers would display electronic and magnetic properties that are typical of molecules or metals. Experiments at beamline ID08 using a combination of scanning tunnelling microscopy (STM), X-ray magnetic circular dichroism (XMCD), and charge transfer multiplet calculations have provided a response to these questions.

Co-deposition of transition-metal ions and organic ligands on single-crystal surfaces offers the potential to design supramolecular metal-organic grids with programmable structural features, where the interaction with the substrate is used to stabilise a planar geometry [2]. This approach was favoured over the deposition of magnetic molecules synthesised in solution, since it allows a more direct comparison of the electronic configuration of the magnetic sites depending on the ligand and metallic environment. Figure 80 shows the supramolecular assembly of Fe and terephthalic acid (TPA) molecules on a Cu(100) surface. Each Fe atom is coordinated to four TPA molecules through Fe-carboxylate bonds, with supramolecular Fe(TPA)$_4$ units organised in a square lattice with 15x15 Å^2 periodicity. STM images indicate that, despite the 4-fold lateral coordination to the carboxylate ligands and the residual interaction with Cu, Fe centres are chemically active, forming an array of open coordination sites that may selectively bind other ligands, for example O$_2$ forming pyramidal-like O$_2$-Fe(TPA)$_4$ complexes.

Pristine and O$_2$-saturated Fe(TPA)$_4$ monolayers were prepared and characterised *in situ*, exploiting the UHV STM facility connected to the XMCD end-station. X-ray absorption spectra (XAS) were recorded at the $L_{2,3}$ edges of Fe and K-edge of O, in magnetic fields of up to 6 T with the sample held at 8 K. The results (Figure 81), interpreted with the aid of charge transfer multiplet calculations, show that the Fe *d*-orbitals interact mainly with the O ligands and are only weakly perturbed by the metallic substrate. Furthermore, both Fe(TPA)$_4$ and O$_2$-Fe(TPA)$_4$ constitute high-spin Fe^{2+} complexes, against the tendency of the Cu electrons to reduce the Fe moment via *4s-3d* hybridisation and Kondo screening.

Angle-dependent XMCD measurements revealed strong in-plane magnetic anisotropic of Fe(TPA)$_4$ complexes opposite to Fe/Cu(100) (Figure 81d) and that the easy axis direction can be controlled by the symmetry of the ligand bonds,

Principal publication and authors

P. Gambardella (a,b),
S. Stepanow (a,c), A. Dmitriev (c),
J. Honolka (c), F. de Groot (d),
M. Lingenfelder (c),
S.S. Gupta (e), D.D. Sarma (e),
P. Bencok (f), S. Stanescu (f),
S. Clair (g), S. Pons (g), N. Lin (c),
A.P. Seitsonen (h), H. Brune (c),
J.V. Barth (i) and K. Kern (c,g),
Nat. Mater. **8**, 189 (2009).
(a) Centre d'Investigacions en Nanociència i Nanotecnologia (ICN-CSIC), UAB Campus, Barcelona (Spain)
(b) Institució Catalana de Recerca i Estudis Avançats (ICREA), Barcelona (Spain)
(c) Max-Planck-Institut für Festkörperforschung, Stuttgart (Germany)
(d) Department of Chemistry, Utrecht University (The Netherlands)
(e) Solid State and Structural Chemistry Units, Indian Institute of Science, Bangalore (India)
(f) ESRF
(g) Institut de Physique de la Matière Condensée, Ecole Polytechnique Fédérale de Lausanne (EPFL), Lausanne (Switzerland)
(h) Institut de Minéralogie et de Physique des Milieux Condensé, Université Pierre et Marie Curie, Paris (France)
(i) Physik-Department E20, Technische Universität München, Garching (Germany)

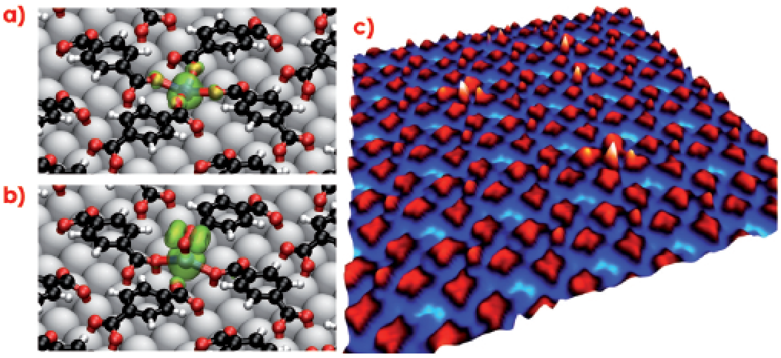

Fig. 80: Planar supramolecular layers of Fe-TPA complexes self-assembled on Cu(100). a) ball and stick model of Fe(TPA)$_4$ array as calculated by density functional theory. Blue dots indicate the position of Fe atoms, red O, black C, white H; the green halo represents the spin density. b) O$_2$-Fe(TPA)$_4$ array. c) STM image of a Fe(TPA)$_4$ monolayer grown on Cu(100). Selective uptake of O$_2$ by Fe sites is indicated by a change of STM contrast (white spots). Lateral image size is 84 x 84 Å^2.

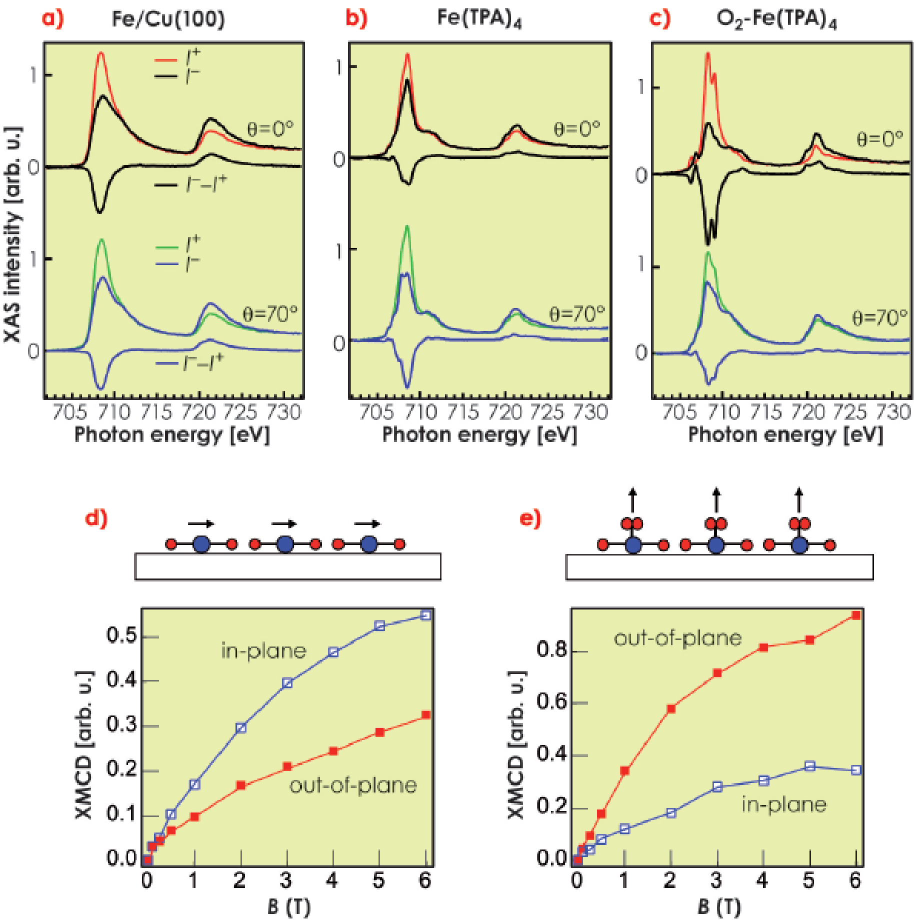

Fig. 81: Circularly polarised XAS of a) 0.025 monolayers Fe/Cu(100), b) Fe(TPA)$_4$, and c) O$_2$-Fe(TPA)$_4$ for parallel (I^+) and antiparallel (I^-) orientation of the photon helicity with field-induced magnetisation. Spectra were recorded in the electron-yield mode at normal (θ = 0°) and grazing incidence (θ = 70°), d) Field-dependent magnetisation of Fe(TPA)$_4$, and e) O$_2$-Fe(TPA)$_4$.

independently from the metal substrate. Apical O$_2$ ligands at Fe sites drive an abrupt spin reorientation transition, rotating the Fe easy axis out-of-plane and favouring the formation of an unusually strong orbital moment of about 0.55 ± 0.07 μ_B per Fe atom. With respect to bulk molecular crystals, the planar and open coordination structure of the self-assembled Fe array makes such a system extremely sensitive to chemisorption, providing straightforward control of the preferred Fe spin orientation.

In conclusion, we have demonstrated that it is possible to construct planar metal-organic networks and to control their magnetic properties at the interface with a metal substrate. This constitutes an essential step towards the inclusion of molecular materials into heterogeneous magnetoelectronic devices.

References

[1] L. Bogani and W. Wernsdorfer, *Nat. Mater.* **7**, 179 (2008).

[2] S. Stepanow, N. Lin and J.V. Barth, *J. Phys. Condens. Matter* **20**, 184002 (2008); M.A. Lingenfelder *et al.*, *Chem. Eur. J.* **10**, 1913 (2004).

Principal publication and authors

J. Bartolomé (a), F. Bartolomé (a), L.M. García (a), E. Roduner (b), Y. Akdogan (b), F. Wilhelm (c) and A. Rogalev (c), *Physical Review B* **77**, 184420 (2008).

(a) Instituto de Ciencia de Materiales de Aragón, and Dpto. Física de la Materia Condensada, CSIC-Universidad de Zaragoza (Spain)

(b) Institut für Physikalische Chemie, Universität Stuttgart (Germany)

(c) ESRF

Emerging magnetic moment in Pt$_{13}$ nanoparticles

A fascinating property of matter at the nanosize scale is the appearance of new physical phenomena which do not exist in the bulk. For example, bulk Pt has a very weak magnetic response, only present if a magnetic field is applied since it is a Pauli paramagnet. It is known that the presence of a magnetic material such as cobalt may induce a magnetic moment on Pt, this has been evidenced by X-ray magnetic circular dichroism (XMCD) of Pt covering a Co nanoparticle [1]. However, it has recently been found that small Pt$_{13}$ clusters may develop a magnetic moment when embedded in NaY zeolite [2]. A number of questions remained open after this exciting report, based on conventional magnetisation measurements: what is the contribution to the spontaneous moment coming from the orbital moment, and whether the observed magnetic moment could have arisen from a spurious source such as Fe contamination of the zeolite.

In this work we show without any ambiguity that Pt_{13} nanoparticles do indeed have a magnetic moment at low temperature, by means of XMCD at the Pt $L_{2,3}$ edges. The sample, which consisted of NaY zeolite charged with 6% by weight of Pt, was air sensitive, thus it was maintained at all stages enclosed in a Kapton sealed capsule, custom-made for this experiment. The experiment was performed at beamline **ID12**, at T = 7 K, and by varying the applied field. Since XMCD is an element selective technique, any contribution caused by other elements could be disregarded, and a non-zero signal may be assigned to the Pt itself. Previous EXAFS experiments have determined that the structure of the Pt_{13} clusters is compatible with an icosahedral shape, with a central Pt atom surrounded by 12 others (see **Figure 82**). The cluster has a very large surface to volume ratio, and fits closely to the zeolite cage. In fact, only one out of 25 cages in the zeolite is occupied by Pt_{13} clusters.

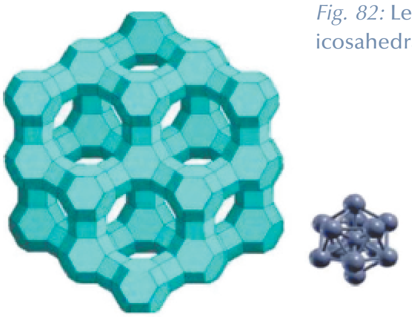

Fig. 82: Left: NaY zeolite. Right: Pt_{13} icosahedral cluster.

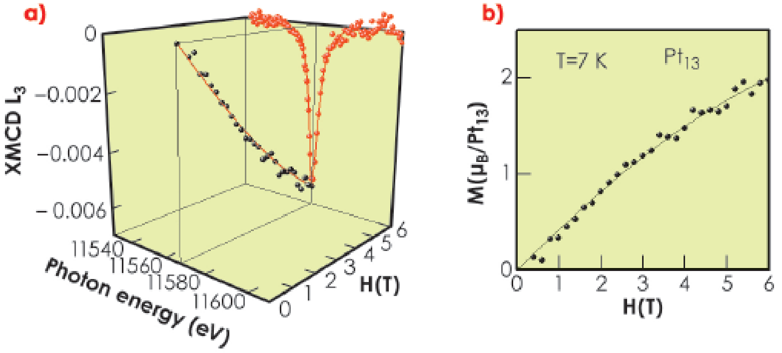

Fig. 83: a) Normalised isotropic Pt $L_{2,3}$-edge XMCD spectra of the Pt_{13} sample at H = 6 T (●), XMCD*(H)* curve (●). b) Magnetisation of a Pt_{13} cluster (●). Fit to a Langevin function with $\mu = 3.6\ \mu_B$, and magnetic fraction of Pt atoms f = 0.14 (–).

The XMCD spectra at the L_2 and L_3 edges were measured for T = 7 K and a maximum applied field of 6 Tesla (**Figure 83a**). The magnetic moment determined by the sum rule analysis is much larger than the Pauli paramagnetic contribution at that field, so it is proven that the nanoparticle supports a non-zero moment. In fact, the ratio of orbital to spin moment is as high as 0.32; *i.e.* more than 25% of the magnetic moment is of orbital origin. It can be attributed both to the high spin-orbit coupling of Pt and to surface effects such as Pt 5d quasiband narrowing, due to the breaking of symmetry of the Pt at the surface of a Pt_{13} cluster when compared to Pt in the bulk.

The XMCD at the energy of the L_3 peak was followed as a function of applied field (**Figure 83a**), and found to behave as a superparamagnetic particle with a moment of 3.7 Bohr Magneton (**Figure 83b**). Only about 15 to 20% of the Pt_{13} particles contribute to the XMCD signal. The zeolite may interact with the Pt_{13} particles, exchanging electrons and thus filling the available holes in the 5d band, thus rendering a good fraction of the particles non-magnetic.

To conclude, we have demonstrated that size effects on the electronic quasiband structure of a Pt_{13} cluster may induce a non-zero magnetic moment on Pt. Under the current assumption that the magnetic moment has its origin in unpaired electrons, the total spin of the particle is in the range S ≈ 2, with an orbital moment contribution of 25%. This is the first time that such a large orbital moment has been reported on a Pt_{13} particle.

References

[1] J. Bartolomé, L.M. García, F. Bartolomé, F. Luis, F. Petroff, C. Deranlot, F. Wilhelm and A. Rogalev, *J. Magn. & Magn. Mat.* **316**, e9-e12 (2007).
[2] X. Liu, M. Bauer, H. Bertagnolli, E. Roduner, J. van Slageren and F. Phillipp. *Phys. Rev. Lett.* **97**, 253401 (2006); X. Liu, M. Bauer, H. Bertagnolli, E. Roduner and J. van Slageren, F. Phillipp, *Phys. Rev. Lett.* 102, e049902 (2009).

X-ray detected optical activity

Principal publication and authors

A. Rogalev, J. Goulon, F. Wilhelm and A. Bosak, in *Magnetism and Synchrotron Radiation, Springer Proceedings in Physics* **133**, 169-190 (2010).

Since its discovery, optical activity in the visible light range has become one of the most powerful spectroscopic tools in physics, chemistry and biology and has fascinated many successive generations of scientists. Optical activity is a manifestation of *spatial dispersion*, *i.e.* the dependence of optical properties of matter on the wavevector of light. Being a first order

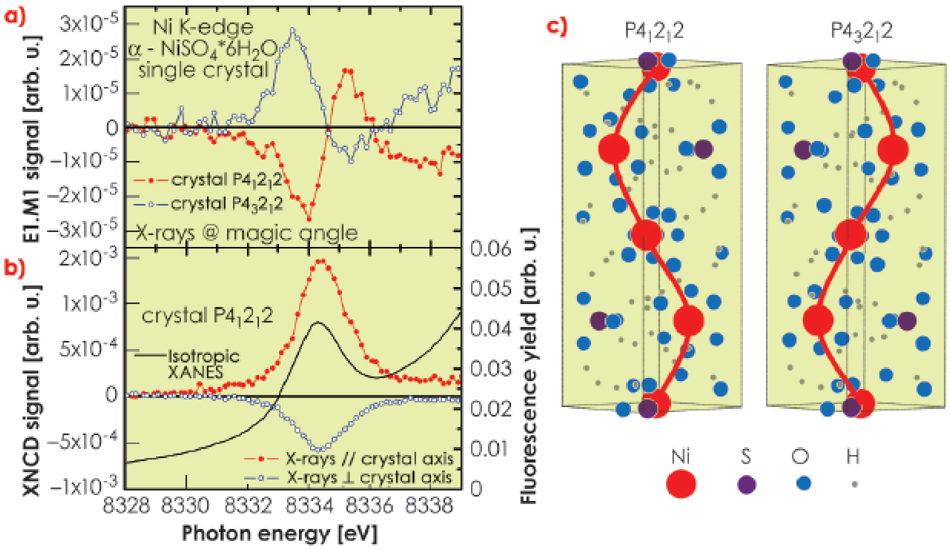

Fig. 84: The pre-edge part of the Ni K-edge XNCD spectra for two enantiomeric uniaxial single crystals of α-$NiSO_4x6H_2O$. a) XNCD spectra assigned to the E1.M1 interference term, measured at the magic angle. b) XNCD spectra recorded with the X-ray wavevector parallel and perpendicular to the optic axis. The isotropic XANES spectrum is also added for the sake of comparison. c) Crystal structure of the two enantiomers.

spatial dispersion effect (linear in the wavevector), optical activity is associated with transition probabilities which mix multipoles of opposite parity, *e.g.*, electric dipole - magnetic dipole (E1.M1) or electric dipole - electric quadrupole (E1.E2). The Curie symmetry principle states that this is only possible in systems with broken inversion symmetry. However, there was rather little motivation to look for optical activity in the X-ray range until X-ray natural circular dichroism (XNCD) was unambiguously detected at the ESRF in quite a few non-centrosymmetric crystals [1]. It stems from the E1.E2 interference terms which can be large in the hard X-ray range, as opposed to the E1.M1 term which is known to be responsible for optical activity in the visible but is regarded as negligible in core level spectroscopies.

Given that the E1.E2 interference term is a traceless tensor, not all crystals with broken space inversion symmetry, only 13 crystal classes, can exhibit optical activity in the X-ray range associated with the E1.E2 term. There is virtually no hope of detecting XNCD spectra in isotropic samples (powders or liquids) except if the E1.M1 contribution becomes non-negligible: in this case the system should exhibit enantiomorphism, *i.e.* it can exist in both right- and left-handed forms. We tried very hard to measure XNCD spectra in solutions of chiral complexes but strong radiation damage of the sample prevented us from obtaining any reproducible result.

In order to establish what could be the ultimate order of magnitude of the weak E1.M1 interference terms, we decided to carry out careful XNCD measurements on a single crystal of α-$NiSO_4x6H_2O$. This uniaxial crystal (with four formula units per unit cell) belongs to the enantiomorphous tetragonal space groups, $P4_12_12$ or $P4_32_12$ (see Figure 84). This compound has long been known to exhibit natural optical activity only in the crystalline state, due to a chiral arrangement of non-chiral units: four (nearly) perfect $Ni(H_2O)_6^{2+}$ octahedrons are located along a screw axis which is parallel to the tetragonal axis of the crystal, *i.e.* the crystallographic **c** axis which is the optical axis.

For such a uniaxial crystal, the angular dependence of the XNCD signal should vary as ($3\cos^2\Theta$-1), where Θ denotes the angle between the X-ray wavevector and the crystal optical axis. As illustrated with Figure 84b, this is exactly what we observed: the XNCD spectrum recorded with the X-ray wavevector perpendicular to the optical axis is about twice as weak and it has the opposite sign with respect to the XNCD spectrum recorded in the parallel configuration. This result provided us with an excellent illustration of the fact that the E1.E2 mechanism is quite efficient at the K-edge of transition metals. Unfortunately, it is also strong enough to mask any significant contribution of the weaker E1.M1 interference term, at least under such experimental conditions.

Actually, the only chance to detect a weak E1.M1 XNCD signal is when the optical axis of the crystal is set at the magic angle, *ca.* 54.73° with respect to the X-ray wavevector. This is because the XNCD signal due to E1.E2 interference term should vanish in this geometry so that only the E1.M1 term could ultimately contribute to the XNCD spectrum. We have performed a whole series of angle dependent XNCD measurements for both enantiomers. The results are shown in **Figure 84a**, where we focused on the XNCD spectra recorded in the pre-edge region of the Ni K-edge X-ray absorption spectrum. The dichroism spectra reproduced in **Figure 84a** may reasonably be assigned to the E1.M1 interference term. As expected, the XNCD spectra have the opposite sign for the two enantiomers and their amplitudes are as small as $3x10^{-5}$ with respect to the edge-jump. To the best of our knowledge, this appears to be the smallest static circular dichroism signal ever measured in the X-ray range. It is noteworthy that the E1.M1 XNCD signal is *ca.* 60 times smaller than the signal assigned to the dominant E1.E2 mechanism and has systematically the opposite sign with respect to the E1.E2 contribution measured with a crystal of the same enantiomer.

Reference

[1] J. Goulon, A. Rogalev, F. Wilhelm, N. Jaouen, C. Goulon-Ginet and C. Brouder, *J. Phys.: Condens. Matter* 15, S633 (2003).

Orbital reconstruction and a 2D electron gas at the interface between insulating transition metal oxides

Principal publication and authors

M. Salluzzo (a), J.C. Cezar (b), N.B. Brookes (b), V. Bisogni (b), G.M. De Luca (a), C. Richter (c), S. Thiel (c), J. Mannhart (c), M. Huijben (d), A. Brinkman (d), G. Rijnders (d), and G. Ghiringhelli (e), *Phys. Rev. Lett.* **102**, 166804 (2009).

(a) CNR-INFM COHERENTIA, Napoli (Italy)
(b) ESRF
(c) University of Augsburg (Germany)
(d) MESA+ Institute for Nanotechnology, University of Twente (The Netherlands)
(e) CNR-INFM Coherentia and Dipartimento di Fisica, Politecnico di Milano (Italy)

In 2004, Ohtomo and Hwang discovered that an electron gas can be generated at the $LaAlO_3/SrTiO_3$ (LAO/STO) interface, *i.e.* by combining two insulating transition metal oxides [1]. High carrier mobility [1], electric field tuneable superconductivity [2] and magnetic effects [3], have been found in this system. Very interestingly, the conductivity of this interface is obtained only when specific conditions are met, and in particular when an atomic layer of LaO, belonging to the $LaAlO_3$, is deposited on top of a TiO_2-terminated STO single crystal, thereby realising an n-type interface doped with electrons. Additionally, it has been shown that LAO/STO bilayers only generate a conducting interface if the thickness of the LAO film reaches a critical value of 4 unit cells [4]. This behaviour is consistent with the so-called "polarisation catastrophe" mechanism, which attributes the induction of carriers at the interface to the large electrostatic potential of the charged AlO_2^- and LaO^+ layers. However, this remains a subject of debate; other hypotheses have been considered, including the possible induction of a metallic state in the STO layers associated with stoichiometric defects, like oxygen vacancies and cationic substitution.

To clarify this issue we have used X-ray absorption spectroscopy (XAS) at the titanium $L_{2,3}$ edge to study the unoccupied 3d states of the STO layers close to the interface. The experiments were performed at beamline **ID08**. The LAO/STO heterostructures were grown by pulsed laser deposition. We have compared results from samples grown in Augsburg [4] and Geneva [2], showing low temperature superconductivity, and samples grown in Twente [3] exhibiting magnetic effects. In order to have interface sensitivity we took measurements using the total electron yield (TEY) technique, characterised by a probe depth between 2 and 4 nm, at incidence angles varying from 90° (normal to the interface) to 20° (grazing).

The XAS process is strongly influenced by the splitting of the 3d levels and therefore provides information on the

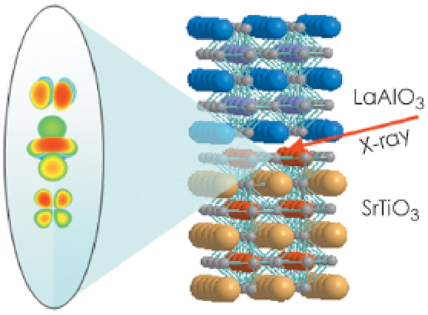

Fig. 85: a) Schematic diagram of the XAS and LD experiment illustrating the main concept used to study the orbital anisotropy of the 3d Ti states at the LAO/STO interface.

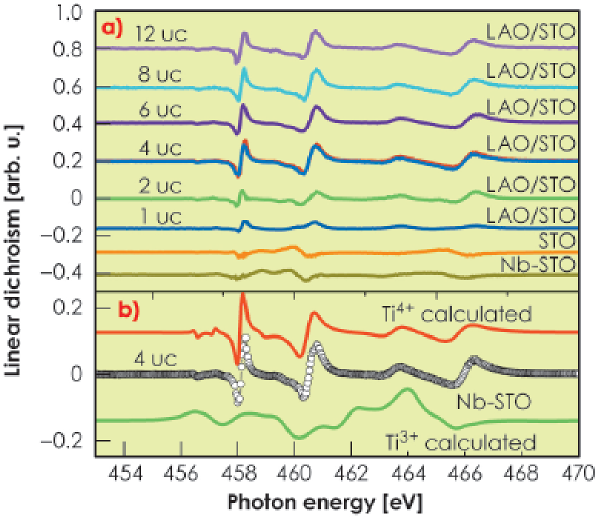

Fig. 86: a) Experimental linear dichroism (I_c-I_{ab}) as a function of the number of LAO layers; b) Comparison between multiplet calculations for anisotropic Ti^{4+} (red line) and Ti^{3+} (green line) 3d states and the data acquired on a 4 unit cell (uc) LAO/STO (open circles).

crystal field. By using linearly polarised light, it is possible to select an in-plane (d_{xy}, $d_{x^2-y^2}$) or an out-of-plane (d_{xz}, d_{yz}, and d_{z^2}) orbital as final state and measure the linear dichroism (LD), which is the difference between XAS spectra with out-of-plane (I_c) and in-plane polarisation (I_{ab}) (**Figure 85**).

The key results are shown in **Figures 86a and 86b**, where the LD spectra are plotted as a function of the number of LAO layers and compared to ion scattering calculations. Bare, TiO_2 terminated, undoped and Nb-doped, STO are characterised by a small dichroism, due to the abrupt truncation of the surface. The linear dichroism spectra is well reproduced by a small positive splitting of 40 meV between in-plane (d_{xy}, $d_{x^2-y^2}$) and out-of-plane (d_{xz}, d_{yz}, and d_{z^2}) states of the Ti^{4+} ions. By depositing only one LAO unit cell on the top of a TiO_2 terminated STO, the dichroism changes sign, but it remains small. Very strikingly, the linear dichroism becomes pronounced only above 4 u.c, when the interface becomes conducting, and then it remains constant up to a LAO thickness of 12 unit cells. This result has to be associated to an abrupt change of the anisotropy in the 3d electronic states, and therefore to an orbital reconstruction of the interfaces, which removes the 3d degeneracy completely. Nevertheless, the orbital reconstruction is not attributed to the transfer of electrons to the in plane $3d_{xy}$ states, which in case of localisation would change the valency of a fraction of Ti^{4+} ions to Ti^{3+}. Rather, the linear dichroism is perfectly reproduced by assuming a splitting between in plane and out-of -plane 3d states of Ti^{4+} ions of 60 meV and 100 meV for t_{2g} and e_g states respectively (**Figure 86b**).

These results demonstrate that the realisation of a conducting interface is correlated to an orbital reconstruction of the Ti 3d states. This reconstruction pushes the $3d_{xy}$ orbitals to lower energy and electrons can be transferred to the interface mainly to these $3d_{xy}$ states, without occupying localised states. This also explains why the linear dichroism does not have a contribution from Ti^{3+} states.

References
[1] A. Ohtomo and H.Y. Hwang, *Nature* **427**, 423 (2004).
[2] N. Reyren *et al.*, *Science* **317**, 1196 (2007).
[3] A. Brinkman *et al.*, *Nature Mater.* **6**, 493 (2007).
[4] S. Thiel *et al.*, *Science* **313**, 1942 (2006).

Ising magnetism and ferroelectricity in Ca_3CoMnO_6

Principal publication and authors
H. Wu (a), T. Burnus (a),
Z. Hu (a), C. Martin (b),
A. Maignan (b), J.C. Cezar (c),
A. Tanaka (d), N.B. Brookes (c),
D.I. Khomskii (a) and
L.H. Tjeng (a), *Phys. Rev. Lett.* **102**, 026404 (2009).
(a) II. Physikalisches Institut, Univesität zu Köln (Germany)
(b) Laboratoire CRISMAT, Caen (France)
(c) ESRF
(d) Hiroshima University (Japan)

Multiferroic materials, having coexisting magnetism and ferroelectricity, are of great technological and fundamental importance, given the prospect of controlling charges by applying magnetic fields and spins by voltages. Their spectacular cross-coupling effects can be explored to construct new forms of multifunctional devices [1]. Spiral magnetic order, resulting from magnetic frustration, is a common way to induce ferroelectricity. Very recently, a nonspiral magnetism-driven ferroelectric material was discovered, namely, the Ising chain magnet Ca_3CoMnO_6 [2]. **Figure 87a** shows its characteristic *c*-axis spin chain structure which is arranged into a hexagonal lattice in the *ab* plane. Along the chain alternate the octahedrally and trigonal prismatically coordinated Mn and Co ions. To understand the observed ferroelectricity, we performed *ab initio* electronic structure calculations, and carried out X-ray absorption spectroscopy (XAS) measurements at beamline **ID08**.

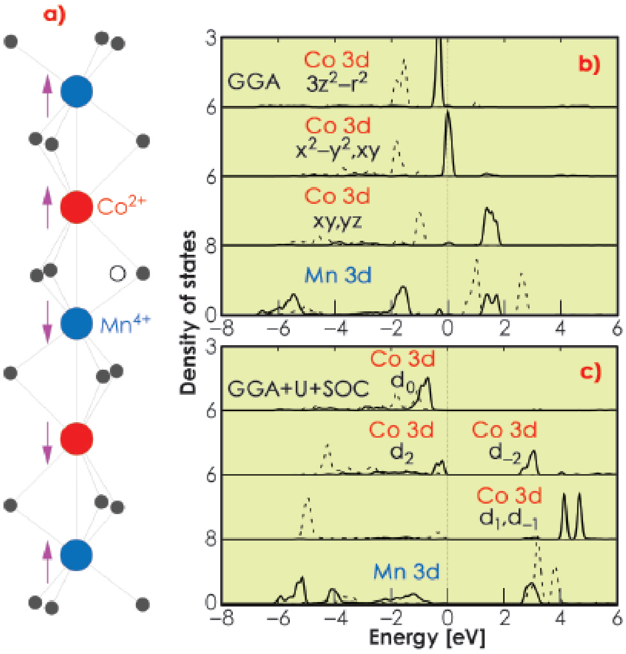

Fig. 87: a) The characteristic ↑↑↓↓ spin chain of Ca_3CoMnO_6 with alternate MnO_6 octahedra and CoO_6 trigonal prisms. Orbitally resolved density of states given by: b) GGA; c) GGA+*U*+SOC. The dashed (solid) curves refer to the majority (minority) spin. The Fermi level is set at zero energy. The nearly degenerate $3z^2$-r^2 (d_0), x^2-y^2 and xy ($d_{\pm 2}$) levels of the high-spin Co^{2+} ion in a trigonal crystal field well split by the Hubbard *U* and SOC.

We computed the total energy of the material in two different ion arrangements, one with the octahedral Mn (Mn_{oct}) and trigonal Co (Co_{trig}), and the other with Mn_{trig} and Co_{oct}. We used the generalised gradient approximation plus Hubbard *U* (GGA+*U*) calculations, also including the spin-orbit coupling (SOC). The structure having Mn_{oct} and Co_{trig} was found to be much more stable, by 1.6 eV/f.u., and the Mn turns out to be in a 4+ state and the Co in a high-spin (HS) 2+ state. **Figure 88** shows the Co $L_{2,3}$ (upper panel) and Mn $L_{2,3}$ (lower panel) XAS spectra of Ca_3CoMnO_6 and the references $EuCoO_3$, CoO, $LaMnO_3$ and MnO, as well as the simulated spectra given by full multiplet cluster model calculations. By looking closely at the energy positions and the line shapes of all the spectra, one can reliably conclude the experimental spectra match the HS $Co^{2+}{}_{trig}$ and $Mn^{4+}{}_{oct}$ state, thus confirming our theoretical results.

Figure 87b shows the orbitally-resolved density of states by a GGA calculation, which indicates the narrow band character of this strongly correlated oxide. Moreover, the HS trigonal Co^{2+} has the nearly degenerate $3z^2$-r^2 and (x^2-y^2, xy) levels. Because of the in-plane character of both the x^2-y^2 and xy orbitals, their strong Coulomb repulsion prevents their double occupation in the minority-spin channel. Therefore, the $3z^2$-r^2 orbital is

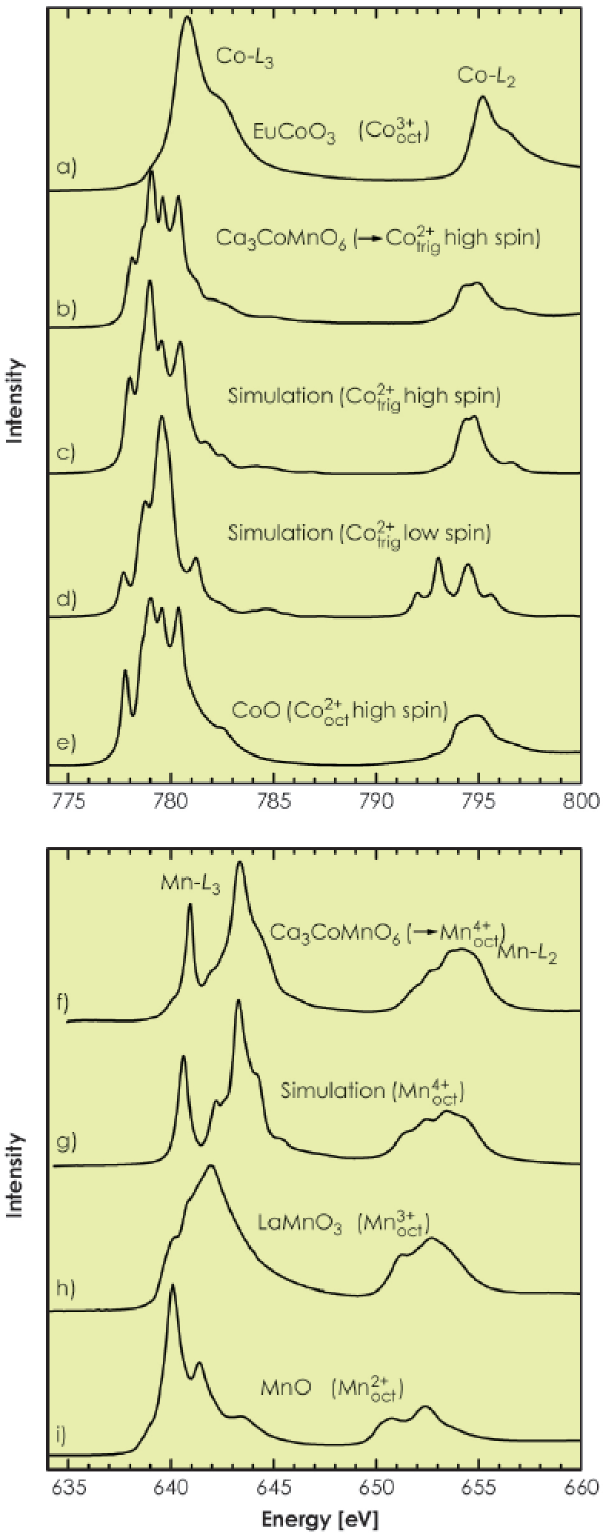

Fig. 88: The experimental and simulated XAS spectra of Ca_3CoMnO_6 and the references $EuCoO_3$, CoO, $LaMnO_3$ and MnO. Ca_3CoMnO_6 turns out to have the high-spin trigonal Co^{2+} and octahedral Mn^{4+}.

doubly occupied, and the minority-spin x^2-y^2 and xy are half filled but not apt to form a planar orbital ordering along the *c*-axis chain. Instead, when the spin-orbit coupling is included, the (x^2-y^2, xy) doublet splits into d_2 and d_{-2}, and the gain of the full spin-orbit coupling energy due to the d_2 occupation (see **Figure 87c**) is calculated to be about 70 meV. As a result, a huge orbital magnetic moment of 1.7 μ_B is generated at the Co^{2+} site, and the spin-orbit coupling firmly fixes the parallel spin and orbital moments along the *c*-axis chain.

The experimentally observed ↑↑↓↓ magnetic structure of the Co-Mn-Co-Mn Ising spin chains may be partially due to the finite antiferromagnetic interchain couplings. An exchange striction in those ↑↑↓↓ spin chains breaks the spatial inversion symmetry. Our calculations show that each spin chain has alternate short and long Co-Mn distances after a lattice relaxation. This, together with the Co^{2+}-Mn^{4+} charge order, produces the observed ferroelectricity.

We conclude that Ca$_3$CoMnO$_6$ has the octahedral Mn^{4+} and high-spin trigonal Co^{2+}. The Co^{2+} has a huge orbital moment due to the trigonal crystal field, Coulomb correlation and spin-orbit coupling, and all this determines the significant Ising magnetism. The exchange striction in the ↑↑↓↓ spin chains and the Co^{2+}-Mn^{4+} charge order lead to the ferroelectricity.

References
[1] S.W. Cheong and M. Mostovoy, *Nature Mater.* **6**, 13 (2007).
[2] Y.J. Choi, H.T. Yi, S. Lee, Q. Huang, V. Kiryukhin, and S.-W. Cheong, *Phys. Rev. Lett.* **100**, 047601 (2008).

Probing multiferroics using circularly-polarised X-rays

Principal publication and authors
F. Fabrizi (a,b), H.C. Walker (a,b), L. Paolasini (a), F. de Bergevin (a), A.T. Boothroyd (c), D. Prabhakaran (c), and D.F. McMorrow (b), *Phys Rev Lett* **102,** 237205 (2009).
(a) ESRF
(b) London Centre for Nanotechnology and Department of Physics and Astronomy, University College London (UK)
(c) Department of Physics, Clarendon Laboratory, University of Oxford (UK)

The surprising discovery of a strong coupling between ferroelectric and magnetic order parameters in the transition metal oxide TbMnO$_3$ has led to a resurgence of interest in magnetoelectric multiferroics. TbMnO$_3$ represents a new class of material where the onset of ferroelectricity is driven by the formation of an inversion symmetry breaking non-collinear magnetic order. The large coupling between the two types of order represents a considerable challenge, on the one hand, in terms of understanding its origin, and an opportunity, on the other hand, from the enticing prospect of new types of devices. Key to both endeavours is the need to develop novel techniques for imaging the formation of multiferroic domains under applied external fields.

We have developed the use of circularly polarised X-rays for non-resonant magnetic scattering, and demonstrated how it allows us to gain a complete picture of the complex magnetic structures displayed by the new multiferroics. A particularly appealing aspect of our technique is that it readily enables the imaging of the spatial distribution of magnetic domains. Historically there are few examples of the use of circularly-polarised X-rays in diffraction from non-collinear magnetic systems; however, the handedness of circularly-polarised X-rays naturally couples to the handedness of cycloidal spin structures. When circularly-polarised X-rays are used in combination with a linear polarimetry analysis of non-resonant magnetically-scattered photons, one obtains information about the magnetic structure complementary to that found in neutron diffraction. The polarisation state of the photon is described by the Stokes parameters, and it is through the determination of the Stokes parameters, obtained on exciting the non-resonant magnetic scattering process with circularly-polarised incident X-rays, that one can demonstrate the ability to control the population of the cycloidal magnetic domains by an applied electric field.

In TbMnO$_3$ the relevant phase transition to a non-collinear cycloidal spin arrangement occurs at T = 27 K and is concomitant with the onset of a spontaneous electric polarisation. The two different magnetic sublattices make it a particularly challenging test case for any new magnetic structure refinement

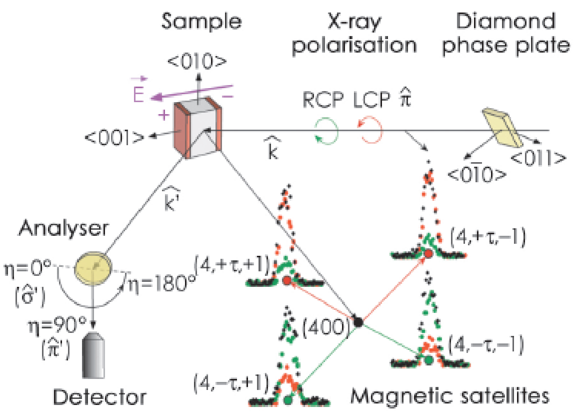

Fig. 89: Experimental setup and polarisation dependence of (4 ±τ ±1) non-commensurate satellite magnetic reflections in $TbMnO_3$, measured after cooling to T = 15 K in a negative applied electric field.

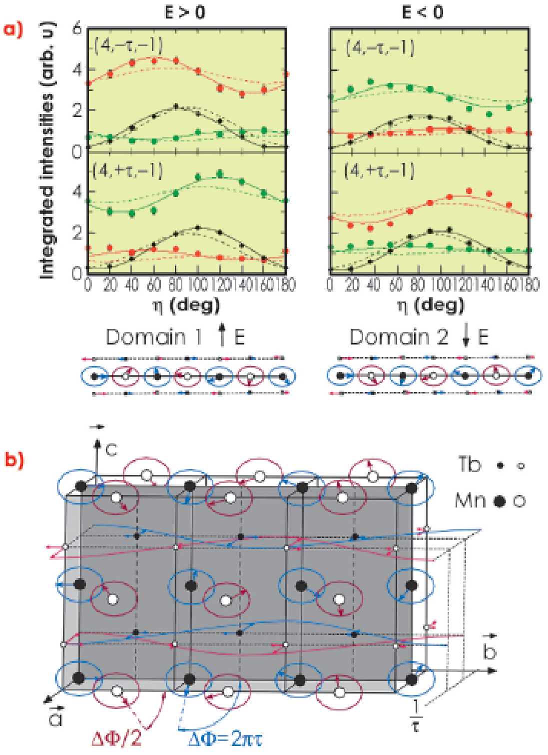

Fig. 90: a) Polarisation dependence of magnetic satellites (4 ±τ -1) for two applied electric field directions and the projection in the b-c planes of the two cycloidal domains. Continuous (broken) lines are calculations based on an X-ray (neutron) scattering model. b) Magnetic structure of $TbMnO_3$ determined by the present work.

method. However, whilst typically magnetic structure refinement requires measuring as many magnetic reflections as possible, here the coupling of the photon polarisation state and the experimental geometry, see **Figure 89**, enables the refinement using only four satellite magnetic reflections.

The experimental sensitivity to the imbalance in magnetic domain populations produced by cooling the sample on application of an electric field was initially tested. **Figure 89** shows the complementary behaviour of the intensities of four magnetic satellites (4 ±τ ±1) for left and right circular polarisation (LCP, RCP) depending on the sign of τ. This is in strong contrast to the results expected for equi-populated domains, for which the signal should be very similar for LCP (red dots) and RCP (green dots). Also shown are the intensities for linear incident polarisation (black dots), which are similar for all four satellites. On switching the electric field, there is a reversal in the behaviour of the LCP and RCP magnetic satellite intensities, because the direction the magnetic cycloid changes its sense of rotation.

Taking advantage of the non-resonant X-ray magnetic scattering cross-section and the coupling between the polarisation state and the experimental geometry, the Stokes dependence of the scattering from different magnetic reflections was measured, and a fit to the data made for different magnetic structure models, see **Figure 90**. Not only does this technique provide unique insight into the formation of cycloidal domains, leading to a quantitative description of the domain state, but it also allowed the refinement of an earlier magnetic structure model obtained from neutron diffraction studies. In particular, the absolute sense of rotation and the phase shifts of the individual magnetic sublattices has been analysed in detail.

These techniques present an exciting opportunity for a new class of experiments in which the magnetic state of complex magnetic materials can be probed and the magnetoelectric domain formation controlled under applied external electric and magnetic fields. In the future, the combination of this technique with highly focussed X-ray beams will produce real-space images of the formation of non-collinear magnetic domains.

Charge localisation and orbital glass state in multiferroic $LuFe_2O_4$

Principal publication and authors
A.M. Mulders (a,b),
S.M. Lawrence (a), U. Staub (c),
M. Garcia-Fernandez (c),
V. Scagnoli (d), C. Mazzoli (d),
E. Pomjakushina (e,f),
K. Conder (e) and Y. Wang (g),
Phys. Rev. Lett. **103**, 077602 (2009).
(a) Department of Imaging and Applied Physics, Curtin University, Perth (Australia)
(b) The Bragg Institute, ANSTO, Lucas Heights (Australia)
(c) Swiss Light Source, Paul Scherrer Institut, Villigen (Switzerland)
(d) ESRF
(e) Laboratory for Developments and Methods, PSI, Villigen (Switzerland)
(f) Laboratory for Neutron Scattering, ETHZ & PSI, Villigen (Switzerland)
(g) Department of Applied Physics, The Hong Kong Polytechnic University (China)

New materials that exhibit strong magnetoelectric coupling are fascinating because a large coupling between ferroelectric and magnetic interactions is rare, and its origin often unclear. The properties of such materials make them extremely useful in devices where the coexistence of both charge and spin components can be exploited and one property can be used to drive the other. For instance, the electric manipulation of magnetic fields could provide much faster information storage and retrieval in hard disks, since it is easier and much faster to switch an electric field than a magnetic field. Another example is memory storage, where coupled charge and spin properties allow the storage of n^2 bytes at the space of n bytes; hence 1 Gigabyte would be replaced by 1 Exabyte of information in a similar space.

In most ferroelectric materials, electric polarisation arises from covalent bonding between anions and cations or the orbital hybridisation of electrons. Alternatively, ferroelectric polarisation may arise from frustrated charge order as reported for $LuFe_2O_4$. This compound is of particular interest because, in addition to ferroelectricity, magnetism originates from the same Fe ions and this holds the promise of strong magnetoelectric coupling. The ferroelectric and magnetic order takes place at and near ambient temperature which provides the potential for room temperature multiferroics.

With resonant X-ray Bragg diffraction (RXD) we investigate the electronic order of the Fe ions in $LuFe_2O_4$, using polarisation dependence and element specificity to distinguish various ordering phenomena and order parameters.

Figure 91 shows the Fe K edge resonance of several superlattice reflections characterised by wavevector (1/3 1/3 1/2). Their intensities gradually disappear above the charge ordering temperature (see inset). Non-resonant scattering associated with the crystallographic distortion that accompanies the ferroelectric polarisation dominates the diffracted intensity before and after the edge. The anomalous diffraction of the Fe ions adds phase shifted contributions to the

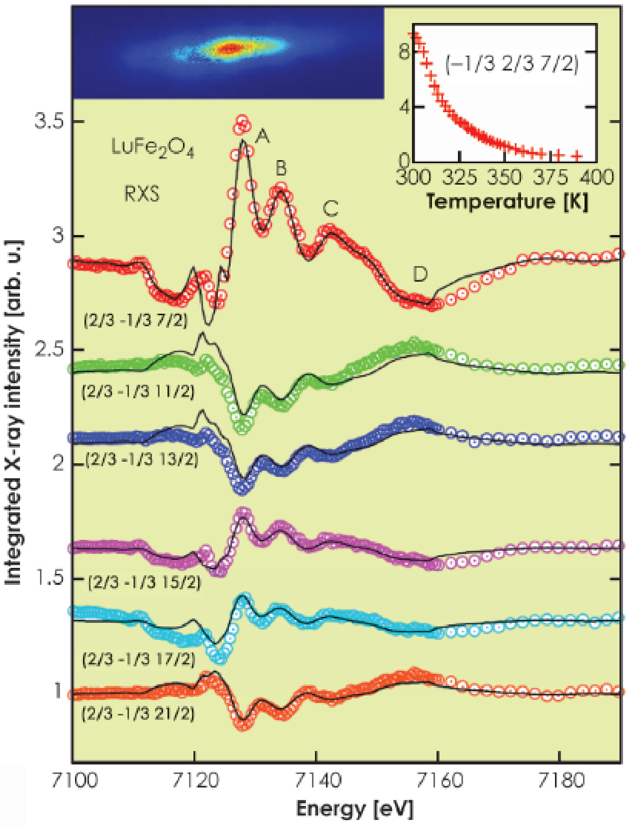

Fig. 91: Integrated resonant diffraction intensity of the charge order (2/3 -1/3 *l*/2) reflections recorded with 2D detector at the MS beamline at the SLS at T = 15 K (see inset top left for *l* = 11), corrected for background, polarisation, absorption and sample geometry, normalised (shifted for clarity) and compared to charge order model described in the text. The inset (top right) shows that the superlattice intensity gradually disappears at the ferroelectric ordering temperature.

scattering amplitude resulting in enhanced or decreased intensity at the K-edge. The solid curves in **Figure 91** are the result of a fit of the data with Fe^{2+}/Fe^{3+} charge order.

Fe^{3+} with five 3d electrons is close to spherical while Fe^{2+} with six 3d electrons exhibits doubly degenerate orbital degree of freedom, which is expected to give rise to small lattice distortion and orbital order of the Fe^{2+} orbitals. However, such orbital order is not observed. **Figure 92** shows that the polarisation of the light does not rotate during the diffraction process and that magnitude of the resonance is independent of the orientation of the crystal. This demonstrates that the Fe^{2+} orbitals have random orientations. These findings of an orbital glass state are in agreement with calculations of Nagano [1].

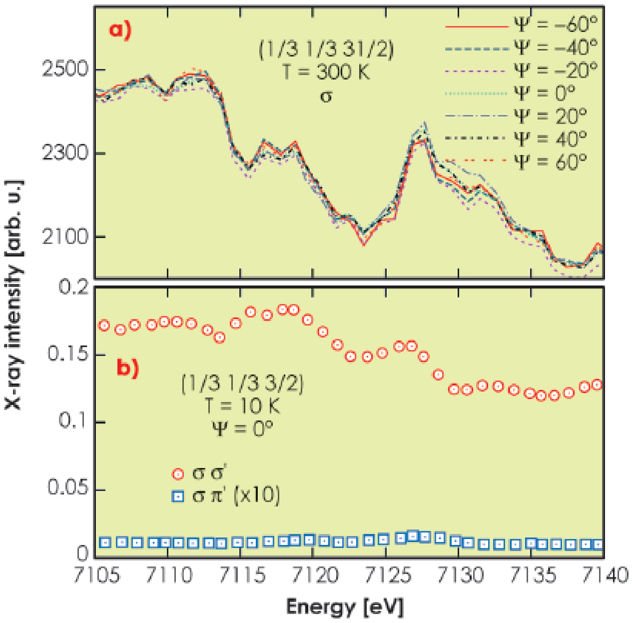

Fig. 92: XRD recorded at **ID20**. a) Intensity of the (1/3 1/3 31/2) reflection as function of azimuthal angle. b) Intensity of the (1/3 1/3 3/2) reflection with unrotated polarisation (σσ′) and rotated polarisation (σπ′). The latter intensity is multiplied by 10 for clarity.

Orbital order plays a major role in the electronic properties of transition metal oxides, including magnetoresistance, metal insulator transitions and magneto-electric coupling. The appearance of an orbital glass-like state is very rare and truly interesting because it is a novel and very poorly studied electronic ground state. This state has significant consequences for the magnetoelectric properties. The orientation of the orbitals determines the magnetic exchange interactions and is part of the intricate coupling between charge and spin.

Reference

[1] A. Nagano, M. Naka, J. Nasu, and S. Ishihara, *Phys. Rev. Lett.* **99**, 217202 (2007).

Field-induced magnetostructural phase transition in Ca_2FeReO_6 studied via XMCD under 30 T pulsed magnetic field

Principal publication and authors

M. Sikora (a), O. Mathon (b), P. van der Linden (b), J.M. Michalik (c), J.M. De Teresa (c), Cz. Kapusta (a), and S. Pascarelli (b), *Phys. Rev. B* **79**, 220402R (2009).

(a) AGH University of Science and Technology, Krakow (Poland)
(b) ESRF
(c) ICMA, Universidad de Zaragoza-CSIC, Zaragoza (Spain)

Ordered double perovskites have attracted substantial attention over the past 10 years due to strong spin polarisation of the electrical carriers and high Curie temperature [1,2]. These properties could lead to the discovery of a material with a reasonable degree of magnetoresistance (MR) at room temperature and so to application of the materials in magnetoelectronics. The most promising series, namely A_2FeMoO_6, A_2FeReO_6, A_2CrReO_6, and A_2CrOsO_6 (A = alkaline earth metals), are being investigated intensively to find the material with optimal performance. Among the intriguing characteristics of these compounds are the differences in magnetic properties of 4*d*- and 5*d*-based analogs despite their almost identical crystal structure. For example, the Re-based double perovskites show strong magnetostructural coupling as well as considerably higher Curie temperature than their Mo-based counterparts. The strong magnetostructural effects are attributed to the interplay between structural degrees of freedom with unquenched Re orbital moment. This interplay is especially pronounced for the compound Ca_2FeReO_6, which undergoes a metal-insulator (MI) phase transition at T_S~150 K associated with structural deformations of the ReO_6 octahedra and redistribution in the Re 5*d* orbitals occupancy. Neutron diffraction, high-field magnetoresistance, and magnetostriction experiments suggest

Fig. 93: Rhenium $L_{2,3}$-edge XMCD spectra measured at $T = 10$ K using the ESRF minipulsed field installation (inset).

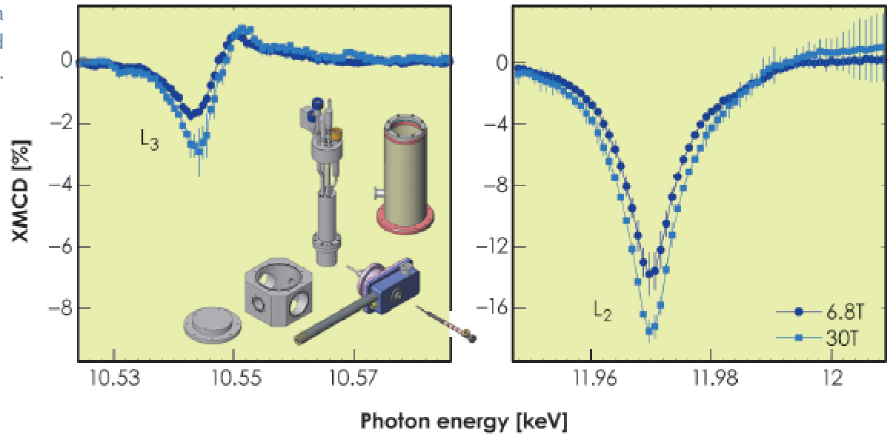

Fig. 94: Temperature and field evolution of the normalised Re and bulk magnetisations. The latter was adapted from data published in ref. [4]. Increase of magnetisation is denoted by colour change from dark-red to bright-yellow. Smoothed iso-*M* curves are presented at arbitrary values as guides for the eyes.

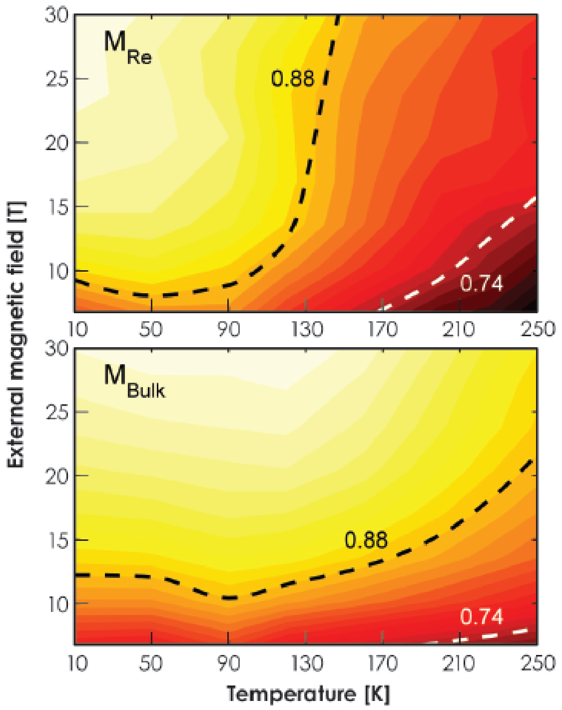

that at low temperature the two magnetostructural phases, of considerably different electron transport properties, coexist and that their relative population depends on temperature and magnetic field giving rise to large negative magneto-resistance, MR~2000% at $T = 100$ K [2].

To investigate the role played by the Re orbital moment in the mechanism of the structural phase transition, a high field X-ray magnetic circular dichroism (XMCD) experiment was performed. We studied the field and temperature evolution of the Re orbital (L) and spin (S) components of the magnetic moment derived from $L_{2,3}$-edge spectra (**Figure 93**) by means of sum rules. The main challenge was to acquire the spectra at high magnetic field, $B > 20$ T, in a temperature range wide enough to induce a substantial change in the relative phase fraction. Such experimental conditions have become available only recently, employing the energy-dispersive acquisition technique available at beamline **ID24** in combination with a minipulsed field setup [3].

Analysis of the B and T evolution of Re orbital-to-spin magnetic moment ratio gives unequivocal evidence that the two magnetocrystalline phases observed in Ca_2FeReO_6 are characterised by different spin-orbit coupling. The insulating phase, observed at low temperature and field, is being suppressed by the metallic phase, characterised by larger absolute value of L/S, either upon heating above T_S or upon application of a strong magnetic field of several Tesla.
The shape comparison of bulk magnetisation with the XMCD derived Re one (**Figure 94**) reveals a striking difference, which is attributed to electron redistribution between antiferromagnetically coupled Re and Fe sites upon temperature and field change. Quantitative analysis revealed that Re magnetisation is significantly higher in the insulating phase with respect to bulk. This gives evidence that the metal-insulator phase transition is accompanied by the evolution in the population of Re t_{2g} orbitals as well as with the charge-transfer between Fe and Re sites. Both effects have a strong influence on the hopping integral of the double-exchange-like interaction between Re and Fe sites and, thus, on the electronic properties of the compound.

References
[1] K.-I. Kobayashi, T. Kimura, H. Sawada, K. Terakura and Y. Tokura, *Nature (London)* **395**, 677 (1998).
[2] D. Serrate, J.M. DeTeresa and M.R. Ibarra, *J. Phys.: Condens. Matter* **19**, 023201 (2007).
[3] P. van der Linden, O. Mathon, C. Strohm and M. Sikora, *Rev. Sci. Instrum.* **79**, 075104 (2008).
[4] J.M. Michalik, J.M. DeTeresa, J. Blasco, P.A. Algarabel, M.R. Ibarra, C. Kapusta and U. Zeitler, *J. Phys.: Condens. Matter* **19**, 506206 (2007).

The nature of disorder in ordered double perovskite, Sr$_2$FeMoO$_6$

Principal publication and authors
C. Meneghini (a,b), S. Ray (c,d), F. Liscio (a), F. Bardelli (a,b), S. Mobilio (a,b,e) and D.D. Sarma (c,d), *Phys. Rev. Lett.* **103**, 046403 (2009).
(a) Dipartimento di Fisica, Universita di Roma Tre (Italy)
(b) CNR TASC Laboratory c/o GILDA-ESRF Grenoble (France)
(c) Indian Institute of Science, Bangalore (India)
(d) Indian Association for the Cultivation of Science, Kolkata (India)
(e) Laboratori Nazionali di Frascati dell'INFN (Italy)

The ideal concept of a crystalline solid as a perfect periodic structure is at the core of our understanding of a wide range of material properties. In real systems *disorder* is ubiquitous and is indeed complex as it can occur in many different ways in which the random distribution of defects is only a special and extreme case. As a matter of fact the physical properties of materials can be strongly influenced by the nature of the disorder, therefore they must be carefully described to properly understand the physics of complex systems. There is great interest in systems where the simultaneous presence of disorder and strong electron-electron correlation effects leads to exciting physics and potential applications. This is the case for Sr$_2$FeMoO$_6$ double perovskites, in which the perfect alternate occupancy of Fe and Mo sublattices gives rise to complete spin carrier polarisation, large magnetoresistance and high Curie temperature. Antisite defects, created by interchanging Fe and Mo ionic positions, affect the magnetic and magneto-transport response of this compound. The distribution of antisite defects is normally considered within the two extreme scenarios illustrated in **Figure 95**: homogeneously distributed (**Figure 95a**) or segregated in patches (**Figures 95b and c**), where the defects recover the original lattice periodicity but for all of the Fe ions occuping the nominal Mo sites and vice versa. Since the magnetic and magnetotransport properties of Sr$_2$FeMoO$_6$ are profoundly affected by the extent of disorder, we are interesting in discovering the nature of such disorder. The long range order parameter S, obtained from X-ray powder diffraction (XRPD) data, accounts for the number of antisite defects, in term of probability of Fe(Mo) on the Mo(Fe) sublattice, but cannot distinguish a homogeneous distribution from a defect segregation model; in the literature, the former is generally implicitly assumed. X-ray absorption fine structure spectroscopy (XAFS) is a local probe which allows the direct measurement of the probability ξ to have ordered configurations (Fe-Mo pairs) around the absorber. In case of completely random defect distribution, this probability is ξ_{Rand}= $(S^2+1)/2$, values of ξ greater than ξ_{Rand} would mean defect segregation. To understand the nature of disorder in Sr$_2$FeMoO$_6$ compounds, five samples were synthesised with different degrees of long range order and investigated by XRPD and XAFS (Fe and Mo K edges) at **BM08**, the GILDA beamline. The XRPD pattern analysis show S in between 0.18 and 0.96 (**Figure 96a**). Despite the ample differences in long range order, the XAFS spectra (**Figures 96b and 96c**) are all similar. This observation suggests that a high degree of Fe/Mo local order is preserved even when the long range disorder is excessively high. Accordingly, the quantitative analysis of XAFS spectra resulted in the experimental ξ (measured at the Fe and Mo K edges) to be always higher than ξ_{Rand} (**Figure 95d**). To obtain further details of the local disorder of Sr$_2$FeMoO$_6$, we built 3D models of a cubic lattice in which Fe and Mo are arranged on different sublattices (**Figures 95a-c**). Antisite defects were introduced accordingly to the experimental S and were organised in antiphase regions with average diameter D. The size of antiphase regions were refined in order to fit the short range parameter of the model ξ_D to the experimental values ξ obtained by XAFS. Such modelling establishes that the antiphase domains have dimensions around 1 nm and are

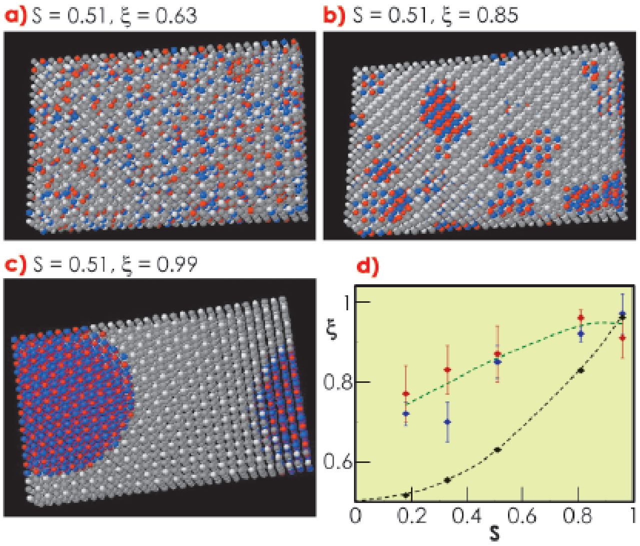
a) S = 0.51, ξ = 0.63
b) S = 0.51, ξ = 0.85
c) S = 0.51, ξ = 0.99
d)

Fig. 95: a-c) slices of 3D models of Fe/Mo cubic lattice with the same long-range order parameter (S) and different order probability (ξ) Dark (light) grey sites represents Fe(Mo) ordered positions, red (blue) sites represents Fe(Mo) on the Mo(Fe) sublattice. d) In the graph, the black points represent theoretical ξ_{rand} values, red and blue are the experimental ξ derived from Fe and Mo XAFS data respectively. Dashed lines are guide for the eyes.

weakly affected by changes of S. Previous magnetic studies as a function of disorder suggested that the presence of multiple nanosized antiphase domains is more likely than highly extended domains with relatively fewer number of antiphase boundaries. This theory is definitively confirmed by the present results.

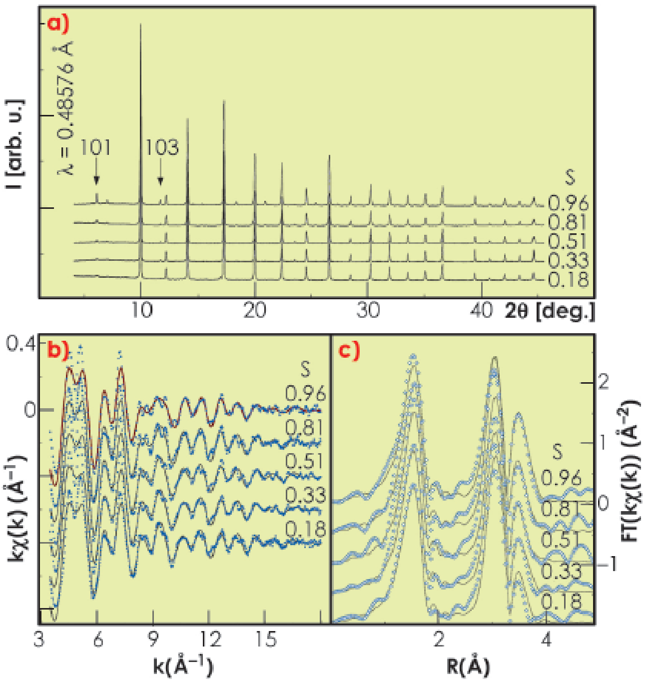

Fig. 96: a) X-ray powder diffraction data for the investigated samples: the intensity of the superlattice peaks (101, 103) is related to the long range order parameter S. b) the Mo K edge XAFS data and c) their Fourier transforms. Blue points and dark lines are respectively the experimental data and the best fits.

Our study demonstrates that a high degree of cation order is preserved locally even in samples with a high degree of long range disorder. The structural simulations suggest that the formation of antiphase patches is favoured over the homogeneous distribution of antisite defects. Therefore, the short and long range order features in Sr_2FeMoO_6 can be understood in terms of locally ordered regions forming nanosized antiphase domains. This peculiar "disorder" profoundly affects magnetic properties of this interesting material.

Hollow K-shell atoms created via single-photon double ionisation

Electron correlation effects lie at the heart of our understanding of atomic structure. Yet their quantitative description, in particular in many-body systems, is far from complete. To shed new light on atomic electron correlation effects, the single-photon double K-shell photoionisation (DPI) was investigated. In this weak process, a single photon removes the two innermost electrons and produces a "so-called" hollow K-shell atom, *i.e.* an atom with an empty inner-most shell and outer shells occupied. Because of the single-particle nature of the photon-electron interaction, the K-shell double photoionisation is driven by many-electron interactions.

The photon energy dependence of the K-shell DPI of Mg, Al and Si was investigated. This is the first study of these elements and also for such a wide range of photon energies from the DPI threshold up and beyond the maximum of the double-to-single photoionisation ratios P_{KK}. The experiments were carried out at the beamlines ID21 and ID26 using the Fribourg von Hamos Bragg-type curved crystal X-ray spectrometer [1]. The experimental method was based on high-resolution measurements of X-ray spectra following the radiative decay of the K-shell double vacancy states (see Figure 97a). The P_{KK} were deduced from the relative intensities of the resolved hypersatellite $K\alpha^h$ ($1s^{-2} \rightarrow 1s^{-1}2p^{-1}$) to the diagram $K\alpha$ ($1s^{-1} \rightarrow 2p^{-1}$) X-ray transitions. DPI cross sections were determined by employing the relation $\sigma^{2+} = P_{KK}\sigma^{+}$, where σ^{+} stands for the single K-shell photoionisation cross section.

The double-to-single K-shell photoionisation ratios for neutral Mg, Al and Si versus the scaled excess energy $(E-E^{2+})/Z^{*2}$, where E^{2+} stands for the DPI threshold and Z^* is the effective nuclear charge, are shown in Figure 97b. The effective charge was derived from the binding energy of the remaining K-shell electron E^+ using the hydrogenic formula $E^+ = Z^{*2}$ Ry, where Ry = 13.6 eV. In order to evince the relative importance of the initial- and final-state electron-electron interaction

Principal publication and authors
J. Hoszowska (a), A. Kheifets (b), J.-Cl. Dousse (a), M. Berset (a), I. Bray (c), W. Cao (a), K. Fennane (a), Y. Kayser (a), M. Kavčič (d), J. Szlachetko (a,e) and M. Szlachetko (a), *Phys. Rev. Lett.* **102**, 073006 (2009).
(a) Department of Physics, University of Fribourg (Switzerland)
(b) Research School of Physical Sciences, Australian National University, Canberra (Australia)
(c) ARC Centre for Matter-Antimatter Studies, Curtin University, Perth (Australia)
(d) J. Stefan Institute, Ljubljana (Slovenia)
(e) ESRF

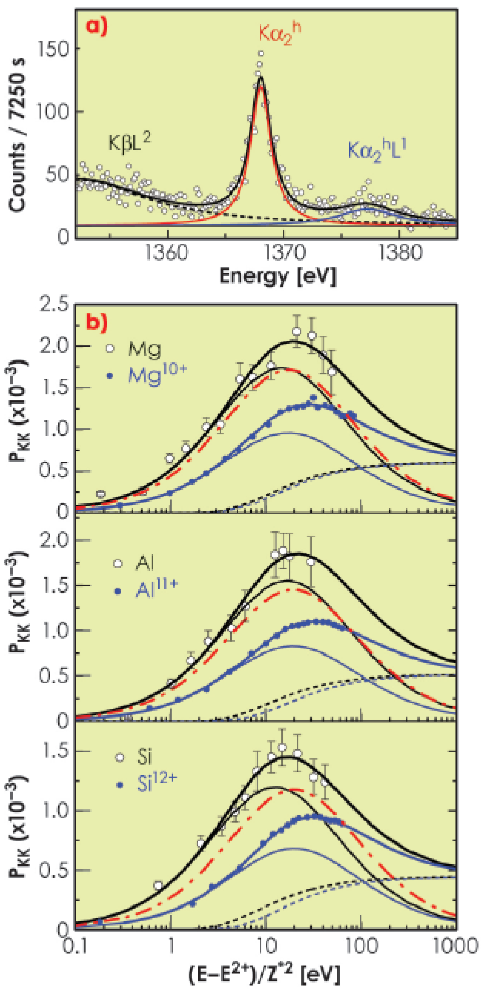

Fig. 97: a) K-hypersatellite X-ray emission spectrum of Mg. b) Double-to-single K-shell photoionisation ratios for neutral atoms (open circles) compared to the CCC calculations for He-like ions (closed circles) as a function of the scaled excess energy. Solid thick lines - best fits, dashed lines - SO, thin solid lines - KO, and dot-dashed lines - KO terms of He-like ions scaled by Z^4/Z^{*4}.

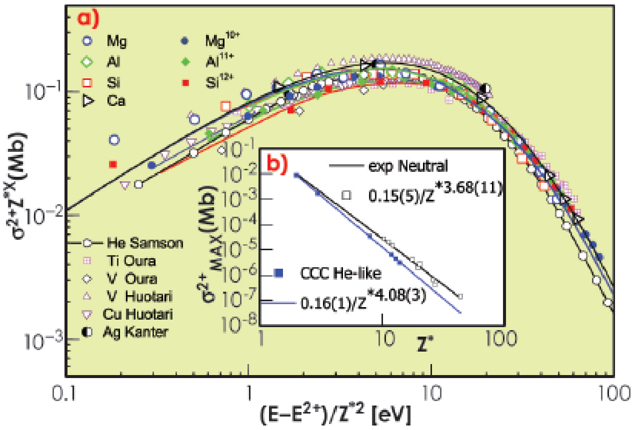

Fig. 98: a) Scaled experimental DPI cross sections for Mg, Al and Si compared to the scaled CCC calculations for He-ions and experimental data for higher Z elements versus the scaled excess energy. b) Power-law fits to the maximum values of σ^{2+} as a function of Z^*. For He-like ions, $Z^* = Z$.

to the K-shell DPI, we have fitted the P_{KK} adopting an approach based on an incoherent summation of the shake-off (SO) and knock-out (KO) terms. Shake-off corresponds to a sudden ejection of the photoelectron following single-photon absorption and a subsequent change of the atomic potential, which may lead to a removal of the remaining 1s electron to the continuum. In case of knock-out, the outgoing photoelectron knocks out the second 1s electron in an (e,2e)-like electron impact half collision. Furthermore, we have raised the question as to the role played by outer-shell electrons in the K-shell DPI. To this end, the P_{KK} for neutral atoms were compared to convergent close-coupling (CCC) calculations [2] for He-like ions Mg^{10+}, Al^{11+} and Si^{12+}. The KO terms of He-like ions scaled by Z^4/Z^{*4} were found to be close to the ones for neutral atoms. Our results suggest that KO dominates near threshold and at intermediate photon energies, and that the electron scattering contribution is more important for neutral atoms than in two-electron systems.

It is established that for two-electron ions, the DPI cross sections scale as $1/Z^4$. With this perspective, we have examined whether it is the case for neutral atoms. Indeed, the DPI cross sections were found to scale, but with a weaker exponent $1/Z^{*3.68}$. Furthermore, the scaled σ^{2+} for neutral atoms and for the He isoelectronic series were found to collapse onto a single curve (see **Figure 98**).

In conclusion, we investigated the double ionisation of the two innermost atomic electrons upon single-photon absorption in neutral atoms and the corresponding simple systems, two-electron ions. An empirical model to separate the knock-out and shake-off mechanisms of the K-shell DPI was proposed. The results suggest that the *post*-photoabsorption electron correlation effects on K-shell DPI of neutral atoms are different in comparison with corresponding two-electron systems. A universal scaling behaviour of the DPI cross sections with the effective nuclear charge for neutral atoms in the range $2 \leq Z \leq 47$ was established.

References
[1] J. Hoszowska, J.-Cl. Dousse, J. Kern and Ch. Rhême, *Nuclear Instrum. Methods Phys. Res.*, A **376**, 129-137 (1996).
[2] A. Kheifets and I. Bray, *Phys. Rev.* A **58**, 4501-4511 (1998).

Correlation between I-Ag distance and ionic conductivity in AgI-doped fast-ion-conducting glasses

Principal publication and authors
A. Sanson (a,b), F. Rocca (a), C. Armellini (a), G. Dalba (c), P. Fornasini (c) and R. Grisenti (c), *Physical Review Letters* **101**, 155901 (2008).
(a) CNR-IFN and FBK-CeFSA, Trento (Italy)
(b) Department of Computer Science, University of Verona (Italy)
(c) Department of Physics, University of Trento (Italy)

Fast-ion-conducting (FIC) glasses, whose values of ionic conductivity are comparable to those of liquid electrolytes, are of wide interest for their potential technological applications. Understanding the transport properties in FIC glasses is a challenging problem whose solution may allow one to design new glasses with optimised properties for various applications. Much experimental and theoretical effort has led to some general rules and empirical relations for high ionic conductivity, but a transport model based on local structure is not yet widely accepted [1].

AgI-doped glasses are the best conducting among FIC oxide glasses, with room-temperature conductivities approaching $10^{-1}\ \Omega^{-1}\text{cm}^{-1}$. Although the influence of the AgI doping salt on the glass structure and on the ionic conductivity has been widely investigated, leading to some commonly accepted ideas, a full connection between local structure and ionic conductivity is still lacking. To this aim, EXAFS spectroscopy is particularly well suited, thanks to the selectivity of atomic species, and to the high sensitivity to details of short-range structure.

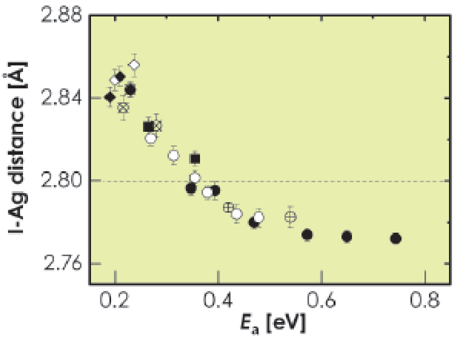

Fig. 99: I-Ag distance measured by EXAFS in different families of AgI-based glasses at LN temperature, plotted against the activation energy for dc ionic conductivity. The symbols refer to the glass family: ⊗ = AgI-Ag_2O-1•B_2O_3, ○ = AgI-Ag_2O-2•B_2O_3, ⊕ = AgI-Ag_2O-3•B_2O_3, ● = AgI-Ag_2O-4•B_2O_3, ■ = AgI-$AgPO_3$, ◊ = AgI-Ag_2MoO_4, ♦ = AgI-Ag_2WO_4. The dashed line corresponds to the value of crystalline β-AgI.

An EXAFS investigation of the local structure around iodine was made in different families of AgI-based glasses (borates, phosphates, molybdates, tungstates) affected by different values of ionic conductivity. EXAFS measurements at the K edge of iodine were performed, at liquid nitrogen temperature, at beamline **BM29**. Crystalline β-AgI was also measured as reference.

From a phenomenological point of view, the dc ionic conductivity follows an Arrhenius law $\sigma T = A \exp(-E_a / k_B T)$, where the activation energy E_a is the mean energy required for a cation jump. EXAFS results clearly show that a general correlation exists between the I-Ag bond distance and the activation energy E_a. **Figure 99** shows the I-Ag distance obtained from EXAFS for the different glasses examined, plotted against the corresponding activation energy for dc ionic conductivity. The I-Ag distance progressively increases from 2.77 Å in glasses with low ionic conductivity (*i.e.* high activation energy and low AgI content), to about 2.85 Å in glasses with high ionic conductivity (*i.e.* low activation energy and high AgI content). Remarkably, glasses with activation energy lower than about 0.35 eV display longer I-Ag distances than crystalline β-AgI, and vice versa.

These results indicate that the I-Ag distance is modified in parallel with the conductivity enhancement of AgI-doped FIC glasses, showing a behaviour that is common to glasses with very different matrices. In agreement with recent works [1, 2], we attribute the expansion of the I-Ag distance to the progressive increase of the number of Ag ions with mixed oxygen and iodine coordination, the strength of the Ag-O bond favouring the expansion of the I-Ag bond.

The activation energy can be written as a sum of two terms: the first one (binding energy) is the mean energy a cation requires to leave its site, the second one (strain energy) is the mean kinetic energy a cation needs to open a "doorway" in the structure to pass through. The decrease of the activation energy induced by salt doping was up to now associated to a lowering of the strain energy [2]. The EXAFS result (*i.e.*, the decrease of the activation energy with increase of the I-Ag distance), suggests that also the binding energy term gives a significant contribution on the enhancement of the ionic conductivity.

References
[1] P. Mustarelli, C. Tommasi, and A. Magistris, *J. Phys.Chem. B* **109**, 17417 (2005), and references therein.
[2] S. Adams and J. Swenson, *Phys. Rev. Lett.* **84**, 4144 (2000).

Time-resolved elucidation of intermediate species of catalysts in solution

After the serendipitous discovery of methylrhenium trioxide CH_3ReO_3 (MTO) in 1979, this compound has been found to be an important active and selective catalyst, able to catalyse a vast variety of reactions, mainly in the liquid phase, that are essential to our lives. Examples of its use are the oxidation of a large amount of organic compounds including olefins, alkenes, aromatics, and sulphur and nitrogen containing compounds; aldehyde olefination and related reactions; and olefin methathesis [1]. Its paramount role in the world of catalysis came not only from the myriad of reactions that MTO catalyses but also because MTO is very easy to synthesise and handle, and it is thermally stable and soluble in practically all sorts of solvents, ranging from pentane to water. When dissolved in water, it has the additional key advantage of making the process environmentally clean, so its use is sought by industry today.

Following an *in situ* catalytic reaction to reveal the structure of the intermediate species as the reaction progresses has been a long-standing challenge. Achieving this could help researchers develop advanced catalysts with tailor-made properties to enhance selectivity. It is known that methylrhenium dioxide (MDO) is an important intermediate, with strong reducing capabilities, that plays a crucial role in many of the reactions catalysed by MTO. However, until today, its transient existence made it impossible to isolate as a sole structural compound.

To discover the real structure of MTO in solution and elucidate the reaction intermediate MDO during the course of the reaction, we followed the reaction of 20 mM of MTO with 1.6*M* of H_3PO_2 in water and acidic medium using the time-resolved stopped-flow/energy-dispersive X-ray absorption near-edge structure (ED-XANES)/UV-visible setup on beamline ID24. The reaction was followed at the Re L_3 edge over a period of 90 s with a time resolution of 150 ms. The UV-visible spectrometer was synchronised at the millisecond timescale to gain complementary information and to provide a means of cross-checking the results.

In parallel with the experimental methodology, significant progress has recently been achieved concerning the theoretical analysis of the spectra. In particular, we have developed theoretical algorithms and the software program FitIt [2] for the refinement of the local structure from XANES, which is sensitive to many more structural parameters than EXAFS (more distant coordination shells, in many cases bond angles). For time-resolved data, our approach allows determination of both the percentage of structurally different species as a function of time and the structure of intermediates. This method combines principal component analysis (PCA) of the experimental data, multidimensional interpolation of XANES as a function of structural parameters, and *ab initio* XANES calculations. FitIt was used here for the analysis of a series of XANES spectra obtained in the time-resolved experiment.

We found that MTO in water has three water molecules coordinated to the metal. The best-fit values of structural parameters are Re=O distance of 1.69 Å and average Re–OH_2 distance of 2.85 Å.

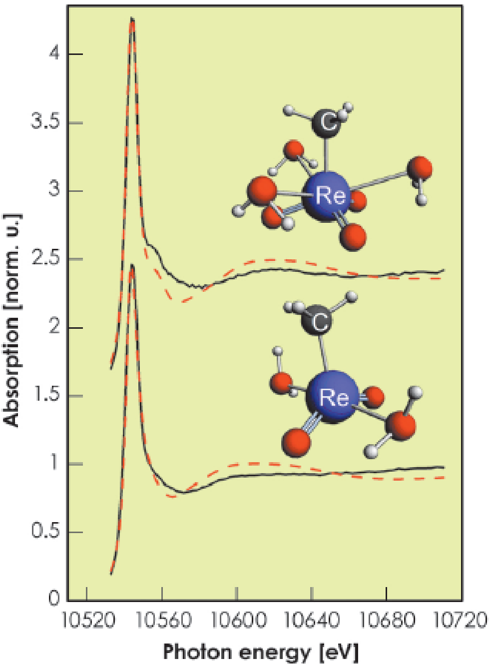

Fig. 100: Re L_3-edge XANES spectra of initial (top) and intermediate (bottom) complexes. Experimental (solid line) and theoretical (dashed line) spectra are shown. Structural models are shown in the insert. Re and C atoms are marked; grey (red) spheres are H (O) atoms.

Principal publication and authors

G. Smolentsev (a), G. Guilera (b), M. Tromp (c), S. Pascarelli (d) and A.V. Soldatov (a), *J. Chem. Phys.* **130**, 174508 (2009).

(a) Center for Nanoscale Structure of Matter, Southern Federal University, Rostov-on-Don (Russia)
(b) ALBA Synchrotron, Barcelona (Spain)
(c) University of Southampton (UK)
(d) ESRF

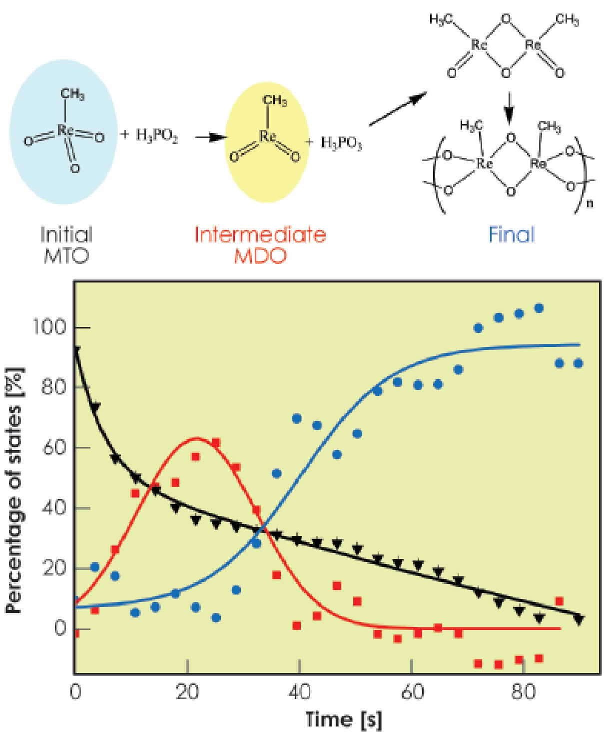

Fig. 101: Chemical reaction of MDO polymerisation and concentration profiles for the initial (black), intermediate (red) and final (blue) states.

These results are in agreement with X-ray diffraction and EXAFS fitting results, which gives credit to this method of determining the structures of unknown species. Furthermore, we found that at this time regime the reaction occurs via one single intermediate species (MDO) before polymeric MTO is formed. The best-fit structural parameters for MDO are Re=O distance of 1.71 Å and average Re–OH_2 distance of 2.13 Å. **Figure 100** shows theoretical and experimental spectra of both initial and intermediate species and **Figure 101** shows the corresponding concentration profiles of the reaction.

This significant finding illustrates the power and efficiency of this method of analysis for studying reactions in solution, the main advantage being the possibility to fit the structure of phases that cannot be isolated experimentally. This methodology can therefore be applied not only to chemistry in solution but also to a wide myriad of chemical transformations in heterogeneous environments.

References
[1] G.S. Owens, J. Arias, and M.M. Abu-Omar, *Catal. Today* **55**, 31 (2000).
[2] www.nano.sfedu.ru/fitit.html.

Redox-dependant sulphate coordination of neptunium in aqueous solutions

Principal publication and authors
C. Hennig (a),
A. Ikeda-Ohno (a,b),
S. Tsushima (a) and
A.C. Scheinost (a), *Inorg. Chem.* **48**, 5350 (2009).
(a) Institute for Radiochemistry, Forschungszentrum Dresden-Rossendorf (Germany)
(b) Synchrotron Radiation Research Center, Japan Atomic Energy Agency (Japan)

Neptunium is a by-product of nuclear energy generation. ^{237}Np accumulates during the reactor operation time and later in the nuclear waste repository in large quantities. Neptunium is considered to be one of the most problematic actinide elements for nuclear waste storage due to its rich redox chemistry combined with a relatively high solubility in aqueous solution [1]. Although the redox phenomena have been investigated for several decades, the underlying mechanisms and the coordination of the species are not well known. Extended X-ray absorption fine structure (EXAFS) spectroscopy, in combination with electrochemistry, is a powerful tool to determine the complex structure of Np species in aqueous sulphate solution as a function of the redox conditions. The experiments were performed at the Rossendorf Beamline (**BM20**), the only beamline at the ESRF dedicated to studies of actinides in solution.

The samples were prepared by dissolving $Np^{VI}O_2(ClO_4)_2 \cdot nH_2O$ in aqueous solutions of sulphate, to give an Np concentration of 0.05 M. Different neptunium oxidation states such as Np^{4+}, Np^{5+} and Np^{6+} were generated by potentiostatic electrolysis. Np L_3-edge EXAFS measurements were carried out in transmission mode using a Si(111) double-crystal monochromator, and two Pt-coated mirrors for rejection of higher harmonics.

Sulphate is able to coordinate neptunium either in monodentate or in bidentate coordination mode, as shown in **Figure 102**. Both modes can be differentiated by determining the

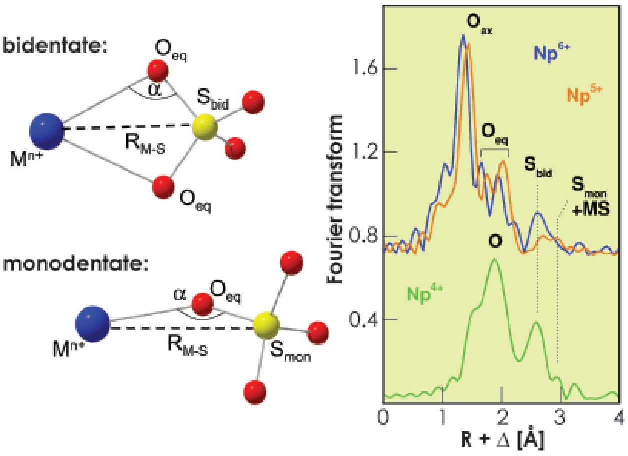

Fig. 102: a) Coordination mode of sulphate. b) Fourier Transforms of the Np L_3-edge EXAFS spectra of 0.05 M Np sulphate species in aqueous solution of 2.0 M $(NH_4)_2SO_4$.

distances between neptunium and sulphur atoms, R_{Np-S}, because sulphur is a relatively heavy backscatterer, easily detectable with EXAFS. The sulphate in bidentate coordination shows a Np-S_{bid} distance of ~3.1 Å, whereas monodentate sulphate shows a Np-S_{mon} distance of ~3.6 Å. At oxidation states V and VI, the complex structure is similar, which can be seen from the small changes in the spectra plotted on top of each other in **Figure 102**. Neptunium in these oxidation states forms trans-dioxo cations NpO_2^{n+} (n=1 and 2 for Np^{5+} and Np^{6+}, respectively). The two double-bond oxygens, commonly called axial oxygens (O_{ax}), do not easily form bonds with ligands. The sulphate coordination is hence restricted to the oxygen atoms in the equatorial plane (O_{eq}). The Np-O_{ax} bond length decreases from 1.83 Å (Np^{5+}) to 1.76 Å (Np^{6+}), indicative of a bond strength enhancement with increasing charge of neptunium. In non-complexing media the redox reaction is restricted to a fully reversible electron transfer according to NpO_2^{2+} + e- ↔ NpO_2^{+}. In complexing media this redox reaction can be disturbed by side reactions in the equatorial plane. This latter situation occurs by the sulphate coordination: the cyclovoltammogram shows a non-reversible character of the Np^{5+}/Np^{6+} redox couple at ~ 0.8 V (**Figure 103**). The EXAFS measurements show that bidentate sulphate coordination prevails at the hexavalent oxidation state, whereas for Np^{5+} the complexation is weaker and forms both mono- and bidentate sulphate complexes. The cyclovoltammogram shows also, that the Np^{4+}/Np^{5+} redox couple, occurring at ~ –0.4 V, is fully irreversible. The EXAFS spectrum of Np^{4+} indicates the loss of the axial oxygens and the formation of a quasi-spherical shell of oxygen atoms. These oxygen atoms belong to sulphate groups which are again predominantly bidentately coordinated.

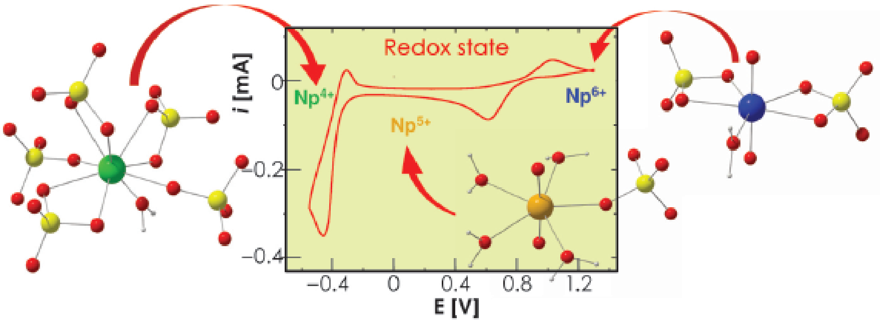

Fig. 103: Cyclic voltammograms of 0.05 M Np(VI) in an aqueous solution of 2.0 M $(NH_4)_2SO_4$ at pH 1.1, Au working electrode, start potential: 1.3 V, initial scan direction: cathodic, scan rate: 400 mV/s. The sulphate coordination of the Np^{4+}, Np^{5+} and Np^{6+} solution species is shown as ball and stick drawing.

The combined EXAFS and cyclovoltammetry data reveal an unexpected pattern of sulphate coordination and redox behaviour: although the actinyl ion NpO_2^{n+} remains preserved in the redox reaction between Np^{5+} and Np^{6+}, the sulphate coordination in the equatorial plane changes. This results in a deviation from the usual reversible redox behaviour. In contrast, the irreversible nature of the transition from Np^{5+} to Np^{4+} is expected due to the loss of the axial oxygen atoms and the complete replacement of water ligands by sulphate. This example demonstrates that EXAFS is able to detect the reaction mechanisms of quasi-reversible and even irreversible redox reactions.

References

[1] Z. Yoshida, S. G. Johnson, T. Kimura, J. R. Krsul, in *The Chemistry of the Actinide and Transactinide Elements (3rd Ed.)*, L. R. Morss, N. M. Edelstein, J. Fuger (Eds.), Springer, 699 (2006).

Acknowledgment

This work was supported by the Deutsche Forschungsgemeinschaft, Contract HE2297/2-2.

Structural biology

2009 has been an extremely productive and successful year for the Structural Biology Group and the scientific community that uses the ESRF's facilities. No doubt the highlight has been the award of the Nobel Prize for Chemistry to Ada Yonath, from the Weizmann Institute (Israel) and Venkatraman Ramakrishnan, of the MRC Laboratory of Molecular Biology in Cambridge (UK), both of whom are long-term users of the ESRF. They share the prize with Thomas Steitz, from Yale University. As well as being regular users of the MX beamlines, these scientists, their groups and the projects they bring with them have contributed extensively to the increased automation and sophistication of the beamlines.

The conversion of beamline ID14-3 to a protein solution scattering beamline is almost complete. The beamline is operated as a collaboration between the ESRF and the EMBL Grenoble outstation and was officially inaugurated during the Council meeting in June 2009. Through a trilateral collaboration between the ESRF and both Grenoble and Hamburg EMBL outstations, equipment has been developed which, it is hoped, will enable higher throughput and increased reliability. Whilst still in its prototype stage, the liquid handling robot has proved a great success with the users of this beamline. Articles from the beamline are now reaching the publication stage and the very first results are reported here. Access to complementary facilities for protein solution scattering continues to be improved. We have completed the first stages of setting up a joint application procedure for small-angle neutron scattering (ILL) and X-ray scattering (ESRF) experiments.

The highlights presented in this chapter demonstrate the increasing complexity, medical relevance and impact of structural biology research undertaken at the ESRF. The articles cover a wide range of current research and demonstrate the ongoing vitality and pertinence of the field. The first steps towards regenerating the ESRF Structural Biology programme will start in 2010 with the construction of the (eventual) replacement for ID14, beamline ID30. This new beamline will further develop the sophistication and automation of the elusive hunt for crystals that diffract. We confidently expect that this facility will ultimately provide a paradigm shift in the prosecution of structural biology using synchrotron radiation. We look forward to an exciting 2010.

G. Leonard
and S. McSweeney

A. Yonath and V. Ramakrishnan outside the latter's lab at the MRC Laboratory of Molecular Biology in Cambridge, September 2009 (*Photo courtesy of M. Schmeing*).

Complement activation and regulation based on crystal structures of $(C3bBb\text{-}SCIN)_2$ and C3b-factor H(1-4)

The complement cascade is an ancient defence mechanism of the mammalian immune system that consists of more than 30 proteins circulating in blood and fluids surrounding tissues or present on cell surfaces. Activation of the complement system generates potent chemoattractants and markers for immune clearance that covalently attach to cell surfaces. Amplification of this process by the alternative pathway is mainly determined by the formation of short-lived protease complexes, known as C3 convertases (half-life time of ~90 seconds). C3 convertase cleaves the central complement component C3 into its active form C3b, which exposes its thioester bond through which it covalently attaches to nearby surfaces. This process must be tightly controlled by complement regulators in order to prevent non-specific attack of host cells. These regulators stop C3b production either by accelerating the decay of the C3 convertases or by serving as a cofactor for protease factor I (FI) in degrading existing C3b (thereby preventing formation of new convertases). Factor H (FH) is a highly abundant, soluble complement regulator, which can either function in the fluid phase or on the host cell surface by recognition of host specific components, such as glycosaminoglycans.

The unstable C3 convertase complex (of the alternative pathway) is formed by the 12-domain ligand C3b and the 2-domain protease fragment Bb. An immune evasion protein SCIN secreted by *Staphylococcus aureus* was used to stabilise the C3 convertase. The structure of the resulting complex $(C3bBb\text{-}SCIN)_2$, with MW ~500 kDa, was determined at 3.9 Å resolution using diffraction data collected on beamline **ID14-4**. In the dimer arrangement seen in the crystal, the two convertase complexes are arranged with C2 symmetry (**Figure 104**). In each monomer, the protease fragment Bb is attached to the C-terminal Asn 1641 of C3b. This residue chelates the Mg^{2+} bound in the metal ion-dependent adhesion site (MIDAS) in Bb. SCIN stabilises dimer formation of the C3 convertase complex by bridging the opposing C3b molecules. The dimeric arrangement yields unprecedented structural insights into the unique substrate specificity and enzymatic activity of this protease complex. Substitution of one C3b by the substrate C3 places the scissile bond of C3 in front of the active site of the opposing C3bBb complex. This hypothetical enzyme:substrate model explains the activity of three inhibitors that block the substrate binding to C3 convertases. Thus, specificity and activity of the C3 convertase is likely to be determined by dimerisation of the substrate C3 with the cleavage product C3b that serves as a ligand in the C3bBb protease.

To gain insight into complement regulation, we solved the crystal structure of C3b in complex with the first four 'complement-control protein' (CCP) domains of FH (FH(1-4)) to 2.7 Å resolution, using data collected at **ID14-4**. The structure reveals an

Principal publications and authors

J. Wu (a), S.H.M. Rooijakkers (b), M. Ruyken (b), R. van Domselaar (b), K.L. Planken (c), A. Tzekou (d), D. Ricklin (d), J.D. Lambris (d), B.J.C. Janssen (a), J.A.G. van Strijp (b) and P. Gros (a), *Nature Immunology* **10**, 721-727 (2009);
J. Wu (a), Y.-Q. Wu (d), D. Ricklin (d), B.J.C. Janssen (a), J.D. Lambris (d) and P. Gros (a), *Nature Immunology* **10**, 728-733 (2009).

(a) Crystal and Structural Chemistry, Bijvoet Center, Utrecht University (The Netherlands)
(b) Medical Microbiology, University Medical Center Utrecht (The Netherlands)
(c) Van 't Hoff Laboratory for Physical and Colloid Chemistry, Utrecht University (The Netherlands)
(d) Department of Pathology & Laboratory Medicine, University of Pennsylvania (USA)

Fig. 104: Crystal structure of the labile C3 convertase (C3bBb) stabilised by the staphylococcal complement inhibitor SCIN. The observed dimeric arrangement suggests that substrate specificity and catalytic activity is determined by dimerisation of the substrate C3 and ligand C3b.

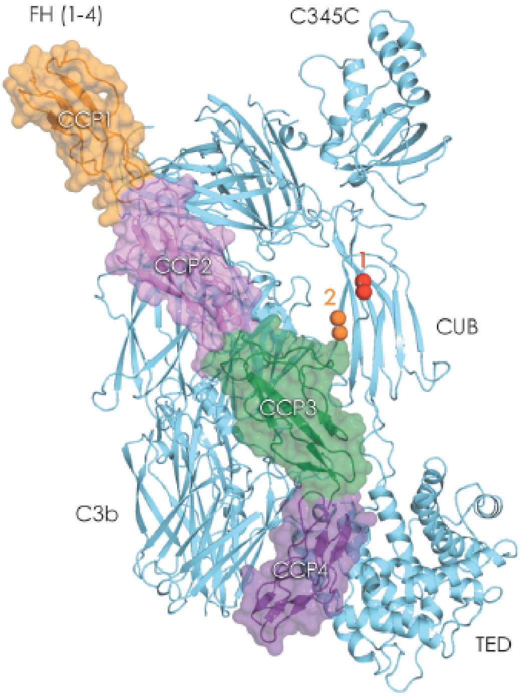

Fig. 105: Crystal structure of C3b in complex with FH domains 1-4. FH domains 1-2 are likely to be directly responsible for displacing the protease fragment Bb from the C3bBb complex. In addition, C3bFH provide a binding place for the protease FI, putatively involving CCP1-3 of FH and domains C345C and CUB of C3b. FI cleaves the chain of the CUB domain of C3b twice (scissile bonds are indicated in spheres) to produce inactive iC3b.

extensive and discontinuous interface between FH(1-4) and C3b that stretches over a distance of 100 Å and buries an area of 4,500 Å^2 (**Figure 105**). Comparison of C3b-FH(1-4) and C3bBb indicates a functional role for domains CCP1-2 of FH in displacing Bb from C3b, which underpins the 'decay acceleration activity'. Moreover, FH(1-4) binds adjacent to the CUB domain of C3b that contains two cleavage sites for the protease FI. This arrangement and biochemical data suggest that in 'cofactor activity' FH domains CCP1-3 and possibly C345C and CUB of C3b form the binding site for FI. Additional contacts between CCP4 and the thioester domain may stabilise the overall arrangement while the protease makes consecutive cuts in the chain of the bridging CUB domain.

Molecular basis for activation of Rho GTPases by DOCK guanine nucleotide exchange factors

Principal publication and authors
J. Yang, Z. Zhang, S.M. Roe, C.J. Marshall and D. Barford,
Science **325**, 1398-1402 (2009).
Institute of Cancer Research, Chester Beatty Laboratories, London (UK)

Malignant tumour cells are characterised by their abilities to invade local tissues and migrate (metastasis) to sites separate from the primary tumour. Metastasis is the main factor accounting for cancer treatment failure and is responsible for 90% of cancer deaths. Thus, intensive research efforts are directed at understanding the cellular and molecular basis of tumour cell motility and invasion.

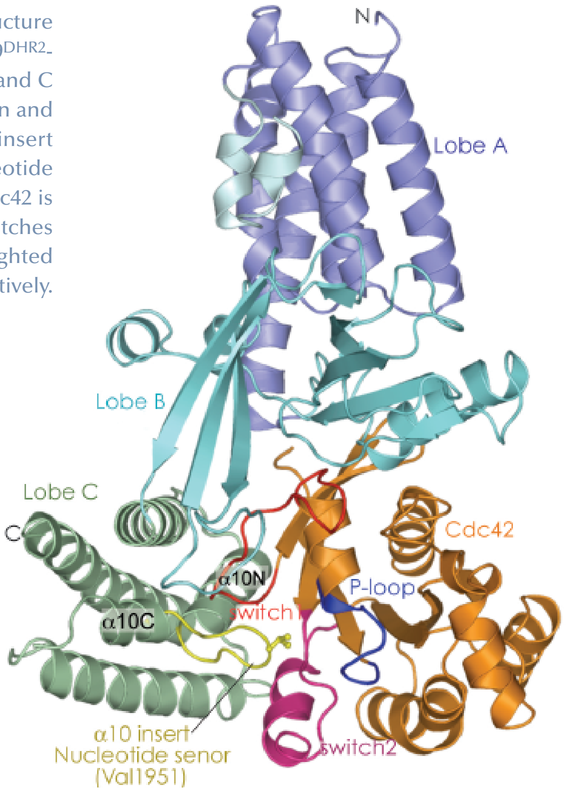

Fig. 106: View of the crystal structure of the nucleotide-free DOCK9^{DHR2}-Cdc42 complex. Lobes A, B, and C are coloured in blue, cyan and green respectively. The α10 insert containing the Val 1951 (nucleotide sensor) is shown in yellow. Cdc42 is coloured orange with switches 1 and 2 and the P loop highlighted in red, purple and blue respectively.

Eukaryotic cells undergo cell migration through dynamic changes in their actin-based cytoskeleton, in a process controlled by small GTPases of the Rho family and coupled to reversible protein phosphorylation. Rho GTPases inter-convert between inactive GDP-bound and active GTP-bound states, a process controlled by guanine nucleotide exchange factors (GEFs) that catalyse exchange of GDP for GTP at the nucleotide-binding site. Two distinct families of Rho GEFs, Dbl homology (DH) and DOCK, activate Rho GTPases [1,2]. DOCK proteins have been implicated in the activation of Rac and Cdc42 in cell migration, morphogenesis and phagocytosis [3,4] and have been shown to be important components in tumour cell movement and invasion. DOCK9 belongs to the D subfamily of Rho GEFs that specifically activate Cdc42.

Prior to our work, the structural basis of nucleotide release catalysed by the DH family of Rho GEFs had been established but the molecular mechanisms of DOCK proteins were unknown. Moreover, the structural events that occur when GTP binds to a GEF-GTPase complex, immediately preceding discharge of the activated GTPase, had not been defined. To understand these processes we investigated the catalytic GEF domain of DOCK9. The catalytic domains of GEFs form stable complexes with nucleotide free GTPases. To determine the structure of a DOCK9 DHR2 domain ($\text{DOCK9}^{\text{DHR2}}$) in complex with the Rho GTPase Cdc42, we collected single wavelength anomalous dispersion data at beamline **ID29**. We found that the DOCK9 DHR2 domain, which has a different structure from DH GEF catalytic domains, is organised into three lobes of roughly equal size (lobes A, B and C), with the Cdc42-binding site and catalytic centre generated entirely from lobes B and C (**Figure 106**). Lobe A is an anti-parallel array of five α-helices and forms extensive contacts with lobe B to stabilise the DOCK9 DHR2 domain. Lobe B adopts an unusual architecture comprising two anti-parallel β-sheets disposed in a loosely packed orthogonal arrangement. Lobe C is a four-helix bundle. Helix α10 of lobe C, the most conserved region of DHR2 domains is interrupted by a seven-residue loop - the α10 insert (nucleotide sensor).

The first step of the exchange cycle is to promote nucleotide release by inducing a reduced affinity for nucleotide (**Figure 107**). This is achieved as follows: Upon binding to $\text{DOCK9}^{\text{DHR2}}$, first the conformational transition of switch 1 of Cdc42 exposes the nucleotide-binding site. Second, this movement of switch 1 is linked to rotation of the P-loop Cys 18 thiol group that disrupts a hydrogen bond with the nucleotide α-phosphate. Third, by intruding into the GTPase nucleotide-binding site, Val 1951 of the $\text{DOCK9}^{\text{DHR2}}$ α10 insert directly occludes nucleotide-coordinated Mg^{2+}. Because magnesium enhances nucleotide affinity by neutralising the negatively charged phosphate groups, its exclusion profoundly reduces nucleotide affinity.

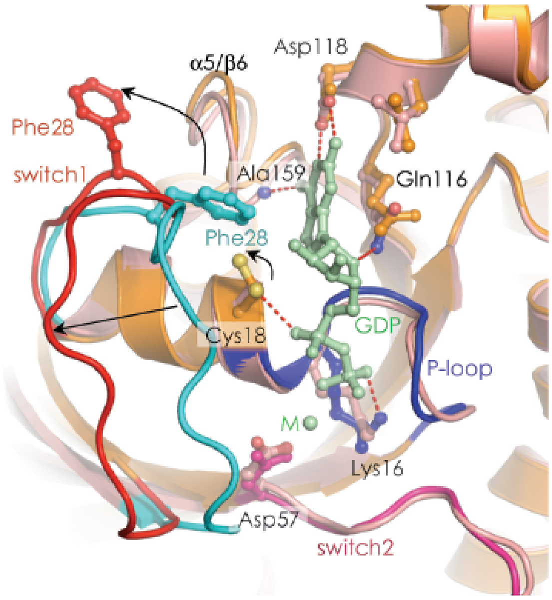

Fig. 107: The mechanism of $\text{DOCK9}^{\text{DHR2}}$-mediated nucleotide release. The conformational transition of switch 1 of Cdc42 is shown with an arrow indicating the motion of the Cys18 thiol.

To understand the second step of the exchange cycle, loading of GTP-Mg^{2+} and discharge of the activated Cdc42-GTP-Mg complex, we determined the structure of a GTP-bound ternary complex (data collected at DLS 104). We found that in this structure, Mg^{2+} bound to GTP caused a displacement of the α10 insert that removes the clamp from switch 1, and induces a set of interdependent conformational changes within other regions of the $\text{DOCK9}^{\text{DHR2}}$-Cdc42 interface. This reorganisation of the complex disrupts $\text{DOCK9}^{\text{DHR2}}$ contacts to switch 1. In this process activation of Cdc42 is detected by the presence of Mg^{2+} tightly bound to GTP, triggering displacement of the α10 insert and propagation of conformational changes to the $\text{DOCK9}^{\text{DHR2}}$-Cdc42 interface. Because GDP does not induce equivalent conformational changes, GTP may specifically promote discharge of the GTP-bound Cdc42 from $\text{DOCK9}^{\text{DHR2}}$ to complete the catalytic exchange reaction. Thus, the α10 insert of DOCK proteins acts as sensor of the GDP and GTP bound states of Rho GTPases to mediate the catalytic cycle of GDP release and subsequent discharge of the GTP-bound, activated GTPase.

References

[1] J.L. Bos, H. Rehmann and A. Wittinghofer, *Cell* **129**, 865-877 (2007).
[2] K.L. Rossman, C.J. Der and J. Sondek, *Nat Rev Mol Cell Biol* **6**, 167-180 (2005).
[3] J.F. Cote and K. Vuori, *Trends Cell Biol* **17**, 383-393 (2007).
[4] N. Meller, S. Merlot and C. Guda, *J Cell Sci* **118**, 4937-4946 (2005).

Principal publication and authors

A. Guskov (a), J. Kern (b, c), A. Gabdulkhakov (a), M. Broser (b), A. Zouni (b) and W. Saenger (a), *Nat. Struct. Mol. Biol.* **16**, 334 (2009).

(a) Institut für Chemie und Biochemie/Kristallographie, Freie Universität Berlin (Germany)

(b) Institut für Chemie/Max Volmer Laboratorium für Biophysikalische Chemie, Technische Universität Berlin (Germany)

(c) Physical Biosciences Division, Lawrence Berkeley National Laboratory, Berkeley (USA)

Abundance of cofactors in photosystem II

Oxygenic photosynthesis is driven by photosystems I and II (PSI and PSII), two large protein-cofactor complexes found in the thylakoid membranes of plants, algae and cyanobacteria. The structure of PSII is of special interest as it contains the unique Mn_4CaO_x cluster that catalyses the photolysis of water: $2H_2O \rightarrow O_2 + 4H^+ + 4e^-$. These electrons reduce plastoquinone (PQ) at the Q_B-site to plastoquinol (PQH_2) with the concomitant uptake of protons from the cytosol:

$$PQ \xrightarrow{+2e^- +2H^+} PQH_2$$

The crystal structure of homodimeric PSII at 2.9 Å resolution was determined from data collected at beamline ID14-2. Each monomer (see Figure 108) contains 20 assigned protein subunits and 92 cofactors (35 chlorophylls, two pheophytins, two haems, 12 β-carotenoids, 25 lipids, seven detergent molecules (β-dodecylmaltoside), three plastoquinones, the Mn_4Ca cluster, one bicarbonate, two Ca^{2+}, one Fe^{2+}, and one Cl^-). The surprisingly high amount of lipids in comparison with other complexes involved in oxygenic photosynthesis might be related to special functions of lipids in PSII. Lipids found at the monomer-monomer interface and around the reaction centre seem to be an ideal lubricating component involved in the processes of dis- and reassembly of PSII needed for the replacement of photodamaged subunit D1 [1]. The largest lipid cluster, composed of eight lipids, forms an intrinsic lipid bilayer providing a hydrophobic environment in the large plastoquinone/plastoquinol exchange cavity that features two channels connecting the binding site of plastoquinone Q_B with the plastoquinone pool in the thylakoid membrane. A newly observed third plastoquinone (Q_C), in combination with the positions of the channels, allowed us to propose possible mechanisms for rapid plastoquinone/plastoquinol exchange in PSII (Figure 109): a) alternating mechanism, where both channels work as entry/exit in an alternating way; b) wriggling, where one channel is exclusively for entry and the other is only for exit; c) single channel mechanism, where only one channel is involved in plastoquinone/plastoquinol exchange.

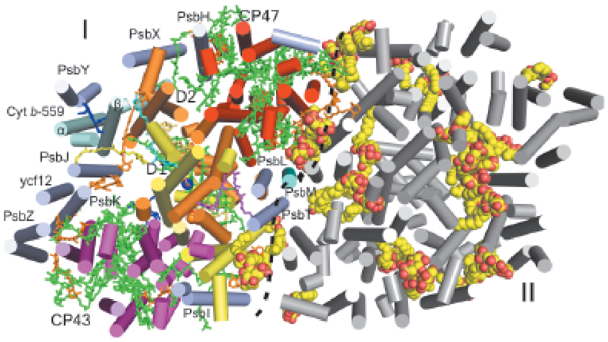

Fig. 108: The homodimeric PSII complex. Overview of PSII from the cytoplasmic side (membrane-extrinsic subunits omitted). The monomer-monomer interface is indicated by a black dashed line. Helices are shown as cylinders with the subunits D1 (yellow), D2 (orange), CP43 (magenta), CP47 (red), cyt b-559 (cyan, subunits α and β) and the remaining eleven small subunits (light blue) labelled in monomer I. Cofactors are shown as stick models: Chl (green), Car (orange), haem (blue). In monomer II (grey helices), lipids and detergents are shown as spheres (carbon yellow, oxygen red).

Additionally, four smaller lipid clusters within the PSII monomer may participate in auxiliary oxygen channelling to the cytosolic side of the thylakoid membrane. This is shown by the positions of xenon atoms in the crystal structure of PSII derivatised with gaseous xenon (part of the data collected at beamlines ID23-1 and ID23-2) that might indicate pathways for oxygen release from the Mn_4CaO_x cluster.

A combination of native and anomalous data (collected at ID29) allowed us to assign unambiguously a chloride ion (as

Fig. 109: Simplified scheme of plastoquinone/plastoquinol exchange in PSII. a) Alternative mechanism, both channels work as entry/exit; b) wriggling – channel I is only for entry and channel II for exit; c) single channel mechanism – only channel II is used for exchange. Red arrows indicate movement of PQ, blue of PQH_2. See principal publication for details.

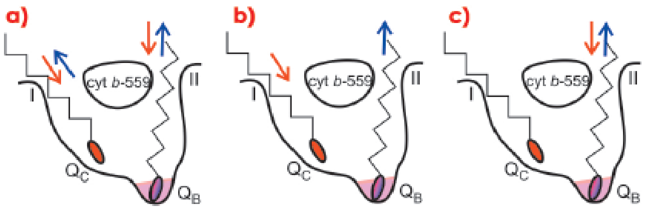

well as its analogue bromide) in close vicinity to the Mn_4CaO_x cluster. The chloride ion is located 6.5 Å from the cluster in a positively charged environment provided by strictly conserved amino acids and connected with the cluster via putative water molecule(s). A possible shift in the position of Mn ions due to radiation damage (reduction of Mn(III) and Mn(IV) to Mn(II)) must be kept in mind.

Theoretical calculations using the obtained structural model allowed us to describe a complex transport system within PSII. The arrangement of possible substrate and product channels suggests a strict spatial separation of water, oxygen and proton fluxes to and from the Mn_4CaO_x cluster. We identified nine distinct channels connecting the cluster with the lumenal side of PSII, the four wider ones and the five narrower ones being possible water and oxygen or proton channels, respectively. The position of chloride in the proton channel(s) might be necessary to facilitate proton escape from the cluster by tuning pKa values of the surrounding amino acids and excludes its direct involvement in the water splitting chemistry. The nature of the oxygen channels was recently confirmed by derivatisation of PSII crystals with gaseous krypton and co-crystallisation with DMSO [2].

Acknowledgements

This work was supported by grants from the German Research Council (SFB 498, projects A4, C7).

References

[1] Y. Nishiyama, S.I. Allakhverdiev and N. Murata, *Biochim Biophys Acta* **1757**, 742 (2006).

[2] A. Gabdulkhakov, A. Guskov, M. Broser, J. Kern, F. Müh, W. Saenger and A. Zouni, *Structure* **17**, 1223 (2009).

Complex between Neisseria meningitidis factor H binding protein and two domains from human complement factor H

Principal publication and authors

M.C. Schneider (a,d), B.E. Prosser (b), J.J.E. Caesar (b), E. Kugelberg (a), S. Li (a), Q. Zhang (a), S. Quoraishi (b), J.E. Lovett (b), J.E. Deane (b), R.B. Sim (c), P. Roversi (b), S. Johnson (b), C.M. Tang (a), and S.M. Lea (b), *Nature* **458**, 890-893 (2009).

(a) Centre for Molecular Microbiology and Infection, Imperial College, London (UK)

(b) Sir William Dunn School of Pathology, University of Oxford (UK)

(c) MRC Immunochemistry Unit, Department of Biochemistry, University of Oxford (UK)

(d) Present address: Harvard Medical School, Boston, Massachusetts (USA)

Complement is an essential component of the innate and acquired immune system, and consists of a series of proteolytic cascades that are initiated by the presence of micro-organisms. In health, activation of complement is precisely controlled through membrane-bound and soluble plasma-regulatory proteins including factor H (fH), a 155 kDa protein composed of twenty domains (termed complement control protein repeats, or CCPs). Many pathogens have evolved the ability to avoid immune-killing by recruiting host complement regulators and several pathogens have adapted to avoid complement-mediated killing by sequestering fH to their surface. Using data collected at both the ESRF (**ID29** and **BM14**) and Diamond (UK) we have solved the first crystal structure of a complement regulator in complex with its pathogen surface-protein ligand (**Figure 110**). This reveals

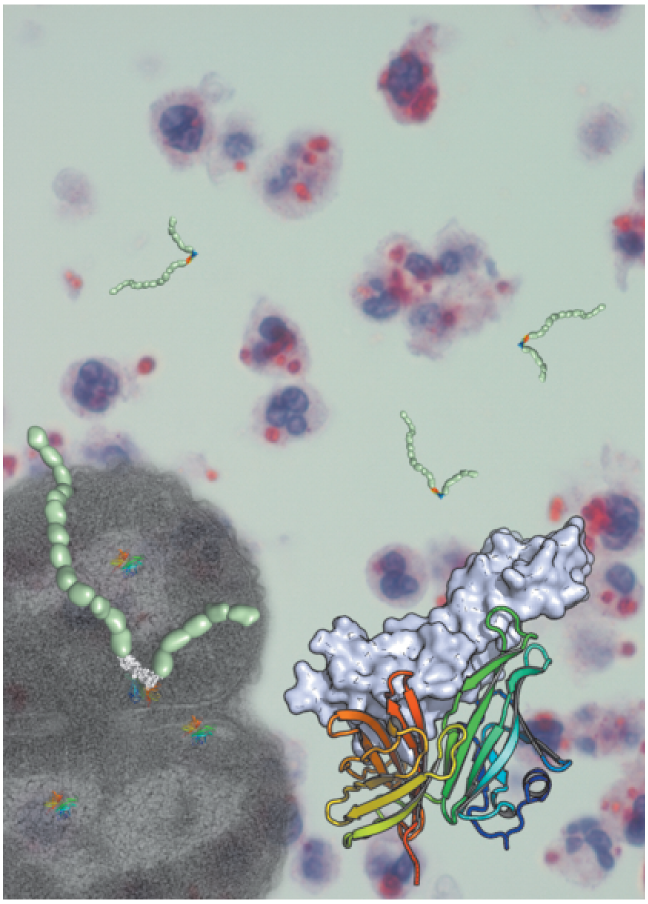

Fig. 110: The foreground shows a representation of two SCR domains from complement factor H (grey surface) in complex with the Neisserial factor H binding protein (cartoon, rainbow colouring). In the background an electron micrograph of *Neisseria meninigitidis* is overlaid on a field of *N. meninigitidis* infecting cells.

Acknowledgements
This work was funded by grants from the Wellcome Trust and the Medical Research Council UK to SML and CMT. EK is an EMBO Fellow.

how the important human pathogen *Neisseria meningitidis* subverts immune responses by mimicking the host, using protein instead of charged-carbohydrate chemistry to recruit the host complement regulator, factor H.

The structure also indicates the molecular basis of the host-specificity of the interaction between factor H and the meningococcus, and informs attempts to develop novel therapeutics and vaccines.

Principal publication and authors
A.S. Doré (a), M.L. Kilkenny (a), N.J. Rzechorzek (a,b) and L.H. Pearl (a), *Mol. Cell*, **34** (6), 735-745 (2009).
(a) CR-UK DNA Repair Enzymes Group, Section of Structural Biology, The Institute of Cancer Research, London (UK)
(b) Department of Biochemistry, University of Cambridge (UK)

DNA Damage? Call 9-1-1

Eukaryotic cells respond to DNA damage through a coordinated response in which repair systems are recruited, and the cell cycle arrested, until the damage has been rectified or terminated by apoptosis if too extreme. One such DNA damage sensor is the multifunctional heterotrimeric DNA sliding clamp complex, Rad9-Rad1-Hus1 (9-1-1). In response to DNA damage, 9-1-1 is loaded onto DNA by a specialised form of the replication factor C (RFC) complex. Cell-cycle signalling is then mediated by multiple complexes, specifically the recruitment/stimulation of the checkpoint kinase ATR/ATRIP complex, and ultimately Chk1. 9-1-1 may also play a direct role in DNA damage repair via interaction with a number of DNA repair client enzymes including 'long-patch' (or 'PCNA-scaffolded') DNA base excision repair components and trans-lesion polymerases.

The crystal structure of the human 9-1-1 complex at 2.9 Å resolution was determined using data collected on **ID14-1** and **ID29**. As previously suggested, 9-1-1 has a toroidal architecture similar to PCNA and other DNA clamps (**Figure 111a**). The 9-1-1 ring encompasses an elliptical hole of sufficient size to accommodate a DNA duplex as experimentally observed for the bacterial β-clamp. The individual subunits have the same secondary structure topology as other DNA clamps with the outside of the ring formed by faces of β-sheets, and the hole, lined by α-helices, presenting a basic inner surface to interact with the DNA backbone (**Figure 111b**).

As a heterotrimer, 9-1-1 has a chiral arrangement, with Rad9, Rad1 and Hus1 in anti-clockwise order as viewed from the 'top' (studies of PCNA have defined the 'top' being the face that provides the binding sites for client enzymes) (**Figure 111b**). Inspection of the intermolecular subunit interfaces shows clear sterical and chemical specificity for this chiral arrangement.

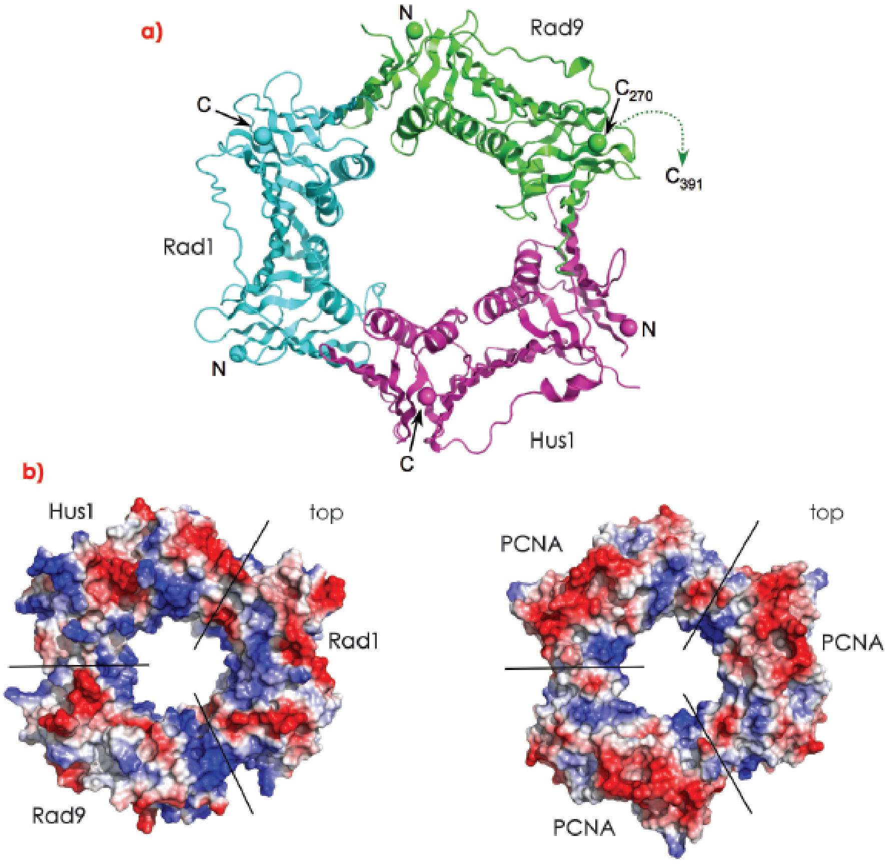

Fig. 111: Structure of the Rad9-Rad1-Hus1 complex. a) Secondary structure cartoon of the 9-1-1 ring, coloured: Rad9-green, Rad1-cyan and Hus1-magenta. The unstructured ~120 residue C-terminal tail of Rad9 is marked. b) Electrostatic surfaces of 9-1-1 (left) and PCNA (right). Both clamps exhibit strong positive potential (blue) around the central channel through which DNA passes.

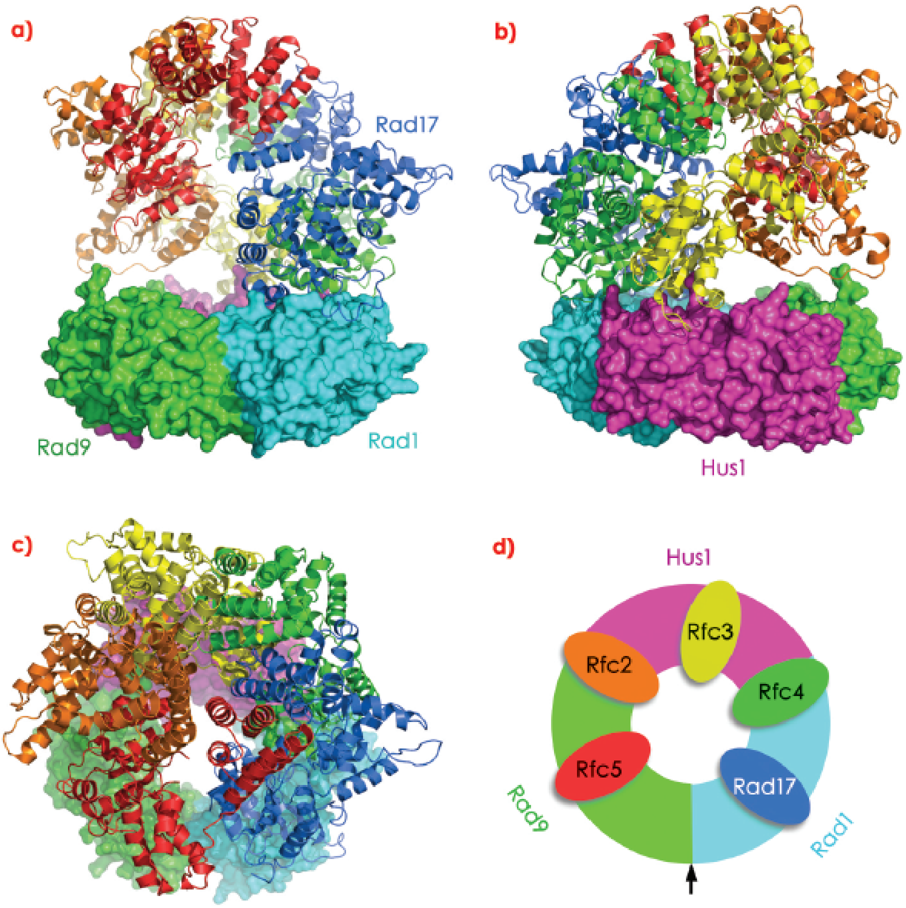

Fig. 112: Clamp loader interactions with 9-1-1. a) Model of a 9-1-1-Rad17-RFC complex. In this model, Rad9 and Hus1, interact with the Rfc2,3,4 and 5 subunits, while Rad1 presents a distinct interaction surface to interact with the 9-1-1-specific Rad17 subunit.
b) As a) but rotated 180° around the vertical.
c) As a) but rotated 90° around the horizontal.
d) Schematic of the modelled interactions between Rad17-RFC and 9-1-1. The arrow denotes the predicted 9-1-1 “break-point” for DNA loading.

The 9-1-1 subunits also show substantial differences in structure, particularly in the region that in PCNA provides the typical binding site for ligand proteins (Figure 111a) [1]. Classically, proteins binding to PCNA contain a ‘PIP’ box motif and involve the insertion of three hydrophobic side chains on a short helical segment into a pocket on PCNA. Ligand residues C-terminal to this hydrophobic PIP-box motif may also form an anti-parallel β-sheet interaction with the inter-domain linker (IDL) connecting the two lobes of the PCNA monomer. The IDL segments in all three 9-1-1 subunits are well ordered and exhibit different conformations (Figure 111a). While Rad9 could accommodate a hydrophobic PIP-box motif, this binding pocket is completely blocked in Rad1, and partially blocked in Hus1.

Like PCNA, 9-1-1 is loaded onto DNA via a ring-open intermediate in an ATP-dependent mechanism mediated by the specialised Rad-RFC complex where the Rfc1 subunit is replaced by Rad17. Crystallographic analysis of a yeast RFC-PCNA complex in the presence of ATPγS [2] reveals a complex pattern of interactions between the RFC complex and hydrophobic PIP-box binding pockets on PCNA. With the determined structure of the 9-1-1 IDLs, and availability of the hydrophobic PIP-box binding pockets in each subunit, it is possible to model a 9-1-1-Rad17-RFC complex (Figure 112). This maps the biochemically predetermined break point in PCNA to the Rad9-Rad1 interface in 9-1-1, the least substantial of the three interfaces – burying only ~1100 Å^2, and is consistent with biochemical data.

Finally, we found that interaction of ligand proteins with 9-1-1 appears to be regulated by genotoxic stress, with the cell cycle regulator $p21^{cip1/waf1}$ binding to 9-1-1 in competition with the LP-BER component FEN1. Unlike PCNA, which as a homotrimer possesses three equivalent binding sites, there appears to be a single site on the 9-1-1 heterotrimer to which FEN1 and $p21^{cip1/waf1}$ bind in competition.

The crystal structure of 9-1-1 provides a clear molecular view of this multifunctional checkpoint clamp revealing significant differences between the three subunits. In particular, the PIP-box binding pocket which provides the main binding site for ligand proteins, is substantially altered in all the subunits of 9-1-1 with implications for clamp loading via the Rad17-RFC complex and regulation through cell cycle regulators such as $p21^{cip1/waf1}$.

References

[1] J.M. Gulbis, Z. Kelman, J. Hurwitz, M. O’Donnell and J. Kuriyan, *Cell*, **87**, 297-306 (1996).
[2] G.D. Bowman, M. O’Donnell and J. Kuriyan, *Nature*, **429**, 724-730 (2004).

Structure of a bacterial homologue of a ligand-gated ion channel

Principal publication and authors
N. Bocquet (a), H. Nury (a), M. Baaden (b), C. Le Poupon (a), J-P. Changeux (a), M. Delarue (a) and P.-J. Corringer (a), *Nature* **457**, 111 (2009).
(a) Pasteur Institute, Paris (France)
(b) Institut de Biologie Physico-Chimique, CNRS UPR 9080, Paris (France)

Cell-cell communication in both the central nervous system and peripheral nervous system occurs through the release in the synaptic cleft of a small chemical called a neurotransmitter (*e.g.* acetylcholine) followed by its capture by a corresponding receptor. This receptor then transforms a chemical event into an electrical event by opening the pore in its transmembrane domain (TMD) to a flux of ions which are then free to diffuse through the cell membrane down an electrochemical gradient. The molecular basis of this phenomenon, known as signal transduction, is still largely unknown and the subject of very active research.

Among ligand-gated ion channel receptors, members of the so-called Cys-loop family have been intensively studied because of their potential pharmacological properties [1].
This family comprises both cationic channels (*e.g.* acetylcholine and 5HT3 (serotonin) receptors) and anionic channels (*e.g.* glycine and GABA (γ-aminobutyric acid) receptors). Until very recently, the structural information available on this family of proteins was limited to crystal structures of extra cellular domains (ECDs) [2] and a low-resolution (4 Å) model of a full-length protein derived from cryo-EM data [3]. The situation changed dramatically after the discovery of other members of this family in the bacteria [4]. This resulted in the 3.3 Å structure of a full-length Cys-loop family receptor (ELIC) from the bacterium *Erwinia chrysantema.* This structure showed the pore of the receptor in a closed conformation [5].

Our groups focused on a receptor (GLIC) from *Gloeobacter violaceus*, a very ancient cyanobacterium. On a functional level, we showed that this ion-channel can be activated by protons [6]. On a structural level we were able to solve its structure, at acidic pH and 2.9 Å resolution, using diffraction data collected at beamlines **ID14-EH1** and **ID23-1**. Hundreds of crystals had to be screened to find the one that finally allowed the structure determination and access to synchrotron radiation and highly automated beamlines was essential to the success of this project.

Once the structure was revealed, it was apparent that, contrary to ELIC, the pore was in an open conformation. This was to be expected given the acidic pH of the crystallisation conditions. This opened up the possibility of discussing possible mechanisms of cys-loop receptor gating by comparing GLIC and ELIC crystal structures and restricting the analysis to common core residues (the two receptors have only 18% amino acid sequence identity). Among the different structural rearrangements between the two forms, a so-called twist movement, previously identified by normal mode analysis, was prominent.

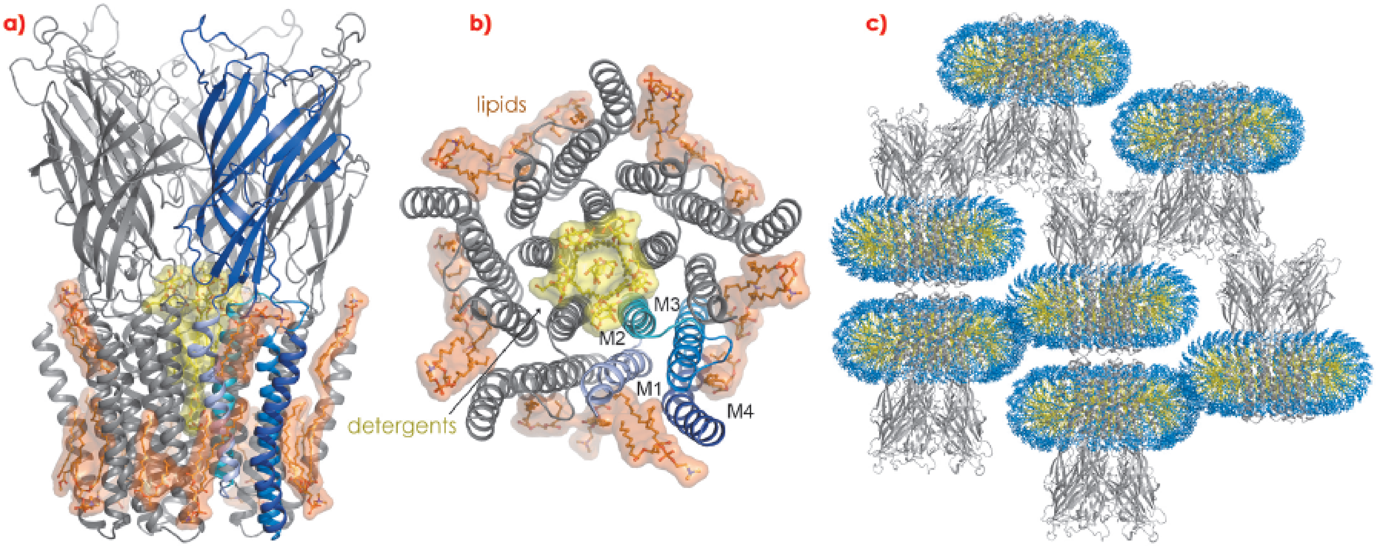

Fig. 113: General view of the crystal structure of the full-length ligand-gated bacterial ion channel GLIC: a) side view, b) top view c) packing interactions with modelled micelle in the crystal.

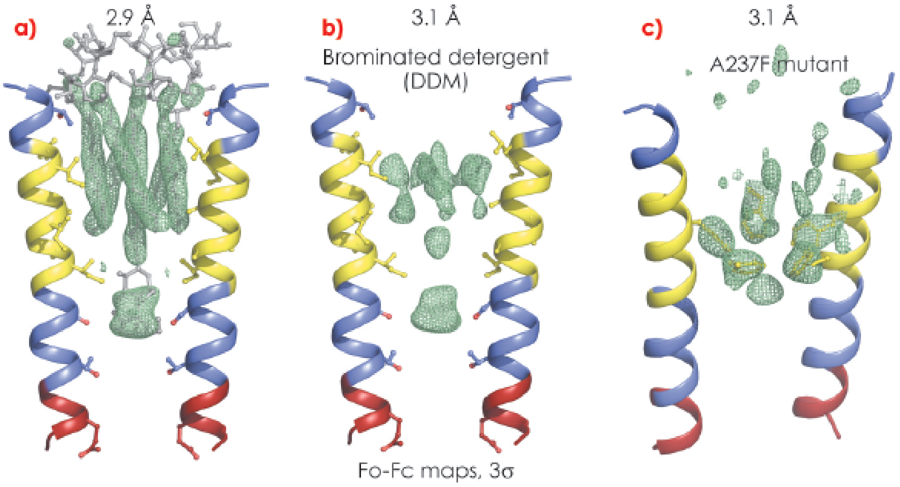

Fig. 114: Experimental electron density for the detergents in the pore: a) wild type protein with DDM (*n*-decyl-β-D-maltopyranoside), b) wild type protein with brominated DDM, c) A237F mutant with DDM.

In the crystal structure of GLIC, some lipids were readily seen in the electron density in the vicinity of the TMD (**Figure 113a,b**). Modelling of the micelle "belt" around the TMD, compatible with the number of detergents bound in solution as determined from sedimentation experiments, resulted in a model entirely compatible with the crystal packing (**Figure 113c**). However, the big surprise in the crystal structure was that there was clear electron density in the pore itself. This could be unambiguously attributed to detergent molecules used to solubilise the protein (**Figure 114a**). *N.B.* The shape of the electron density does not change if one truncates the data to 3.1 Å.

To convince ourselves that the open pore conformation observed was not influenced by the binding of detergent inside it, we performed two other experiments: i) we collected diffraction data in the presence of *brominated* detergent, whose larger volume would suggest that all six detergent molecules seen in the original structure cannot bind simultaneously. We found an unaltered pore structure and a much weaker electron density for the detergents (**Figure 114b**); ii) we collected diffraction data for a mutant A237F where the side-chain phenylalanine was predicted (and observed) to protrude into the pore and exclude the detergent: again we found that the pore geometry is unaffected but that the density for detergent is now much weaker (**Figure 114c**).

Finally, we studied the stability of the open form in a fully hydrated and lipidic environment via a 20-ns long molecular dynamics simulation with about 200,000 atoms. The pore maintained an open form during that period of time.

There are many more questions to be answered for this family of proteins, which we are addressing through a combination of computational (molecular dynamics), structural (diffraction) and functional (electrophysiology) experiments on mutants and various different constructs.

References
[1] A. Taly *et al., Nature Rev. Drug Discovery* **8**, 733-750 (2009).
[2] K. Brejc *et al., Nature* **411**, 269-276 (2001).
[3] N. Unwin, *J. Mol. Biol.* **346**, 967-989 (2005).
[4] A. Tasneem *et al., Genome Biol* **6**, R4 (2005).
[5] R. Hilf and R. Dutzler, *Nature* **452**, 375-379 (2008).
[6] N. Bocquet *et al., Nature* **445**, 116-119 (2007).

The structural basis of LPS recognition by the TLR4-MD-2 complex

Principal publication and authors
B.S. Park (a), D.H. Song (a), H.M. Kim (a), B.S. Choi (a), H. Lee (b) and J-O. Lee (a,c), *Nature* **458**, 1191 (2009).
(a) Department of Chemistry, KAIST, Daejeon (Korea)
(b) Department of Biology, Chungnam National University, Daejeon (Korea)
(c) Institute of BioCentury, KAIST, Daejeon (Korea)

Lipopolysaccharide (LPS) is a major component of the outer membrane of Gram negative bacteria and is a potent activator of the human innate immune system. Minute amounts of LPS released into the blood stream by invading bacteria are an early sign of infection and prepare the immune system to counteract further infection. The immune response to LPS can also lead to fatal septic shock syndrome if the inflammatory response is amplified and uncontrolled. The core receptors recognising LPS are CD14, Toll-like receptor4 (TLR4), and MD-2. Binding of LPS to CD14 is enhanced by LBP (LPS-binding protein). Transfer of LPS from CD14 to TLR4-MD-2 heterodimers causes multimerisation of the receptor complex in the plasma membrane and triggers an intracellular signalling cascade. MD-2 is associated with the extracellular domain of TLR4 and is responsible for LPS binding. To date, ten members of the TLR family recognising a wide variety of microbial products have been identified in humans [1].

In 2007, using beamline **ID14-2**, we succeeded in determining the crystal structure of the TLR4-MD-2 complex

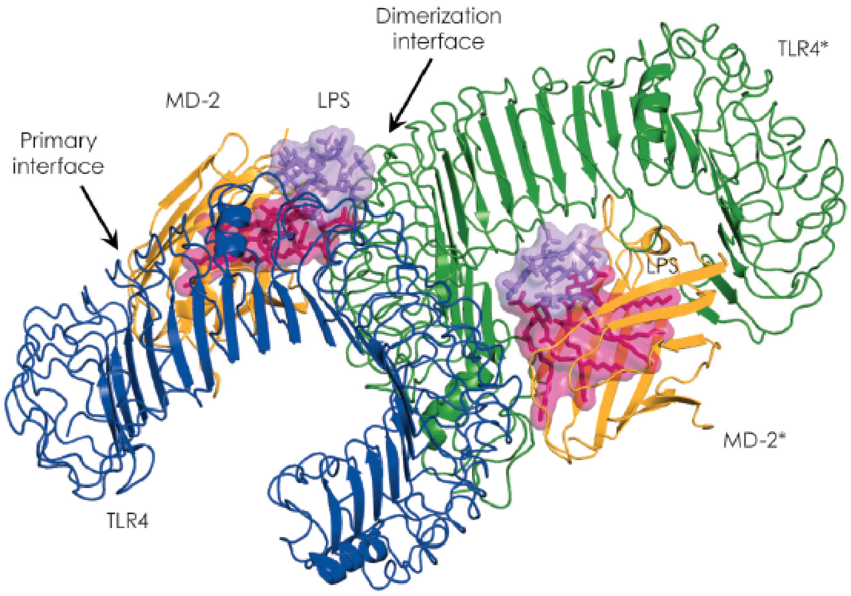

Fig. 115: Overall structure of the TLR4–MD-2–LPS complex. The primary interface between TLR4 and MD-2 is formed before binding LPS, while the dimerisation interface is induced by binding LPS.

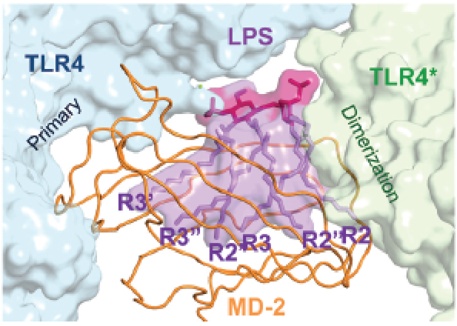

Fig. 116: The main dimerisation interface of the TLR4–MD-2–LPS complex. The inner core of LPS is omitted for clarity.

[2]. The structure revealed that MD-2 interacts with the N-terminal and central area of the concave surface of TLR4. We also determined the structure of the TLR4-MD-2 in complex with Eritoran, an antagonist of TLR4-MD-2 and a candidate drug for severe sepsis. Eritoran binds to a large hydrophobic pocket in MD-2. At that time, however, we could not obtain diffraction-quality crystals of TLR4-MD-2 bound to LPS and therefore could only propose a model of the complex based on biochemical experiments. Early this year we finally succeeded in crystallising the TLR4-MD-2-LPS complex, and determined its structure at 3.1 Å resolution using the microfocus beamline **ID23-2** [3]. Fortunately for us, the structure closely resembles the model we proposed two years ago. Binding of LPS induces the formation of a symmetrical dimer of two TLR4-MD-2-LPS complexes (**Figure 115**). The LPS bound to MD-2 directly bridges the two TLR4 molecules. The main dimerisation interface of MD-2 is located on the opposite side of the primary TLR4-MD-2 interface and interacts with the C-terminal domain of TLR4. Five of the six lipid chains in LPS are completely buried inside the MD-2 pocket but the sixth is partially exposed to the surface of MD-2 and forms a hydrophobic interaction with TLR4 (**Figure 116**). Hydrophilic side chains in the surrounding regions of MD-2 and TLR4 support the hydrophobic core of the interface by forming hydrogen bonds and ionic interactions. The two phosphate groups of lipid A reinforce this major dimeric interface by interacting with positively charged residues in TLR4 and MD-2.

Our crystal structure accounts for the structure-activity data for LPS accumulated over decades of research. Of the factors governing the immunological activity of LPS, the most important is the total number of lipid chains. Lipid A with six lipid chains has optimal inflammatory activity, while those with five lipid chains are ~100 fold less active, and those with four, such as Eritoran, completely lack agonistic activity. Based on our crystal structure we were able to predict that in LPSs with less than six lipid chains, all the chains move further into the pocket to fill the empty space, so that there is a substantial energetic penalty when they move back to the surface of MD-2 to dimerise with TLR4. Deletion of any of the two phosphate groups reduces endotoxic activity ~100 fold.

In summary, the crystal structure shows that multiple structural components of the TLR4-MD-2 receptor are involved in recognition of LPS. Further work is required to establish how these components interact with the structurally diverse LPS variants found in different bacterial species.

References
[1] N.J. Gay and M. Gangloff, *Annu Rev Biochem* **76**, 141 (2007).
[2] H.M. Kim, B.S. Park, J.I. Kim, S.E. Kim, J. Lee, S.C. Oh, P. Enkhbayar, N. Matsushima, H. Lee, O.J. Yoo and J-O. Lee, *Cell* **130**, 906 (2007).
[3] B.S. Park, D.H. Song, H.M. Kim, B.S. Choi, H. Lee and J-O. Lee, *Nature* **458**, 1191 (2009).

The cap-snatching endonuclease of influenza virus polymerase resides in the PA subunit

Principal publication and authors
A. Dias (a), D. Bouvier (a), T. Crepin (a), A.A. McCarthy (a,b), D.J. Hart (a,b), F. Baudin (a), S. Cusack (a, b) and R.W.H. Ruigrok (a), *Nature* **458**, 914-918 (2009).
(a) Unit of Virus Host Cell Interactions, UMI 3265 UJF-CNRS-EMBL, Grenoble (France)
(b) EMBL Grenoble Outstation, Grenoble (France)

Every year influenza virus causes seasonal epidemics that affect 5-10% of the world population and kill up to 500,000 people. In nature, the virus primarily infects aquatic birds which can further infect domestic chickens and pigs. Sporadically, the virus jumps the species barrier from these domestic animals to humans causing a world-wide pandemic that can infect 30-50% of the population in a single winter season. This is what may happen with the pandemic swine-origin H1N1 virus because few people have protective antibodies against it.

As with all genes, those of influenza virus need to be transcribed into messenger RNA (mRNA) that is subsequently translated into proteins by ribosomes. However, viruses have no metabolism of their own and must use the ribosomes of the cells they have infected. Therefore, the viral mRNA molecules must resemble cellular mRNAs otherwise the ribosomes will not recognise them. One of the characteristics of all cellular mRNAs is that they start with a molecular tag, a "cap", that is added to the molecule by cellular RNA capping enzymes during the process of transcription of DNA genes into RNAs. Because the genes of influenza virus are made of RNA that cannot be read by the cellular RNA polymerase, the virus encodes its own polymerase that can copy RNA from a RNA template. However, the resulting RNA molecules are uncapped and the viral enzyme cannot use the cellular functions to make a cap structure. This problem is encountered by all RNA viruses and each RNA virus family has found its own solution to modify its mRNA such that it is recognised by host cell ribosomes. Influenza employs perhaps the most devious method of all viruses: cap-snatching! The virus replicates in the nucleus of the infected cell; the place where cellular mRNAs are produced. Its RNA polymerase is a trimer (**Figure 117**) in which the PB1 subunit carries the actual RNA polymerase function. To make capped viral mRNA, the PB2 subunit binds the cap structure of cellular mRNAs and then an endonuclease activity, revealed in this work to be located in the PA subunit, cleaves the cellular mRNA producing a 10-13 nucleotide, capped RNA primer. This primer is then transferred to the polymerase active site on the PB1 subunit and is extended using the viral genes as templates, thus making capped viral mRNA.

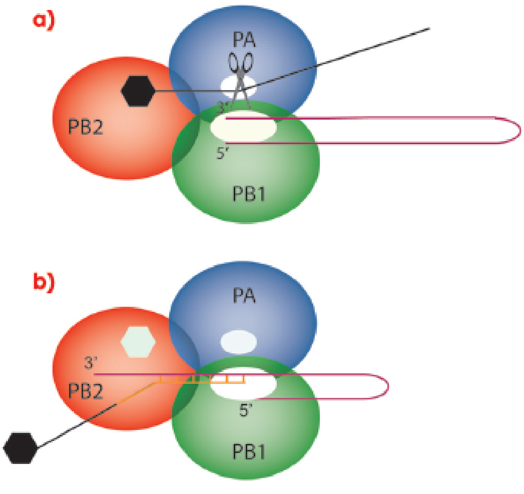

Fig. 117: Cap-snatching mechanism of the influenza virus polymerase. In a) the PB2 subunit of the trimeric viral polymerase binds to the cap of a cellular mRNA molecule. The endonuclease activity of PA then cleaves the cellular mRNA which is used in b) by the PB1 subunit as a primer for viral mRNA synthesis.

Fig. 118: Secondary structure representation of the endonuclease domain of the influenza virus polymerase; β-sheets in yellow and α-helices in blue. The active site lysine 134 and the amino acid side chains that ligand the two metal ions (represented as green spheres) in the active site are indicated.

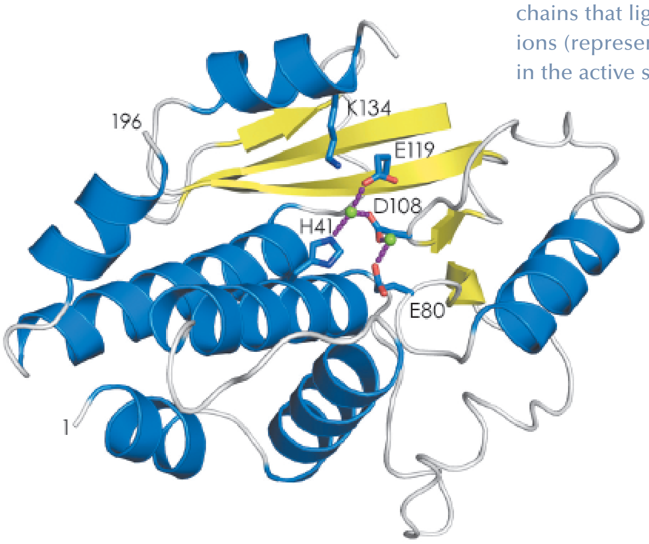

The structure of the active site that binds the cap structure was determined last year [1]. Using data collected at beamlines ID23-1 and ID14-4, we have now determined the structure of the endonuclease domain that belongs to the PD-(D/E)XK nuclease superfamily, revealing an active site containing two metal ions (Figure 118). The biochemical work that led up to the crystallisation of the two active domains also showed that they fold independently and have the same activity as the domains in the intact polymerase trimer. This has opened up the possibility of performing high-throughput screening of small molecules to find inhibitors of cap-binding or endonuclease activities. Before this work such experiments were impossible because complicated and unstable viral polymerase preparations had to be used. Once inhibitors have been identified, co-crystallisation with the individual domains will reveal their binding mode and guide further modifications to produce molecules that bind with higher affinity and specificity.
This should contribute to the generation of a new class of anti-influenza drugs that, although arriving too late for the present H1N1 pandemic, will be ready for the next (inevitable) one.

Reference
[1] D. Guilligay, F. Tarendeau, P. Resa-Infante, R. Coloma, T. Crepin, P. Sehr, J. Lewis, R.W.H. Ruigrok, J. Ortin, D.J. Hart and S. Cusack, *Nature Struct. Mol. Biol.* **15**, 500-506 (2008).

Unusual bipartite mode of interaction between the nonsense-mediated decay factors, UPF1 and UPF2

Principal publication and authors
M. Clerici (a,b),
A. Mourão (c,d,e), I. Gutsche (b),
N.H. Gehring (f,g),
M.W. Hentze (d,f),
A.E. Kulozik (f,g), J. Kadlec (a,b),
M. Sattler (c,e) and
S. Cusack (a,b), *Embo J* **28**, 2293 – 2306 (2008).
(a) European Molecular Biology Laboratory, Grenoble Outstation (France)
(b) Unit of Virus Host-Cell Interactions, UJF-EMBL-CNRS (France)
(c) Munich Center for Integrated Protein Science, Technische Universität (Germany)
(d) European Molecular Biology Laboratory, Heidelberg (Germany)
(e) Institute of Structural Biology, Helmholtz Zentrum München (Germany)
(f) Molecular Medicine Partnership Unit, EMBL and University of Heidelberg (Germany)
(g) Department of Pediatric Oncology, Children's Hospital, University of Heidelberg (Germany)

The ribosome – the cellular machinery responsible for protein synthesis – reads the codons (triplets of bases coding for amino acid residues) of messenger RNAs to assemble polypeptide chains. A particular triplet, the stop codon, signals to the ribosome the end of the coding region and triggers translation termination. A mutagenic event (*e.g.* a genetic mutation) can randomly introduce an abnormal stop codon (nonsense mutation) into the coding region of a messenger RNA. This would cause premature translation termination and thus the production of a truncated protein. Such aberrant proteins often display severe toxic effects on cells and are responsible for several diseases like thalassemia and cystic fibrosis.

Eukaryotic cells have evolved a defense mechanism against such mutations called nonsense-mediated mRNA decay (NMD) [1]. A fundamental role in NMD is carried out by the exon junction complex (EJC), a multi-protein complex deposited by the splicing machinery onto the mRNA just upstream from each exon-exon junction. The ribosome stalled at a premature termination codon recruits other factors – notably the NMD protein UPF1 – and forms the so-called SURF complex (named after the component proteins SMG1, UPF1 and eRF1-3). Unless the premature termination codon is found in the last exon, an EJC complex is found downstream of the SURF complex. The NMD factor UPF2, associated with the

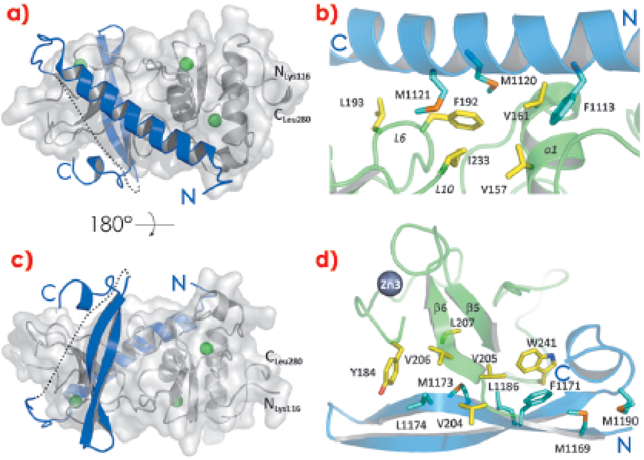

Fig. 119: a), b) UPF2 (blue) is represented as ribbons and UPF1 (grey) as ribbons and a transparent surface. UPF1 zinc atoms are shown in green. The UPF2 missing linker is represented as a dotted line. c) The principal residues of the UPF2 N-terminal helix (cyan) and the UPF1 CH domain (yellow) that form the hydrophobic interface between the two molecules are represented as sticks. d) The main interacting residues of UPF2 C-terminal β-hairpin (cyan) and UPF1 CH domain (yellow) are represented as sticks.

EJC through its interaction with UPF3, recognises and binds UPF1 on the SURF complex thus bridging the two macromolecular complexes. This key recognition triggers a series of downstream events that finally lead to the degradation of the mRNA, protecting the cell from the production of a potentially dangerous truncated protein.

Here we report structural studies on the unusual interaction between the C-terminal region of UPF2 and UPF1. UPF1 is an RNA helicase with an additional N-terminal Cys/His-rich domain (CH domain). The crystal structure of the UPF1-UPF2 complex (obtained at beamline **ID14-4**) shows that UPF2 adopts an unusual bipartite mode of interaction with UPF1, binding via separated alpha-helical and beta-hairpin elements connected by a long linker on opposite sides of the CH-domain of UPF1 (**Figure 119**). Complementary NMR and ITC measurements show that the interacting region of UPF2 is intrinsically disordered in the unbound state and folds upon binding to UPF1, with the beta-hairpin element having the highest affinity. An additional crystal structure (obtained at beamline **ID29**) shows that UPF1 CH domain is docked onto the helicase in a fixed configuration even in the absence of UPF2. Small-angle X-ray scattering (SAXS) measurements performed on the BioSAXS beamline **ID14-3** confirmed that the relative orientation of the two domains is maintained in solution independently of bound UPF2 (**Figure 120**).

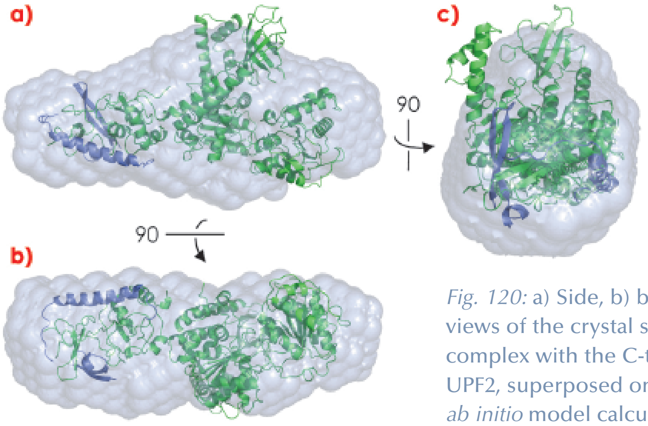

Fig. 120: a) Side, b) bottom and c) front views of the crystal structure of UPF1 in complex with the C-terminal domain of UPF2, superposed on the corresponding *ab initio* model calculated from the SAXS scattering curve.

In summary, we show that the UPF1-binding region of UPF2 shares the typical features of intrinsically disordered regions, which are known to mediate very specific and often transient interactions. We propose that UPF2 uses its disordered C-terminal region as a long, flexible "fishing line" to allow rapid recognition and binding of UPF1, the co-folding upon binding ensuring high specificity. This mechanism is appropriate as, by virtue of its flexibility, the UPF2 fishing line can explore large volumes and overcome topological constraints to ensure that the key connection is made between the EJC and UPF1 on the stalled ribosome, thus leading to efficient degradation of premature termination codon-containing aberrant mRNAs.

Reference

[1] G. Neu-Yilik and A.E. Kulozik, *Adv Genet* **62**, 185-243 (2008).

Studies of UvrA2 provide insight into DNA binding and damage recognition

Principal publication and authors

J. Timmins (a), E. Gordon (a), S. Caria (a), G. Leonard (a), S. Acajjaoui (a), M.-S. Kuo (b), V. Monchois (b) and S. McSweeney (a), *Structure* **17**, 547–558 (2009).

(a) ESRF

(b) PX-Therapeutics, Grenoble (France)

DNA damage is a common occurrence that compromises the functional integrity of DNA. DNA repair pathways are ubiquitous and the principles of damage recognition are conserved from bacteria to humans. Nucleotide excision repair is the primary pathway for repair of the structurally diverse lesions caused by ultra-violet light and involves the recognition and removal of damaged DNA by a dual-incision event. In prokaryotes, the Uvr proteins carry out the excision and have been the focus of many studies for over 20 years. The proteins UvrA and UvrB are responsible for the ATP-dependent recognition of DNA damage whilst UvrC is required for the subsequent incision events. Despite extensive biochemical and genetic studies, it is still not well understood how nucleotide excision repair is capable of recognising such a wide variety of lesions, but as structural information on

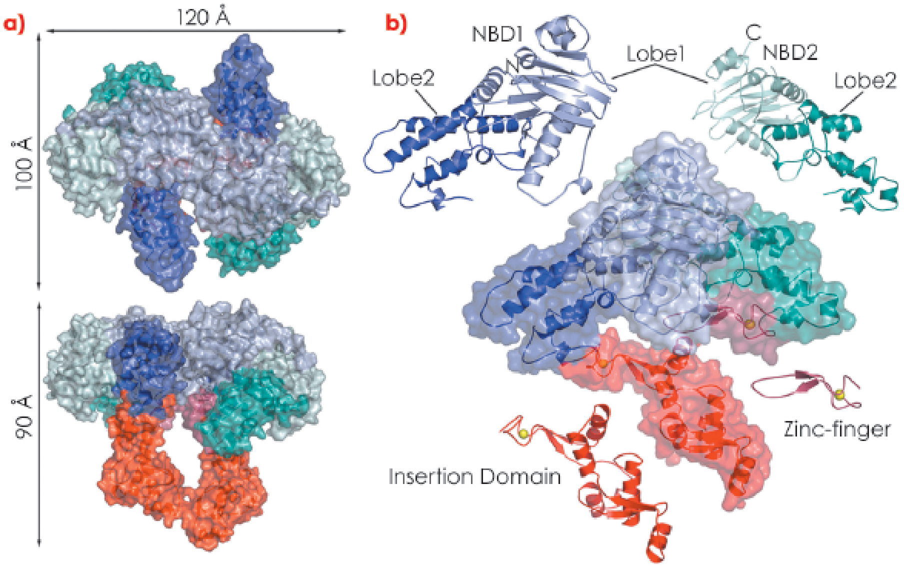

Fig. 121: Crystal structure of *D. radiodurans* UvrA2. Surface and ribbon representations of dimeric (a) and monomeric drUvrA2 (b). The domains are coloured as follows: NBD1 (blue), NBD2 (cyan), insertion domain (red) and zinc-finger (raspberry). Zinc ions are illustrated as yellow spheres.

the UvrABC proteins is becoming available and through in depth biochemical analysis of the repair process, a picture is starting to emerge.

UvrA is responsible for initial DNA damage recognition and subsequently acts as a molecular matchmaker by efficiently promoting the stable assembly of UvrB onto damaged DNA sites. A more comprehensive description of the molecular mechanisms of UvrA's action would therefore constitute an important contribution to our understanding of the initial steps in bacterial nucleotide excision repair. In this work, we have undertaken a structural and biochemical study of a UvrA protein (drUvrA2) from the radiation-resistant bacterium *Deinococcus radiodurans*. Unlike E. coli, *D. radiodurans'* genome encodes two UvrA proteins, drUvrA1 and drUvrA2. drUvrA1 represents the full-length UvrA protein, which is present in all bacteria and has recently been classified as a Class I UvrA. Recently, the first three-dimensional structure of such a Class I UvrA from *Bacillus stearothermophilus* (bstUvrA) was reported [1]. drUvrA2, a Class II UvrA, displays a high sequence identity with drUvrA1, E. coli UvrA and bstUvrA, but is missing the UvrB binding domain recently identified in bstUvrA. Although the exact roles and substrates of Class II UvrAs remain elusive, the high level of conservation suggests that the molecular mechanisms involved in substrate recognition are most likely similar to those used by Class I UvrAs.

In our study, we show that drUvrA2 shares many of the biochemical (ATPase activity, nucleotide-dependent dimerisation, preferential binding to damaged DNA) and structural features observed for UvrAs. We have solved and refined the structure of ADP-bound drUvrA2 in two crystal forms to resolutions of 2.3 Å (C2; 3 mol/asu) and 3.0 Å (C222; 2 mol/asu) respectively, providing us with a view of five distinct monomeric and three dimeric conformational states. drUvrA2 assembles as a head-to-head dimer in which each monomer consists of two tandemly arranged ATPase binding cassettes (**Figure 121**). As expected from primary sequence analysis, our structure of drUvrA2 reveals that the UvrB-interacting domain is missing along with its associated Zn-binding site (two CXXC motifs). As a result, drUvrA2 possesses only two of the three Zn-binding sites found in the classical Class I UvrAs. As in the case of bstUvrA, a large insertion domain was accommodated in the amino-terminal nucleotide binding domain (NBD-I) of drUvrA2, while a more classical zinc-finger is inserted into the carboxy-terminal NBD-II.

Our studies have also shown that drUvrA2 alone can recognise and bind preferentially to damaged bases within

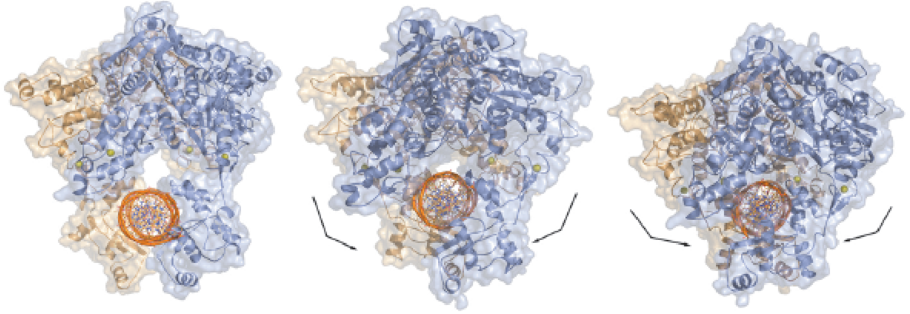

Fig. 122: Models of dsDNA binding to symmetrical dimers assembled from the three different molecules of drUvrA2 refined in C2 space group.

DNA oligonucleotides. This work was complemented by a mutational study of drUvrA2 that showed that two regions of UvrAs are essential for DNA binding: a positively charged groove formed on the concave side of the core ABC domains and the newly identified insertion domains. Taken together our structural, biochemical and mutational analysis of drUvrA2 provides the first detailed description of a class II UvrA and also contributes to an extended model for how UvrAs might interact with DNA (**Figure 122**), which has implications for a fuller understanding of the mechanisms involved in the initial steps of nucleotide excision repair.

Reference

[1] D. Pakotiprapha, Y. Inuzuka, B.R. Bowman, G.F. Moolenaar, N. Goosen, D. Jeruzalmi and G.L. Verdine, *Mol. Cell* **29**, 122 (2008).

Fluorescence of plant light-harvesting complex II in single crystals

Principal publication and authors

T. Barros (a), A. Royant (b,c), J. Standfuss (a), A. Dreuw (d) and W. Kühlbrandt (a), *EMBO Journal* **28**, 298 (2009).
(a) Department of Structural Biology, Max Plank Institute of Biophysics, Frankfurt am Main (Germany)
(b) Institut de Biologie Structurale Jean-Pierre Ebel (France)
(c) ESRF
(d) Institute for Physical and Theoretical Chemistry, Johann Wolfgang Goethe-University Frankfurt (Germany)

Most of the solar power utilised in photosynthesis is collected and transmitted to the energy-converting reaction centres by peripheral light-harvesting complexes. Among these, the chorophyll *a/b* light-harvesting complex of photosystem II (LHC-II) is the major antenna complex in plants, accounting for roughly half of the total chlorophyll content in chloroplasts, and thus for most of the green matter in the biosphere. Recently, the role of LHC-II in energy-dependent non-photochemical quenching (qE) has come into focus. qE is a photoprotective mechanism used by plants to dissipate surplus excitation energy safely when the photochemical capacity of the photosystem is exceeded in strong light. Of the two X-ray structures of LHC-II in the protein data bank, the one at higher resolution (2.5 Å, pdb code 2BHW) was determined from data collected at the beamline **ID14-1** with crystals of the pea complex [1]. The other structure at 2.7 Å resolution is that of the spinach complex (pdb code 1RWT). With these two structures in hand, the search was on for the exact position of the quenching centre in the complex, and the molecular mechanism of quenching. A prominent model for the quenching process proposes that a conformational change switches LHC-II from its active, energy-transmitting state to an inactive, quenched state in which excitation energy is dissipated in the form of heat.

For a better understanding of the quenching mechanism, it was therefore important to know which of these two hypothetical states of the LHC-II was represented by the crystal structures. An earlier spectroscopic study [2] had concluded from an apparent red-shift and the shorter fluorescence lifetime of LHC-II crystals that the spinach structure showed the quenched state. Despite the large differences in crystallisation conditions and crystal forms, the two crystal structures are virtually identical, this would mean that the pea complex is in the same quenched state. We decided to investigate this further by analysing the fluorescence properties of LHC-II in single crystals at the ESRF Cryobench laboratory.

The possibility of examining individual single crystals mounted in cryo-loops, as opposed to a suspension of crystals used in the previous studies, and to align the crystals precisely relative to the incident light beam were decisive for the success of our study. We demonstrated that fluorescence emission spectra of single LHC-II crystals are critically dependent on crystal orientation (**Figure 123**). In certain orientations, the low-temperature emission spectrum shows strong fluorescence emission at 680 nm. This is characteristic of the

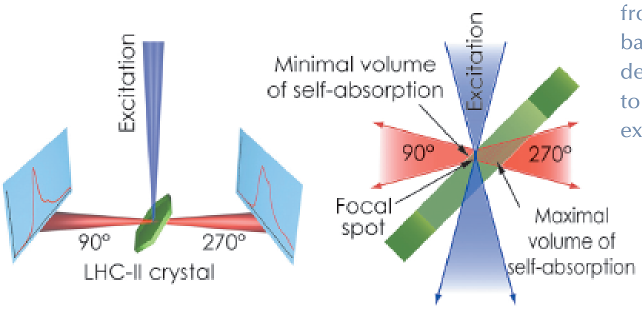

Fig. 123: The optical system of the Cryobench used to record fluorescence spectra of LHC-II single crystals in two different detection geometries, corresponding to front-side (at 90°) and back-side (at 270°) detection with respect to the crystal and the exciting light beam.

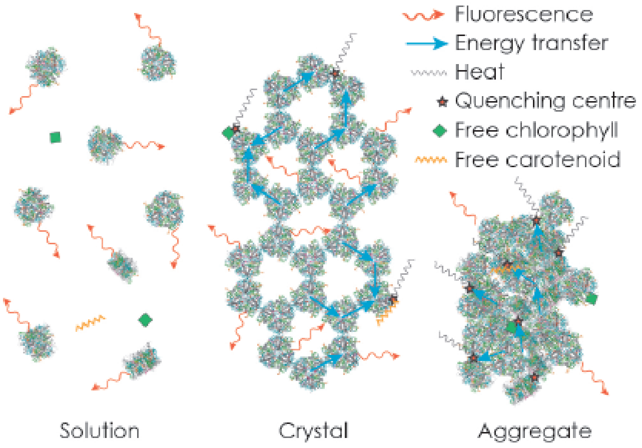

Fig. 124: The strong fluorescence of LHC-II in detergent solution is quenched in crystals and aggregates due to random interactions of trimers, or of trimers with free pigments.

References
[1] J. Standfuss, A.C. Terwisscha van Scheltinga, M. Lamborghini and W. Kühlbrandt, *Embo J* **24**, 919 (2005).
[2] A.A. Pascal, Z. Liu, K. Broess, B. van Oort, H. van Amerongen, C. Wang, P. Horton, B. Robert, W. Chang and A. Ruban, *Nature* **436**, 134 (2005).

active, energy-transmitting complex and had previously been observed only with LHC-II in detergent solution. In other crystal orientations, in which the emitted photons travel through the thickness of the crystal before arriving at the recording device, a broad 700 nm band predominates, demonstrating that the apparent red-shift of LHC-II fluorescence in single crystals is due to self-absorption. These observations prove that both crystal structures of LHC-II show the complex in an active, energy-transmitting state.

We then extended our study to provide further evidence for our conclusion by an extensive analysis of the fluorescence lifetime of LHC-II in single crystals. For reference, we performed a parallel analysis of LHC-II fluorescence lifetimes in detergent solution and aggregates, commonly thought to represent the active and quenched state of the complex, respectively.
Our results indicated that the average fluorescence lifetime of LHC-II in single crystals at 100 K, although much shorter than in solution, is significantly longer than in aggregates, indicating a smaller extent of quenching. The time-resolved data also revealed that a substantial fraction of the LHC-II trimers in the crystals retains the long fluorescence lifetime of the complex in solution, so that the observed shorter fluorescence lifetime must occur due to migration of the excitation energy to quenching centres randomly distributed within the crystal (**Figure 124**). We conclude that quenching of excitation energy in LHC-II is due to the molecular interaction with external pigments *in vitro* or other pigment-protein complexes *in vivo*, and does not require a conformational change within the complex.

X-ray imaging

X-ray imaging techniques are used for innovative research in an ever broadening range of scientific areas. The variety is demonstrated by the articles in this chapter from the emerging field of palaeontology and of nano-imaging for biology and materials science. Also included are contributions on Biomedical applications, on Materials and Environmental science, and on Cultural Heritage.

Biomedical research is exemplified by three articles. The first is on the use of synchrotron radiation computed tomography for tumour functional mapping. This approach provides absolute values of different microcirculatory parameters for tumours and surrounding brain tissues. These measurements are of crucial importance for radiotherapy. The second article reports on functional imaging using the K-edge subtraction technique, here used to study the lung and bronchial response to methacholine treatment (a drug targeting lung function) in ovalbumin-sensitised rabbits. This work may have direct clinical implications and helps in furthering our understanding of asthma mechanisms and for tailoring drug-targeting strategies. The third article emphasises the importance of the nanoprobe beams produced at station ID22NI for biomedical purposes through a study of the metallobiology of the neuromelanin pigment in the human brain and its possible role in the pathogenesis of Parkinson's disease.

X-ray imaging is widely used for Materials Science studies. The publications presented here take full advantage of the new capabilities of the imaging beamlines, *i.e.* fast 3D imaging and nanoprobe-related imaging. A full 3D microtomographic image can be recorded in only a few seconds on ID15 and ID19. This allowed *in situ* real-time studies of the dendritic solidification and coarsening in an Al–10 wt.% Cu alloy. The hard X-ray nanoprobe (ID22NI) was used to study the defects in GaN:Mg, and to produce sub-micrometre holotomography of multiphase metals. The following highlight describes the 3D investigation of cometary grains, collected during the NASA Stardust mission, by nanoscale X-ray fluorescence tomography.

Cultural Heritage studies and artefact preservation are increasingly important in Europe for both cultural and economic reasons. Synchrotron radiation has proven itself to be a valuable tool, allowing studies not otherwise possible. Over the past few years, Cultural Heritage related activities have undegone an extensive and successful development at the ESRF, as witnessed by the increase in the number of proposals to the Proposal Review Panel on Environment and Cultural Heritage (EC). X-ray imaging techniques play an important role in this area. This is exemplified by an article describing the full characterisation of a degraded cadmium yellow (CdS) pigment in an oil painting.

Within Cultural Heritage, we wish to emphasise the particular case of palaeontology. Since the first fossil was scanned at ESRF in 2000, palaeontology has become an important topic: the

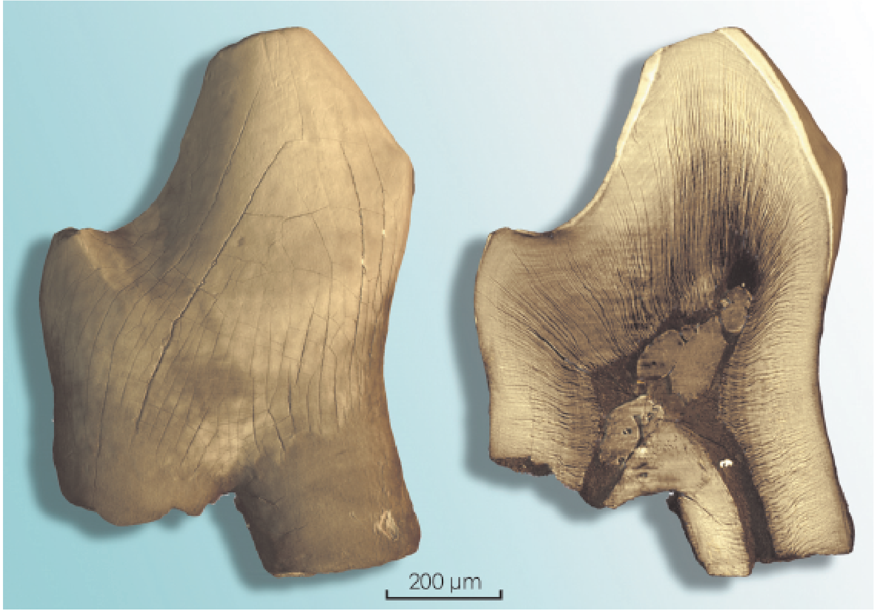

Fig. 125: 3D Rendering and virtual histological slice of a 145 million years old Cretaceous mammalian tooth from Cherves-de-Cognac (Charente, France). This minute fossil tooth was imaged using sub-micrometre resolution holotomography on **ID19.** The highly monochromatic source, in addition to short acquisition time, leads to unprecedented image quality for this kind of microfossil. The detailed 3D morphology gives access to the internal histological information of dental microstructures including its developmental record. Study of the growth lines in such fossils should bring new evidence of the controversial physiological thermal regulation in our mammalian ancestors as well as in dinosaurs (*Courtesy: J. Pouech, J.-M. Mazin and P. Tafforeau*).

paleontological-related proposals have grown to about 20% of the proposals using microtomography. This research regularly leads to high impact publications (four in Nature/Science/PNAS in 2009) and to numerous PhD theses, and they have attracted substantial interest from the media and the public. In the present chapter, we present two publications performed using holotomography, the first on a very unusual (thought impossible) fossil fish brain, and the second to untangle the evolution of giant sperm in ostracod microcrustaceans. Another recent example is the sub-micrometre resolution holotomography of a mammalian tooth, presented in Figure 125, which reveals the internal histological information of dental microstructures, including the growth lines that constitute a record of an individual's development.

The scientific success of the X-ray imaging techniques would only be short-term without the constant effort of the ESRF staff and users to implement new imaging techniques that will lead to new scientific research. This is exemplified in the present chapter by a contribution on the extension of high-resolution laminography (which allows three-dimensional imaging of flat specimens) to weakly absorbing materials, through the use of propagation-based phase contrast. Another example is given in Figure 126, which shows a series of images providing complementary information recorded using a grating interferometric device. This phase-contrast technique can be applied to a wide variety of materials; it will be implemented for routine access for our users.

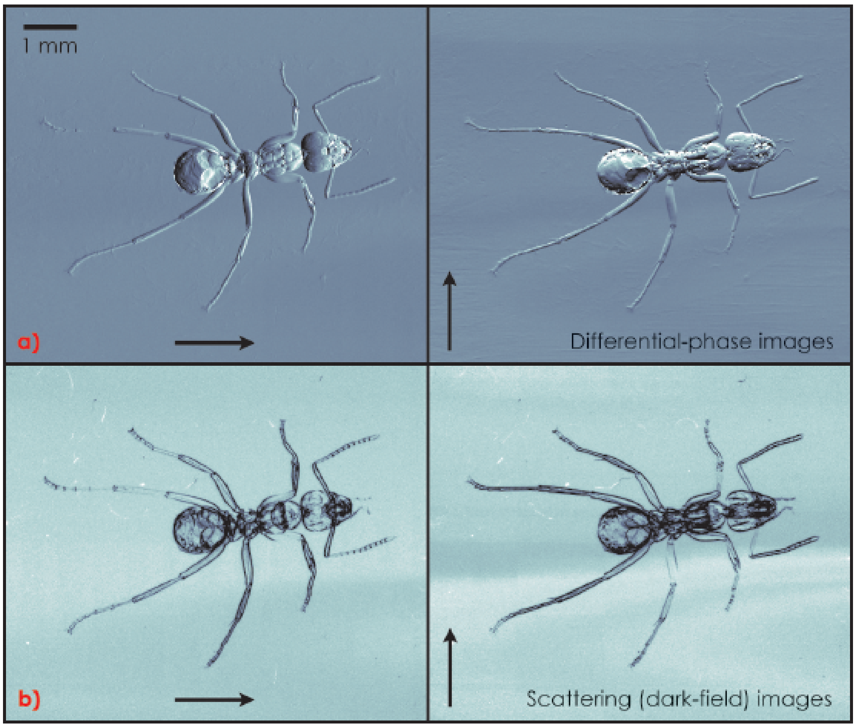

Fig. 126: Radiographs of an ant taken with a two-dimensional X-ray grating interferometer (2D GIFM) with 23 keV X-rays. GIFM is a novel method that yields X-ray images with ultra-high sensitivity in several complementary contrast modes. With the standard interferometer, differential phase and dark-field images can be obtained along only one particular direction. An extended 2D version of the device has been implemented at **ID19** permitting simultaneous access to the image signals along multiple directions. The two orthogonal sensitivity orientations of (a) differential phase contrast and (b) dark-field (scattering) contrast are indicated by arrows (*Courtesy I. Zanette and T. Weitkamp*).

Several important publications have been produced by the two radiotherapy programmes under development at ID17: Stereotactic Synchrotron Radiation Therapy (SSRT) and Microbeam Radiation Therapy (MRT). These articles deal with the understanding of the response of healthy and tumoral tissues to X-ray treatment and with the refinement of clinical trials protocols for ID17.

X-ray imaging plays a substantial role in the ESRF Upgrade Programme, through which we intend to continue providing our users with the best instruments for their projects. A long (160 m) canted beamline at the ID16 location is planned for the ambitious Nano Imaging and Nano Analysis (UPBL4, NINA) project. A refurbishment of the parallel and coherent beam imaging beamline ID19 will also be implemented, with emphasis on palaeontological activities in close association with the Palaeontology Facility.

We are confident that these developments, coupled with the scientific know-how acquired using X-ray imaging at the ESRF, will allow the limits of the techniques to be extended, making possible scientific results which are not attainable today.

J. Baruchel

Biomedical applications

Tumour functional mapping using synchrotron radiation computed tomography

Dynamic contrast enhanced medical imaging (DCE-MI), using MRI (magnetic resonance imaging) or CT (computed tomography), is a promising technique for the detection, characterisation and monitoring of many lesions such as solid tumours. Its use has recently been extended to *in vivo* assessment of the microcirculatory function of the tissues. An intravenous bolus of contrast agent is followed as a function of time in tissues through local variations of grey levels in pixels or in regions of pixels. The evolution of the contrast agent concentration depends on microcirculatory characteristics which are assessed by using pharmacokinetic modelling. Several phenomena can hamper microcirculatory assessments and, in practice, the variability in data acquisition techniques and data analysis is so important between research centres and/or hospitals that results cannot be easily compared. Thus, objective quantification of microcirculatory parameters by this technique could appear limited.

To test the potential of DCE-MI in terms of microcirculatory parameter quantification, we analysed images acquired from a controlled DCE-MI protocol in order to minimise potential artefacts or bias that could hamper the results. We tested whether it was possible to characterise different structural elements of C6 rat brain tumours by their differing microcirculatory behaviour. The acquisition was provided in stereotactic conditions using the monochromatic synchrotron radiation CT (SRCT) technique available at ID17, the Biomedical Beamline. Compared to other techniques, SRCT offers a high signal to noise ratio and does not suffer from beam hardening. In particular, the technique allows the measurement of absolute rather than relative values. The analysis was provided by selecting the more relevant pharmacokinetic model among several compartmental models, for the set of selected anatomic regions. The model selection was guided by using quality criteria [1] that tested the consistency between original data and modelling information provided by each pharmacokinetic model. This *a posteriori* analysis avoids any potential misinterpretation of results and helps in evaluating the reliability of the final parametric results.

DCE-SRCT sequences were analysed using purpose-built software (PhysioD3D). The software provided parametric maps of tumours and surrounding brain tissues, each map corresponding to different microcirculatory parameters: blood flow, blood volume, mean transit time, capillary permeability index and artery to tissue delay (**Figure 127**). It also provided specific maps for quality control. Structure regions were selected in the original sequences, guided by the parametric maps and corresponding *post mortem* histological slices. Finally microcirculatory parameters in the defined regions were compared.

Remarkably, the regional organisation of the tumour zones, visible on the hematoxylin-eosin-stained slices, were reproduced on a parametric map for which high quality criteria were found (**Figure 127**). Quantitative results in the

Principal publication and authors
D. Balvay (a), I. Troprès (b), R. Billet (c), A. Joubert (c), M. Péoc'h (c), C.A. Cuenod (a) and G. Le Duc (c), *Radiology* **250**, 692-702 (2009).
(a) LRI, PARCC, Inserm 970 – Service Radiologie HEGP, Paris (France)
(b) IFR1, Université Joseph Fourier – Unité IRM 3T, CHU Grenoble (France)
(c) ESRF

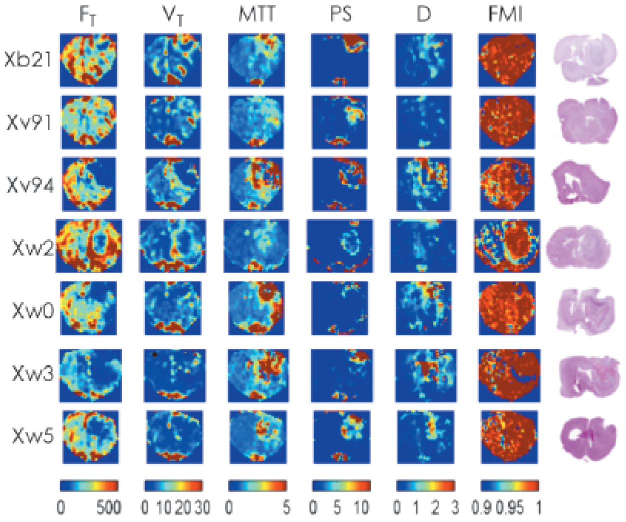

Fig. 127: Examples of parametric maps of c6 glioma-bearing rat brains displayed alongside the corresponding histological slices, for 7 rats. From left to right: blood flow (F_T), blood volume (V_T), mean transit time (MTT), permeability (PS), artery to tissue delay (D), quality criteria (FMI, in red for optimal quality) and histological slices.

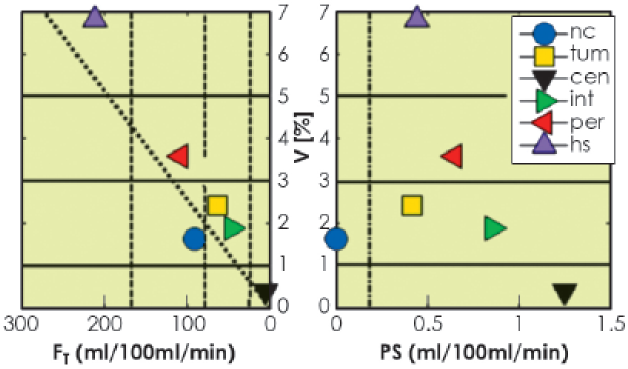

Fig. 128: Microcirculation characteristics of tumour and healthy tissues for blood flow (F_T), blood volume (V) and permeability (PS). The different regions: healthy caudate nucleus (nc), global tumour (tum), and tumour structures: centre (cen), intermediate zone (int), periphery (per) and hot spots (hs) have different averaged microcirculatory parameters (markers) corresponding to significant microcirculatory behaviour when markers are separated by a line.

selected regions (**Figure 128**) indicated that each type of tumour tissue is characterised by abnormal capillary permeability, due to a damaged blood-brain barrier, and by lower intravascular transit time (V/F_T). Quantitative results also indicated that the internal structures of the tumour could be characterised by their specific blood flow and blood volume values, increasing in the following order: centre, intermediate, periphery and hot spots.

The consistency between DCE-SRCT and histological maps such as the ability of DCE-SRCT to significantly differentiate microcirculatory behaviour between tumour elements could position this technique as a reference. In particular, the assessment of absolute concentrations allows comparison between centres and estimation of calibration factors.

Reference

[1] D. Balvay, F. Frouin, G. Calmon and C.A. Cuenod, *Magn. Reson. Med.* **54**, 868-877 (2005).

Methacholine and ovalbumin airway challenges assessed by synchrotron lung imaging

Principal publication and authors

S. Bayat (a), S. Strengell (b), L. Porra (c,d), T.Z. Janosi (e), F. Petak (f), H. Suhonen (d), P. Suortti (c,d), Z. Hantos (f), A.R.A. Sovijärvi (b) and W. Habre (e), *Am J Respir Crit Care Med.* **180**, 296-303 (2009).
(a) Université de Picardie Jules Verne, EA4285 Péritox-INERIS and CHU Amiens (France)
(b) Department of Clinical Physiology and Nuclear Medicine, Helsinki University Central Hospital (Finland)
(c) ESRF
(d) Department of Physics, University of Helsinki (Finland)
(e) Geneva Children's Hospital, University Hospitals of Geneva and Geneva University (Switzerland)
(f) Department of Medical Informatics and Engineering, University of Szeged (Hungary)

Asthma is one of the most common chronic inflammatory diseases of the airways of our lungs. It is characterised by airway hyperresponsiveness and severe airway narrowing leading to heterogeneous distal lung ventilation. Although several imaging modalities have demonstrated this heterogeneity both in human subjects and animal models, the mechanisms of such complex airway behaviour remain poorly understood. This is in part due to the lack of an ideal imaging technique.

Recently, we introduced a computed tomography (CT) technique for imaging lung function that combines both high spatial and temporal resolution, allowing for truly quantitative measurements of regional ventilation [1]. This technique has the ability to image both lung function and the underlying lung morphology simultaneously. It uses radiation from a synchrotron source, which, as opposed to standard X-ray sources, allows selection of a monochromatic X-ray beam from the full spectrum while conserving enough intensity for imaging. Stable Xe gas is administered as an inhaled contrast agent. Two images are acquired simultaneously using two energies that bracket the K-absorption edge of Xe, their subtraction yields the distribution of the Xe gas inside the lungs. One advantage of this so-called K-edge subtraction (KES) method over the CT techniques using standard X-ray sources is that it allows a direct quantification of the absolute density of the Xe gas at any given point in a lung CT image. Another advantage is that contrast resolution is markedly improved by avoiding non-selective contrast and beam hardening, which occurs with conventional X-ray sources. Moreover, both structural and functional images are obtained simultaneously. Sequential imaging using this technique allows the quantification of regional lung ventilation.

Computational models have shown that even for uniform smooth muscle activation of a symmetric fractal bronchial tree, the presence of minimal heterogeneity breaks the symmetry and leads to large clusters of poorly ventilated lung units [2]. The goal of the present study was to determine whether the mechanism of airway challenge is also involved in the heterogeneity of response in the bronchial tree. We characterised the changes that occur in the pulmonary system during a nonspecific challenge with methacholine (Mch), a substance acting on muscarinic receptors on airway smooth muscle cells causing constriction and following airway provocation with a specific allergen, ovalbumin (Ova) in sensitised rabbits. The functional changes were assessed by respiratory mechanical measurements allowing partitioning of the airway and tissue changes, based on the overall low-frequency impedance (Zrs) measurements of the respiratory system. We combined these results with those obtained with KES imaging, which allowed simultaneous measurements of the changes in the calibre of conducting airways and regional lung ventilation (Figure 129). Functional localisation of the primarily affected lung compartment revealed radical differences between the changes due to Ova and Mch provocation (Figure 130), despite similar magnitudes of increase in airway resistance (Raw). Our results demonstrate that through intravenous (IV) infusion, the effect of Mch in the lungs predominates in central airways, with minor changes in the lung periphery. In contrast, following Ova provocation through the same IV route, both the mechanical and the functional imaging parameters indicated the development of severe ventilation heterogeneity and airway closure in the lung periphery. Despite different underlying mechanisms, inhaled Mch induced a heterogeneous lung response similar to that observed with the IV allergen.

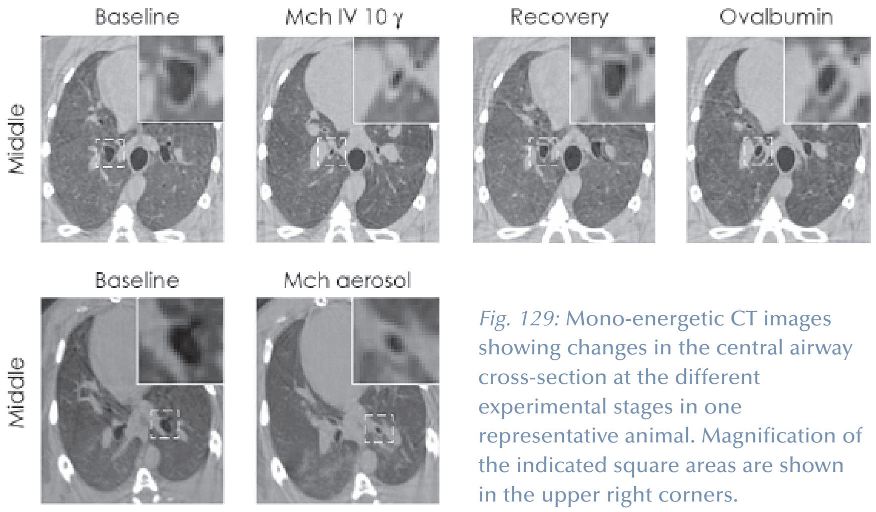

Fig. 129: Mono-energetic CT images showing changes in the central airway cross-section at the different experimental stages in one representative animal. Magnification of the indicated square areas are shown in the upper right corners.

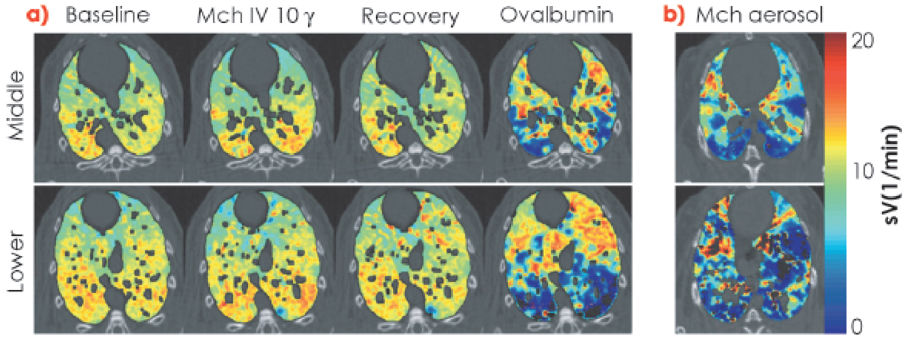

Fig. 130: a) images of specific ventilation in one representative sensitised rabbit at baseline, during methacholine (Mch) infusion, upon recovery and after Ova provocation; γ: μg/kg/min, Ova: ovalbumin; b) images of regional ventilation in one representative control rabbit following Mch aerosol inhalation. Black colour indicates zero specific ventilation.

In conclusion, in this study we found that the pattern of lung response caused by Mch, a non-specific stimulus, and Ova in a sensitised organism, in other words a specific stimulus, are fundamentally different through the IV route. Although inhaled Mch induced a heterogeneous lung response similar to that observed with the IV allergen, these similar patterns are due to different mechanisms. These findings suggest that both the mechanism and route of airway challenge play an important role in determining the heterogeneity of airway response. These findings may have important implications for further understanding of the disease mechanisms and drug-targeting strategies for asthma.

References
[1] S. Bayat *et al.*, *J Appl Physiol.* 100, 1964-73 (2006).
[2] J.G. Venegas *et al.*, *Nature* **434**, 777-82 (2005).

The metallobiology of neuromelanin pigment in the human brain studied by synchrotron X-ray microspectroscopy

Neuromelanin is a dark coloured granular pigment which forms within dopamine and noradrenaline-containing neurons of the substantia nigra (SN) pars compacta and the locus coeruleus in the human brain (Figure 131a). Little is known about this uniquely human pigment; its structure, biosynthesis pathway and physiological functions are not yet completely understood. We have recently demonstrated that neuromelanin production in human dopamine neurons occurs in three phases; an

Principal publication and authors
S. Bohic (a,b), K. Murphy (c), W. Paulus (d), P. Cloetens (b), M. Salomé (b), J. Susini (b) and K. Double (c), *Anal Chem.* **80**, 9557-9566 (2008).
(a) INSERM U-836 (Team 6, Rayonnement Synchrotron et Recherche Médicale), Grenoble Institut des Neurosciences (France)
(b) ESRF
(c) Prince of Wales Medical Research Institute and the University of New South Wales (Australia)
(d) Institute of Neuropathology, University Hospital, Munster (Germany)

initiation phase occurring around the age of three, growth in pigment volume during adolescence and maturation and darkening of the pigment in adulthood [1]. One hypothesised role for neuromelanin is metal homeostasis; metal-handling systems are suggested to be dysfunctional in a number of neurodegenerative diseases. Interestingly, neuromelanin-containing neurons degenerate dramatically in the common neurodegenerative disorder Parkinson's disease. Thus, it is important to examine the cellular metallobiology of neuromelanin in the healthy brain and its possible role in the pathogenesis of Parkinson's disease.

The isolation of neuromelanin from the human SN is an intricate procedure that may alter the physicochemical integrity of neuromelanin granules and requires pooling multiple brain samples to obtain sufficient yield for standard biochemical and biophysical techniques. An alternative is a detailed intracellular analysis of neuromelanin. To meet these challenges, we employed a synchrotron microprobe and the recently developed nanoprobe (**ID22NI**) to characterise the microchemical environment of neuromelanin in tissue sections from both young and mature human brains *in situ* and for the first time (**Figure 131b**).

Our quantitative data demonstrated a marked increase in many neuromelanin-associated elements during the intense period of physical and brain development during childhood and adolescence, with smaller but progressive increases with aging. Many of the elements present in the pigment are crucial for normal brain function, particularly in the SN. Neuromelanin is the major Fe storage site in SN neurons in healthy individuals [1] and, using whole brain analysis, a linear increase in Fe concentration with age in the SN has been reported. Our results confirmed this trend and extend it to the intracellular level for the different neuromelanin maturation stages. Furthermore, Fe speciation obtained via X-ray absorption microspectroscopic analysis showed that Fe within neuromelanin exists in a configuration similar to that in ferritin (a Fe-binding protein present in glial cells in the brain) and that Fe is stored in a Fe^{3+} active form at all neuromelanin developmental stages. Significantly, the nanoprobe enabled us to visualise the localisation of essential elements associated with neuromelanin at a resolution (80 nm) not previously achievable and demonstrated a heterogeneous distribution of various elements within the pigment itself (**Figure 131c**). Fe-rich microdomains exhibiting irregular shapes were of micrometre or submicrometre size and were most apparent in the elderly with larger numbers of Fe-rich areas rarely observed in the less mature pigment. Variability in the polymer's metal binding domains suggests that these sites may serve different functions, with labile sites available for cellular reactions and denser sub-micrometre

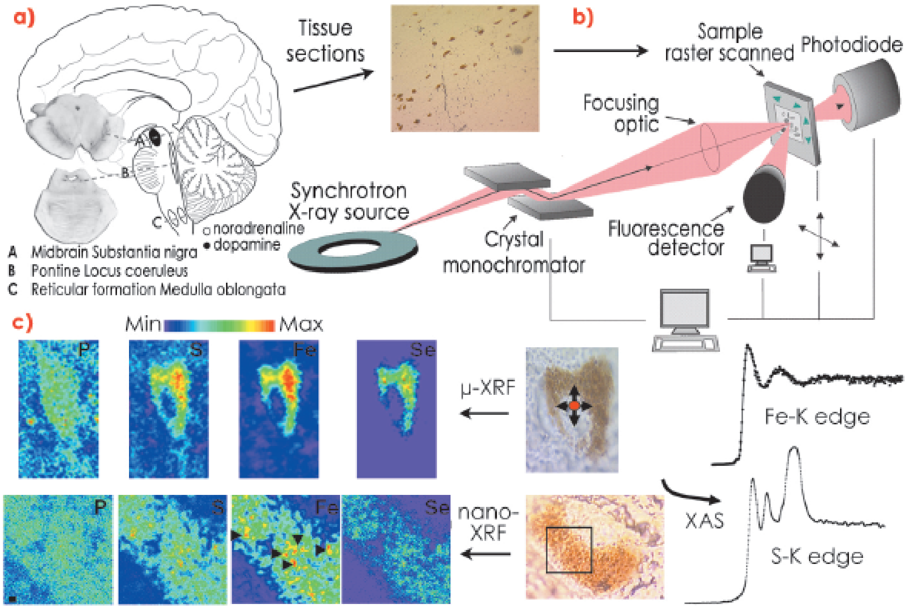

Fig. 131: a) The three main regions containing neuromelanin-producing cells in the human brain: A, substantia nigra of the midbrain; B, locus coeroleus within the pons; C, ventrolateral reticular formation in the medulla oblongata. b) Scheme showing the different steps involved in the synchrotron X-ray microspectroscopic analysis of pigmented neurons of the substantia nigra. The 8 µm thick brain tissue sections are mounted on a thin polymer film. c) Iron (Fe) and sulphur (S) intracellular speciation (X-ray absorption spectroscopy, XAS) were performed at **ID22** and **ID21** respectively. Using X-ray fluorescence (XRF), neuromelanin-containing neurons were raster scanned to generate a pixel-by-pixel spectral image providing topographical elemental maps. Arrow heads show iron-rich microdomains within neuromelanin aggregates.

aggregates that irreversibly scavenge potentially neurotoxic species.

We also found a marked increase in Se concentrations in neuromelanin with age, accompanied by a net increase of Mn in the elderly brain. While the chemical form of selenium in neuromelanin could not be investigated in the current study, this finding suggests a stimulation of cellular defence mechanisms mediated by selenoproteins during aging.

Finally, S speciation studies at the submicrometre level revealed the presence of reduced sulphur compounds and various forms of oxidised sulphur compounds in neuromelanin. Furthermore, a significant increase in sulfonate in neuromelanin in the mature brain suggests *in vivo* metabolism of the pigment occurring via an as yet unidentified pathway.

Such micro- and nano- analytical methods with high sensitivity, multiple-element and speciation capabilities, requiring only a single tissue section, will open exciting new avenues for the study of intracellular biotransformation pathways, particularly the role of trace metals in the brain.

Reference
[1] K.L. Double, V.N. Dedov, H. Fedorow, E. Kettle, G.M. Halliday, B. Garner and U.T. Brunk, *Cell Mol Life Sci.* **65**, 1669-1682 (2008).

Materials science

In situ and real-time 3D microtomography investigation of dendritic solidification and coarsening in an Al-10wt%Cu alloy

Mechanical properties of metallic components produced by casting processes are strongly dependent on their microstructure including the presence of defects such as pores and cracks formed during solidification. This microstructure is usually characterised on 2D sections by optical or scanning electron microscopy after careful preparation of the surface. This characterisation, however, does not give information about the manner in which the microstructure has been generated and the origin of the defects. *In situ* observations are now possible thanks to the development of ultrafast X-ray microtomography carried out at high resolution on both the ID15 and ID19 beamlines. The further advantage of tomography is that the observations are in 3D which is very important to study the development of dendrites and the formation of defects during solidification of alloys.

The solidification experiments were carried out at beamline ID19 with an Al-10wt%Cu alloy using cylindrical specimens of 1.4 mm in diameter and about 3 mm in height. The specimen was glued on the top of an alumina rod placed on the rotating stage. It was heated until completely molten and then slowly cooled at 3°C/min while being supported by its own oxide skin. The solidification experiment was

Principal publications and authors
N. Limodin (a,b), L. Salvo (a), E. Boller (c), M. Suéry (a), M. Felberbaum (d), S. Gailliégue (e) and K. Madi (e), *Acta Materialia* **57**, 2300–2310 (2009);
S. Terzi (a,f), L. Salvo (a), M. Suéry (a), A.K. Dahle (f) and E. Boller (c), *Acta Materialia* **58**, 20-30 (2010).
(a) SIMaP, Université de Grenoble, Saint-Martin d'Hères (France)
(b) MATEIS, INSA Lyon, Villeurbanne (France)
(c) ESRF
(d) STI-LMX, EPF Lausanne (Switzerland)
(e) Centre des Matériaux, ParisTech, Evry (France)
(f) ARC CoE for Design in Light Metals, The University of Queensland, Brisbane, (Australia)

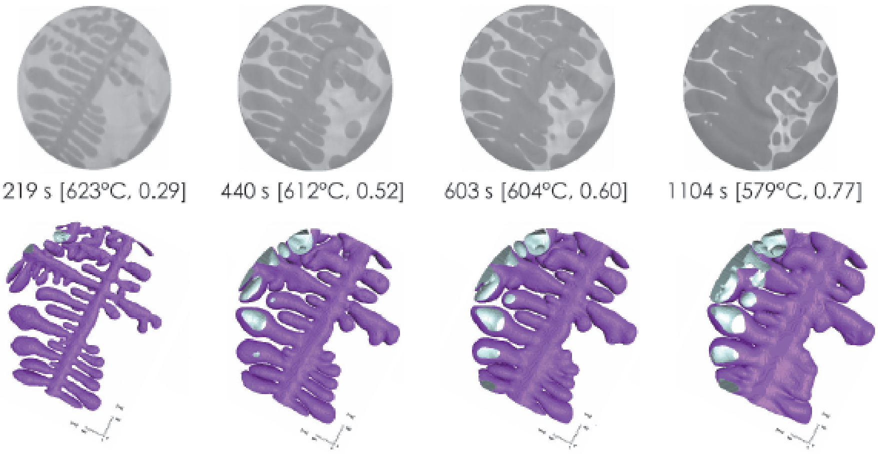

Fig. 132: 2D and 3D observations of the evolution of a dendrite with solidification time; the temperature and the volume fraction of solid are indicated within brackets.

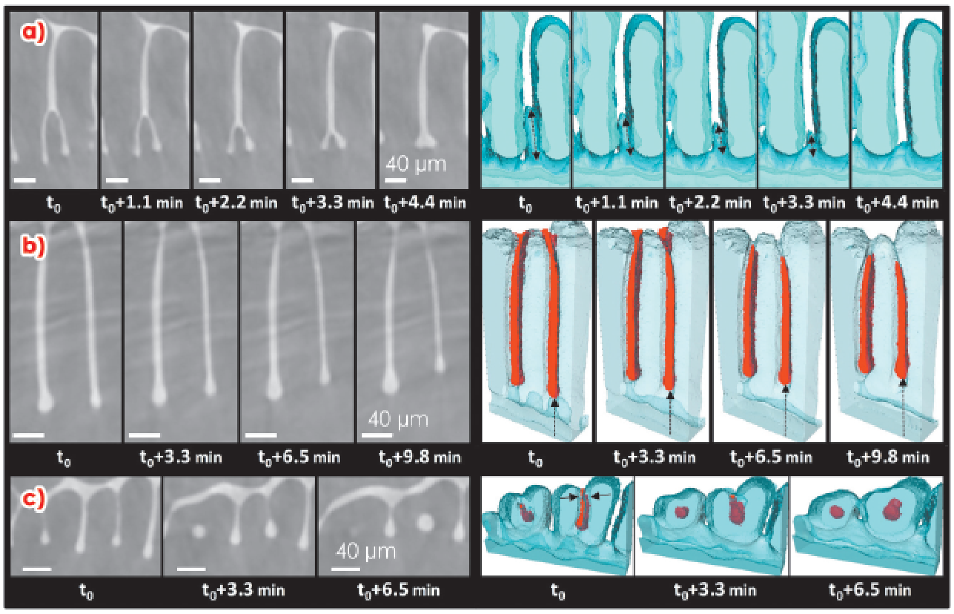

Fig. 133: Sequence of 2D (left) and 3D (right) images extracted from the volume of the specimen held for various times at 570°C showing the different coarsening mechanisms occurring on the scale of the dendrite arms (dark grey on the 2D images): a) progressive small dendrite arm melting;
b) progressive interdendritic groove advancement; c) progressive interdendritic groove advancement and joining of the tips of the dendrite arms, leading to the formation of entrapped liquid.

carried out in a furnace made of two $MoSi_2$ heaters enclosed inside a cubic-shaped chamber. The furnace has a hole at the bottom through which the specimen is inserted and there are two windows on the sides to allow the passage of X-rays. The scan time to take 450 projections over a 180° rotation of the specimen was 22 s. Radiographs were recorded using the FReLoN 14-bit dynamic CCD camera.

This experiment allowed *in situ* observations of the continuous growth of the dendritic structure of the alloy as shown in **Figure 132**, both in cross-section and in 3D. The figure clearly shows the various coarsening mechanisms which operate during solidification, namely dissolution of small dendrite arms and filling of the gap between two adjacent arms. However, since the solid fraction increases during solidification, these mechanisms are due to both solidification and coarsening induced by the reduction of the solid-liquid interface area.

To isolate the coarsening mechanisms, similar experiments were also carried out while maintaining the alloy isothermally in the semi-solid region and thus at constant solid fraction. For these experiments, the specimen was heated in a specially designed electrical resistance furnace at 6°C/min until 570°C and held isothermally at this temperature. The scan time was 30 s and a scan was taken every 65 s to characterise the evolution of microstructure during holding. At this temperature, the solid volume fraction was 72%.

Figure 133 shows details of the microstructural evolution at the scale of the dendrites. The observed coarsening mechanisms are somewhat different from those proposed in the literature so that the published models do not properly account for the observed kinetics of dendrite evolution. Improved models have thus been proposed based on our observations.

These experiments clearly demonstrate that *in situ* tomography is a very powerful technique for characterising the microstructural evolution of solid-liquid mixtures both during solidification and isothermal holding. The physical mechanisms that operate at the scale of the individual dendrites can be directly observed, thus allowing more realistic models to be proposed. However, the liquid and the solid phases must exhibit sufficiently different absorption contrast to be clearly distinguished and to allow for quantitative analysis. There are still some other limitations, particularly in terms of kinetics of the phenomena, but the continuous improvement in the equipment and techniques will make it possible to overcome these limitations in the future.

Study of defects in GaN:Mg by hard X-ray nanoprobe

Principal publication and authors
G. Martinez-Criado, R. Tucoulou, P. Cloetens, J.A. Sans and J. Susini, *Appl. Phys. Lett.*, **95**, 151909 (2009).
ESRF

Mg is the most efficient p-type dopant for the GaN semiconductor. However, to achieve significant hole concentrations in GaN, the Mg doping levels should exceed 10^{19} cm^{-3}, which induces microstructural planar defects [1]. Various pyramidal structures have been reported in GaN films grown by metal-organic chemical vapour deposition (MOCVD) wherein they

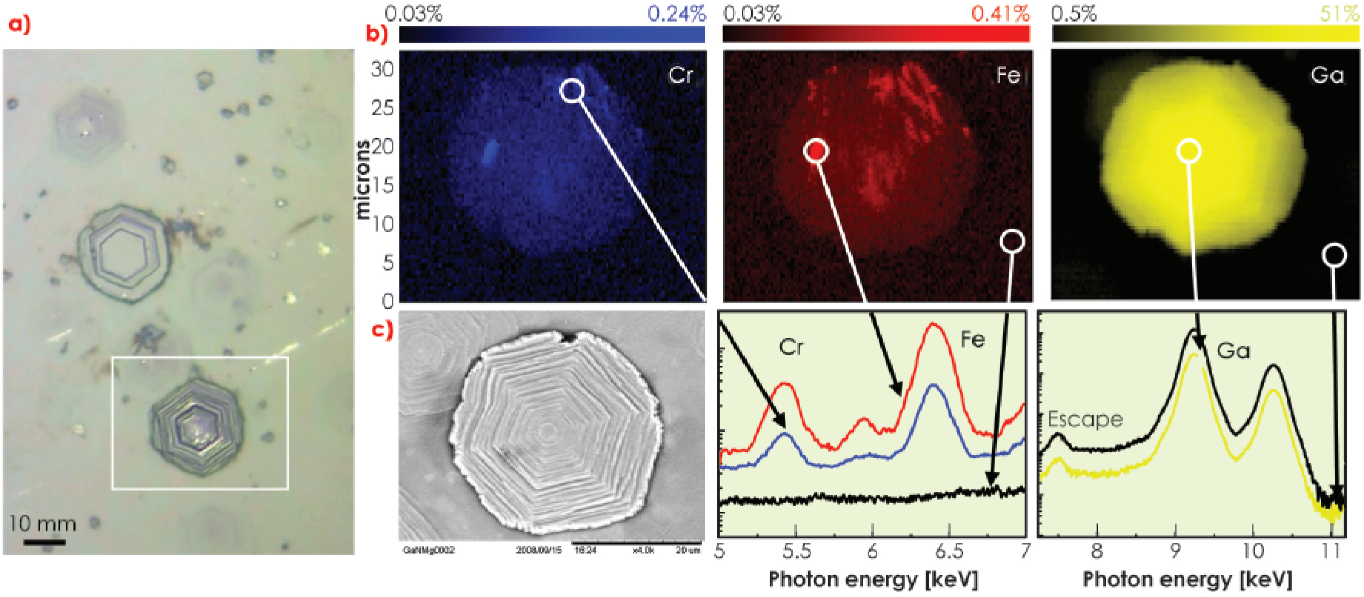

Fig. 134: a) Optical micrograph of the Mg-rich hexagonal pyramids in GaN. b) XRF images: BRY plot displaying the Ga-, Cr- and Fe-K$_\alpha$ intensity distributions with their corresponding concentrations in the colour scales. c) SEM image of the pyramidal defect.

depended on the growth polarity. They have been identified as Mg-rich pyramidal inversion domains, resulting from phase segregation effects [2]. Although the origin is not completely understood, it seems that the nucleation occurs at the sample surface, inducing changes in the stacking sequence from hexagonal to cubic structures or formation of Mg_3N_2 precipitates [3]. However, no direct experimental evidence has been provided so far to support the above mechanism and there is insufficient understanding of the underlying structural process. Therefore, the aim of this research was to study the three-dimensional Mg-rich hexagonal pyramids formed with Ga polarity in MOCVD grown GaN:Mg films by hard X-ray nanoprobe.

Figure 134 shows the XRF data collected at **ID22NI**, both optical micrograph and scanning electron microscopic (SEM) images. The presence of elemental traces of Cr and Fe is revealed. A blue-red-yellow (BRY) plot displays the Ga-, Cr- and Fe-K$_\alpha$ intensity distributions. As expected, the Ga arrangement presents equally spaced and periodic planes sequentially stacked from the hexagonal base. However, the impurities Cr and Fe exhibit a close correlation on their spatial locations without the 3D pyramidal shape, suggesting a possible Cr-Fe related secondary phase formation. However, no evidence for such a phase has been observed. A rough estimation of the elemental trace content yields [Fe] ≈ [Cr] ≈ 0.03% in the lowest concentrated areas, whilst [Fe] ≈ 0.41% and [Cr] ≈ 0.24% for the highest concentrated areas. Our observations emphasise the underlying diffusion mechanism, indicating local impurity agglomeration predominantly on the hexagonal base, supporting the occurrence of such pyramids by the kinetics of a number of additional impurities (not only light elements like O, C and H) that accompanied the Mg incorporation [4]. This is consistent

Fig. 135: a) Calculated and measured XANES data around the Ga K-edge for perpendicular/parallel incidence on the pyramid centre and outside. b) Calculated and measured XLD recorded at the Ga K-edge with the beam focused on the pyramid centre and outside of it.

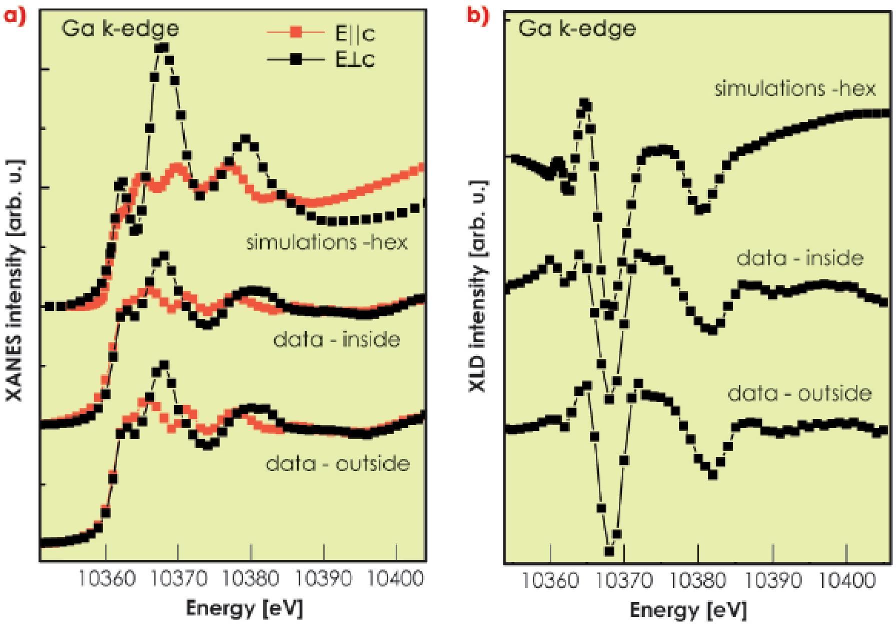

with earlier reports that suggest dopant or impurity segregation is responsible for the defect formation in GaN:Mg [5].

Figure 135 shows XANES probed inside and outside of such pyramids. For GaN, typically two polytypes exist: zincblende (cubic, T_d) and wurtzite (hexagonal, C_{6v}). Thus, in the case of the cubic GaN, an isotropic material, the XANES spectra should not depend on the angle of incidence θ, and the allowed transitions $1a_1 \rightarrow t^*_2$ are expected to be invariant with θ. Contrary to this, in the case of the hexagonal GaN, the XANES data are expected to depend on θ, more specifically the intensities of the resonances and not their linewidths and energy positions. The allowed transitions $1a_1 \rightarrow a^*_1$ will be strongest when the electron field vector is parallel to the *c* axis, while $1a_1 \rightarrow e^*_1$ will be strongest when the electron field vector is parallel to the (x,y) plane. While the e^*_1 final state results from mixing of p_x and p_y orbitals and can be considered as a plane orbital, the a^*_1 state can be considered as a vector orbital along the z axis (p_z orbitals). Here, the data do not show a clear superposition of the hexagonal spectrum plus a contribution associated with GaN having cubic symmetry. Since the energy positions and linewidths of the resonances are found to be independent of θ, it can be concluded that the pyramidal defects are quite pure hexagonal. From the comparison of the X-ray linear dichroism (XLD), our findings also show that these defects exhibit excellent crystallographic alignment. There is no remarkable damping effect revealing a strong influence of the Cr and Fe impurities in any preferential crystallographic direction.

In summary, we have investigated three-dimensional Mg-rich hexagonal pyramids in GaN by hard X-ray nanoprobe. Elemental maps of Ga, Cr and Fe were acquired and impurity concentrations estimated on the sub-micrometre scale. Structural analysis based on XANES and XLD revealed Ga atoms in tetrahedral coordination in the wurtzite structure. XLD collections around Ga atoms have shown no local atomic distortion inside the hexagonal defects, providing direct evidence for the highly short range structural order.

References

[1] W. V. Lundin *et al.*, *Semiconductors* **43**, 963 (2009).
[2] M. Leroux *et al.*, *Phys. stat. sol. (a)* **192**, 394 (2002).
[3] M. Hansen *et al.*, *Appl. Phys. Lett.* **80**, 2469 (2002).
[4] Hongbo Yu *et al.*, *J. Cryst. Growth* **289**, 419 (2006).
[5] Qiang Sun *et al.*, *Phys. Rev. B* **73**, 155337 (2006).

Sub-micrometre holotomography of multiphase metals

Principal publication and authors

G. Requena (a), P. Cloetens (b), W. Altendorfer (a), C. Poletti (a), D. Tolnai (a,c), F. Warchomicka (a) and H. P. Degischer (a), *Scripta Materialia* **61**, 760-763 (2009).
(a) Institute of Materials Science and Technology, Vienna University of Technology, Vienna (Austria)
(b) ESRF
(c) Eötvös Loránd University, Department of Materials Physics, Budapest (Hungary)

The microstructural characterisation of multiphase materials by conventional 2D metallography can be insufficient if, for instance, connectivity between phases exists, or the orientation of constituents varies throughout the volume. In this case, 3D characterisation tools are needed. Synchrotron microtomography is a powerful technique capable of revealing the architecture of materials. Furthermore, the coherence of the beam can be exploited by applying quantitative phase-contrast tomography or holotomography [1] to image components with similar attenuation. The spatial resolution achievable by parallel beam synchrotron microtomography is about 1 µm. This can be improved using magnifying optics [2]. So far this has been achieved for samples with diameters < 100 µm using relatively low energies. 3D imaging of engineering alloys requires high energies and representative sample sizes to correlate the properties

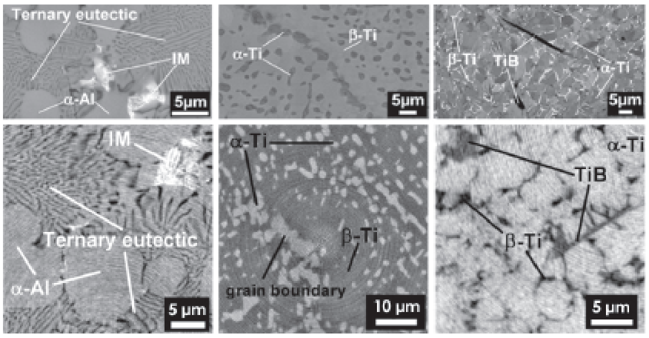

Fig. 136: From left to right: The materials are AlMg7Si4 alloy, Ti1023 alloy and Ti64/TiB/5w. Upper images are scanning electron micrographs; lower images are portions of slices of holotomographic reconstructions (magnified holotomography using KB optics).

with the microstructure achieved by the processing method.

Magnified synchrotron holotomography using a Kirkpatrick-Baez (KB) optics system [3] was carried out at the nanoimaging end-station ID22NI for Al- and Ti-alloy samples of 0.4 mm diameter. The focal point with a size of 80 nm (H) by 130 nm (V) and medium monochromaticity ($\Delta E/E = 2\text{x}10^{-2}$) was produced by a set of multilayer coated crossed bent mirrors. Energies of 17.5 keV and 29 keV as well as effective pixel sizes of 60 nm and 51 nm were used for the Al-alloy and Ti-alloys, respectively. Phase retrieval for holotomography was achieved from recordings at four focal-point-to-sample distances.

Examples of three light alloys are presented. Their microstructures are shown in the scanning electron micrographs (SEM) at the top of Figure 136:

- AlMg7Si4 alloy: the microstructure exhibits a fine ternary eutectic formed by Al, Si and Mg_2Si with lamellar structures >150 nm. Fe-rich intermetallics appear within the primary α-Al.

- Ti-10V-2Fe-3Al alloy (Ti1023): the alloy contains ~30% of hcp α phase distributed within bcc β grains not observable by absorption contrast.

- Ti-6Al-4V (Ti64) alloy reinforced with 5 vol% TiB needles (Ti64/TiB/5w): the Ti64 alloy matrix consists of α grains separated by narrow β zones and TiB needles.

Holotomography is well adapted to these materials as there is low absorption contrast between the present phases.

Portions of the reconstructed holotomography slices are shown at the bottom of Figure 136. The grey level scales linearly with the electron density of the constituents revealing all the phases observed in the SEM micrographs. Volume views of the minority phases are shown in Figure 137.

- AlMg7Si4: the ternary eutectic with interconnected Si-Mg_2Si structures as thin as ~ 180 nm (green) are identified. The intermetallic particles and α-Al are made transparent in Figure 137a.

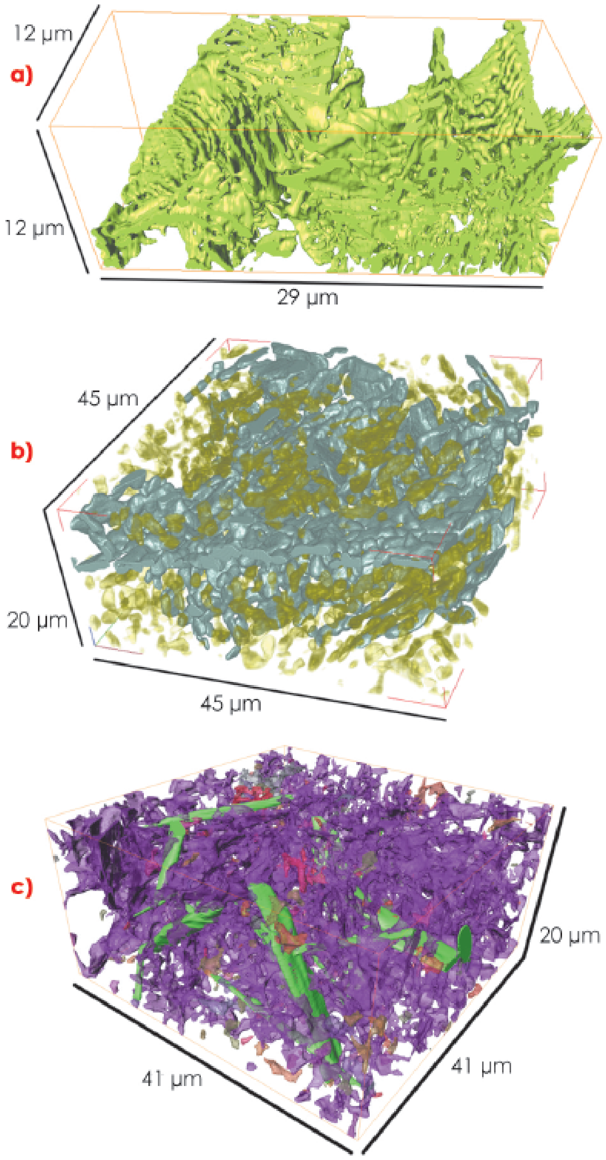

Fig. 137: Rendered volumes of the materials: a) interconnected Si-Mg_2Si structure (green) in AlMg7Si4; b) larger α particles remaining from pre-forging (blue) and individual secondary α grains (semi-transparent green) in Ti1023; c) TiB needles (green) and irregularly shaped β grains in Ti64/TiB/5w (other colours).

- Ti1023: α grains > 200 nm are identified. In Figure 137b, an interconnected structure of α particles remained from an incomplete break-up of the lamellar structure during pre-forging (blue), while secondary α grains (green) are embedded in the β phase.

- Ti64/TiB/5w: the α and β phases in the Ti64 matrix are identified down to 200 nm. In Figure 137c, TiB needles (green) are connected to irregularly shaped β grains (other colours), forming an interpenetrating structure within the α phase.

In summary, magnified synchrotron holotomography using KB optics

References

[1] P. Cloetens, W. Ludwig, J, Baruchel, D. Van Dyck, J. Van Landuyt, J.P. Guigay and M. Schlenker, *Appl. Phys. Lett.* **75**, 2912-2914 (1999).
[2] P. J. Withers, *Materials Today* **10**, 26-34 (2007).
[3] R. Mokso, P. Cloetens, E. Maire, W. Ludwig and J.Y. Buffiere, *Appl. Phys. Lett.* **90,** 144104 (2007).

was used to characterise the 3D-architecture of Al- and Ti-alloy samples of ~0.4 mm diameter with energies of 17.5 and 29 keV, respectively. Using the nano-focusing KB-system for such a high energy (29 keV) is reported for the first time. This experimental setup combining synchrotron radiation, KB optics and holotomography opens a new level of resolution (≥ 180 nm) for non-destructive 3D imaging of representative samples of multiphase metals.

Principal publication and authors

G. Silversmit (a), B. Vekemans (a), F.E. Brenker (b), S. Schmitz (b), M. Burghammer (c), C. Riekel (c) and L. Vincze (a), *Analytical Chemistry,* **81**, 6107 (2009).

(a) X-ray Microspectroscopy and Imaging (XMI) group, Department of Analytical Chemistry, Ghent University (Belgium)

(b) GeoScience Institute, Goethe University, Frankfurt (Germany)

(c) ESRF

3D elemental imaging of cometary matter by nanoscale X-ray fluorescence tomography

NASA's Stardust spacecraft collected comet coma particles from the Comet 81P/Wild2 as well as interstellar grains and returned them to Earth [1]. The cometary micro-particles were captured using aerogel collectors, which contain a low-density silica-based solid with a porous, foam-like structure, about 1000 times less dense than glass. This low density minimises the deceleration particles experience upon impact with the aerogel. The spacecraft passed through the comet coma on the 2nd of January 2004. Particles impacted on the aerogel collector with a relative speed of approximately 6.1 km/s, leaving carrot or bulbous shaped impact tracks in the aerogel (**Figure 138**).

The uniqueness of these extraterrestrial particles calls for *in situ* (*i.e.* particle still enclosed in the aerogel matrix) and non-destructive analysis. Imaging of major, minor and trace elements within various absorbing matrices is possible using μ-XRF (X-ray fluorescence). Simple linear μ-XRF scanning of the sample along a vertical and horizontal raster through the μ-beam results in integrated two-dimensional (2D) projections of the elemental distributions within the sample. However, these projections do not contain depth information, as the complete intersection of the beam with the sample is measured. This depth information can be reconstructed with μ-XRF tomography.

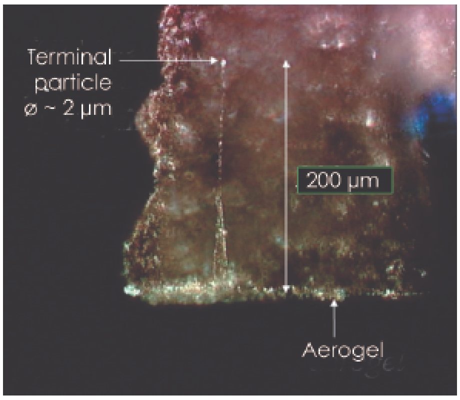

Fig. 138: Stardust Track No.C2044,0,37 in the aerogel and the cometary grain analysed in this study.

The fully three-dimensional (3D) distribution of main and trace elements from within the terminal particle was determined based on sub-micrometre XRF tomography at a spatial resolution level of 200 nm. This experiment was performed at beamline **ID13**, using an excitation energy of 12.7 keV. An essentially symmetric sub-micrometre X-ray beam of 220 x 170 nm^2 (HxV) (4–5x10^9 ph/s) was obtained using a crossed linear Fresnel lens system provided by C. David [2]. Full 2D nano-XRF images for each tomographic view (pixel size: 100 nm) were collected, taking approximately 48 hours of measuring time. The reconstruction of the 3D elemental distributions was performed using a voxel size of 100 nm. An RGB composite image of the low intensity isosurface distributions of Fe (red), Cr (green) and Se (blue) for different angular views is given in **Figure 139**.

The inhomogeneous distribution of elements in the terminal particle helps to understand the nature of the studied material and to distinguish between artificial elemental concentrations and that of the chemistry of the captured cometary particle [1]. During the preliminary examination phase, it was shown that some elements, such as Cu, Zn and Ga show substantial enrichment over chondritic composition [1]. The observed Se-concentrations show the largest variation of hot spot analyses documented by Flynn *et al.* [1].

Both increased values over chondritic composition and the variable elemental concentrations from hotspot analyses could be explained by the observed 3-dimensional distribution of elements. The terminal particle studied in this work shows a Se-enrichment surrounding the top of the grain which is a clear indication for compressed aerogel in front of the impacted cometary dust particle. It can be clearly seen that the Se distribution forms a shell around the particle which does not originate from the particle itself. XRF measurements on the aerogel collectors used to capture the particles revealed the presence of trace levels of Se, which represents the most likely origin of the Se-lines within the measured nano-XRF spectra. The Se-rich external layer surrounding the particle is attributed to the partial melting and subsequent solidification of the aerogel around the terminal particle, as a result of the high speed impact of the comet coma particle.

The plate-like three dimensional distributions of Cr and Fe in the terminal grain resembles the structure of cryptocrystalline olivine-pyroxene chondrules. This interpretation is further supported by recent findings of chondrule-like objects in Wild-2 [3], which is a further strong argument for large scale mixing within the protoplanetary disc.

As demonstrated by the above example on this unique cometary material, the sub-microscopic three-dimensional reconstruction of trace-level elemental distributions within this 2 µm individual particle not only reveals the heterogeneous nature of the cometary grain, but also enables elemental constituents originally present in the cometary matter to be distinguished from those present as impurities within the embedding aerogel host matrix.

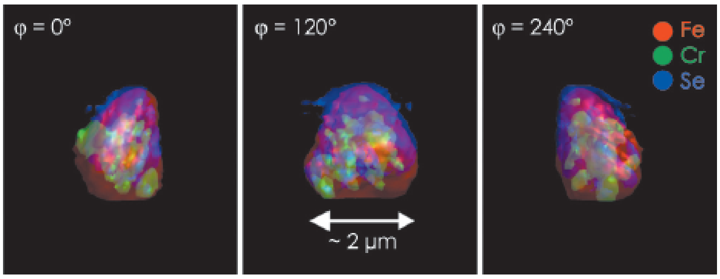

Fig. 139: Reconstructed low intensity isosurface composite images for different azimuthal viewing angles.

References

[1] G.J. Flynn *et al. Science* **314,** 1731 (2006).

[2] B. Nöhammer, C. David, M. Burghammer and C. Riekel, *Applied Physics Letters*, **86**, 163104 (2005).

[3] T. Nakamura, T. Noguchi, A. Tsuchiyama, T. Ushikubo, N.T. Kita, J.W. Valley, M.E. Zolensky, Y. Kakazu, K. Sakamoto, E. Mashio, K. Uesugi and T. Nakano, *Science* **321**, 1664 – 1667 (2008).

Characterisation of a degraded cadmium yellow (CdS) pigment in an oil painting by means of synchrotron radiation based X-ray techniques

Cadmium sulphide exists in two crystalline and one amorphous form. The hexagonal form (α-CdS) is found in nature as the mineral *greenockite* while the cubic form (β-CdS) is called *hawleyite*; greenockite is frequently used as yellow pigment in modern paints. Manufacturers started to make intense use of this pigment from the moment cadmium became commercially available as a base material (around the 1840's). This popularity was mainly due to the pigment's high tinting and covering power, bright yellow colour, wide applicability (artists' paint, metallurgy, ceramics, medical use, etc.) and suitability for mass production. In addition, at the beginning of the 20th century, CdS was thought to be highly stable in oil paint and water colours, which was not the case for chrome yellow ($PbCrO_4$), the only bright yellow alternative available for painting at that time. Consequently, prominent 19th-20th century painters such as Claude Monet, Vincent Van Gogh and Pablo Picasso frequently employed CdS, as was amply documented by earlier analytical research. Yet, in spite of its excellent reputation with regards to permanency, fading of the yellow colour of CdS and loss of adhesion of the oil paint has been reported.

On several paintings by James Ensor (1860-1949), an avant-garde painter, a gradual fading of originally bright yellow CdS areas is observed. This phenomenon is associated with the formation of small white-coloured globules on top of the original paint surface. Figure 140 shows Ensor's painting "Still Life with Cabbage" from which small amounts of yellow paint and the whitish material were examined

Principal publication and authors

G. Van der Snickt (a), J. Dik (b), M. Cotte (c,d), K. Janssens (a), J. Jaroszewicz (a), W. De Nolf (a), J. Groenewegen (b) and L. Van der Loeff (e), *Anal. Chem.* **81**, 2600 (2009).

(a) University of Antwerp (Belgium)
(b) Delft University of Technology (The Netherlands)
(c) C2RMF (France)
(d) ESRF
(e) Kröller-Müller Museum (The Netherlands)

Fig. 140: a) Optical photograph of the oil painting 'Still life with Cabbage' by James Ensor (ca.1921, KM 105.303); b) detail of the exposed yellow paint surface (X40) showing white globules; c) Detail of the right-lower corner of the painting: the yellow paint covered by the frame retains its vivid yellow colour while the paint in the exposed areas has become dull due to the formation of the white globules.

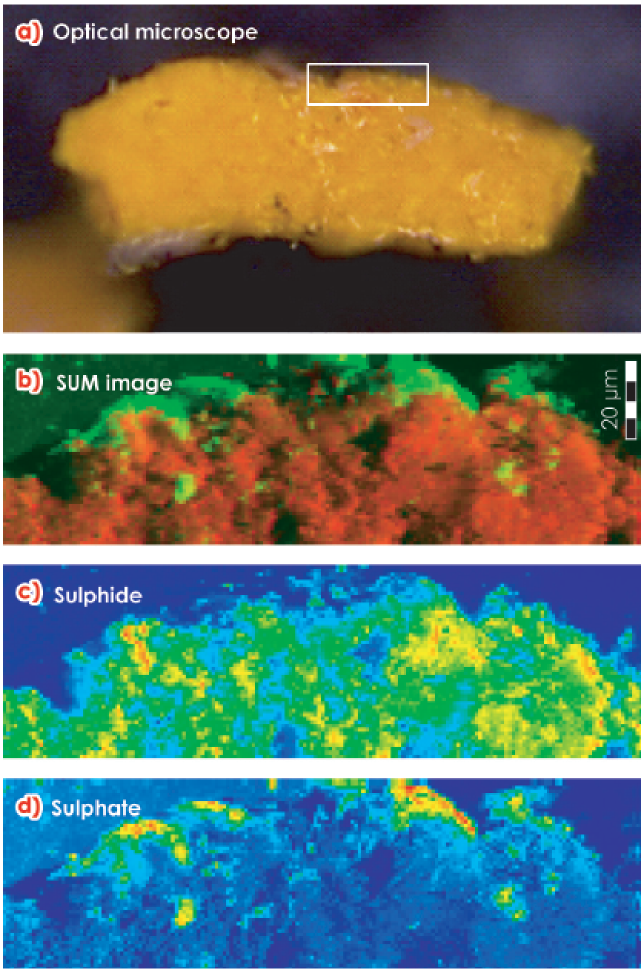

Fig. 141: a) Optical micrograph of a cross section of partially degraded yellow paint. White rectangle: area where S-chemical state maps (b-d) were obtained. b) Red-green composite of (c) and (d), red: sulphides and green: sulphates; c) sulphide distribution; d) sulphate distribution. Map size = 184 x 50 µm^2; step size = 1 x 1 µm^2.

at the ESRF. Microscopic X-ray absorption near edge spectroscopy (µ-XANES) experiments at **ID21** were used to demonstrate that sulphur, originally present in sulphidic form (S^{2-}) is oxidised during the transformation to the sulphate form (S^{6+}). The presence of cadmium sulphate ($CdSO_4.2H_2O$) and ammonium cadmium sulphate ($(NH_4)_2Cd(SO_4)_2$) at the surface was confirmed by microscopic X-ray diffraction measurements at **ID18F**. The latter salt is suspected to result from a secondary reaction of cadmium sulphate with ammonia. The Cd itself remains in its original oxidation state (Cd^{2+}). S-chemical state maps recorded from cross-sections reveal that during the last 100 years, the oxidation front has penetrated into the yellow paint up to ca. 1-2 micrometres (**Figure 141**).

The superficial deterioration was exclusively detected in areas where the paint was directly exposed to a combination of light and humidity, allowing the following photo-induced reaction to take place:

$$CdS + 2O_2 + H_2O \rightarrow CdSO_4.H_2O$$

The formation of the globules can be attributed to a process of recurring moistening and drying of the paint surface that induces the repeated dissolution and (re)precipitation at and near the surface of the highly hygroscopic cadmium-sulphate; fluctuating climatic conditions in the museum gallery are likely to drive this process.

To prevent further progression of the oxidation process and loss of colour-vividness, the amount of UV radiation reaching the painting surface must be limited while care must be taken to stabilise the relative humidity level of the surrounding atmosphere.

The impossible fish brain revealed by synchrotron holotomography

Animal fossils are generally remains of mineralised hard tissues (*i.e.* bones, teeth or shells), but traces of soft tissues, otherwise destroyed during decay, may be preserved under exceptional circumstances. Accessing this kind of information for extinct organisms becomes increasingly important for our understanding of the evolution of life on our planet. Third generation synchrotrons, and especially the ESRF, now yield evidence of such exceptional soft tissue structures, hitherto regarded as unavailable to palaeontologists. The mineralised brain was discovered in the fossil of a 300 million year-old fish. Findings such as this provide key information about the evolution of life from a very long time ago.

The discovery started with a first test using synchrotron microtomography in absorption mode on the skull of an iniopterygian (an extinct fish group distantly related to present day sharks and ratfish), performed on beamline **ID19**. **Figure 142a** shows this specimen which had been rapidly preserved after death in a phosphate concretion. The original purpose of the experiment was to provide the first 3D evidence of the skull for this group of cartilaginous fish which have rarely been preserved in 3D. In addition to the morphology of the skull, the first microtomography test showed a strange, small, and nearly symmetrical object inside the braincase. Despite the insufficient initial resolution and the faint contrast due to the absorption imaging mode, the unexpected structure has similarities with the brain of a modern shark. Exceptional calcification of fossil soft tissues (notably muscles) is already known, but brain and nerve tissues decay so quickly that their preservation was considered impossible. In order to confirm the nature of this object, we decided to apply a far more sensitive method, one that was only recently optimised for such dense specimens: quantitative phase contrast tomography (or holotomography). This method revealed the structure (**Figure 142b**) in much more detail and with improved contrast. **Figure 143a** shows the 3D reconstruction of the skull with the enigmatic structure in the middle. The structure displays a morphology characteristic of an early vertebrate brain, with optic lobes, cerebellum, spinal cord and major cranial nerves (**Figure 143b**). This is the first ever discovery of a mineralised brain replica. The large optic lobes and small cerebellum suggest the habitat of this fish: a bottom-dwelling ambush predator with very large eyes and limited manoeuvrability.

How could this exceptional soft tissue preservation occur? Experiments have recently been carried out to understand how fast soft tissues decay in various kinds of organisms, and how bacteria could initiate a rapid transformation of 'flesh' into 'rock' [1]. 'Decay experiments' performed on extant sea urchin embryos demonstrated that, within a few days and under anoxic conditions, bacteria can deposit enough calcium phosphate on the surface of a decaying organic tissue to preserve its shape, until further growth of the crystals makes it resistant to the pressure from the sediment [2].

Principal publication and authors

A. Pradel (a,b), M. Langer (c), J.G. Maisey (d), D. Geffard-Kuriyama (a), P. Cloetens (c), P. Janvier (a) and P. Tafforeau (c).
PNAS, **106**, 5225-5228 (2009).
(a) UMR7207 du CNRS, Muséum National d'Histoire Naturelle, Paris (France)
(b) UPR9034 du CNRS, Gif-sur-Yvette (France)
(c) ESRF
(d) American Museum of Natural History, New York (USA)

Fig. 142: a) The skull of a 300 million iniopterygian fish from Kansas (USA) preserved in a concretion formed in a reducing shallow water marine environment (foreground). b) bacteria-induced soft tissue preservation of the brain revealed by synchrotron holotomography.

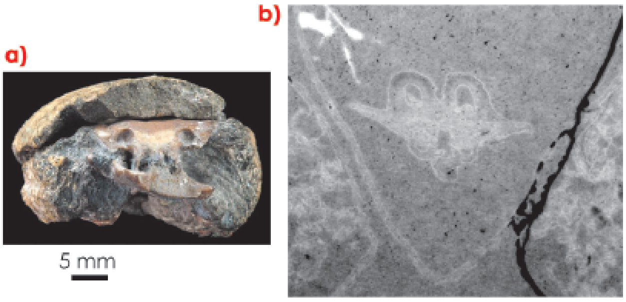

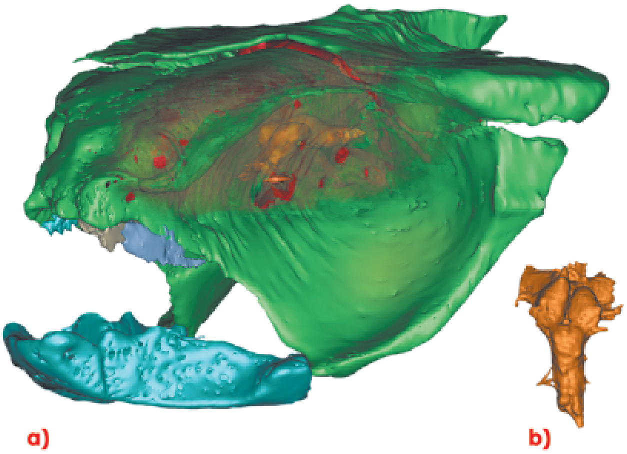

Fig. 143: a) 3D segmentation of the same fossil fish skull showing the position of the mineralised brain (orange) and b) dorsal view of the preserved brain.

It appears clearly that the abundance of bacteria, calcium and phosphorus ions, in a very low energy, anoxic, reducing environment, is critical for soft tissue preservation. Therefore, exceptional tissue preservation most frequently occurs near the gut and often concerns muscles of the body wall. The preservation of a brain, although probably due to the same microbial induction, was really unexpected. Our specimen, like many other fossils from the same Carboniferous site in Kansas, may be in fact a regurgitation pellet from a larger shark. The fish may have macerated for a while in the intestine of the shark, where it was enriched with bacteria and phosphorus from other digested prey.

A world specialist of fish brains once declared at a meeting: "I would sell my soul to see the brain of *Eusthenopteron*" (the 380 million year-old, iconic fossil "intermediate" between fishes and land vertebrates). Our discovery, albeit 80 million years younger, shows that one may not need to go that far to see the "brain of *Eusthenopteron*"; a synchrotron beamline like **ID19** may be enough.

References
[1] D.E.G. Briggs, *Ann. Rev. Earth Planet. Sci.* **31**, 275-301 (2003).
[2] E.C. Raff, J.T.Villinski, F.R.Turner, P.C.J. Donoghue and R.A. Raff., *PNAS* **103**, 5846-5851(2006).

Untangling the evolution of giant sperm in ostracod microcrustaceans using holotomography

Principal publication and authors
R. Matzke-Karasz (a), R.J. Smith (b), R. Symonova (c), C.G. Miller (d) and P. Tafforeau (e), *Science* **324**, 1535 (2009).
(a) Ludwig-Maximilians-University Munich (Germany)
(b) Lake Biwa Museum, Kusatsu (Japan)
(c) Charles University, Prague (Czech Republic)
(d) Natural History Museum London (UK)
(e) ESRF

Some animal groups have extraordinarily long and thin filamentous spermatozoa. This characteristic usually occurs only in a single or just a few species up to a subgenus like in *Drosophila*. However, there is one exception: ostracods, which are micro-crustaceans living worldwide in all kinds of water bodies. Within their superfamily *Cypridoidea*, all circa 1600 living, mainly freshwater, species show reproduction with giant sperm (sperm length up to 7 times the body length in *Heterocypris sydneia*). The fact that giant sperm are present in the whole taxon suggests that this way of reproduction developed in the early phase of the evolution of this group.

In addition to giant sperm, an intricate set of reproductive organs developed in this group. Both genders have a complete system of reproductive organs on either side of the body. Males possess a paired sperm pump (or Zenker organ) within the sperm ducts, which is mainly a sclerotised chitinous tubular structure. Two vaginas of the female accommodate the two penes of the male during copulation to receive the giant sperm, which are then transferred to a pair of storage organs (or seminal receptacles), before they are used for egg fertilisation.

Ostracods are the most abundantly preserved arthropods in the fossil record dating from at least the Ordovician (450 Myr). Their exceptional fossil record is due to their calcitic bivalved carapace, usually 0.3 to 3 mm long, that is readily preserved. Unlike the carapace, the body and appendages are only very rarely recorded as fossils, and mostly with only a poor preservation of the appendages. An exception to this is *Harbinia micropapillosa* from the Santana Formation of the Cretaceous of Brazil (about 100 million years old). Specimens of this species are hosted in the Natural History Museum's collection in London (NHM). Previous scanning electron microscopic studies of this species showed that the external surface of the soft parts is frequently preserved in very high quality by apatite. This present study reaveals the internal features for the first time.

Of 23 specimens of *H. micropapillosa* (a loan of the NHM), and 18 specimens of the living *Eucypris virens* (used as comparative material), holotomographic scans were performed at beamline **ID19** with a monochromatic beam at an energy of 20 keV and a detector pixel size of 0.678 micrometres. Each holotomographic data set was composed of four different scans using 1500 projections over 180 degrees: one absorption scan (sample to detector distance of 5 mm) and three propagation phase contrast scans at increasing distances (20 mm, 40 mm,

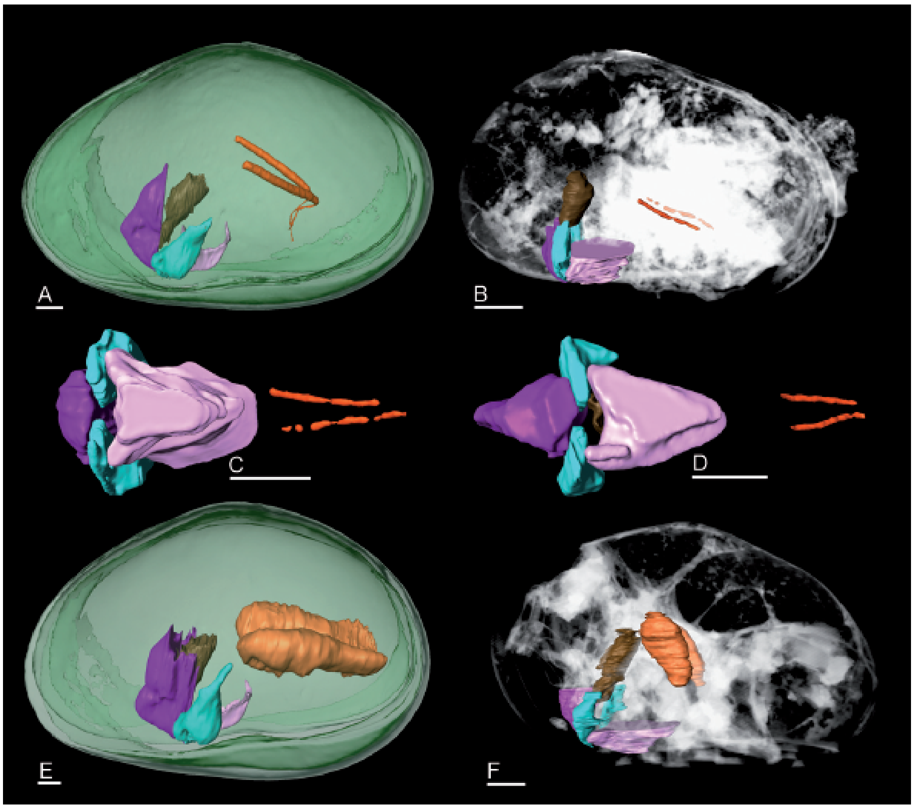

Fig. 144: Reproduction organs in *Eucypris virens* (extant) and *Harbinia micropapillosa* (fossil). Anterior to the left. (A and E) lateral view of male (A) and female (B) *E. virens* with several organs shown for comparison. (B and F) lateral view of male (B) and female (F) *H. micropapillosa* with several organs shown in context of whole body reconstruction. (C and D) ventral views of several organs including tubes of Zenker organs of male *H. micropapillosa*. *Colours:* orange: central tubes of Zenker organs in males, seminal receptacles in females; brown: oesophagus; turquoise: mandible; purple: upper lip; pink: lower lip; green: valves; grey-scales: whole body reconstruction. All scale bars 100 µm. Original data underlying the cited publication can be downloaded from the ESRF Palaeontological Microtomographic Database (http://paleo.esrf.eu).

70 mm). Phase retrieval was computed for each projection angle with an algorithmic approach adapted to absorbing samples. Reconstructed holotomographic slices of fossil specimens were then optimised by attenuating the most contrasted parts (mostly due to pyrite infilling) and by normalising the air background.

Each fossil specimen of less than 1 mm body length was finally represented by a stack of 1200 to 1500 virtual slices, which were further processed within 3D-visualising software.

Processing of the holotomographic data obtained on the fossil specimens of *H. micropapillosa* revealed structures of biological origin within the main body of the animals (**Figure 144**).
In males, a pair of tubes close to the penes can be identified as traces of Zenker organs, while large paired cavities near the mid-point of the body represent the seminal receptacles in female specimens. The receptacles must have been filled with sperm in order to be preserved as two cavities – rare fossil evidence of insemination. Since both Zenker organs and large seminal receptacles are only known from ostracods reproducing with giant sperm, this extraordinary method of reproduction must have developed in this group of ostracods at least 100 million years ago. The conformity of fossil and recent reproductive organs suggest that giant sperm probably developed only once in this group.

Thanks to the outstanding resolution and contrast features of holotomography at the ESRF we found that in freshwater ostracods, reproduction with giant sperm has been a successful and stable feature for a long time – despite high biological costs. Exploring the advantages of this exceptional kind of reproduction will be the focus of our ongoing research.

Methods

Phase-contrast and holographic computed laminography

Principal publication and authors
L. Helfen (a), T. Baumbach (a), P. Cloetens (b) and J. Baruchel (b), *Appl. Phys. Lett.* **94**, 104103 (2009).
(a) Institute for Synchrotron Radiation (ISS/ANKA), Karlsruhe Institute of Technology (Germany)
(b) ESRF

Computed tomography is an established method for three-dimensional imaging at synchrotron sources. When applied to laterally extended specimens like plate-like objects, measurements are usually afflicted by artefacts due to the limited accessible angular range.

Recently, synchrotron radiation computed laminography was developed [1] to complement computed tomography for imaging of laterally extended specimens. Since the method enables us to zoom in to regions of interest of macroscopically large devices with microscopic resolution, it is optimised for acquisition and reconstruction of 3D data sets from rather flat specimens with lateral extensions much larger than the detector acceptance window. Like computed tomography, it takes advantage of the higher photon flux and high brilliance available at synchrotron sources resulting in a reduced data acquisition time and improved contrast due to the use of monochromatic radiation.

We have extended the applicability of laminography to high-resolution 3D imaging of weakly-absorbing specimens whose integrity needs to be preserved. This is especially important in the case of precious specimens, for materials which might suffer from sample extraction or when time-resolved measurements are required on a specimen under load and with engineering-relevant boundary conditions. The method uses the unique properties of partial coherence delivered through propagation-based phase contrast.

Computed laminography relaxes the geometrical requirements of computed tomography – which is characterised by tomographic rotation around an axis perpendicular to the beam path – to the more general case of using an inclined rotation axis. The flat specimen is mounted with its normal approximately parallel to the rotation axis.

Propagation-based phase contrast is included into computed laminography measurements via detecting the intensity patterns at varying propagation distances downstream of the laterally extended specimen. Similar to phase-contrast computed tomography, the principle of phase-contrast computed laminography can be divided into three steps:
1) radiographic data acquisition involving projection of the original 3D object function and wavefield propagation to finite detector distances; 2) retrieval of the corresponding two-dimensional phase and amplitude distribution maps;
3) reconstruction of the 3D laminographic image function for the specimen's region of interest. Unlike in phase-contrast computed tomography, there exists *a priori* knowledge about the variation of the propagation distance along the projection of the rotation axis which can be included in the phase retrieval step 2 (see principal publication).

Using the example of a diffusion layer developed for fuel cells, 3D data reconstructed by phase-contrast computed laminography are presented in **Figure 145**, both for the edge-detection regime (a,d,f) and for holographic phase retrieval (c,e,g). The diffusion layer consists of a sheet of interconnected spheres mainly made of carbon. When applying holographic phase retrieval [2] from four propagation distances, the reconstructed image (see c,e,g) is directly sensitive to the refractive index decrement distribution $\delta(x,y,z)$ so that contrast appears between the spheres' volume material and the surrounding voids. This allows easy segmentation, generally not sensitive to noise [see the cross-sectional slice (c) and 3D rendition (e) with magnification in (g)]. When working with only one propagation distance in the edge-detection regime (see a,d,f), we are sensitive to the Laplacian of $\delta(x,y,z)$. As a result, the surfaces of the microparticles become emphasised in

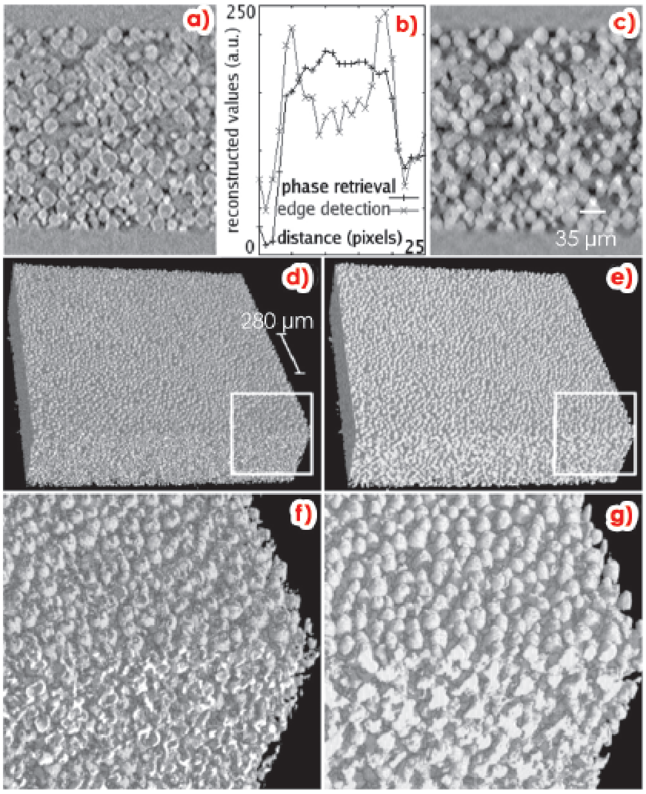

Fig. 145: Region-of-interest imaging of a diffusion layer sheet developed for fuel cells by phase-contrast laminography. For the edge-detection regime (a,d,f) a single specimen-detector distance of 0.03 m was used. For the holographic reconstruction (c,e,g) the distances 0.03, 0.045, 0.105 and 0.215 m were used. The images (a) and (c) are reconstructed cross-sectional slices along the direction of the rotation axis, the images (d) and (e) 3D renditions of the ROI imaged, with magnifications in (f) and (g), respectively. The plots (b) compare profiles in (a) and (c) along the line given in (c). Axis inclination 30°,
X-ray energy 20.5 keV, voxel size 1.4 µm.

the image. In many cases, this already gives sufficient information about the specimen's structure at the region of interest investigated. For a more quantitative comparison, cuts through a single sphere are compared by the profiles in (b).

The results demonstrate the feasibility of laminographic phase-contrast techniques. It is noteworthy that, contrary to computed tomography, the images are acquired without any specimen preparation (*i.e.* sample extraction), just by zooming into the region of interest of a macroscopically large specimen.

In summary, phase-contrast laminography complements phase-contrast computed tomography for non-destructive 3D imaging of weakly contrasted structures. The Karlsruhe Institute for Technology has installed a dedicated instrument for computed laminography at beamline ID19.
By completely avoiding a transilluminated specimen holder it is especially adapted to phase-contrast measurements. It allows one to zoom into arbitrary regions of interest and to scan macroscopically large specimen areas of up to 150x150 mm with spatial resolutions presently down to the micrometre scale. Avoiding the need for destructive sample extraction, the method and its instrumental realisation will provide new insight into microstructures and their evolution in application fields where layers, sheets or panels of light (*e.g.* organic) materials are used; for example in biological specimens, filter materials, paints and paintings or composite materials.

References

[1] L. Helfen, T. Baumbach, P. Mikulík, D. Kiel, P. Pernot, P. Cloetens and J. Baruchel. *Appl. Phys. Lett.* **86**, 071915 (2005).
[2] P. Cloetens, W. Ludwig, J. Baruchel, D. van Dyck, J. van Landuyt, J.P. Guigay and M. Schlenker, *Appl. Phys. Lett.* **75**, 2912 (1999).

Enabling Technologies

Instrumentation and the associated enabling technologies underpin every aspect of the scientific activity of the ESRF. The overall performance of our beamlines depends critically on innovative and successful X-ray instrumentation R&D programmes. A typical example is given in this section with the development of an original strategy for an extreme energy resolution monochromator. R&D on the sample environment is of particular importance as emphasised by two articles focussed respectively on the controlled dehydration of macromolecular crystals and on the development of customised microfurnaces.

The way scientists interact with beamline components depends on the software controlling these components; the ensuing data processing depends on the capacity and versatility of the available computing environment. With the Upgrade Programme on its way, it was recognised early on that our organisational structure was not optimal for facing the many challenges inherent to our aim of modernising the ESRF. This led to the creation of the Instrumentation Services and Development Division (ISDD) early in 2009, and will lead to the creation of the Technical Infrastructure Division (TID) in 2010. Both divisions bring together all in-house experts to create the necessary synergies in the various technical specialities needed to design and manufacture state-of-the-art X-ray instrumentation and to provide the best possible technical infrastructure for our visiting and in-house scientists.

The work on the Upgrade Programme is advancing well. Several of the work packages financed from the FP7 project *ESRFUP*, are now coming to an end. The results will have a direct impact on the direction of future developments. In this section, we present the outcome of the Grid feasibility study, one of the 13 work packages of the preparatory phase of the Upgrade. Instrumentation development for the Upgrade is of European significance. It is very important that much of this work is carried out in close collaboration and as a common effort with our colleagues in Europe. In this section of the Highlights we present an account of the MAXIPIX detector developments. Other noteworthy collaborations are currently being set up; they will soon produce important results (HIZPAD, NanoFOX, VEDAC, PANData, etc.). Another example of a successful collaboration at the European level is given by the BigDFT project, which aims at proving enhanced computing and calculation capabilities for electronics structure calculations.

Last, but not least, works have started on the extension of the data centre in the Central Building. The new data centre, essentially three times bigger than the current one, will provide the electrical power and associated cooling for the computing infrastructure to store and analyse the data generated by the ESRF in the decade(s) to come.

J. Susini and R. Dimper

Focusing monochromator with extreme energy resolution

Principal publication and authors

V. G. Kohn (a), A. I. Chumakov (b) and R. Rüffer (b), *J. Synchrotron Rad.* **16**, 635 (2009).

(a) Russian research center "Kurchatov Institute" (Russia)

(b) ESRF

High energy resolution is a figure of merit for many synchrotron radiation techniques. The most extreme requests come from inelastic X-ray scattering and nuclear inelastic scattering, where ~1 meV and sub-meV resolution is reached. An even higher energy resolution is needed for demanding scientific cases such as the novel high-T_C superconductors, liquids, and biological materials. Therefore, the improvement of the energy resolution down to 0.1 meV is a key project at several synchrotron radiation facilities.

Attempts to reach an energy resolution of 0.1 meV with conventional optical schemes encounter severe losses of intensity [1,2]. Analysing alternative schemes with higher throughput, we propose an approach with a 'focusing monochromator', whereby the X-ray energy spectrum is swept along the spatial coordinate rather than along the angular coordinate.

The operation of the focusing monochromator is based on a combined action of a focusing lens and a dispersive crystal (**Figure 146**). The lens alone would focus X-rays of all relevant energies towards a single spot. The crystal in a highly asymmetric reflection works as an optical prism [3], sorting the X-rays of different energies into different directions. In the combined action, the lens focuses X-rays *through* the dispersive crystal. Deflecting the X-ray components of different energies by different angles, the crystal re-directs them to different focal spots. The selection of the narrow energy band is provided by a slit located in the focal plane. The more convenient *in-line* geometry of the monochromator is achieved by adding another crystal with the same reflection, but in a symmetrical scattering geometry (**Figure 147**).

The ultimate relative energy resolution $\Delta E/E$ of the focusing monochromator is determined by the angular size of the radiation source as

$$\frac{\Delta E}{E} = \frac{\Delta\theta}{\tan\theta_B}\;\frac{b}{(b-1)}\;,$$

where $\Delta\theta = S/L$ is the angular size of the radiation source as seen from the lens location; S is the spatial source size; L is the source-lens distance; b is the module of the reflection asymmetry parameter; and θ_B is the Bragg angle. This resolution is reached with the slit size equal to the focal spot of monochromatic radiation. Opening the slit, one can gradually increase the bandwidth of the selected radiation up to the entire energy band reflected by the crystal. This offers a useful possibility to perform fast measurements with coarse resolution but high count rate before studying selected features with the ultimate energy resolution.

For a moderately high asymmetry parameter b, the relative energy resolution $\Delta E/E$ is determined only by the angular size $\Delta\theta$ and the Bragg angle θ_B. The smallest angular size of the radiation source available at the ESRF (for a 200 m-long beamline) is 0.1 µrad. Then, the 0.1 meV bandwidth can be

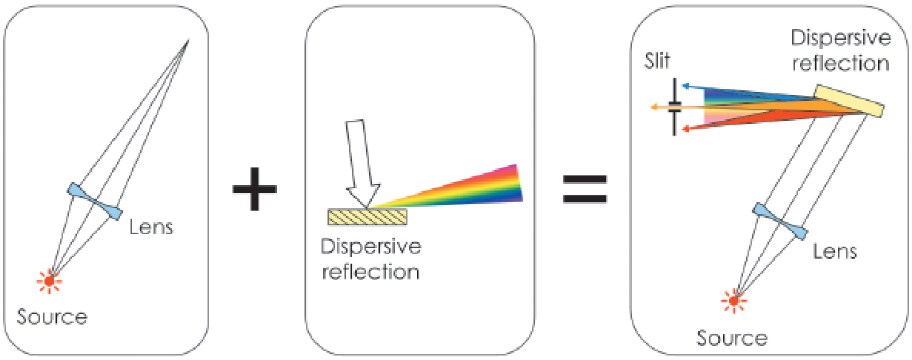

Fig. 146: The concept of a 'focusing monochromator': By the combined action of the focusing lens and the dispersive crystal, X-rays of different energies are focused to different focal spots. Selection of the narrow energy band is achieved by the slit.

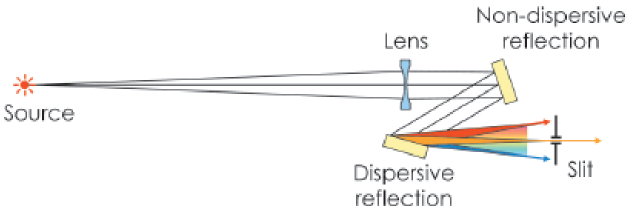

Fig. 147: In-line geometry of the focusing monochromator with an additional crystal in symmetric reflection.

obtained with a Bragg angle of 84 or 87 degrees for X-rays with an energy of 10 keV or 20 keV, respectively.

The proposed optical scheme is expected to provide very high throughput of radiation within the selected energy band. According to the operation requirements (see principle publication), the lens delivers a highly collimated beam well within the angular acceptances of both crystals. In addition, the moderate asymmetry parameter allows one to keep the high reflection coefficient.

From a practical point of view, the proposed design is simple and includes a minimal number of optical elements. Relative to conventional high-resolution optics, the X-ray spot on the crystals of the focusing monochromator is much smaller, well below 10 mm. Therefore, the proposed design should be relatively insensitive to possible imperfections of the crystal quality.

References
[1] M. Yabashi, K. Tamasaku, S. Kikuta and T. Ishikawa, *Rev. Sci. Instrum.* **72**, 4080 (2001).
[2] T. S. Toellner, M. Y. Hu, W. Sturhahn, G. Borel, E. E. Alp and J. Zhao, *J. Synchrotron Rad.* **8**, 1082 (2001).
[3] Yu. Shvyd'ko, *X-Ray Optics*, Springer-Verlag Berlin Heidelberg, 2004.

Controlled dehydration of macromolecular crystals to improve diffraction properties

Principal publication and authors
J. Sanchez-Weatherby (a), M.W. Bowler (b), J. Huet (a), A. Gobbo (a), F. Felisaz (a), B. Lavault (a), R. Moya (a), J. Kadlec (a), R.B.G. Ravelli (c) and F. Cipriani (a), *Acta Cryst. D.* **65**, 1237-1246 (2009).
(a) EMBL Outstation at Grenoble (France)
(b) ESRF
(c) Leiden University Medical Center (The Netherlands)

The weakly diffracting nature of protein crystals often leads to data of insufficient quality to answer the biological question being asked, either due to a failure to solve the structure or to other factors, such as insufficient resolution to accurately determine modes of ligand binding. Methods exist to improve the diffraction properties of macromolecular crystals, dehydration often being found the most effective. Dehydration of protein crystals often has positive effects: reductions in the length of one or more unit cell dimensions are often accompanied by an increase in diffraction data resolution; a decrease in the mosaic spread and improvement in the profile of Bragg peaks. However, despite many descriptions of successful dehydration experiments and the availability of dedicated systems, the technique remains little used as conditions can be difficult to reproduce and the method can be problematic to implement. To standardise the technique, the EMBL and ESRF developed a humidity control device (HC1, **Figure 148**). Based on a modified cryostream nozzle, it produces an air stream at the sample position and allows precise control of the relative humidity (RH) between 50 and 99%. The device is fully compatible with the standard experimental environment at the ESRF and coupled with a synchrotron beamline, dehydration experiments have now become a practical way to improve the diffraction properties of some protein crystals.

The device was initially tested using bovine mitochondrial F_1-ATPase. This complex crystallises in the orthorhombic space group $P\ 2_12_12_1$ with unit cell dimensions of a = 108, b = 140 and c = 285 Å. Crystals of F_1-ATPase are known to react well to dehydration. Indeed, they are inclined to undergo spontaneous dehydration events, where the *c* cell dimension is reduced to *ca* 268 Å, after increasing the precipitant concentration or during prolonged crystal handling. This change in unit cell dimensions occurs rapidly and is favourable as it leads to an increase in intermolecular contacts within the crystal [1]. Further shrinkage of the unit cell dimensions has only been observed using controlled dehydration. Using the HC1b device it was possible to identify six 'stable' states in the dehydration pathway. The collection of low resolution data sets, at room temperature, allowed the full characterisation of these states and identified changes that occur only during dehydration. The six states were initially defined by diffraction patterns (**Figure 149**) containing well defined Bragg peaks from a single lattice with distinct unit cell parameters (if states were not stable, Bragg peaks were often split and multiple lattices existed). The final state, at an RH of 96%, diffracts to around 1 Å better than the more hydrated crystals. Once cryo-cooled, crystals in this final state have lost 20% of their unit cell volume, the number of intermolecular contacts has increased twenty-fold and they diffract X-rays to a resolution better than 2 Å, a remarkable diffraction limit for such a large complex.

The device has recently been made available to the ESRF user community and some initial successes include the chromatin remodelling complex (an improvement in resolution limit from 8 Å to 2.9 Å) and the Na$^+$-translocating NADH:quinone oxidoreductase (NQR) from *Vibrio cholerae* (an improvement in resolution limit from 6 Å to 4 Å). A particularly significant example is with crystals of plant photosystem I that have been observed to undergo a transition between their starting RH of 99% and 97%. An improvement in diffraction limit from around 6 Å to 4 Å is seen which is accompanied by visual improvements in diffraction quality. Currently, the highest resolution data measured from cryo-cooled crystals of this 530 kDa integral membrane protein is 3.4 Å. The dehydrated crystals have the potential to yield data to a significantly increased resolution. Such data would provide improved mechanistic details for this important complex.

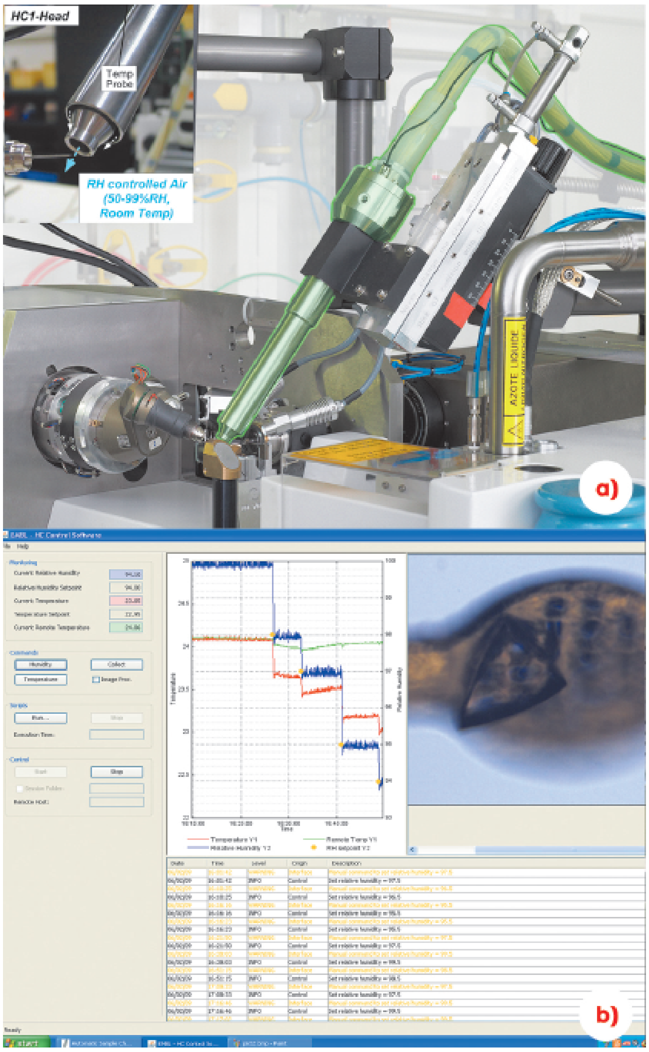

Fig. 148: a) The HC1b humidity control device mounted on an ESRF MX-Beamline. b) The HC1b GUI, a RH step gradient and a crystal being conditioned are shown.

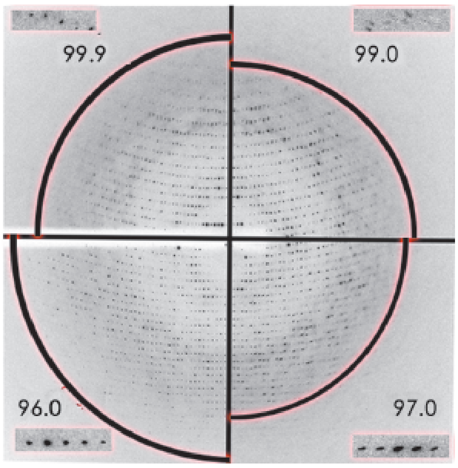

Fig. 149: Changes in X-ray diffraction of an F$_1$-ATPase crystal during dehydration in 4 steps. Each of the four quadrants of the image show the diffraction pattern at each stable dehydration stage (where the arc of the circle is at the following resolutions: 3 Å, 3.8 Å, 4 Å and 2.5 Å). The inserts show a magnified view of the same area on the detector, demonstrating the improvement in Bragg peak profile after dehydration.

As more examples are found, and as more devices are commissioned at other synchrotrons (Diamond, CLS and Max-Lab), it is hoped that general rules on dehydration protocols can be developed. The device also has promise for the collection of higher resolution data from non-cryo-cooled crystals (a new version, the HC2, will control the temperature of the air stream to 5 - 7°C) and for the on-line exchange of water in macromolecular crystals with deuterated water for neutron diffraction experiments.

Reference
[1] M.W. Bowler, M.G. Montgomery, A.G. Leslie and J.E. Walker, *Acta Cryst D* **62,** 991-995 (2006).

Authors
B Gorges, P van der Linden and H. Vitoux.
ESRF

Sample environment: development of customised microfurnaces

Over the last ten years the Sample Environment Support Service has developed a series of microfurnaces for use on the X-ray beamlines. The philosophy of the design has always been to construct a general base with a very large optical access to the sample, and adapt the furnaces to different experiments. The integration of X-ray instruments in a very small space on the beamline is often difficult, in particular for heating systems. The detector must be as close as possible to the sample; the volume of the chamber has to be just a few cm^3. Both the chamber and heater material have to be compatible with a corrosive atmosphere; the compatibility with oxygen is often demanded. The thermal load on the environment must be kept very low, so the thermal insulation of the heating element has to be optimised keeping the input of the electrical power low while the spatial stability of the sample positioning has to be maintained.

The first generation of micro-furnaces was built for the X-ray imaging beamline ID19. This microtomography furnace (Figure 150a), covering the temperature range from room temperature to 1000°C, has been designed to study the structural evolution of materials *in situ* by using synchrotron X-ray microtomography [1]. The furnace has cylindrical symmetry compatible with the required 180° rotation, small dimensions and low absorption. The quartz dome pictured in Figure 150a can easily be replaced by a cap with any other type and shape of window. This generation of furnace has demonstrated a high level of temperature stability and adaptability to the sample shape. One of the recent developments has been an open configuration in air for diffraction tomography experiments (see Figure 150b) on BM05 and ID19. In this case the sample is held in a boron nitride frame, between two silicon plates to optimise the thermal transfer to the sample.

This setup was also modified for use as a gas-flow catalysis cell because of its large diffraction angle which permitted the use of the turbo-XAS method on the dispersive EXAFS beamline ID24 [2]. For this new application, temperatures above the maximum temperature supported by the heater material were required, and so a new heater material had to be found. One of the few suitable candidates appeared to be Maxthal 211 (Ti_2AlC). This material possesses a combination of properties essential for high-temperature non-stick coating applications. It is remarkably resistant to thermal shock, wear, oxidation and corrosion; it is tough and a good electrical and thermal conductor. Our unique solution was to spot weld two stainless steel electrical connectors onto the heater disk. This permits the passage of strong currents through the system, and avoids problems encountered in the past, such as oxidation of the cell elements and electrical connection failure, that could require intervention during an experiment.

Both gas-flow catalysis cells have been developed to work in fluorescence mode for *in situ* and dynamic X-ray absorption experiments on chemical systems. The compact design of the cells and the versatility of the different components of the setup (reactor cell and cooled silicon diode) permit fine-

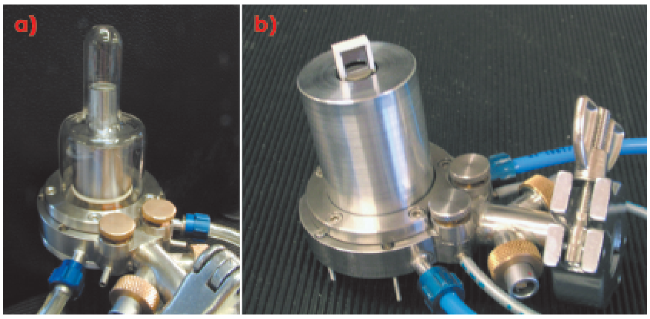

Fig. 150: a) Microtomography furnace 180° rotation. b) Customised microtomography furnace for diffraction tomography.

tuning the system so that the optimal geometrical conditions can be attained. Time-resolved studies were done on low-loaded heterogeneous catalysts under catalytic gas-flow conditions (O_2/H_2 cycles), reaching temperatures up to 850°C with an accuracy of +/-5°C. This unique set of experiments has opened new horizons for car manufacturers in the development of novel catalytic exhaust converters.

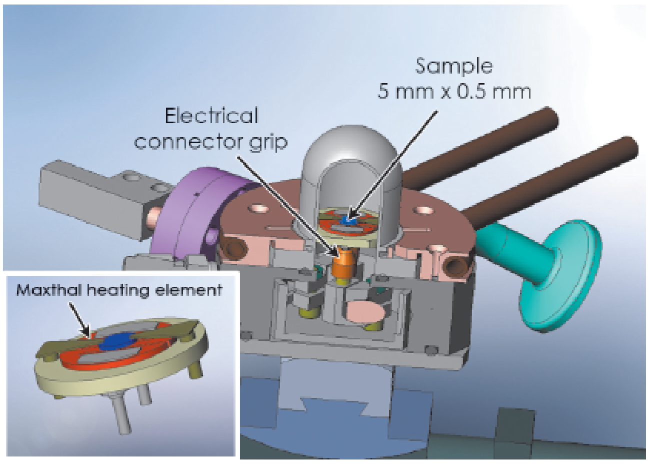

Fig. 151: Maxthal furnace for thermal annealing experiments.

This development allowed the introduction of a novel generation of furnaces aiming at higher temperatures up to 1200°C and high heating speed (see **Figure 151**). One of the main characteristics of this furnace is the miniaturisation; its diameter of 65 mm and height of 60 mm permits the furnace to be mounted on a miniature Huber 1003-MG gonimeter head. The second main characteristic is the high speed of heating and especially the possibility of cool down/quenching at 10°C/second. With this low thermal inertia, the temperature stabilisation stays at ± 0.5°C. The number of parts is kept to a minimum to guarantee good mechanical stability of the sample position. The latest furnace was designed for **ID01** for use in a study on CdS nanocluster annealing. Two different techniques, grazing-incidence small-angle scattering and grazing incidence diffraction were used to study the variation of the morphology of the system and the formation of the crystal structure.

All of the new microfurnaces have been added to the sample environment loan pool resulting in a suite of 18 different furnaces that are available for use at the ESRF beamlines. They can be requested by users and are reserved by beamline staff through the intranet sample environment loan pool application.

References
[1] D. Bellet *et al. J.Appl. Cryst.* **36**, 366-367 (2003).
[2] G. Guilera, *et al. J. Synchrotron Rad.* **16**, 628-634 (2009).

Evaluating the usability of Grid computing for synchrotron science

Authors
F. Calvelo-Vazquez, R. Dimper, A. Götz, C. Koerdt and E. Taurel.
ESRF

Grid computing is a form of geographically dispersed, loosely coupled, and distributed computing to solve very large computational or data-intensive tasks [1]. The intriguing potential of Grid technology has led the ESRF to include a specific chapter in the Purple Book based on the EGEE gLite middleware applied to future data-intensive synchrotron science experiments. Since then, the FP7 grant ESRFUP has provided the funds to conduct a detailed technical feasibility study.

Specific hardware consisting of compute nodes, file servers and Grid middleware servers were installed at ESRF, SOLEIL, PSI, and DESY to act as Grid sites in the European Grid infrastructure EGEE [2].

Each of those Grid Sites provided the following Grid middleware services: one or more Computing Elements (CE), a Storage Element (SE) to provide access to files, a User Interface (UI), a job accounting server (MONBOX), and a site resource information server (BDII). The different components were hosted in a virtualised environment and distributed over a number of Citrix-Xen servers.

The four Grid Sites (ESRF, SOLEIL, PSI, DESY) formed the Virtual Organisation (VO) X-RAY. The VO was registered in the EGEE Grid and became operational once a number of core middleware components were added, consisting of the Workload Management Server (WMS) to handle and distribute the computing jobs over the infrastructure,

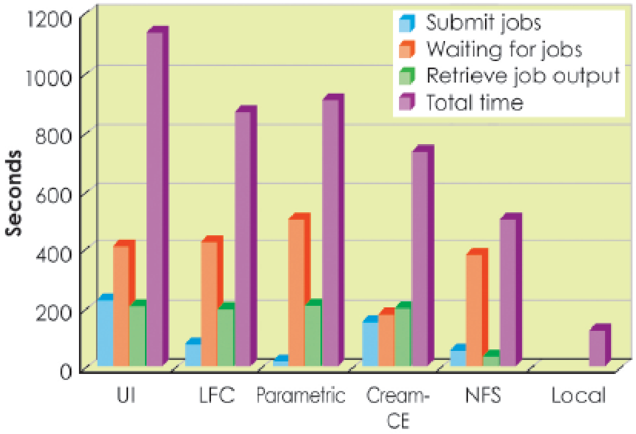

Fig. 152: Execution times of the Spatial Distortion Program (SPD, 18 runs with 10 images each) in different Grid environments and in a local environment, showing the overhead introduced by the various Grid middleware layers.

a global file catalogue (LFC), as well as the Virtual Organization Management Service (VOMS) to manage users and their access rights.

The testbed served to validate various implementations of storage resource managers (dCache and DPM) [3], data transfers with protocols such as GridFTP [4], the handling of Grid certificates, and running of synchrotron science data analysis and modelling code, which had to be ported to the Grid beforehand. From the outset we did not only test purely technical aspects, but also the user friendliness of the gLite middleware suite, knowing that user friendliness is a very important aspect when considering the large diversity of the synchrotron user community.

A typical data analysis application to correct spatial image distortions has been used among others to measure the performances within the X-RAY VO. Several cases have been tested ranging from a setup close to the classic definition of the Grid (the UI mode) to a setup close to a local cluster (the NFS mode). The outcome is summarised in **Figure 152**. Compared to running this application on a local computer, we notice a significant increase in computation time introduced by the various Grid infrastructure layers mainly due to the application data which have to be moved to and from the Computing Elements for processing.

We found out that for most synchrotron science applications the EGEE Grid is not well adapted. The main reasons for this are:

- EGEE Grids are set up as a collection of independent nodes or services and their integration is not optimised. This means data need to be transferred between Grid data storage and the worker nodes every time they are needed. This causes a large overhead over public networks which causes data intensive applications to run slower on the Grid than locally.

- The EGEE Grid is not optimised for running short jobs which are data intensive for the reasons given above. Many of the applications used in reducing or analysing synchrotron science data are short and data intensive.

- The EGEE Grid is not optimised for fast communication between worker nodes required by applications which use MPI to communicate between the distributed applications. Many modelling applications used in synchrotron science use MPI for distributing the workload.

- Public networks are still slow or unreliable for transferring large data sets even with highly optimised Grid protocols like GridFTP. Hence, the Grid is still not an ideal solution for exporting users' data or storing and sharing data via the Grid (**Figure 153**).

- Grid certificates provide a secure way to share resources with users. However they are difficult for users to understand and manage. This means they are only a solution if users really need them.

- The very concept of Virtual Organizations (VOMS) to manage user authentication was not perceived as a good model for the needs of a rather diverse community of researchers working at synchrotron installations. Typically, users asked for more fine grained security models like Access Control Lists (ACLs).

However, the Grid can be a good fit for a certain type of application:

- The EGEE Grid is optimised for running parallel applications which do not need to access data, which do not generate large data sets, and which run between 1 hour and 24 hours. A small

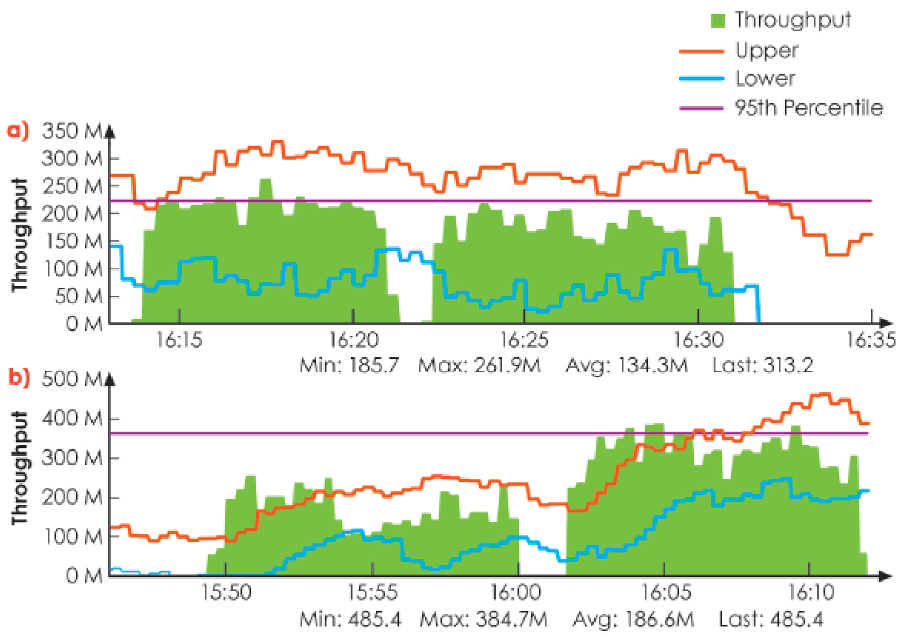

Fig. 153: a) 10-channel GridFTP transfer session (in Mbits/s) over a 1Gbit network uplink. The first green block depicts outbound connections, whereas the second is incoming data. The data transfer was done between PSI and ESRF and represents a typical best case scenario. b) Single channel IPerf tests (in Mbits/s), a measure of the available throughput capacity of a network link relying on the Transmission Control Protocol (TCP), between PSI and ESRF. The outbound performance is very similar to GridFTP, whereas the inbound performance is significantly better.

number of applications used for modelling synchrotron science data fit into this category. For this category the EGEE Grid is well suited. However, this concerns only a very small number of users.

In view of the bad overall fit of the Grid for most typical synchrotron science applications, the fact that setting up and maintaining an EGEE Grid installation is very resource intensive, and finally the fact that synchrotron science users are not limited by the currently available computing resources, we think the EGEE Grid in its current implementation is not suited for synchrotron science.

References

[1] I. Foster *et al.*, International J. Supercomputer Applications, 15(3), 2001.

[2] EGEE – Enabling Grids for E-sciencE, http://eu-egee.org.

[3] F. Donno *et al.*, *Journal of Physics: Conference Series,* **119** (2008) 062028.

[4] GridFTP, http://www.ogf.org/documents/GFD.20.pdf

MAXIPIX, a fast readout photon-counting pixel detector

X-ray scattering techniques such as XPCS, surface scattering, and SAXS require a low noise 2D detector capable of covering a large range of time and intensity scales. To meet these requirements, we have developed "MAXIPIX", a fast readout photon-counting pixel detector based on the Medipix2 [1] photon-counting readout chip developed by CERN.

Besides the photon-counting detection mode that provides essentially noise-free data, Medipix2 has other desirable qualities such as a readout dead time of less than 300 microseconds and a small pixel pitch of 55 x 55 micrometres square. These qualities make it particularly suitable for applications requiring high temporal and/or spatial resolution. To make best use of these capabilities, we developed a specific readout board called "PRIAM" for the simultaneous readout of five Medipix2 chips at their maximum speed ratings. We also developed a range of detector modules with flex cable connection to the high bandwidth PRIAM board input ports. Each module implements one or several Medipix2 chips bump-bonded to a 500 µm thick monolithic silicon pixelated sensor. Available detection surfaces are 14 x 14 mm^2 (single chip), 28 x 28 mm^2 (2x2 chips), and 71 x 14 mm^2 (5x1 chips) (**Figure 154a**). The resulting frame rate is more than 1 kHz with a single chip and up to 350 Hz with multichip modules. The PRIAM board, the detector module and their power supplies are hosted in a compact housing, resulting in the MAXIPIX detector (**Figure 154b**). MAXIPIX is

Principal publication and authors

C. Ponchut (a), J. Clément (a), J.M. Rigal (a) E. Papillon (a), J. Vallerga (b), D. LaMarra (c) and B Mikulec (d), *Nucl. Instr. and Meth. A* **576**, 109 (2007).
(a) ESRF
(b) University of California Berkeley (USA)
(c) University of Geneva (Switzerland)
(d) CERN (Switzerland, France)

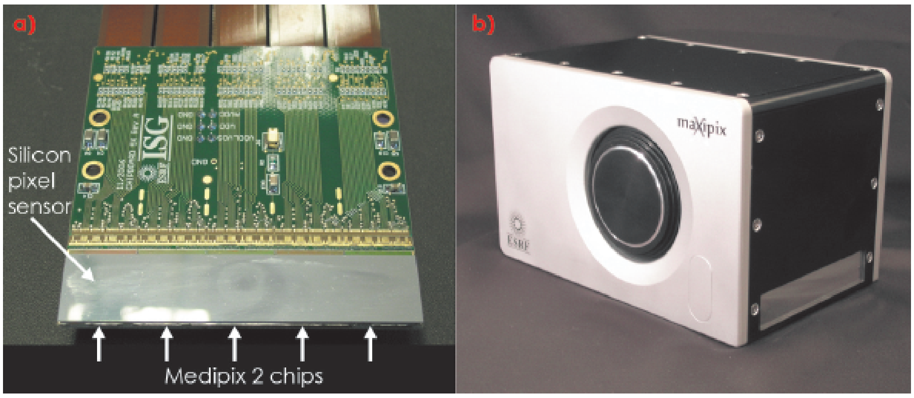

Fig. 154: a) Multi-element detector module with 5 Medipix2 chips and 1280 x 256 pixels. b) MAXIPIX detector head.

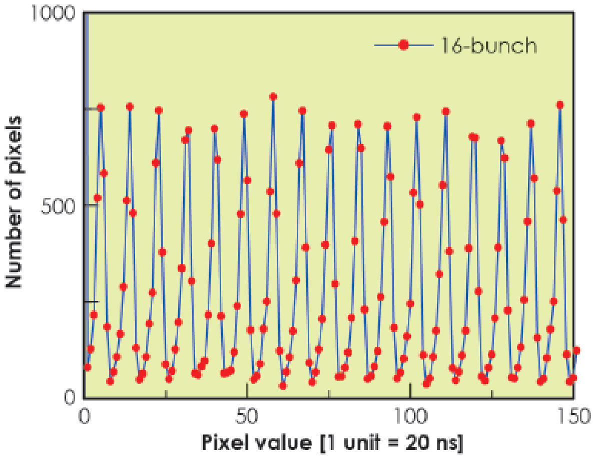

Fig. 155: Histogram of pixel values in images taken with MAXIPIX/Timepix in16-bunch machine mode, showing the time structure of the beam.

operated using a Linux-based high data rate acquisition station developed by the ESRF and achieving 1.6 Gbit/s data transfer rates.

The short readout dead time is exploited not only for high frame rate acquisition, but also for acquisition of high statistics data by frame accumulation with virtually no dead time losses.

The PRIAM readout board is also compatible with Timepix [2], a version of Medipix2 implementing a time stamping mode in addition to the standard photon-counting mode. This allowed clear resolution of the 176 ns period of the 16-bunch mode of the ESRF source (Figure 155) and opens new possibilities for time-resolved 2D detection in the 100 ns time range.

The MAXIPIX development was focused on high time and space resolutions rather than on a large physical detection area, thereby complementing other photon-counting systems like XPAD or PILATUS.

MAXIPIX is already in use at several ESRF beamlines. The principal applications are inelastic scattering (ID16), XPCS (ID10A), surface diffraction (ID03) and scattering (BM5, ID10B), coherent nanodiffraction (ID01), and micro-SAXS (ID13). In particular, the frame rate and spatial resolution characteristics proved to be particularly well suited to dynamic XPCS experiments [3], whereas the small pixel size together with the noiseless detection was exploited to improve the analyser performance on ID16 [4].

One limitation is the insufficient X-ray absorption efficiency of the silicon sensor above 20 keV. Hence our main development activity at present is focused on pixel sensors based on high-Z semiconductor materials in order to raise the energy limit to 50 keV or more. Recent tests on Medipix2 prototype modules with CdTe and GaAs sensors have shown the rapid advances made in high-Z sensor technologies. We expect to be able to deploy high-Z MAXIPIX versions to beamlines shortly. This will be of benefit to various existing applications. Moreover, it will open new perspectives, in particular in materials science and medical imaging.

In summary, we have built a versatile detector which is now routinely used on beamlines and which enabled improvements in several experimental methodologies. This provides motivation for further development programmes intended to widen the range of its applications.

Acknowledgement
The authors wish to thank the Medipix2 collaboration and in particular X. Llopart and L. Tlustos (CERN) for their advice on Medipix2 chip operation and their support in Medipix2 multichip assemblies testing.

References
[1] X. Llopart, M. Campbell, R. Dinapoli, D. SanSegundo and E. Pernigotti, *IEEE Trans. Nucl. Sci.* **49**, 2279-2283 (2002).
[2] X. Llopart, R. Ballabriga, M. Campbell, L. Tlustos and W. Wong, *Nucl. Instr. and Meth. A* **581**, 485 (2007) and erratum *Nucl. Instr. and Meth. A* **585**, 106 (2008).
[3] C. Caronna, Y. Chushkin, A. Madsen and A. Cupane, *Phys. Rev. Lett.* **100**, 055702 (2008).
[4] S. Huotari, G. Vankó, F. Albergamo, C. Ponchut, H. Graafsma, C. Henriquet, R. Verbeni and G. Monaco, *J. Synch. Rad.* **12**, 467-472 (2005).

Graphic cards on supercomputers for high performance electronic structure calculations

Authors
L. Genovese and P. Bruno.
ESRF Theory Group

Quantum mechanics and electromagnetism are widely perceived as leading to a "first-principles" approach to materials and nanosystems: if the needed software applications and corresponding hardware were available, their properties could be obtained without any adjustable parameters (nuclei characteristics being given). Still, such "first-principles" equations (*e.g.* N-body Schrödinger equation) are too complex to be handled directly. Fundamental quantities cannot be represented faithfully for N bigger than about a dozen on the computing hardware that is available today.

The Density-Functional Theory (DFT), in its Kohn-Sham single particle approach, is at present the most widely used methodology to address this problem. The complexity of the "first-principles" approach can be significantly reduced at the expense of some approximations. On the basis of such methodologies, in the eighties, it became clear that numerous properties of materials, like total energies, electronic structure, and dynamical, dielectric, mechanical, magnetic, vibrational properties, can be obtained with an accuracy that can be considered as truly predictive.

The physical properties which can be analysed via such methods are tightly connected to the computational power which can be exploited for calculation. A high-performance computing (HPC) DFT program will make the analysis of more complex systems and environments possible, thus opening a path towards new discoveries.

The deployment of massively parallel supercomputers in the last decade has opened new paths toward the exploitation of the computational power, by changing the programming paradigms in view of improved efficiency. In other words, the more computing power is available combined with code parallelisation, the better the predictions from a DFT program.

Another point is the nature of the basis set to expand the wavefunctions of the systems. The range of applications of a DFT program is tightly connected to the properties of the basis set. Non-localised basis sets like plane waves are highly suitable for periodic and homogeneous systems. Localised basis sets, like Gaussians, can achieve moderate accuracy with small numbers of degrees of freedom, but are in turn non-systematic, which may lead to over completeness and numerical instabilities before convergence is reached.

Daubechies wavelets have virtually all the properties which one might desire in view of DFT calculations. They are both orthogonal and systematic (like plane waves), and also localised (like Gaussians). In addition, they have some other properties (multi-resolution, adaptivity) thanks to which the computational operations can be expressed analytically.

BigDFT is a European project which started in 2005. Grouping four European laboratories, its aim was to build a new DFT program from scratch, based on Daubechies wavelets, and conceived to run on massively parallel architectures.

At the end of the project, in 2008, the first stable version of the BigDFT code was distributed under the GNU-GPL license, thus freely available for everyone [1]. This version was robust, and showed very good performances and excellent efficiency (about 95%, see Figure 156) for parallel and massively

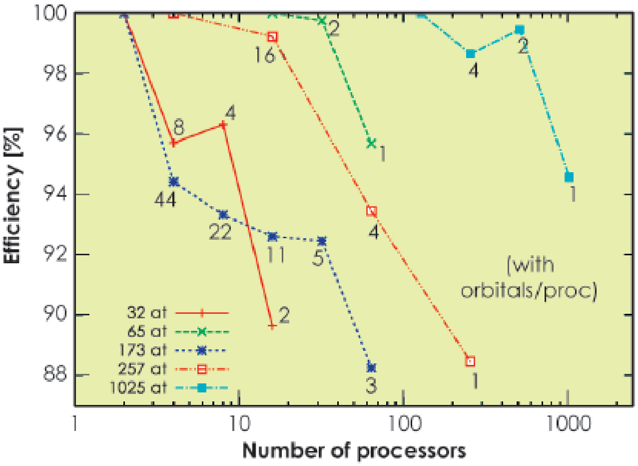

Fig. 156: Efficiency of the parallel implementation of the software for several runs with different numbers of atoms. Excellent performance (around 95%) was recorded.

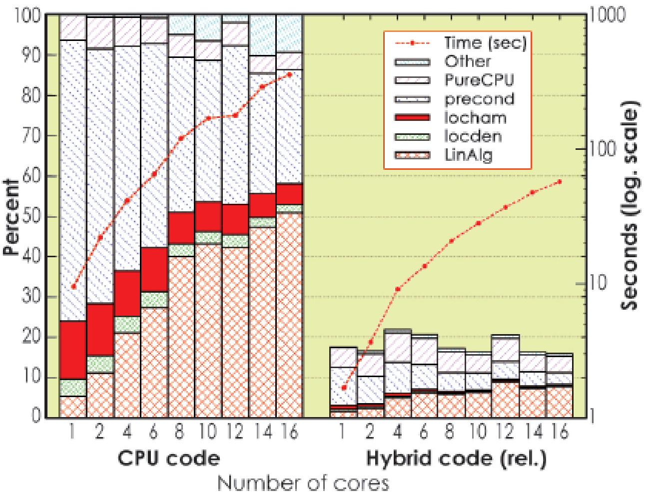

Fig. 157: Relative speed increase for the hybrid BigDFT program with respect to the equivalent CPU-only run, as a function of the number of CPU cores. A speed increase of a factor of around 6 with the hybrid CPU-GPU architecture, in double precision computation can be obtained, without altering parallel efficiency.

parallel calculations. Following this, the BigDFT code started to be used by different laboratories for high performance DFT calculations.

Recently, new emerging architectures have shown their potential for high-performance computing. The Graphics Processing Units (GPU), intitially used by the computer gaming community, can be used for general purpose calculations, among which research applications. This gives rise to the so-called "hybrid" architectures, in which several CPUs can be combined with one or more GPU, in order to further increase the computational power. The porting of different sections of the BigDFT code to run on the GPU was then performed. The first hybrid version of the code was prepared in April 2009.

The GPU-based acceleration fully preserves the efficiency of the code. In particular, the code is able to run on many cores which may or may not have a GPU associated, and thus on parallel and massively parallel hybrid machines. Considerable increases in execution speed can be achieved, between a factor of 20 for some operations and a factor of 6 for the whole DFT code (see Figure 157). Such results can however be further improved by optimising the present GPU routines, and by accelerating other sections of the code.

For the first time, a systematic electronic structure code has been able to run on hybrid (super)computers in massively parallel environments [2]. These results open a path towards the use of hybrid architectures for electronic structure calculations. Unprecedented performance can be obtained for the prediction of new material properties.

For these results, the Bull-Joseph Fourier Prize 2009 was awarded to Luigi Genovese of the ESRF Theory Group.

References
[1] L. Genovese, A. Neelov, S. Goedecker, T. Deutsch, S.A. Ghasemi, A. Willand, D. Caliste, O. Zilberberg, M. Rayson, A. Bergman and R. Schneider, *J. Chem. Phys.* **129**, 014109 (2008).
[2] L. Genovese, M. Ospici, T. Deutsch, J.-F. Méhaut, A. Neelov, S. Goedecker, *J. Chem. Phys.* **131**, 034103 (2009).

Accelerator and X-ray Source

Throughout 2009, the Accelerator and Source Division has continued its efforts to ensure reliable operation as well as preparing for the forthcoming upgrade.

A number of developments have been carried out; the most important of these are described hereafter.

Beam parameters of the storage ring

Table 2 presents a summary of the characteristics of the storage ring electron beam.

Table 3 gives the main optic functions, electron beam size and divergence at various source points. For insertion device source points, the beta functions, dispersion, sizes and divergences are calculated in the middle of the straight section.

Energy	[GeV]	6.03
Maximum current	[mA]	200
Horizontal emittance	[nm]	4
Vertical emittance (minimum achieved)	[nm]	0.025
Revolution frequency	[kHz]	355
Number of bunches		1 to 992
Time between bunches	[ns]	2.82 to 2816

Table 2: Principal characteristics of the electron beam.

Two representative source points for each type of bending magnet (even or odd number) have been selected, corresponding to observation angles of 3 and 9 mrad from the exit. The bending magnets are such that the magnetic field is 0.4 T and 0.85 T at the tangent point when the radiation is extracted at 3 and 9 mrad angles, respectively. Electron beam profiles are Gaussian and the size and divergence are presented in terms of rms quantities. The associated full width half maximum sizes and divergences are 2.35 times higher. Horizontal electron beam sizes and divergences are given for the uniform filling modes and apply to almost all filling patterns except for single bunch, for which a slightly larger size and divergence are attained because of the increased energy spread of the electron beam. Vertical electron beam sizes and divergences apply to uniform, 2 x 1/3, and hybrid filling modes only. To increase the lifetime of the stored beam, the vertical beam sizes and divergences are increased by about 50% in the 16 and 4 bunch filling patterns.

		Even ID (ID02, ID06…)	Odd ID (ID01, ID03…)	Even BM (BM02, 4,…) 3 mrad	Even BM (BM02, 4,…) 9 mrad	Odd BM (BM01, 3,…) 3 mrad	Odd BM (BM01, 3,…) 9 mrad
Magnetid Field	[T]	Variable	Variable	0.4	0.85	0.4	0.85
Horiz. beta functions	[m]	37.5	0.3	1.3	0.9	2.1	1.6
Horiz. dispersion	[m]	0.144	0.033	0.059	0.042	0.088	0.073
Horiz. rms e- beam size	[µm]	415	51	95	75	131	112
Horiz. rms e- divergence	[µrad]	10.3	108	115	111	102	97.4
Vert. beta functions	[m]	3.0	3.0	41.2	41.7	31.6	31.7
Vert. rms e- beam size	[µm]	8.6	8.6	32	32	28	28
Vert. rms e- divergence	[µrad]	2.9	2.9	1.3	1.3	0.9	0.9

Table 3: Beta functions, dispersion, rms beam size and divergence for the various source points.

Table 4: Current, lifetime, bunch length and energy spread for a selection of filling modes.

Filling pattern		Uniform	7/8 +1	Hybrid	16-bunch	4-bunch
Number of bunches		992	870	24x8+1	16	4
Maximum current	[mA]	200	200	200	90	40
Lifetime	[h]	60	65	30	16	9
Rms energy spread	[%]	0.11	0.11	0.11	0.12	0.16
Rms bunch length	[ps]	20	20	25	48	55

The lifetime, bunch length and energy spread mainly depend on the filling pattern. These are given in **Table 4** for a few representative patterns. Note that in both 16-bunch and 4-bunch filling patterns, the energy spread and bunch length decay with the current (the value indicated in the table corresponds to the maximum current). The bunch lengths are given for the usual radio frequency accelerating voltage of 9 MV (8 MV for 16-bunch and 4-bunch).

Accelerator operation

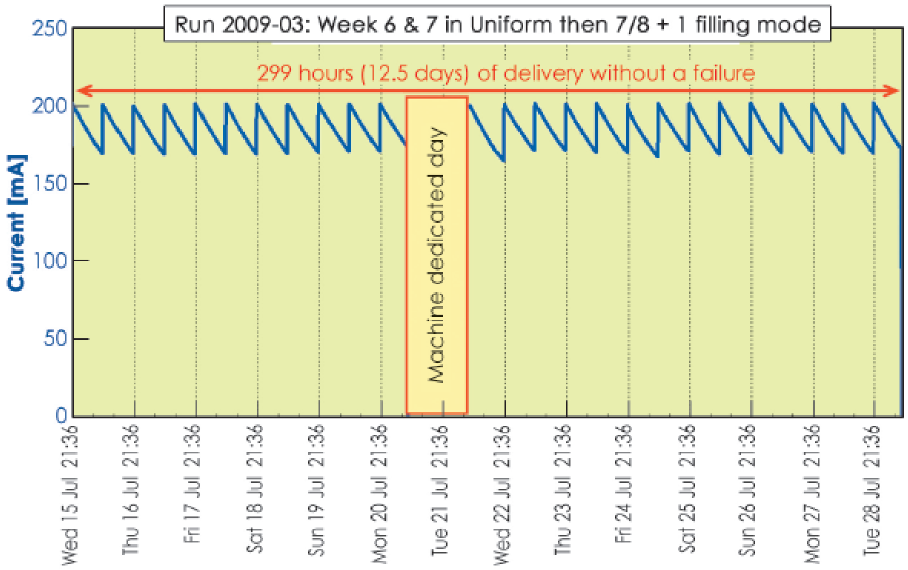

Fig. 158: An example of two weeks of delivery without a single failure, interrupted only by a scheduled Machine Dedicated Day.

In 2009, 701.5 shifts (5612 hours) of beam were initially scheduled. Of these 5612 hours, 5510 were effectively delivered (including 48 hours of refill). This represents a beam availability of 99.04%, which is a record figure in the history of the ESRF. **Table 5** presents an overview of operation in 2009.Dead time due to failures accounts for the remaining 0.96%. The number of failures is lower compared to the previous years, thus leading to an all time record Mean Time Between Failures of 75.8 hours. This excellent performance was the consequence of multiple effects including an active preventive maintenance policy as well as the protection against electrical mains drops provided by the new HQPS II system which has been operational since July 2008. Twenty long

Table 5: Overview of storage ring operation in 2009.

RUN NUMBER	TOTAL 2008	2009-01	2009-02	2009-03	2009-04	2009-05	TOTAL 2009
Start		16/01/09	27/03/09	05/06/09	21/08/09	16/10/09	
End		18/03/09	27/05/09	29/07/09	07/10/09	21/12/09	
Total number of shifts	**834**	183	183	162	141	198	**867**
Number of USM shifts	**685**	146.1	148	133	113.1	161.3	**701.5**
Beam available for users (h)	**5334.7**	1154.7	1163.7	1048.5	882.7	1260.4	**5510.1**
Availability	**98.32%**	**99.44%**	**99.34%**	**99.27%**	**98.43%**	**98.63%**	**99.04%**
Dead time for failures	**1.7%**	0.6%	0.7%	0.7%	1.6%	1.4%	**1%**
Dead time for refills	**0.97%**	0.7%	1.1%	0.7%	0.9%	0.9%	**0.9%**
Average intensity (mA)	**142.3**	154	135	182	122	142	**115**
Number of failures	**85**	12	13	11	15	23	**74**
Mean time between failures (h)	**64.5**	97.4	91.1	96.7	60.3	56.1	**75.8**
Mean duration of a failure (h)	**1.09**	0.5	0.6	0.7	0.9	0.8	**0.73**

delivery periods (*i.e.* more than 100 hours) without a single interruption took place in 2009. In particular, the last 2 weeks of the third run when the beam was delivered continuously for 12.5 days, only interrupted by the scheduled Machine Dedicated Day (**Figure 158**).

All the 2009 shutdowns were quite busy due to preparation of the upgrade including straight section lengthening, installation of a new Linac gun, new diagnostics tools, etc. The highlight of this year was the completion of the installation of the Libera BPMs (details below) with no disturbance to operation.

Filling patterns

Figure 159 presents the distribution of filling modes delivered in 2009. Compared to 2008, no significant changes were made to the distribution. The filling mode labelled "7/8 + 1" developed in 2006-2007 has become the standard multibunch mode. It provides an interesting compromise combining the benefit of a long lifetime multibunch mode while allowing time structure studies with the single bunch.

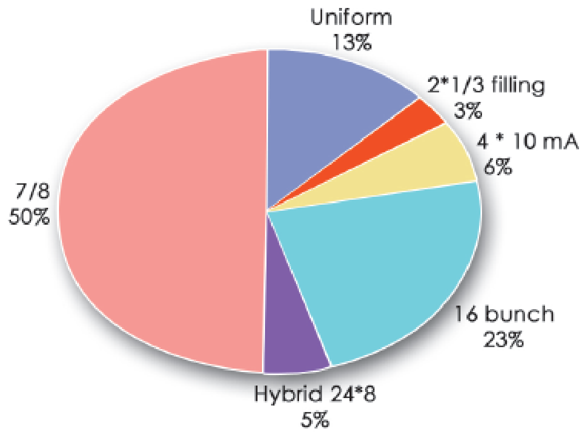

Fig. 159: Distribution of longitudinal filling modes in 2009.

A renovated linac pre-injector system

The 6 GeV electrons injected into the storage ring are accelerated by a chain of accelerator systems known as the injector system. The main components of the injector include a linear accelerator which accelerates the electrons from 90 keV to 170 MeV and a booster synchrotron which accelerates the electrons from 170 MeV to 6 GeV. The 90 keV electron beam injected into the linear accelerator is produced by a thermoionic triode electrostatic gun. A few years ago, the manufacturer of the cathodes specific to our gun design discontinued the production of these cathodes. These cathodes are rather fragile and over time lose emissivity; they need to be replaced at regular intervals. The ESRF was therefore forced to re-examine its long term strategy concerning the linac gun. The opportunity was taken to improve the gun and transport system. The chosen transport system is very similar to that developed by Thales for SOLEIL. It makes use of a triode gun design initially built for the CLIO facility at Orsay. The layout of the new gun and transfer line is shown in **Figure 160**. The removal of the old gun and transfer line and the installation and commissioning of the new one, including the control

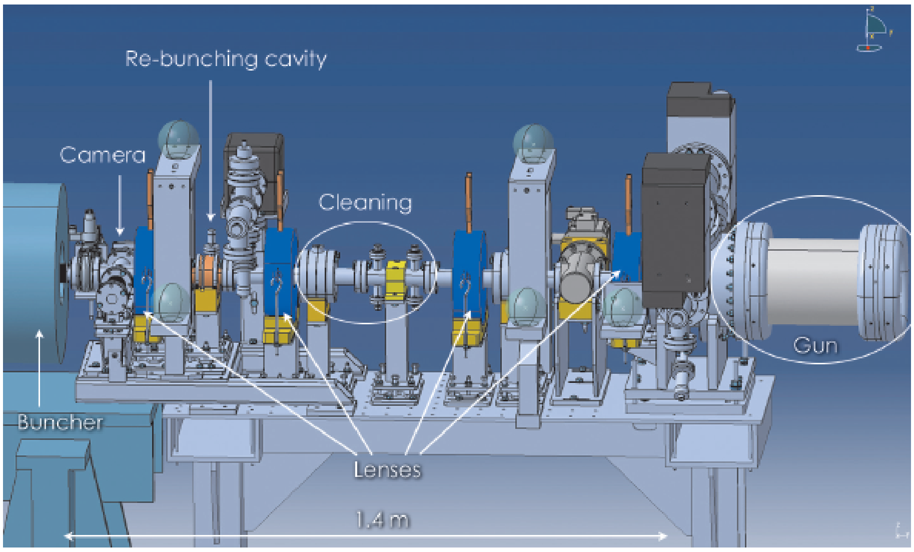

Fig. 160: Mechanical layout of the new pre-injector system.

Mode of operation	Short pulse	Long pulse
Pulse duration	1 ns	1 μs
Charge per pulse	0.5 nC	10 nC
Transverse Emittance with cleaning off/on (πmm mrad)	35/80	15
Capture Efficiency in 10 deg of ϕ	35%	52%
Capture Efficiency in 20 deg of ϕ	53%	65%
Capture Efficiency in ±1% of $\Delta E/E$	47%	62%
Cleaning efficiency	>99%	
Transmission thru the iris cleaning on.	85%	

Table 6: Performance of the new gun and transport system calculated from simulation.

system, was carried out in less than three weeks during the August 2009 shutdown. Since then, the new pre-injector system has been in permanent operation.

The electrons are emitted from a heated cathode and accelerated up to 90 KeV by a DC electric field. The current emitted by the cathode is controlled through a voltage applied to a grid located next to the cathode. The electron beam produced is transversally focused by the accelerating electric field in the gun as well as by four solenoid lenses spaced regularly along the transport line (shown in blue in **Figure 160**). Two vertically deflecting electrodes and one iris are installed between lens 2 and lens 3 (for beam cleaning). A pre-bunching RF cavity has been installed between lens 3 and 4 (for an increased capture in the linac RF field). Finally a retractable fluorescent screen has been added after lens 4 aimed at imaging the electron beam before it enters the buncher cavity (22 cell standing wave RF structure operating at 3 GHz) of the linac. Horizontal and vertical steerer coils are located in each of the four lenses. The main engineering difficulties involve the association of the high voltage needed for the acceleration in the gun, the fast pulsing of the cathode, grid and plate deflection to control the electron pulse duration and the 3 Ghz radio frequency field required for the pre-bunching cavity. Indeed, the electromagnetic compatibility of the different components has to be carefully optimised.

Table 6 shows the predicted performance of the new gun and transport system in both the short and long pulse mode of the linac operation.

While a number of the parameters predicted in **Table 6** still need detailed experimental confirmation, the initial results are in line with the predictions. It has been observed that the pre-bunching cavity enhances the capture process by a factor of two. A total transfer efficiency of 60% between the beam generated in the gun and the beam captured in the booster synchrotron has been recorded in short pulse mode (0.4 nC , 1 ns).

The transverse deflecting electrodes allow the deflection of the electron emitted by the cathode with the wrong timing in such a way that a single bunch of high purity can be captured at 352 Mhz in the booster ring before it is sent into the storage ring. This process of improving the purity in a single bunch (cleaning) is essential for some beamlines requiring special filling patterns in which a very high contrast ratio between the main and adjacent pulses is mandatory. By sending a 700 V pulse with 1.5 ns FWHM duration, it has been possible to improve the bunch purity of the previous gun by more than two orders of magnitude.

References
[1] T. Perron, E. Rabeuf, E. Plouviez, V. Serriere, A. Panzarella and B. Ogier, *EPAC'08*, http://accelconf.web.cern.ch/AccelConf/e08/papers/wepc087.pdf.

Upgrade of the electron beam position monitoring system

Minimising disturbances to the beamline users

The most essential diagnostic in the storage ring of a third generation light source is the beam position monitoring system and its associated orbit correction system. The quality of such systems largely determines the final beam stability which is of utmost importance for many beamlines.

The ESRF storage ring is equipped with 224 (32 cells x 7 BPM/cells) beam position monitors (BPMs) located at regular intervals along the ring circumference. Each BPM station is constituted of 4 insulated buttons which capture weak radio frequency (RF) signals when the electron beam is passing through. The relative amplitudes of these weak signals depend on the position of the beam. The electronics processing these signals have been in use for 17 years. They were originally developed in-house as no suitable solution was available from industry. The four weak RF signals from the BPM buttons are multiplexed, and then filtered, amplified and demodulated by a unique signal processor, including the ADC. This concept allows a number of imperfections in the signal processor to be cancelled-out. In recent years higher performance electronics have been commercially available; they make use of modern digital electronics. As part of the upgrade programme, the ESRF has decided to upgrade its BPM electronics as well as the steerers and orbit correction system. A digital electronics system named Libera-Brillance has been selected. The replacement of the old electronics by a Libera required some recabling which makes the change nearly irreversible. Following extensive tests carried out in 2008 on a few Libera systems, the decision was made to spread the replacement over a 5 month period in order to allow smooth continuous operation of the accelerator systems and the beamlines with full beam stability. One of the most critical issues was to maintain the same absolute position accuracy for every beamline before and after the BPM electronics replacement. The work took place partly during shutdown and during MDTs. As the new system gave a new positional offset for each BPM station, a precise measurement and cancellation was performed following each of the Libera electronics installation. Thirteen out of thirty-two cells were upgraded during the winter shutdown of 2008-2009. The remaining cells were upgraded during Machine Dedicated Time (MDT) in batches of one to three cells (7 to 21 BPM). This meant four hours of beam interruption during each MDT day followed by 8 hours of BPM offset measurements made with beam in the storage ring. The reproducibility of BPM positions measured before and after the upgrade as well as the very few complaints from beamlines concerning orbit changes leads us to believe that the goal of minimal disturbance to the user programme was indeed achieved.

Improved performance and functionality

The new Libera-Brilliance system yields a strongly improved performance in all modes of operation. The increased resolution and reduced noise content was most vividly demonstrated at the time when part of the storage ring had been upgraded while another part was still under the old system (see Figure 161). The system also includes functionalities like a beam position interlock (which kills the beam in case of excessive beam displacements that could damage part of the ring vacuum chambers) and various flexible buffers for data acquisition. The control of the BPMs is made through the Tango control system. It includes 224 device servers running on 4 dedicated powerful PCs running under Linux and connected to a dedicated Ethernet

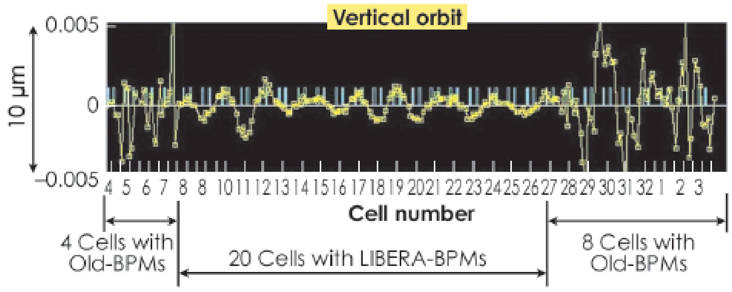

Fig. 161: Intermediate situation recorded in January 2009 with 20 out of 32 cells equipped with the new BPM electronics. The graph shows the difference between two vertical orbits along the ring circumference performed at intervals of a few seconds. The BPMs on cell 8-29 are processed with the new Libera electronics and shows orbit change in the order of 1 micrometre rms. Indeed the pattern observed is typical of that observed in a real orbit drift while the noise in each BPM sensor is much lower. The signals from BPMS 29-8 are processed with the old electronics and show a much larger noise introduced in the electronics itself.

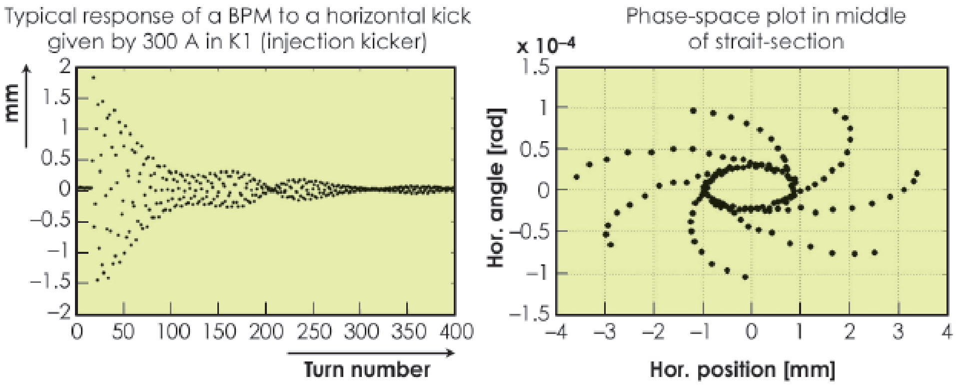

Fig. 162: a) BPM horizontal measurement turn-by-turn over 400 turns following an horizontal kick. b) Phase-space plot of the horizontal beam motion in the middle of high beta straight section of the ring reconstructed from the turn by turn data of two adjacent BPMs.

VLAN with 1 GBits links. Each BPM is controlled by a device server. On top of these 224 device servers is another Tango device server which collects all horizontal and vertical position data using Tango group calls allowing a synchronised measurement of all BPMs within 15 milliseconds.

Thanks to the highly flexible and fast digital electronics processing, several flows of data are simultaneously available with different acquisition rates and averaging, resulting in different noise levels. The normal mode of acquisition is slow acquisition (SA) in which position data is output at 10 Hz, which provides a 100 ms time integration and results in the lowest noise measurement. The SA mode is the default mode of operation based on which the orbit is corrected every 30 seconds.

Another mode is the fast acquisition (FA) mode with data processed at 10 kHz with a higher noise level and a low latency (<130 microseconds). The FA mode will be used in future DC-AC orbit correction systems stabilising time varying orbit deviations in a frequency range continuous from DC to a few hundred hertz. The 10 kHz data stream will be distributed over a network of fibre-optic links, using a dedicated broad-coast protocol which is executed in each Libera unit, to a number of processors which drive in real time the 96 corrector power supplies located all along the ring circumference.

In addition to these SA and FA modes each Libera generates data turn-by-turn at the storage ring revolution frequency of 355 kHz. This data is stored in buffers, which are synchronised within all BPM stations at precisely 9.3 ns. The turn by turn mode is interesting for several reasons. It includes orbit measurement at high frequency (up to 170 kHz). The turn by turn data is essential in the case of re-commissioning of the storage ring after major interventions. It also serves in beam dynamics studies such as phase-advance and amplitude of betatron oscillations inside the magnet lattice of the ring. **Figure 162** presents a typical horizontal position measured turn by turn over the first 400 turns on a BPM following the excitation of the beam by a horizontal kick. **Figure 162** also presents the horizontal phase space trajectory of an electron in the middle of a straight section obtained by processing the position from two adjacent BPMs.

Improved emittance measurement

Until now, the emittance measurements had essentially relied on two independent X-ray pinhole camera systems. One installed on a soft-end dipole in cell 9 (with large energy dispersion) and one on a hard-end dipole in cell 25 (low energy dispersion). These systems produce an image of the electron beam and derive the beam emittance in both horizontal and vertical planes, and also the energy spread of the electron beam. The CCD cameras of these 2 systems have been replaced with (IEEE-1394) digital cameras which have numerous advantages with respect to the previously running analog CCD. This has resulted in an improved resolution in the measured emittance.

In addition, the storage ring is equipped with 11 independent devices which measure the vertical emittance in the centre of the first dipole in cells 3, 5, 10, 11, 14, 18, 21, 25, 26, 29 and 31. They are referred to as 'In-Air-Xray' (IAX) detectors, a simple, compact and dedicated imaging device which measures the vertical divergence of the bending magnet radiation at high photon energy (170 keV). At such energies the copper absorber is largely transparent and a small part of the initial bending magnet power spectrum is transmitted in the air to the detector and produces an image. These imaging devices use the same digital cameras and device-servers as the pinhole camera system and provide emittance measurements at a rate of 15 Hz. Four new units were added in 2009. Further improvements were added to all 'IAX' detectors including an optimum choice of scintillator material and UV imaging optics, and a micro-mechanism that allows *in situ* focusing.

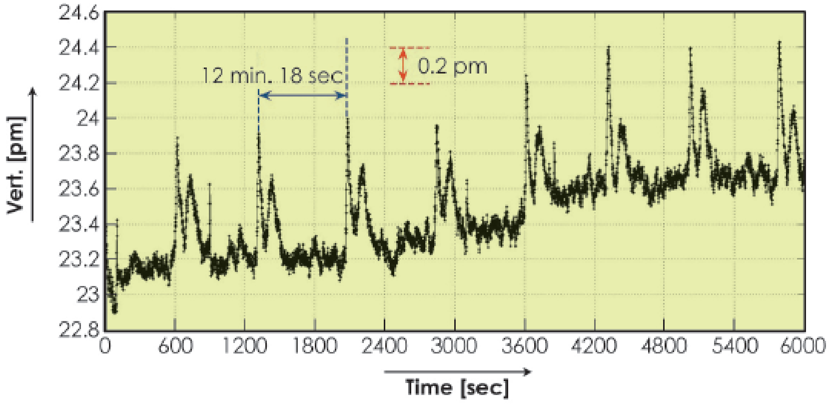

Fig. 163: Vertical emittance processed by averaging all 15 emittance measurement devices measured over a duration of 100 minutes. The averaging over the signal from all cameras allows the detection of very small emittance fluctuations. Indeed, the source of this small emittance blow-up has been identified and eliminated.

By averaging the emittance processed from the pinhole cameras as well as the the 11 IAX detectors, it is possible to detect weak emittance fluctuations such as those presented in **Figure 163** which shows a 0.5 pm emittance blow-up every 12 minutes. Using such averaging at a frequency of 1 Hz, the vertical emittance of 20 pm is measured with a resolution of 0.01 pm.

References

B.K. Scheidt *et al., Proceedings of DIPAC-2005*, p 238 (2005).
F. Epaud, Icaleps-2009, Oct. 12-16, Kobe, Japan (2009).
E.Plouviez *et al., Proceedings of DIPAC-2005*, p 84 (2005).
B.K.Scheidt, *Proceedings of DIPAC 2003*, p 125 (2005).

Facts and Figures

Members and associate countries

(as of January 2010)

Members' share in contribution to the annual budget:

27.5%	*France*
25.5%	*Germany*
15%	*Italy*
14%	*United Kingdom*
4%	*Spain*
4%	*Switzerland*
6%	*Benesync (Belgium, The Netherlands)*
4%	*Nordsync (Denmark, Finland, Norway, Sweden)*

Additional contributions

(percentages refer to Members' total contribution):

1%	*Portugal*
1%	*Israel*
1%	*Austria*
1%	*Poland*
1,05%	*Centralsync (Czech Republic 0,55%, Hungary 0,25%, Slovakia 0,25%)*

The beamlines

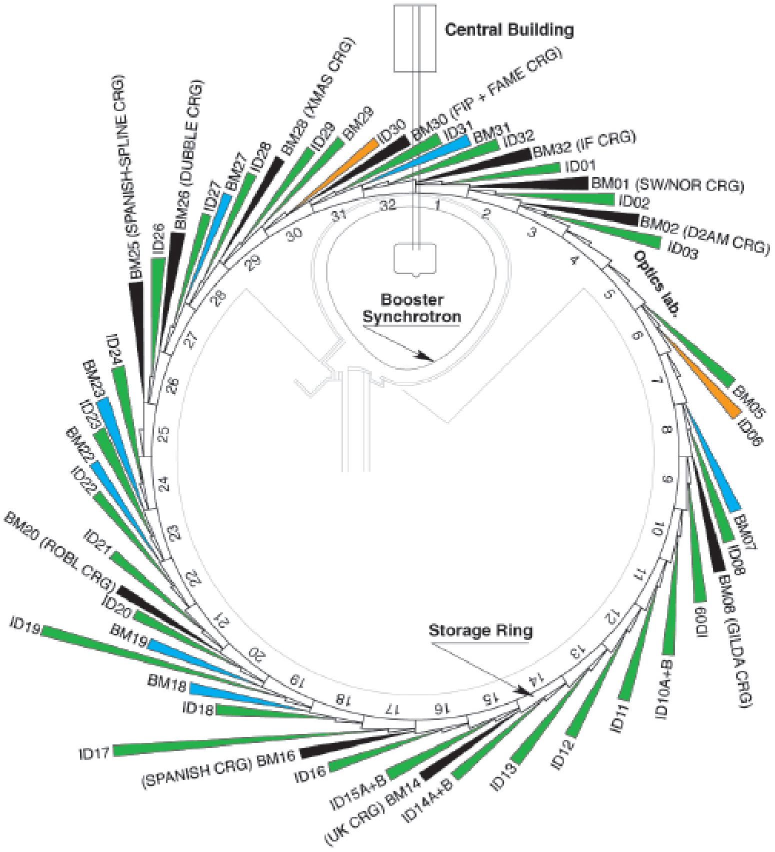

Details of the public ESRF beamlines as well as those operated by Collaborating Research Groups (CRG) are given in Tables 7 and 8. Figure 164 shows the location of the beamlines in the experimental hall.

- 🟩 *Public beamlines*
- 🟧 *Instrumentation test and development beamlines*
- ⬛ *CRG beamlines*
- 🟦 *Free bending magnet ports*

Fig. 164: Experimental hall showing location of the beamlines (public and CRG beamlines).

SOURCE POSITION	NUMBER OF INDEPENDENT END-STATIONS	BEAMLINE NAME	STATUS
ID01	1	Anomalous scattering	Operational since 07/97
ID02	1	High brilliance	Operational since 09/94
ID03	1	Surface diffraction	Operational since 09/94
ID08	1	Dragon	Operational since 02/00
ID09	1	White beam	Operational since 09/94
ID10A	1	Troika I + III	Operational since 09/94
ID10B	1	Troika II	Operational since 04/98
ID11	1	Materials science	Operational since 09/94
ID12	1	Circular polarisation	Operational since 01/95
ID13	1	Microfocus	Operational since 09/94
ID14A	2	Protein crystallography EH 1	Operational since 07/99
		Protein crystallography EH 2	Operational since 12/97
ID14B	2	Protein solution small-angle scattering EH 3	Operational since 12/98
		Protein crystallography EH 4	Operational since 07/99
ID15A	1	High energy diffraction	Operational since 09/94
ID15B	1	High energy inelastic scattering	Operational since 09/94
ID16	1	Inelastic scattering I	Operational since 09/95
ID17	1	Medical	Operational since 05/97
ID18	1	Nuclear scattering	Operational since 01/96
ID19	1	Topography and tomography	Operational since 06/96
ID20	1	Magnetic scattering	Operational since 05/96
ID21	1	X-ray microscopy	Operational since 12/97
ID22	1	Microfluorescence	Operational since 12/97
ID23	2	Macromolecular crystallography MAD	Operational since 06/04
		Macromolecular crystallography microfocus	Operational since 09/05
ID24	1	Dispersive EXAFS	Operational since 02/96
ID26	1	X-ray absorption and emission	Operational since 11/97
ID27	1	High pressure	Operational since 02/05
ID28	1	Inelastic scattering II	Operational since 12/98
ID29	1	Multiwavelength anomalous diffraction	Operational since 01/00
ID31	1	Powder diffraction	Operational since 05/96
ID32	1	X-ray standing wave and surface diffraction	Operational since 11/95
BM05	1	Optics - Open Bending Magnet	Operational since 09/95
BM29	1	X-ray absorption spectroscopy	Operational since 12/95

Table 7: List of the ESRF public beamlines.

SOURCE POSITION	NUMBER OF INDEPENDENT END-STATIONS	BEAMLINE NAME	FIELD OF RESEARCH	STATUS
BM01	2	Swiss-Norwegian BL	X-ray absorption & diffraction	Operational since 01/95
BM02	1	D2AM (French)	Materials science	Operational since 09/94
BM08	1	Gilda (Italian)	X-ray absorption & diffraction	Operational since 09/94
BM14	1	UK CRG	Macromolecular crystallography (MAD)	Operational since 01/01
BM16	1	SPANISH CRG	Structural biology (MAD, SAX)	Operational since 01/03
BM20	1	ROBL (German)	Radiochemistry & ion beam physics	Operational since 09/98
BM25	2	SPLINE (Spanish)	X-ray absorption & diffraction	Operational since 04/05
BM26	2	DUBBLE (Dutch/Belgian)	Small-angle scattering & interface diffraction Protein crystallography + EXAFS	Operational since 12/98 Operational since 06/01
BM28	1	XMAS (British)	Magnetic scattering	Operational since 04/98
BM30	2	FIP (French) FAME (French)	Protein crystallography EXAFS	Operational since 02/99 Operational since 08/02
BM32	1	IF (French)	Interfaces	Operational since 09/94

Table 8: List of the Collaborating Research Group beamlines.

User operation

After 15 years of successful operation of the facility for Users, we look back on user operation over the last year, 2009. As has been the case since midway through 2005, we once again saw the full complement of 31 public beamlines, together with 11 additional beamlines operated by Collaborating Research Groups (CRGs), available for experiments by visiting research teams.

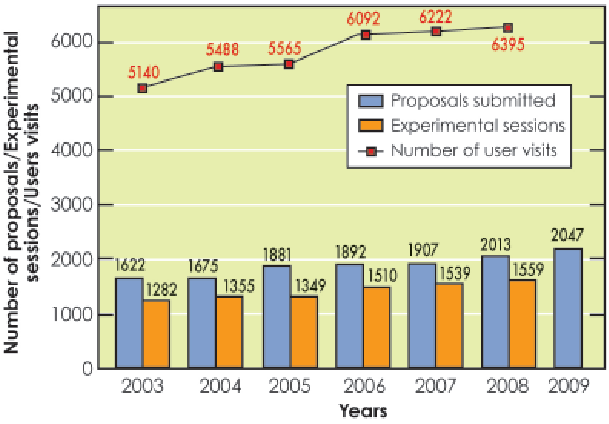

Fig. 165: Number of applications for beamtime, experimental sessions and user visits, 2003 to 2009. N.B. Final numbers of experimental sessions and user visits for 2009 were not available at the time of going to press.

Table 9: Number of shifts of beamtime requested and allocated for user experiments, year 2009.

Scientific field	Total shifts requested	Total shifts allocated
Chemistry	3 583	1 362
Hard condensed matter:		
• Electronic and magnetic prop.	4 698	2 122
• Crystals and ordered structures	3 235	1 382
• Disordered systems	1 545	603
Applied materials and engineering	3 398	1 445
Environmental and cultural heritage matters	2 548	978
Macromolecular crystallography	3 368	2 776
Medicine	1 470	678
Methods and instrumentation	784	351
Soft condensed matter	3 041	1 366
Surfaces and interfaces	3 406	1 462
Totals	**31 076**	**14 525**

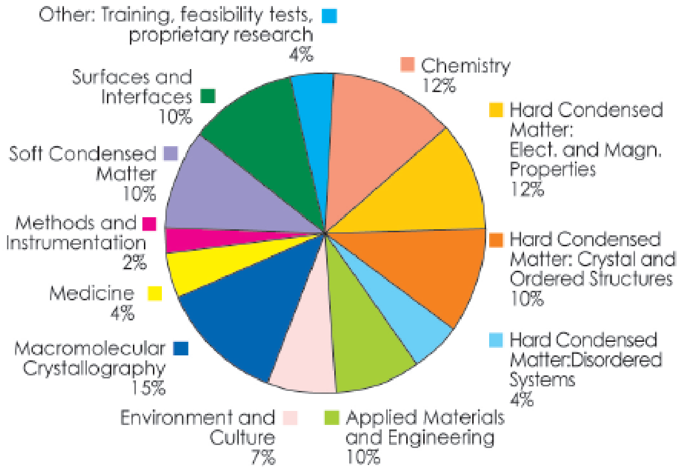

Fig. 166: Shifts scheduled for experiments by scientific area for a total of 7809 shifts, scheduling period 2009/1, March to July 2009.

Figure 165 shows the ever-increasing number of applications for beamtime received since 2003, confirming that, despite the completion of the original beamline construction programme at ESRF and the fact that more synchrotrons are now available to European scientists, there is a constantly increasing demand for use of the ESRF beamlines. The number of applications for beamtime broke through the 2000 barrier for the first time in 2008 and continued to rise still further in 2009.

Proposals for experiments are selected and beamtime allocations are made through peer review. Review Committees of specialists, for the most part from European countries and Israel, have been set up in the following scientific areas:

- chemistry
- hard condensed matter: electronic and magnetic properties
- hard condensed matter: crystals and ordered systems
- hard condensed matter: disordered systems and liquids
- applied materials and engineering
- environmental and cultural heritage matters
- macromolecular crystallography
- medicine
- methods and instrumentation
- soft condensed matter
- surfaces and interfaces.

The Review Committees met twice during the year, around six weeks after the deadlines for submission of proposals (1 March and 1 September). They reviewed a record number of 2047 applications for beamtime, and selected 929 (45.4 %), which were then scheduled for experiments.

Features of this period:

- a significant increase in the number of macromolecular crystallography (MX) rolling proposals submitted between the April and October 2009 proposal rounds – nearly 80 proposals were received and reviewed on a continuous basis under this scheme. This is mainly due to an increase in the number of proposals for the new bio-SAXS beamline, ID14-3, but also includes a significant number of proposals for online spectroscopy experiments.

- once again, in the area of Soft Condensed Matter, around half of all proposals submitted were concerned with biomaterials.

Requests for beamtime, which is scheduled in shifts of 8 hours, totalled 31 076 shifts or 248 608 hours in 2009, of which 14 525 shifts or 116 200 hours (46.7%) were allocated. The distribution of shifts requested and allocated, by scientific area, is shown in Table 9.

The breakdown of shifts scheduled for experiments by scientific area in the first half of 2009 is shown in Figure 166. This same period saw 3268 visits by scientists to the ESRF under the user programme, to carry out 809 experiments. Overall, the number of users in each experimental team averaged four persons as in 2008, and the average duration of an experimental session was 9.6 shifts compared with 10.1 shifts in 2008. This can be further broken down to show an average duration of 3.4 shifts for MX experiments and 13.9 shifts for non-MX experiments. Compared with the 2008 figures (3.4 shifts and 15.0 shifts respectively), this indicates that non-MX experiments have tended to become shorter thanks to many factors including higher automation and increased flux from state-of-the-art optics. This is also reflected in the constant rise in the annual number of experimental sessions and user visits since 2003 as shown in Figure 165, as shorter and therefore more frequent experiments become possible across almost all scientific areas.

User responses to questionnaires show once again that the ESRF continues to maintain its excellent reputation concerning the assistance given by scientists and support staff on beamlines, and travel and administrative arrangements, in addition to the quality both of the beam and of the experimental stations. Facilities on site, such as preparation laboratories, the Guesthouse and a canteen open seven days a week, also make an important contribution to the quality of user support.

J. McCarthy

Commercial activities at the ESRF

The ESRF's prime mission is an academic one: providing state-of-the-art X-ray facilities for university- and institute-based researchers. However, the requirements of industry are also an important ingredient of our missions, highlighted by the ESRF Convention signed in 1988 which accurately predicted that "*synchrotron radiation will in the future be of great significance in many different fields and for industrial applications*".

The proof of the pudding is in the eating, and since the start of ESRF operation in 1994, industrial applications of synchrotron radiation have grown enormously and now cover fields from pharmaceuticals, automotive engineering to metallurgy, cosmetics, food and mining, to name but a few. A key advantage for industry is to be able to study real systems under real operating conditions.

Industrially generated income equated to 2.9% of the ESRF's budget for 2008, with the lion's share being generated through beam time sales, and the remainder through service and material sales (mostly to other synchrotrons), and licensing income. The income is used to support around 16 staff positions (the majority for ESRF user support and operations) and reinjected into the ESRF facilities.

The ESRF deploys an Industrial and Commercial Unit (ICU) which is dedicated to relations with industry and contract management. Together with four industrial engineers (three for macromolecular crystallography and one for X-ray imaging), the ICU is the principle means of generating additional resources for the budget.

Over the last two years, the ICU interviewed all of our main industrial

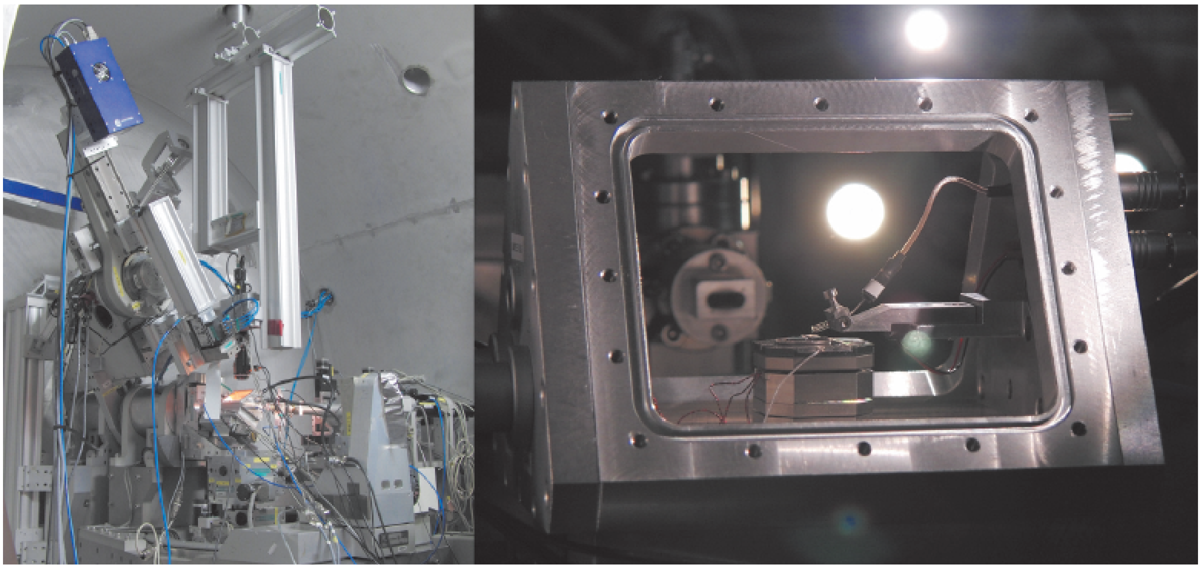

Fig. 167: A Small-Infinity atomic-force microscope installed on ID01 (*Images courtesy: T. Scheler*).

clients, mostly face-to-face, for their feedback on the ESRF industrial experience. The main positive points to emerge were the quality of the data, our scientific expertise, the speed of data acquisition and the quality of the beamlines themselves as well as our flexibility and responsiveness to client's requests. Areas for improvement included full overnight support and some compatibility problems with software on the beamlines. Points on a more practical level concerned the ICU web pages, which have recently been reworked. Feedback is always welcome at any time so we can improve the ESRF industrial experience.

During 2008 and 2009, the first spin-off from the ESRF, Small-Infinity (www.smallinfinity.com), went through the initial stages of creation, making good use of funding and advice from the Grenoble-based GRAIN and GRAVIT innovation incubators to help its development stages. Small-Infinity is founded on the commercialisation of the first atomic-force microscope that can operate directly on X-ray beamlines and is also now developing a cooled-mode device that has strong potential, particularly for biological applications. The cooling-mode technology has evolved out of the EU FP6-funded project "X-TIP" on nanoscale chemical mapping and surface structural modification by the combined use of X-ray microbeams and tip-assisted local detection. The ESRF has devices installed on beamline ID01 (**Figure 167**), already enabling exciting science, with further devices to arrive soon.

As mentioned above, the principal component of ESRF industrial income is from the sale of beam time, mainly to the pharmaceutical industry. Pharmaceutical companies use macromolecular crystallography (MX) as a core technique in drug discovery to provide detailed 3D structural information on their protein targets and binding of drug candidates and fragments. Since 2002 the ESRF has operated the MXpress™ service where clients send samples by courier for data collection on the MX beamlines. The MXpress service adds substantial value for the clients who obtain the best data possible from their samples through the experience and know-how of ESRF scientists who have handled thousands of samples. It is important to note that the development and needs of the MXpress service have provided, and continue to provide, considerable added value to the ESRF generally: automation, reliability and software improvements have all been partially driven and directed by the requirements of such an activity. Other significant contributors to the beam time income are the X-ray imaging beamlines (particularly ID19), the small-angle X-ray scattering beamline ID02, EXAFS on ID24 and powder diffraction on ID31. Samples for imaging scans and powder diffraction are often sent by courier to the ESRF, as for MXpress, for experiments to be performed by ESRF scientific staff.

Looking to the future, industrial activities will remain a useful component of the ESRF, having a strong and visible economic impact as well as providing a useful income. The new Instrumentation Services and Development Division will provide a pivotal critical mass to create long-term relationships with industry for collaborative developments, likely to lead to more transfer to industry of the ESRF's innovative technologies. When the economic climate changes for the better, the ESRF will be in a strong position to broaden its relationships and networks with industry in Europe and worldwide.

For further information on the ESRF commercial programme, proprietary beam time and opportunities, contact us at industry@esrf.eu.

E. Mitchell

Administration and finance

Expenditure and income 2008

Expenditure

		kEuro
Accelerator and Source		
Personnel		5 109.5
Recurrent		1 982.6
Operating costs	*1 506.8*	
Other recurrent costs	*475.8*	
Capital		6 088.1
Accelerator and Source Developments	*6 088.1*	
Beamlines, experiments and in-house research		
Personnel		25 962.3
Recurrent		7 566.8
Operating costs	*4 493.9*	
Other Recurrent costs	*3 072.9*	
Capital		5 524.8
Beamline developments	*3 509.5*	
Beamline refurbishment	*2 015.3*	
Technical and administrative supports		
Personnel		18 055.5
Recurrent		11 318.8
Capital		4 579.2
Unexpended committed funds		
Funds carried forward to 2009		117
Total		**86 304.6**

Income

	kEuro
2008 Members' contributions	70 711.3
Funds carried forward from 2007	0
Other income	
Scientific Associates	4 265.4
Sale of beam time	2 139.4
Compensatory funds	92
Scientific collaboration and Special projects	5 696.5
Re-injection of reserves	3400
Total	**86 304.6**

Revised expenditure and income budget for 2009

Expenditure

		kEuro
Accelerator and Source		
Personnel		5 630
Recurrent		2 250
Operating costs	*1 785*	
Other recurrent costs	*465*	
Capital		7 245
Accelerator and Source developments	*7 245*	
Beamlines, experiments and in-house research		
Personnel		21 180
Recurrent		6 325
Operating costs	*3 260*	
Other Recurrent costs	*3 065*	
Capital		7 426
Beamline developments	*5 280*	
Beamline refurbishment	*2 146*	
Technical and administrative supports		
Personnel		23 345
Recurrent		12 025
Capital		7 642
Industrial and commercial activity		
Personnel		505
Recurrent		180
Personnel costs provision		
Total		**93 753**

Income

	kEuro
2009 Members' contributions	81 686
Funds carried forward from 2008	117
Other income	
Scientific Associates	4 645
Sale of beam time	1 815
Compensatory funds	0
Scientific collaboration and Special projects	5 490
Total	**93 753**

The budget for 2009 includes additional contributions from Members and Scientific Associates of 9 455 kEuro dedicated to the Upgrade Programme. The Upgrade expenditure budget amounts to a total of 11 045 kEuro including 1 550 kEuro of ESRF operating budget.

Expenditure 2008 by nature of expenditure

	kEuro
PERSONNEL	
ESRF staff	47 108.8
External temporary staff	103.3
Other personnel costs	1 915.2
RECURRENT	
Consumables	7 705.6
Services	10 535.9
Other recurrent costs	2 626.8
CAPITAL	
Buildings, infrastructure	2 359.3
Lab. and Workshops	473.6
Accelerator and Source incl. ID's and Fes	6 088.1
Beamlines, Experiments	5 524.8
Computing Infrastructure	1 584.2
Other Capital costs	162
Unexpended committed funds	
Funds carried forward to 2009	117
Total	**86 304.6**

Revised budget for 2009 by nature of expenditure

	kEuro
PERSONNEL	
ESRF staff	48 595
External temporary staff	85
Other personnel costs	2070
RECURRENT	
Consumables	8 280
Services	10 015
Other recurrent costs	2 485
CAPITAL	
Buildings, infrastructure	2 940
Lab. and Workshops	400
Accelerator and Source incl. ID's and Fes	7 500
Beamlines, Experiments	8 886
Computing Infrastructure	2 177
Other Capital costs	320
Total	**93 753**

Financial resources in 2007, 2008, 2009 and 2010, by major programme

(current prices in MEuro for the respective years)

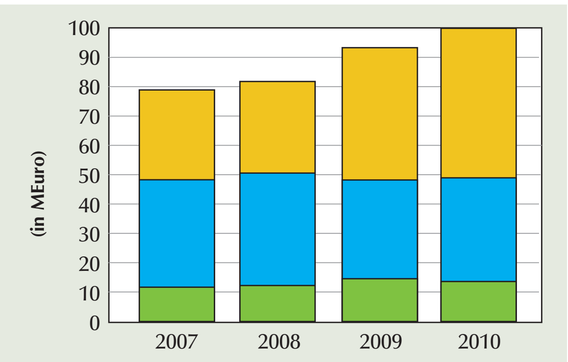

Financial resources in 2007, 2008, 2009 and 2010, by nature of expenditure

(current prices in MEuro for the respective years)

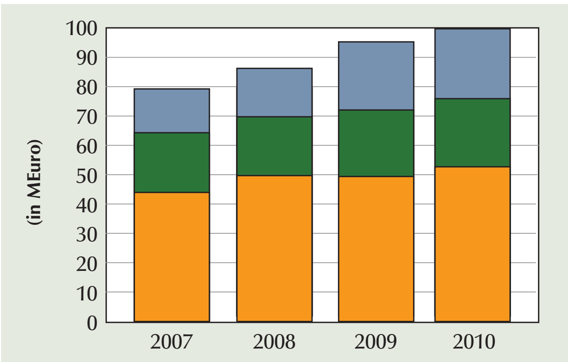

2009 manpower *(posts filled on 31/12/2009)*

	Scientists, Engineers, Senior Administrators	Technicians and Administrative Staff	PhD students	Total
Staff on regular positions				
Accelerator and Source	31	37.4		68.4
Beamlines, instruments and experiments*	228	84.3	23.5	335.8
General technical services	30.6	53		83.6
Directorate, administration and central services	36.5	52.2		88.7
Sub-total	*326.1*	*226.9*	*23.5*	*576.4*
Other positions				
Short term contracts	5.7	10.4		16.1
Staff under "contrats de qualification" (apprentices)		25		25
European Union grants	5			5
Temporary workers				
Total	**336.7**	**262.3**	**23.5**	**622.5**
Absences of staff (equivalent full time posts)				20
Total with absences				*602.5*
Scientific collaborators and consultants	*8*			*8*
External funded research fellows	*4*		*24*	*28*

** Including scientific staff on time limited contract.*

Organisation chart of the ESRF

(as of January 2010)

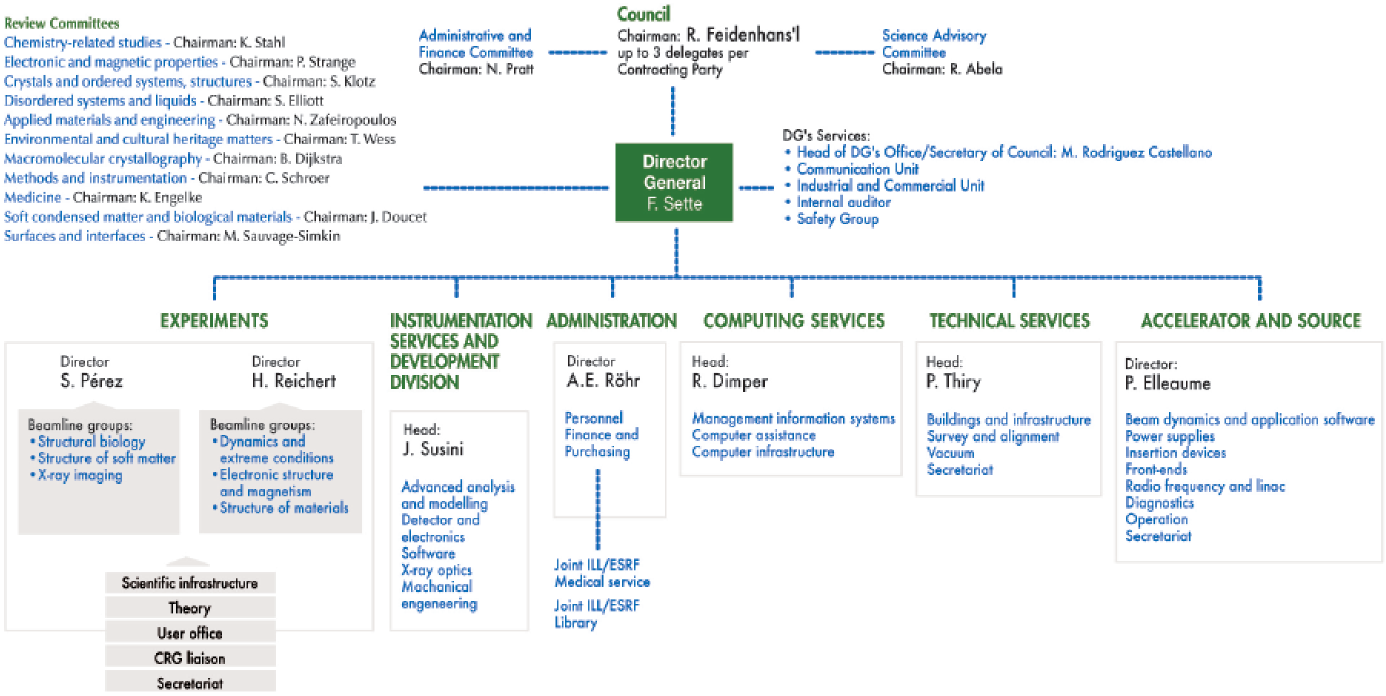

Review Committees

Chemistry-related studies - Chairman: K. Stahl
Electronic and magnetic properties - Chairman: P. Strange
Crystals and ordered systems, structures - Chairman: S. Klotz
Disordered systems and liquids - Chairman: S. Elliott
Applied materials and engineering - Chairman: N. Zafeiropoulos
Environmental and cultural heritage matters - Chairman: T. Wess
Macromolecular crystallography - Chairman: B. Dijkstra
Methods and instrumentation - Chairman: C. Schroer
Medicine - Chairman: K. Engelke
Soft condensed matter and biological materials - Chairman: J. Doucet
Surfaces and interfaces - Chairman: M. Sauvage-Simkin

Administrative and Finance Committee
Chairman: N. Pratt

Council
Chairman: R. Feidenhans'l
up to 3 delegates per Contracting Party

Science Advisory Committee
Chairman: R. Abela

Director General
F. Sette

DG's Services:
- Head of DG's Office/Secretary of Council: M. Rodriguez Castellano
- Communication Unit
- Industrial and Commercial Unit
- Internal auditor
- Safety Group

EXPERIMENTS

Director
S. Pérez

Beamline groups:
- Structural biology
- Structure of soft matter
- X-ray imaging

Director
H. Reichert

Beamline groups:
- Dynamics and extreme conditions
- Electronic structure and magnetism
- Structure of materials

Scientific infrastructure
Theory
User office
CRG liaison
Secretariat

INSTRUMENTATION SERVICES AND DEVELOPMENT DIVISION

Head:
J. Susini

Advanced analysis and modelling
Detector and electronics
Software
X-ray optics
Machanical engeneering

ADMINISTRATION

Director
A.E. Röhr

Personnel
Finance and Purchasing

Joint ILL/ESRF Medical service

Joint ILL/ESRF Library

COMPUTING SERVICES

Head:
R. Dimper

Management information systems
Computer assistance
Computer infrastructure

TECHNICAL SERVICES

Head:
P. Thiry

Buildings and infrastructure
Survey and alignment
Vacuum
Secretariat

ACCELERATOR AND SOURCE

Director:
P. Elleaume

Beam dynamics and application software
Power supplies
Insertion devices
Front-ends
Radio frequency and linac
Diagnostics
Operation
Secretariat

Cover
Design by M. Collignon. Featured images: a) Structure of the η-phase of oxygen, L.F. Lundegaard *et al.*, p 10;
b) Structure of A-amylose by synchrotron microdiffraction of crystals, D. Popov *et al.*, p 64;
c) Dendritic solidification in an aluminium alloy observed by 3D microtomography, N. Limodin *et al.*, p 109;
d) DNA binding to a protein drUvrA involved in DNA damage recognition, J. Timmins *et al.*, p 99.

We gratefully acknowledge the help of:

C. Argoud, J. Baruchel, S. Blanchon, B. Boulanger, N.B. Brookes, K. Clugnet, M. Collignon, E. Dancer, R. Dimper, P. Elleaume, A. Fitch, K. Fletcher, P. Gaget, L. Graham, C. Habfast, E. Jean-Baptiste, A. Kaprolat, M. Krisch, G. Leonard, J. McCarthy, E. Mitchell, T. Narayanan, S. Pérez, H. Reichert, M. Rodriguez Castellano, F. Sette, C. Stuck, J. Susini, S. McSweeney, K. Wong and all the users and staff who have contributed to this edition of the Highlights.

Editor
G. Admans
Layout
Pixel Project
Printing
Müllerdruck Mannheim GmbH & Co. KG

Communication Unit
ESRF
BP220 • 38043 Grenoble • France
Tel. +33 (0)4 76 88 20 56 • Fax. +33 (0)4 76 88 25 42
http://www.esrf.eu